Simone Di Cataldo, BSc, MSc

Ab initio materials design of superhydrides: a quest to high-T_c superconductivity at room pressure

PhD Thesis

to achieve the university degree of

Doctor of Philosophy

PhD degree programme: Physical Sciences

submitted to

Graz University of Technology
Sapienza University of Rome

Supervisors

Univ.-Prof. Dr. Lilia Boeri
Univ.-Prof. Dipl.-Ing. Dr.rer.nat. Wolfgang von der Linden

Institute of Theoretical and Computational Physics
Head: Univ.-Prof. Dipl.-Ing. Dr.rer.nat. Wolfgang von der Linden
Dipartimento di Fisica
Head: Univ. Prof. Dr. Paolo Mataloni

Roma, October 2021

Affidavit

I declare that I have authored this thesis independently, that I have not used other than the declared sources/resources, and that I have explicitly indicated all material which has been quoted either literally or by content from the sources used. The text document uploaded to TUGRAZonline is identical to the present PhD thesis.

12/11/2021

Date

Signature

Don't you understand that we need to be childish in order to understand? Only a child sees things with perfect clarity, because it hasn't developed all those filters which prevent us from seeing things that we don't expect to see.

Dirk Gently's Holistic Detective Agency - Douglas Adams

Sometimes science is more art than science, Morty. Lot of people don't get that

---

Rick Sanchez - Rick and Morty, S1E6

Contents

Abstract

This thesis presents a collection of my main results I obtained studying high-pressure superhydrides, using first-principles methods for crystal structure prediction and superconductivity. *Superhydrides*, i.e. compounds which under high pressure (over a million atmospheres) incorporate a large amount of hydrogen in their crystal structure, are extremely exciting. Among them, superconductors with critical temperatures (T_c's) close to, or even above room temperature were found. In less than one decade, the study of superhydrides has achieved ground-breaking results, and have given rise to a very active research community. This rapid progress was largely driven by an extremely successful synergy between first-principles calculations based on Density Functional Theory and high-pressure experiments.

During the course of my thesis, the focus of the field shifted from finding materials with higher and higher superconducting T_c's, to the search for ambient-pressure high-T_c superconductors, which may find their way into technological applications. In this regard, the attention is shifting from binary to *ternary* hydrides, containing two elements other than hydrogen.

This thesis, based on the results contained in four papers published in 2018-2021, presents my research efforts in this direction. The main research goal was to deepen the understanding of the essential features that lead to the formation of high-T_c hydride superconductors, with the overarching goal of reaching high-T_c superconductivity at ambient pressure. After a general introduction to the history and open questions in the field, I discuss in some detail the theoretical foundations of methods for crystal structure prediction and superconductivity employed in the thesis. These methods are applied in the second part of the thesis to the study of three different systems: sodalite-like yttrium hydrides, calcium boron hydrides, and lanthanum ternary hydrides. The hope of the author is that some of the ideas outlined in this thesis will stimulate future research in ternary hydrides.

Kurzfassung

Diese Dissertation umfasst eine Sammlung der wichtigsten Ergebnisse, die ich bei der Untersuchung von Hochdruck-Superhydriden mithilfe von Ab-initio-Methoden für die Kristallstrukturvorhersage sowie für die Supraleitung erzielt habe. Superhydride sind äußerst interessante Verbindungen, die unter hohem Druck (über eine Million Atmosphären) eine große Menge Wasserstoff in ihre Kristallstruktur einbauen. Unter ihnen wurden Supraleiter mit kritischen Temperaturen (T_c) nahe oder sogar oberhalb der Raumtemperatur gefunden. In weniger als einem Jahrzehnt wurden bei der Untersuchung von Superhydriden bahnbrechende Ergebnisse erzielt, die zur Bildung einer sehr aktiven Forschungslandschaft geführt haben. Dieser rasche Fortschritt wurde maßgeblich durch eine extrem erfolgreiche Synergie zwischen dichtefunktionaltheoriebasierten Ab-initio-Berechnungen und Hochdruckexperimenten ermöglicht.

Im Laufe meiner Arbeit verlagerte sich der Forschungsschwerpunkt von der Suche nach Materialien mit immer höheren supraleitenden T_c-Werten auf die Suche nach Umgebungsdruck-Hochtemperatursupraleitern, die Einzug in technische Anwendungen finden könnten. In diesem Zusammenhang verlagert sich der Fokus von binären zu ternären Hydriden, die neben Wasserstoff zwei andere Elemente enthalten.

Die vorliegende Dissertation beruht auf den Ergebnissen von vier veröffentlichten Artikeln aus den Jahren 2018 bis 2021 und stellt meine Forschungsbemühungen in diesem Fachgebiet dar. Das Hauptforschungsziel bestand darin, das Verständnis über die entscheidenden Faktoren zu vertiefen, die zur Bildung von Hochtemperatursupraleitern führen, mit dem übergeordneten Ziel, Hochtemperatursupraleitung bei Umgebungsdruck zu erreichen. Nach einer allgemeinen Einführung in die Geschichte und die offenen Fragen dieses Gebiets werden die theoretischen Grundlagen der in dieser Arbeit verwendeten Methoden im Detail erläutert. Die beschriebenen Methoden zur Kristallstrukturvorhersage sowie zur Berechnung der supraleitenden Eigenschaften werden im zweiten Teil der Arbeit auf drei verschiedene Systeme angewandt: Sodalith-artige Yttriumhydride, Calcium-Bor-Hydride und ternäre Lanthanhydride. Der Autor hofft, dass einige der in dieser Arbeit dargelegten Ideen die künftige Forschung im Bereich der ternären Hydride anregen werden.

Chapter 1

Introduction

In this thesis, I[1] will present the results of my research of high-temperature superconductivity in hydrogen-rich systems at high pressure (superhydrides), obtained with state-of-the-art methods for crystal structure prediction and superconductivity; superhydride research is an extremely lively field, in which I worked during a period characterized by many exciting discoveries.

Superconductivity is a physical state of matter characterized by zero DC resistivity and perfect diamagnetism. This phenomenon appears below a certain *critical* temperature (T_c), which for most materials is of the order of a few Kelvins. Very few phenomena were able to align the interests of applied and fundamental research as much as superconductivity. On one hand, it is a marvelous phenomenon where a coherent quantum state manifests on a macroscopic scale. On the other hand, there is a large number of technological applications which rely on the transport and magnetic properties of superconductors or would benefit from them, such as devices for nuclear magnetic resonance, fusion reactors, lightweight electrical motors, lossless power cables, or even coils for energy storage. The main obstacle to the large-scale commercialization of these technologies is the extremely high refrigeration cost, and this explains why so much effort has gone towards the research of high-temperature superconductors (high-T_c), i.e. compounds with a T_c higher than 77 K, which is the boiling point of liquid nitrogen.

Superhydrides, in particular, are one of the few systems which realize high-T_c superconductivity: several compounds with T_c's close to, or even above, room temperature were discovered in the last six years only, such as H_3S (203 K), LaH_{10} (260 K), and $C_xS_yH_z$ (287 K) [1–6]. For the first time in the history of superconductors, *superhydrides* were discovered thanks to a strong synergy between theory and experiment: computational studies based on crystal structure prediction methods and Density Functional Perturbation Theory, were able to indicate to experimentalists the materials

[1] I chose to write the thesis using the first singular pronoun *I*, which I find much clearer, albeit less formal. The results, interpretation, and decisions described in this thesis were all made as a group effort, under the supervision of Prof. Boeri, and with the collaboration of my esteemed colleagues. The choice of using the first person throughout the thesis is a merely stylistic one, and should not be interpreted as a claim of ownership.

where high-T_c could be found, dramatically accelerating the rate of discovery. In contrast to the two other classes of known high-T_c superconductors, i.e. cuprates and Fe-based superconductors, hydrides are phonon-mediated superconductors, described by conventional Migdal-Éliashberg theory, and hence their superconducting properties can be predicted entirely from first principles using Density Functional Perturbation Theory. Together with methods for crystal structure prediction, this offers the remarkable possibility of designing superconductors entirely from first principles.

In this thesis I report the results of my research work on superhydrides over the years between 2018 and 2021; a period of time during which LaH_{10} and $C_xS_yH_z$ were discovered, and new questions arose. In general, the main research goals of my thesis can be summarized as follows: 1) the development of an intuition on how the high-T_c/low-pressure results from the elementary properties of atoms (size, electronegativity, valence) and 2) the prediction of a high-T_c superconductor at room pressure. The first goal is motivated by curiosity, trying to explain how the complex and wonderful behavior of nature emerges from the simple properties of elements; the second is driven by the profound impact that the use of high-T_c superconductors could have in many sectors, from healthcare to climate change. During the course of this thesis it became clear that high-T_c can be found in several binary hydrides, but only at very high pressure, hence the major challenge is the stabilization of high-T_c hydrides at ambient pressure.

Among all compounds investigated, a crucial role in the stabilization of superconducting structures seems to be played by the size of the non-hydrogen atoms, e.g. their covalent radius, while their valence and electronegativity is less crucial, as long as the electronegativity is less than that of hydrogen. Although I did not find an ambient-pressure hydride superconductor, I predicted the formation of a high-T_c ternary hydride ($LaBH_8$) at a pressure much lower than previously known hydrides, which leads me to believe that the research I have carried out goes in the right direction. In the next years, interest on ternary hydrides is most likely going to grow, especially if hydride superconductors are predicted at low or ambient pressure, so that experiments will be accessible to many more worldwide groups.

1.1 Structure of the thesis

As shown in Fig. 1.1, the thesis is divided into two parts, .

Part I supplies the relevant experimental and theoretical background information. After a brief historical introduction of the theoretical and experimental advances leading to the discovery of superconductivity in superhydrides (Chapter 2) I will review the main theoretical methods employed in the thesis: crystal structure prediction (Chapter 3) and the theory of conventional superconductivity (Chapter 4).

Part II of this thesis contains my original results on *ab initio materials design of superhydrides*,

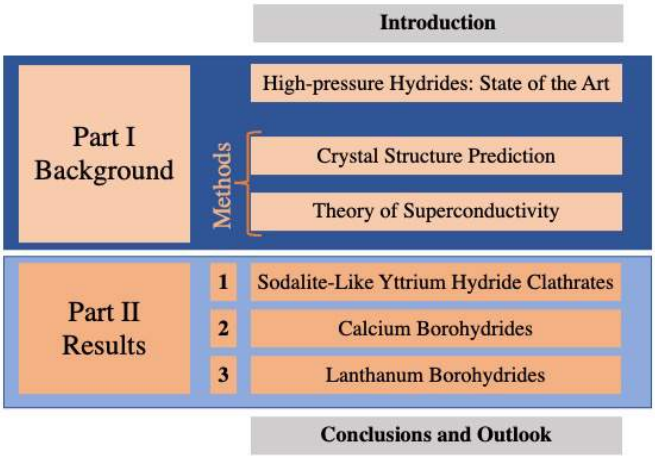

Figure 1.1: Structure of this PhD thesis

which form the basis of the four research articles listed in Appendix A [7–10]. The final goal is the realization of *conventional* high-T_c superconductivity at room pressure, which necessarily has to go through the understanding of how the basic properties of elements affect the formation of high-temperature superconductors.

In Chapter 8, I will draw the conclusions, and shortly discuss future outlooks.

Further details are given in the **Appendices**. In particular, in Appendix A I list the papers published during this thesis, in Appendix B I review the derivation for the Morel-Anderson pseudopotential, in Appendix C I reported the computational details of the studies reported in Chapters 5-7, and in Appendix D I reported two sample input files for programs I employed for crystal structure prediction (`Uspex`), and for solving the anisotropic Migdal-Éliashberg equations.

A summary of the Chapters is given below.

Part I: Background

Chapter 2 contains a historical review of the evolution of the field of superconductivity, leading to the discovery of superhydrides. The research field of superconductivity in hydrides is extremely recent, but the idea that hydrogen-rich materials could exhibit high-T_c superconductivity is rather old. It was first pointed out in 1968/1969 by Neil Ashcroft [11] and Vitaly Ginzburg [12] that, according to BCS theory, an atomic phase of hydrogen should be a high-temperature superconductor.

In fact, due to the light atomic mass and the lack of screening from core electrons, a hypothetical metallic hydrogen phase would exhibit at the same time high phonon frequencies, and relatively strong electron-phonon coupling. Such a phase had been predicted to form at high pressure by Wigner and Huntington at about 35 GPa [13], but metallization of hydrogen turned out to require pressures at least one order of magnitude higher, and has been a major experimental challenge for over fifty years. In the last five years, several groups have reported hints of metallization [14–16]. Nevertheless, in the 70s Ashcroft's hypothesis inspired some early research on metallic hydrides (first *hydride rush*), with T_c's up to 16 K [17, 18]. A few years later, Cohen and Anderson, using empirical arguments based on the theory of conventional superconductivity, calculated a maximum value of about 25 K for the T_c of any phonon-mediated superconductor [19], discouraging research of high-T_c superconductors, with the notable exception of the Soviet Union [20]. The Cohen-Anderson limit was not disproved by the discovery of high-T_c cuprates in 1986 [21], since in this case superconductivity is of *unconventional* origin. A crucial turning point in the history of conventional superconductivity was the discovery of superconductivity at 39 K in magnesium diboride [22], for two reasons. First, because it disproved the Cohen-Anderson limit. Second, because it represented a crucial test for the accuracy of computational methods that had been developed for conventional superconductors. The theory of phonon-mediated superconductivity, extended to the strong-coupling limit, had been fully developed already in 1960 by Migdal and Éliashberg [23, 24]. However, until the late 90's the spectral distribution of electron-phonon interactions (also called Éliashberg function) could not be calculated from first principles, due to the lack of computational power. The first large-scale calculation of superconducting properties of elemental metals dates to 1996 (Savrasov and Savrasov [25]). In MgB_2, not only the T_c was reproduced with considerable accuracy, but also its nature of a two-gap superconductor was correctly predicted by DFT and then measured [26]. First-principles calculations also permitted to identify the mechanism leading to its relatively high T_c, as originating from *metallic covalent bonds* [27]. The return of the research interest on hydrides can be dated back to 2004 with a second publication by Ashcroft [28], who conjectured that hydrogen-rich materials could behave similarly to atomic hydrogen but at much lower pressure, as the other elements would induce a form of *chemical precompression*, by favoring the dissociation of the molecular H_2 bond, whose strength represents the main obstacle to metallization. Thanks to the progress in experimental and theoretical methods, it was possible to test this hypothesis, leading to the first *ab initio* studies on hydrides, such as silicon and gallium hydrides (second *hydride rush*) [29–33].

Following Ashcroft's predictions, one of the first materials to be investigated was silane (SiH_4) [29, 30]. The experiments found evidence of superconductivity with a T_c of 17 K at 96 GPa [34], although the origin of the measured T_c was debated [35].

Using crystal structure prediction and Density Functional Perturbation Theory (DFPT), re-

searchers had a reproducible and unbiased method to identify the crystal structure, and predict its T_c. Then, experimentalists would focus on the most interesting materials; moreover, the development of the Diamond Anvil Cell (DAC) had streamlined the experimental investigation of materials under high pressure. It was following this approach that, in 2014, a structure with H_3S composition and a T_c of 203 K at 200 GPa was discovered by the group of Mikhail Eremets [1,2]. This discovery decisively disproved the Cohen-Anderson limit, and proved the value of *ab initio* calculation as a mean of accelerating discoveries. Following the discovery of H_3S, the computational exploration of all possible binary hydrides was completed in less than five years, leading to the experimental discovery of many more hydride superconductors (LaH_{10}, YH_6, ThH_{10}, CeH_{10}, UH_7) [4,5,36–41]. The experimentally measured T_c's versus time are summarized in Fig. 1.2. The discovery of LaH_{10} was particularly significant. It demonstrated that H_3S was not an isolated case, and consolidated superhydrides as the most exciting research field for superconductivity, marking the start of the third *hydride rush*, which lasts until today. During the last two years, the focus of research has shifted towards *ternary* hydrides. Indeed the spectacular result of room-temperature superconductivity (287 K) was measured in a hydride of carbon, sulfur and hydrogen [6]. Ternary hydrides currently represent the frontier of materials research, pushing the computational methods to their limit, and very few *ab initio* studies have been performed on ternaries [8,9,42,43], two of which are reported in this thesis. The presence of a third element greatly increases the complexity and the computational cost of crystal structure prediction, and improvements in this direction represent one of the leading edges of research.

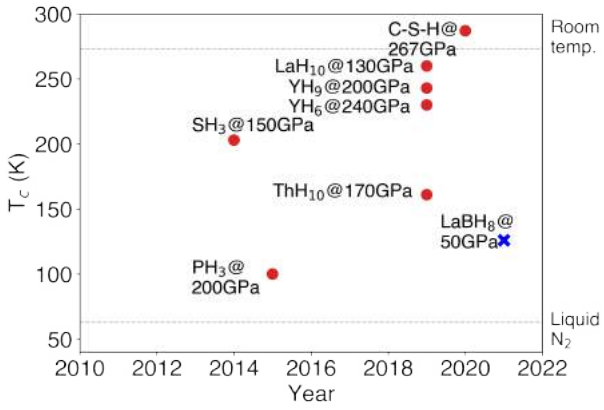

Figure 1.2: Red dots: experimentally measured critical temperatures for superhydrides since 2010. Blue X: prediction of high-T_c superconductivity in $LaBH_8$: a significant result I obtained during my PhD.

In **Chapter 3** I describe the main ideas and developments of the field of crystal structure prediction, which were instrumental to the superhydride discovery. In essence, crystal structure prediction consists in the identification of the ground-state crystal structure given only the chemical composition as initial input. Early attempts to solve this problem date back to the late 90s [44–46], and were typically based on molecular dynamics. They were followed by less physical, but more effective approaches such as evolutionary algorithms and particle swarm optimization [30,47–49], which are inspired by biological systems. More recently, some of these algorithms were also generalized to compute simulta-

neously the stable structures and the stable compositions, with a significant gain in computational efficiency. A special focus will be given to evolutionary algorithm as implemented in `Uspex`, as it is the method employed throughout this thesis work.

In **Chapter 4** I describe the theoretical methods used to compute the T_c's of conventional superconductors. I will start by describing the main ideas and derivations of Bardeen, Cooper and Schrieffer and Migdal-Éliashberg theory, and then move on to explain how the many-body Migdal-Éliashberg theory can be combined with first-principles calculations (DFT + DFPT) to evaluate the superconducting properties of actual materials. I will also show that, in contrast to common knowledge, current *ab initio* theories for superconductivity can correctly take into account the effect ot the residual Coulomb interaction. Although not used in this thesis, I will also shortly review Density Functional Theory for Superconductors (SCDFT).

Part II: Original Results

The second part of the thesis contains my original results. The main goal was to contribute to the discovery of high-T_c superhydrides, possibly at, or close to, room pressure. More specifically, this goal required 1) understanding the mechanisms that led to high-T_c in newly-discovered compounds in terms of the properties of their constituting elements, 2) understanding the causes of the instability of high-T_c hydrides at low pressure, elaborating strategies to decrease the stabilization pressure, and 3) using the accumulated knowledge to predict new, better superhydrides. The four research papers presented in this thesis reflect the rapid evolution of the field: while the main goal remained unchanged, the specific compound under investigation changed rapidly.

In **Chapter 5** I will present my results on sodalite-like yttrium hydride clathrates. At the end of 2018, LaH_{10} had just been discovered. While it was clear in H_3S the mechanism leading to high-T_c was a strong electron-phonon interaction associated to the covalent S-H bond, driven metallic by the high pressure, such a mechanism in sodalite-like hydrides had not been identified. In particular, lanthanum is an electropositive atom, and should not form covalent bonds with hydrogen, so a common explanation for the high-T_c of LaH_{10} was to consider it a realization of *atomic hydrogen*. In addition, the unusual structure of sodalite-like hydrides and their extremely high-T_c superconductivity required testing the validity of commonly held assumptions, such as the role of Coulomb repulsion, which was claimed to be unusually high, and the quality of T_c calculations. Finally, the fact that analogous structures were predicted to form with other guest atoms (Ca, Y) gave rise to the question of whether it was possible to optimize the stability to lower pressure or the T_c with a careful choice of elements. To address these questions, I studied the superconducting properties of two sodalite-like yttrium hydrides, YH_6 and YH_{10}. The choice of yttrium was motivated by the fact that it is chemically similar to lanthanum (they do form the

same superhydrides), but it does not have f orbitals near the Fermi energy, which are problematic to handle in DFT. At 300 GPa I predicted a T_c of 290 K for YH_6 and 310 K for YH_{10} using fully anisotropic Migdal-Éliashberg theory. I found a rather isotropic superconducting gap, despite a very anisotropic distribution of H-derived states over the Fermi surface. This unequivocally pointed to a strong interorbital (interband) interactions (Y-H), which wash out the anisotropy, and disproves the idea that sodalite-like hydrides are a realization of *atomic hydrogen*: if they were, the interorbital Y-H interactions should be absent, or negligible, and the gap should be anisotropic. The Morel-Anderson Coulomb pseudopotential, calculated from first principles, is $\mu^* = 0.11$ for both YH_6 and YH_{10}, very close to the value assumed for most conventional superconductors, and at odds with previous claims [50]. In addition, I identified a precise relation between the size of the hydrogen cage, and the volume occupied by the atom in the middle, which determines its dynamical instability at low pressure: when the average radius of the cage becomes larger than the covalent radius of yttrium, the cage becomes dynamically unstable. On the other hand, the H-H distance positively correlates with both the T_c and the cage size. The optimal compromise between stability and T_c is realized in YH_6, which is predicted to be dynamically stable down to 72 GPa. While clathrate hydrides are *tunable* in some sense, their tunability is limited by the few elements of the periodic table which form them. In order to further improve the superconducting properties one has to consider *ternary hydrides*, where the presence of two elements increases the number of combinations to over 6000 possible choices, and introduce additional flexibility in the elements sizes/valence/electronegativity, potentially allowing for new, undiscovered types of superhydrides. The two following chapters of the thesis adopt two different strategies for the choice of the elements.

In **Chapter 6**, I will discuss the calcium-boron-hydrogen system. The choice of calcium-boron-hydrogen was suggested by reasoning on the chemistry of the elements. The Ca-B-H system had been already studied extensively at ambient pressure for its possible application as hydrogen storage material, but had never been investigated under pressure. It was shown that the low-pressure structures contain insulating molecular crystals with BH_x^- anions (x = 2, 3, 4), that resembled the equivalent hydrocarbons: polyethylene, ethane, and methane, respectively. This suggested that Ca-B-H could form hydrogen-rich structures, with covalent B-H bonds. The idea of our study was that a combination of a weak (Ca) and a strong (B) hydrogen former would reduce the metallization pressure, thanks to the charge transfer/self-doping from calcium to boron; the thus formed metallic B-H bonds would drive high-T_c superconductivity, in a manner similar to H_3S. To test this hypothesis I calculated the stable compositions for the calcium-boron-hydrogen (Ca-B-H) system as a function of pressure, using evolutionary algorithms for crystal structure prediction. In particular, I carried out an extensive structural search to identify all stable compositions and structures at 0, 50, 100, and 300 GPa. I described in detail how pressure affects the bonding pattern of boron and hydrogen, transforming structures from insulating to metallic at a pressure

slightly above 100 GPa. In addition, I identified a high-symmetry metastable phase with $CaBH_6$ composition with a T_c of about 110 K at 300 GPa, which remains dynamically stable down to 100 GPa. The outcome of this study was not particularly exciting. While I did find a superconductor, its T_c is lower than that of binary hydrides, and its metallization pressure is higher.

In **Chapter 7** I will discuss my research on lanthanum ternary hydrides (La-X-H). As opposed to the study described in the previous chapter, this study was inspired by experiments. The original goal was to identify the crystal structure of a *hot* superconductor with a T_c of 550 K that had been reported in the literature [51]. Based on the elements present in the DAC during the experiment, and the hypothesis of a *ternary* hydride phase, I reduced the plausible candidates to six: La-B-H, La-N-H, La-Ga-H, La-C-H, La-Pt-H, and La-Au-H. I calculated the convex hull for these six compounds using variable-composition evolutionary algorithms, and found that only La-B-H and La-N-H system could form stable ternary hydrides, and only boron and gallium formed hydrogen-rich structures that could exhibit a high-T_c. None of the structures found, however, could explain the hot superconductivity, but I serendipitously found a structure with $LaBH_8$ composition which is even more interesting. In fact, while it does form at high pressure, it is dynamically stable down to 50 GPa, where it exhibits a T_c of over 126 K. This results in a figure of merit (Pickard et al. [52]) of $S = 2$ for this structure, which surpasses H_3S and LaH_{10} ($S = 1.3$), and $C_xS_xH_x$ ($S = 1.1$). The $LaBH_8$ crystal structure realizes an extremely efficient packing of La-B atoms, which I pinpointed as the cause of the low-pressure stabilization of the hydrogen sublattice, which is in turn responsible for the high T_c. The prediction of the low-pressure stability of $LaBH_8$ is extremely exciting, and raised a lot of interest in the research community [53–55]. The pressure stabilization of $LaBH_8$, 50 GPa, is still *high* from the point of view of experimentalists and practical realization, but represents a remarkable computational success, as it is about 150 GPa less than H_3S and LaH_{10}.

Overall, my results demonstrate that the research of superconductivity in superhydrides is a very lively field, with high chances of producing research with impact from both a fundamental and applied perspective. In the *Conclusions and Outlook* (**Chapter 8**), I will give my perspective on the field, suggesting potential future research.

Part I

Part I: Background

Chapter 2

High-pressure Hydrides: History and State-of-the-Art

In this chapter I will review the most important advances in the field of superconductivity leading to the discovery of high-T_c superconductivity in superhydrides. The field of superconductivity in general is exceptionally broad, and it would be impossible to review all of it exhaustively. Thus, I will only briefly mention *unconventional* superconductors (non phonon-mediated), and instead I will focus on the key steps which led to the birth of superconductivity in hydrides, which is the topic of this thesis. In particular, I will discuss the discoveries, the methodological developments (theoretical and numerical), and the development of the field of high-pressure science. I will describe these discoveries in chronological order, as it offers a useful, broader perspective. In this chapter I will discuss:

1. The early discoveries in the field of superconductivity.
2. The arguments which led to the hypothesis that hydrogen would of key importance for high-T_c superconductivity (first *hydride rush*).
3. The most important non-hydride superconductors: Cuprates, iron-pnictides, and covalent metals, stressing the difference between *conventional* (phonon-mediated) and *unconventional* superconductors.
4. The development of experiments at high pressure and *ab initio* methods for crystal structure prediction and calculation of superconducting properties
5. Computational research on hydrogen-rich metal alloys (second *hydride rush*)
6. The recent discoveries of superconductivity in H_3S and LaH_{10}, which led to the third *hydride rush*, which is likely to continue throughout this decade [56].

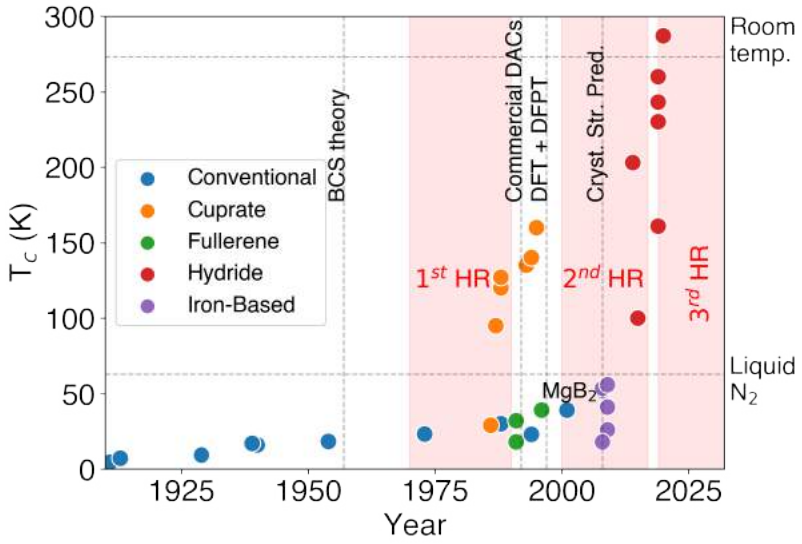

Figure 2.1: History of Superconductivity: experimentally measured critical temperatures for different families of superconductors. Vertical dashed lines mark the diffusion of significant theoretical or computational developments.

2.1 Early History

The history of the most important classes of superconductors is summarized in Fig. 2.1. The points follow a slowly increasing, quasi-linear trend, interrupted by three abrupt increases: cuprates, iron-based superconductors, and hydrides. Superconductivity was experimentally discovered by Heike Kamerlingh Onnes in 1911 while investigating the resistivity of mercury at extremely low temperatures: at 4.2 Kelvin degrees, he observed that the resistivity exhibited a sudden drop to a value of exactly zero [57, 58]. The other distinctive characteristic of superconductors, perfect diamagnetism, was discovered later, in 1933 by Meissner and Ochsenfeld [59]. The many important technological implications of this phenomenon were clear since the very beginning, so much that Onnes himself already tried to build an electromagnet with superconducting windings, but found that magnetic fields also destroyed superconductivity. The first real commercial production of a superconducting wire had to wait until 1962, when an intermetallic alloy, Nb-Ti, was discovered [60]. Nb-Ti is still used in many superconducting magnets worldwide, as it can bear large currents before losing its superconducting properties and, even more importantly, is easy to manufacture.

In 1957, Bardeen, Cooper and Schrieffer introduced the first phenomenological theory of superconductivity, now called BCS theory, which finally described the phenomenon in terms of condensation of pairs of electrons (Cooper pairs), held together by an effective attractive interaction provided by phonons (lattice vibrations). Only a few years later, BCS theory was extended to the strong-coupling case by Migdal and Éliashberg [23, 24]. An important theoretical result is the fa-

mous McMillan formula (as it appears in Ref. [61]), where the critical temperature of a conventional superconductor is expressed in terms of three simple parameters [61, 62]:

$$T_c = \frac{\omega_{log}}{1.2} exp\left[\frac{-1.04(1+\lambda)}{\lambda(1-0.62\mu^*)-\mu^*}\right] \tag{2.1}$$

Where λ is an average measure of the electron-phonon (*e-ph*) coupling, $\omega_{\log}$ is an average of the phonon frequency, weighted with the *e-ph* coupling, and μ^* is the so-called Morel-Anderson pseudopotential, measuring the residual Coulomb repulsion between electrons in a Cooper pair. See Chapter 4 for further details. The above formula is extremely useful for two reasons: 1) it provides a way to predict the T_c of a conventional superconductor from the knowledge of its *e-ph* spectrum, 2) its simplicity allows one to understand intuitively how the coupling and the phonon energies affect the T_c.

In 1968, both Neil Ashcroft and Vitaly Ginzburg independently noticed that, according to BCS theory, a metallic phase of solid hydrogen should be a superconductor with very high T_c [11, 12], due to the extremely high phonon frequencies ($\omega_{\log}$) and the strong electron-phonon coupling (λ) due to the absence of screening from core electrons. This argument can be understood by looking at eq. (2.1): high-energy phonons increase the prefactor $\omega_{\log}$, while unscreened phonons and a large density of states at the Fermi level contribute to increase λ. This work set the first cornerstone of the research field of hydrides, suggesting that high-energy phonons might by a key to achieve high-temperature superconductivity. Early attempts to find hydrogen-based superconductors date back to these years [17, 18], to what J. Flores-Livas et al. named the *first hydride rush* [63]. These attempts were largely based on heuristics and intuition, and were not successful. For instance, in 1971 J. Gilman proposed an hypothetical LiH_2F structure, where hydrogen atoms occupy the interstitial sites of a Li-F rock-salt structure. In hindsight, this was a very insightful hypothesis, but experience has shown that novel materials, especially under pressure, tend to defy the traditional rules of valence, which guide researchers' intuition.

Coeval to the early research on superconductivity, metallization of hydrogen is another ambitious goal in condensed matter, intertwined with that of room-temperature superconductivity. Hydrogen is an extremely reactive element, which in nature is found in the form of covalently-bonded H_2 dimers. In 1935 Wigner and Huntington first estimated that molecular hydrogen would dissociate into an atomic phase at 25 GPa, with metallic properties [13]. At the time a pressure of 25 GPa was beyond any experimental possibility, but the challenge of compressing hydrogen into this metallic phase was seen as a holy grail of high pressure physics. It was later demonstrated by experimental and theoretical work that the metallization pressure of hydrogen is actually much higher [64, 65], and its precise nature remains still object of intense debate [15, 16, 66].

Since its very discovery, the futuristic practical applications of superconductivity were already clear, and by the end of the 1960s the phenomenon had been understood, as a microscopic descrip-

tion had been found. However, the extremely low temperatures required to induce the superconducting state have always been the main limiting factor to its commercial applications, as the need for cooling raises the costs, and limits the applicability. The question whether superconductivity could ever be found at higher temperatures kept inspiring researchers, even though according to eminent theoreticians (Cohen and Anderson) a T_c higher than 25 K should not be possible [19]. Metallic hydrogen seemed an exciting material to investigate, but the pressure required was too high, and many did not believe Ashcroft and Gintzburg's hypotheses. Fortunately, as I will discuss in the following, Cohen and Anderson were spectacularly wrong.

In 1986, Bednorz and Müller discovered superconductivity with a T_c of about 30 K in an experiment on the Ba-La-Cu-O system [21]. This was the first of a new class of superconductors called cuprates, which quickly drew a lot of attention from researchers, and were intensely studied in the following decades. Cuprates are a family of high-temperature superconductors based on copper oxide layers (CuO_2), alternated with spacing layers. Indeed, only one year after the discovery of superconductivity in Ba-La-Cu-O, a T_c of 93 K was measured in the Y-Ba-Cu-O system [67], and Bednorz and Müller were awarded the Nobel prize for their discovery [68]. In the following years many more cuprate superconductors were identified, with the record temperatures of 133 K being found in the Hg-Ba-Ca-Cu-O system, which reaches up to 156 K under pressure [69]. Cuprates hold the record for the highest-temperature superconductor at room pressure. Unlike all superconductors encountered before them, Cuprates are so-called *unconventional* superconductors, i.e. superconductivity is not mediated by phonons[1]. The behavior of cuprates is extremely complex, and still to date object of intense debate.

Iron-based superconductors are the second class of unconventional superconductors to be discovered after cuprates. They were first discovered in 2006 [70], although they became a hot topic only after 2008, when a T_c of 26 K was found in F-doped LaOFeAs [71]. Iron-based superconductors share some similarities with cuprates: they are both *unconventional* superconductors with strong correlations. Going into the details of the complex physics of cuprates and iron-based superconductors is beyond the scope of this thesis, which will instead focus on *conventional* superconductors. The interested reader is referred to the excellent existing reviews [72–78].

In 1985, Kroto et al. serendipitously discovered that upon graphite vaporization, carbon could form large aromatic molecules with C_{60} composition [79]. These peculiar clusters take the form of a truncated icosahedron with 60 vertices, and were named *buckminsterfullerenes* after the architect Buckminster Fuller, who designed similar structures. Carbon fullerenes can condense into weakly-bound, insulating solids named *fullerite*, with *fcc* packing. Due to their extremely high electron affinity, fullerite can be easily doped by intercalation of alkali and alkaline earth atoms into its interstitial sites, which turn the structure into a metal, and a superconductor [80]. At room pres-

[1] Since cuprates are *unconventional* superconductors the Cohen-Anderson limit to T_c was still holding. It was MgB_2 first, and H_3S second that disproved it.

sure, the highest T_c, 33 K, was reported in $Cs_2Rb_1C_{60}$ [81], and 40 K were reached in compressed Cs_3C_{60} [82]. Albeit originally debated, it is now accepted that doped fullerides are phonon-mediated superconductors, although in the strong-coupling molecular limit [83, 84]. Conventional superconductivity from intercalation of electropositive atoms was also achieved in graphite, with CaC_6 and YbC_6 (2005) exhibiting a T_c of 11.5 K [85].

2.2 Magnesium Diboride and covalent metals

In 2001, a T_c of 39 K at ambient pressure was measured in magnesium diboride (MgB_2) [22], and in 2004 boron-doped diamond a T_c of 4 K was measured [86]. Unlike cuprates and iron-based, these two materials are *conventional* superconductors. This enabled researchers to understand which features of the chemical bonding could lead to high-T_c. Indeed, both are examples of *covalent metals*, i.e. metallic materials with covalently bonded elements. In MgB_2 the crystal structure is characterized by a very simple unit cell, consisting of alternated hexagonal layers of covalently-bonded boron and triangular layers of ionized magnesium atoms. The in-plane orbitals of boron (s, p_x, p_y) form a partially unfilled electronic band with σ character, which is extremely sensitive to changes in the B-B distance. In other words, metallic covalent bonds are characterized by a uniquely large electron-phonon matrix element, which responsible for a relatively strong coupling (See eq. (4.57)) [27]. Moreover, boron is a light element, hence phonons are highly energetic, and ω_{log} is large. These aspects combined explain T_c [87], which was record-high for a conventional superconductor. The exact same principle was shown to be responsible for superconductivity at 4 K diamond doped with boron at 3%, arriving up to 7 K with successive experiments with doping at 10% [88–92]. The hole doping causes the Fermi energy to shift into the top of the valence band, which causes phonons around the Brillouin zone center, associated with C-C stretching, to strongly couple with electrons.

The discovery of superconductivity in covalent metals demonstrated that it is possible to overcome the Cohen-Anderson limit in conventional superconductors, and gave a precise combination of requirements for this to be achieved: a covalent metal with high-energy phonons. Unfortunately, materials with these properties combined are rather rare in nature, as covalent materials usually are characterized by closed electronic shells, which make them insulators. Insulating covalent bonds are common at ambient conditions, but they can be turned metallic by changing two important *thermodynamic parameters*: temperature and pressure. High pressures, in particular, can be used to tune the interatomic interaction by directly changing the overlap between orbitals.

2.3 The Birth of High-Pressure Research

High-pressure science dates back to the beginning of the 20th century, with the pioneering work of Percy Bridgman who was awarded the Nobel Prize in 1946 *for the invention of an apparatus to produce extremely high pressures, and for the discoveries he made therewith in the field of high pressure physics* [93]. The most important invention in this field, however, is the diamond anvil cell (DAC), introduced by Weir et al. in 1959 [94]. The design of this device has been constantly improved since then, enabling researchers to reach pressures of up to 1000 GPa (ten millions of atmospheres) [95]. Moreover, since diamond is transparent to electromagnetic radiation in most of its energy spectrum, it also permits all sort of spectroscopic techniques to be used directly during the experiments.

The DAC is in principle very simple, a schematic is shown in Fig. 2.2. It consists of two opposing anvils made of single crystal diamonds. A metal gasket, with a central hole, is placed in between the diamonds. The gasket holds the sample firm and provides a smooth contact surface between the two diamond facets. When the two diamonds are brought together, they squeeze the sample in the gasket. The pressure inside is measured by looking either at the fluorescence of a micrometer-sized ruby, whose frequency depends linearly on pressure, or by directly measuring the highest-frequency Raman mode of diamond, whose pressure dependence is well characterized [96]. The DAC can be modified depending on the quantity of interest. For instance, when performing experiments on superconductors, electrical contacts can be etched directly onto the gasket to measure resistivity.

The first important experiment on superconductivity at high pressure dates back to 1968, when it was shown that above 5 GPa elemental cerium loses its magnetic properties, and becomes superconductive with a T_c of 1.3 K [98]. Similarly, superconductivity was also found in barium and strontium [99, 100] (T_c = 3-4 K). After the 90s the DAC became commercially available, and the field of high-pressure materials science flourished. Pressure was shown to enhance superconductivity in other elements such as [101, 102], iron (after magnetism is suppressed) [103], yttrium [104], and calcium, which exhibits the highest T_c among all elements: 25 K at 161 GPa [105, 106]. As of today, all pure elements have been investigated – a summary of T_c's for the whole periodic table was published by Hamlin [107].

In parallel with high-pressure experiments, modern crystal structure prediction methods also started to be developed at about the same time. Indeed, a crucial aspect of the analysis of high-pressure experiments is the identification of the newly formed crystal structures, which can be extremely hard given only the X-Ray pattern. This is even more important in hydrides, as hydrogen is a very weak X-Ray scatterer. The information on the Bravais lattice and on the position of the other atoms, however, is usually sufficient to unambiguously identify the crystal structure using first-principles calculations. From a thermodynamical point of view, the structures that form are those that *minimize* the relevant thermodynamic potential – enthalpy, in the case of experiments

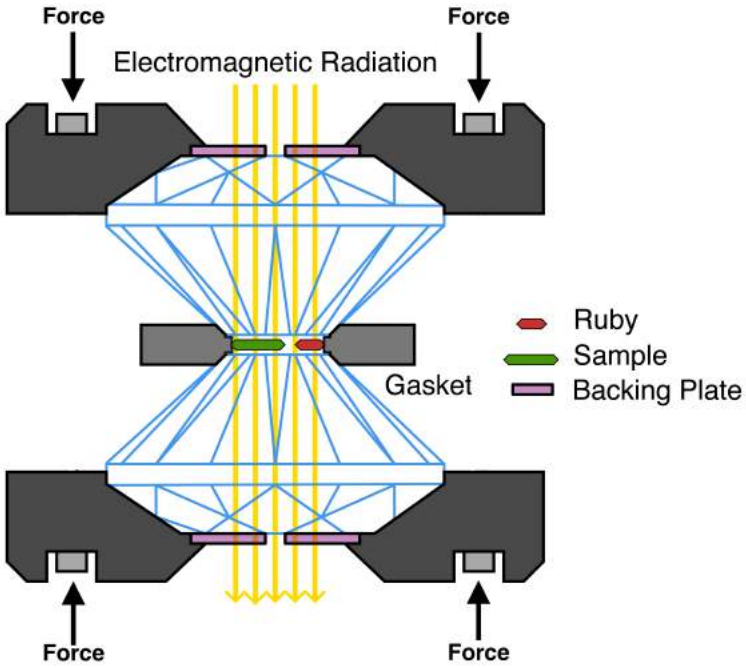

Figure 2.2: Simple schematics of a diamond anvil cell. The sample (green) and the ruby (red) are placed in a metal gasket (grey) and sandwiched among two anvil-shaped diamonds (blue). Two screws are used to bring the diamonds close, and increase the pressure on the sample. Image from Ref. [97].

under pressure. Crystal structure prediction methods are essentially *optimization* algorithms, which are able to find the minimum efficiently. In most cases, they rely on Density Functional Theory to calculate the enthalpy (although other methods are possible); even in the structure search of a simple element the self-consistent equations of DFT are solved thousands of times. During the second half of 2000s, three key factors made crystal structure prediction possible:

1. *Ab initio* methods based on Density Functional Theory were fully established, and easily available. In particular, robust transferable pseudopotentials were available.

2. The cost of computing power had decreased to the point that high-throughput DFT total-energy calculations were possible.

3. *Smart* search algorithms had been developed, making structural searches reproducible and affordable.

All the most important codes for crystal structure prediction date back to this decade [30, 47–49]. *Ab initio* calculations rapidly turned into an invaluable tool to interpret the experimental results, determine the crystal structure observed, and characterize its properties. For instance, a high-pressure structure of $CaCO_3$ [108], and the phase III of hydrogen [65] were identified, in excellent agreement with the experimental data. Experiments at extreme pressures started to rely on crystal

structure prediction for the data interpretation. Sodium, which is a metal at ambient conditions, becomes insulating and transparent above 200 GPa [109], while boron turns into an ionic solid above 20 GPa [110]. In both these cases the experimental X-Ray pattern alone would not have been sufficient to reconstruct the crystal structure: its identification was only possible by comparing the phase diagram, predicted by *ab initio* calculations, and the experimental spectra.

Another aspect of high-pressure physics that emerged at this time, was the so-called *forbidden chemistry*, i.e. the idea that the *textbook* rules of valence and chemistry can be bent and broken under high pressure. This unexpected behavior results from a competition between the energy term, which depends on the electronic orbitals of the elements, and the PV term, which is introduced by pressure, and is minimized by diminishing the volume. So, for instance, sodium becomes insulating, or sulfur becomes trivalent, as a result of extreme pressures. Forbidden chemistry makes *ab initio* predictions even more relevant, as scientists cannot use their knowledge of the room-pressure chemistry to infer the high-pressure behavior. Fortunately such was the predictive power of crystal structure prediction based on DFT, that calculations soon began to even anticipate experiments. As of today, crystal structure prediction has become a staple of materials research [111].

2.4 Superconductivity in Hydrides

The *second hydride rush* started in 2004, again motivated by a paper published by Neil Ashcroft [112]. Inspired by the results on pressurized lithium and on magnesium diboride, he suggested that hydrogen-rich materials under pressure might become high-temperature superconductors. He foresaw that, when bound to a second element, hydrogen would become metallic and superconducting at a pressure much lower than what is required to metallize pure hydrogen, thanks to what he named a *chemical precompression*. At the same time, the interest on hydrogen-rich materials was already high, as they were being studied for hydrogen storage [113].

Ashcroft's hypothesis was followed by several calculations showing that silane (SiH_4) would become metallic and superconducting under pressure [29–31]. Similar predictions were made for GeH_4 and SnH_4 [32, 114]. In 2008, M. Eremets group a reported T_c of 17 K at 96 GPa, following a high-pressure experiment on silane [34]. However, the phase experimentally proposed, with $P6_3$ symmetry, was dynamically unstable. Thermodynamically more stable phases were suggested in further computations [35, 115, 116]. Degtyareva et al. proposed a different interpretation, showing that hydrogen released by silicon could react with the platinum electrodes to form a PtH phase, which at that pressure would be thermodynamically stable and superconducting [117–120], and also matched the experimental X-ray spectrum.

The interest on silane drew some attention to the field, and research groups started to computationally search for thermodynamically-stable hydrides [118, 121, 122], and to re-examine known

hydrogen-rich systems [123]. At the same time, structure prediction methods were improved to simultaneously sample multiple compositions [122, 124].

The first systematic computational study on the formation of superconducting hydrides was performed in the Lithium-Hydrogen system [33]. Unlike previous work, here the stable structure for each composition was determined using a crystal structure prediction algorithm, and the thermodynamical stability of the single composition was examined up to 300 GPa, setting a standard for subsequent research. The authors discovered that charge transfer from lithium to hydrogen and impurity bands of H^- anions can dramatically reduced the metallization pressure in hydrogen-rich systems, and found a structure with LiH_6 composition, stable above 140 GPa. This structure was characterized by the presence of slightly stretched H_2 molecules, and was found to be metallic. The fact that the LiH_6 composition is stable is extremely interesting, as it is an example of forbidden chemistry in which a *superhydride* is formed, i.e. a material with an unusually high hydrogen content. Later experimental work on lithium hydrides under pressure [125] was able to synthesize a LiH_6 phase, which was found to be insulating up to 215 GPa. Although it might be possible that this structure does turn superconductive at even higher pressure, in this case the metallization pressure due to band overlap was probably underestimated, as a Perdew-Burke-Enzerhof exchange-correlation functional was employed.

At the end of 2014, Defang Duan and coworkers published a computational study of the sulfur-hydride system under high pressure [126]. Sulfur and hydrogen form a H_2S molecular phase at ambient pressure, but the H_3S composition was predicted to become stable with respect to decomposition into H_2S+1/2H_2 above 120 GPa. Its crystal structure is predicted to form a phase with a hexagonal lattice ($R\bar{3}m$ space group), which above 150 GPa transitions into a body-centered-cubic Bravais lattice, with sulfur six-coordinated to hydrogen, with which it formed a covalent bond. The H_3S structure was predicted to be a superconductor, with a T_c of 204 K at 200 GPa, an unprecedentedly high value. Only one month after the prediction, Mikhail Eremets's group published the experimental confirmation: they had been working on the same material and had already found a high-T_c superconductor [1, 2, 127], with a T_c that matched well the predicted value. When Duan's prediction was presented, Eremets' group immediately decided to publish their results, which they had been double-checking until then[2].

The discovery of superconductivity in sulfur hydride represented a huge breakthrough for three main reasons:

1. It demonstrated that computational crystal structure prediction methods can be used to predict the formation of materials which defy physical intuition.

2. It set a new record of high-T_c superconductivity in a conventional superconductor, proving that Ashcroft's intuitions were correct, and definitely disproving the Cohen-Anderson limit.

[2]This anecdote was recently shared by M. Eremets in a review article [56]

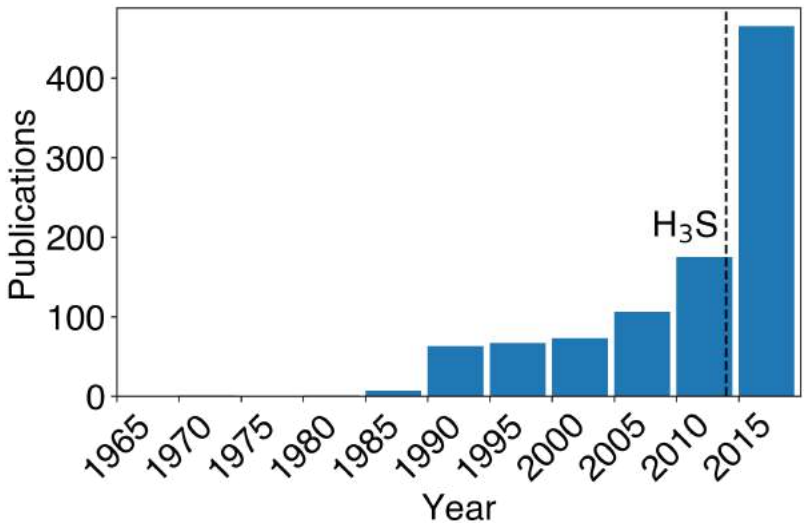

Figure 2.3: Number of papers published on superconductivity in hydrides in a 5-years interval from 1970 to 2020, indexed in Web of Science. Data obtained from the Web of Science analytics tools using the query: *TOPIC = superconductivity AND (hydrogen OR hydride)*

3. It showed that the methods used to calculate the T_c in conventional superconductors had become accurate enough for quantitative predictions.

The factors underlying the record T_c were quickly identified to be an optimal combination of those encountered in MgB_2: high-phonon frequencies (large $\omega_{\log}$), and metallic covalent bonds (large λ) [27, 128]. The covalent S-H bond is driven metallic by pressure [128], and is responsible for the very large electron-phonon coupling, with sulfur being close to having the ideal electronegativity that maximizes the T_c [129]; the small mass of hydrogen causes phonon frequencies to be high; the peculiar crystal structure, which has sizable farther-neighbor hopping, induces a van Hove singularity right below the Fermi energy, which contributes to a large density of states at the Fermi level [130]; and the shape of the Éliashberg function is near the optimum to maximize T_c [131]. In addition, the calculations were further refined with the inclusion of anharmonic and quantum effects [132, 133], which were found to be quite important in hydrogen-rich systems [134], as 1) they tend to favor the formation of high-symmetry phases, and improve the prediction of the stabilization pressure, and 2) they can strongly renormalize the phonon frequencies, and also further improve the agreement between the predicted T_c and the experiment.

The years following the discovery of H_3S saw an rapid increase of the research output in hydrides. As shown in Fig. 2.3, the number of papers about superconductivity in hydrides more than doubles when going from the 2010-2015 to the 2016-2020 period. The main research question in this period was whether other superconducting hydrides existed, which could surpass the properties of sulfur hydride. The candidates were those chemically similar to sulfur, such as phosphorous, selenium, and tellurium. Hydrides with these three elements were all predicted to be high-T_c superconductors,

albeit worse than H_3S [135–138]. In particular, phosphorous hydrides only exhibit superconductivity in their metastable phases, but were successfully synthesized in experiment [139]. To put things in perspective, a summary of the experimentally measured T_cs in hydrides is shown in Fig. 1.2.

It is important to notice that at this point a shift had occurred in the way research was being carried out. The exploration of combinations of hydrogen with all the other elements in the periodic table was performed computationally, using ab-initio crystal structure prediction methods, and experiments were performed only after interesting candidates were published [111]. The years from 2014 to 2019 saw the computational exploration of all possible binary hydrides, i.e. a combination in any proportion of hydrogen with one other element.

In 2012, a computational study predicted the formation of a new class of superconductors in calcium hydrides [121], named sodalite-like clathrates. In 2017, similar structures were also predicted for lanthanum and yttrium hydrides [140]. A newfound structural prototype, with LaH_{10} (YH_{10}) composition, is characterized by a dense network of hydrogen atoms forming a polyhedral cage around the central metal ion, analogously to sodalite crystals, hence the name *sodalite-like* hydrides. This structure was predicted to form at a pressure around 200 GPa, and to exhibit a T_c around 280 K, only 20 degrees below the conventional value for room temperature. The prediction was confirmed, only one year later, with the independent measurement of a T_c of about 260 K in LaH_{10} at 130 GPa, carried out independently by two different research groups [3–5].

The discovery of LaH_{10} encouraged researchers to look for other high-T_c sodalite-like hydrides, and to examine which were the key details of its electronic structure leading to its high-T_c. Sodalite-like hydrides were experimentally confirmed for yttrium: YH_6 and YH_9, with a T_c of 227 and 243 K, respectively [37,38]; and ThH_{10}, with a T_c of 161 K [39], in CeH_{10} (115 K) [40], and in UH_7 (66 K) [41].

Like sulfur hydride, sodalite-like hydrides were thoroughly examined in several computational studies, and the mechanism leading to their formation was essentially identified. They are characterized by a network of metallic and weakly-covalent hydrogen-hydrogen bonds [141]. The H-H weakly-covalent bond forms as a result of the charge transfer from the metal ion, which weakens the bond of the H_2 molecules by occupying their anti-bonding orbitals [33, 121]. In addition, the large heavy ion pressurizes the hydrogen sublattice, stabilizing it [7]. The result is a dense hydrogen network which behaves like atomic hydrogen, but at a much lower pressure. Chapter 5 is dedicated to the research I carried out on sodalite-like hydrides [7].

LaH_{10} also served as a test for the accuracy and the limits of the current computational methods. According to standard DFT the high-T_c structure only forms above 250 GPa, and undergoes small distortions below, while in experiments it is measured down to 130 GPa [142]. The inclusion of anharmonicity and the quantum nature of the proton was successful in reconciling theory and experiment [143]. Other effects, such as a magnetic contribution from the La-d and f states might

as well be important.

After about five years of intense research, the high-pressure phase diagram of all possible binary hydrides had been computationally explored, and high-T_c candidates identified. A clear division emerged of high-T_c hydrides into two main classes: (*i*) covalent hydrides (SH_3, PH_3), in which H and the other element X form a network of covalent bonds, driven metallic by the high pressure [126–129, 132, 135, 138, 144, 145], and (*ii*) metallic hydrides with electropositive elements (alkaline metals or rare earths), such as LaH_{10}, which form high-symmetry, hydrogen-rich structures reminiscent of sodalite structures [4, 5, 7, 36, 121, 140, 146, 147]. In class (*i*), the occurrence of high-T_c superconductivity depends on the degree of covalency of the H–X bonds, and X=S was demonstrated to be a nearly optimal choice [126–129, 132, 135, 138, 144, 145]; in class (*ii*), the dense hydrogen sublattice is characterized by *weak* metallic covalent H-H bonds [141], as opposed to the *strong* H_2 molecule covalent bond. The H-H bonds are characterized by strongly-coupled and high-frequency modes of vibration, which are responsible for the high-T_c. The electropositive guest acts as a charge donor and as a spacer, and stabilizes the hydrogen network, without directly bonding to it; but it dictates the stability pressure [3, 7, 39, 121, 147, 148, 148, 149].

Despite the consistent successes, there were a few notable failures of computational structure prediction. The $Fm\bar{3}m$ phase of YH_{10} was predicted to form [148], but the experimentally stable phases commonly accepted are YH_6 and YH_9 [37, 38]. Even in the very-well studied H_3S system, the state-of-the-art calculations including quantum and anharmonic effects underestimates the transition to the high-T_c $Im\bar{3}m$-phase by about 50 GPa [2, 133]. Since in general crystal structure prediction works extremely well, its failures most likely come from one or more of the effects that are normally not included in the calculations, such as:

1. The contribution of the ground-state vibrational energy to the total energy (so-called zero-point energy), and of temperature to the free energy
2. Presence of localized, strongly-correlated states, which may be ill-described in standard DFT
3. Effects such as alloying, vacancies, local distortions, which do not appear in small unit cells
4. Presence of metastable phases, protected by decomposition by high potential barriers

While point 1) is sometimes included in the most accurate studies, the other three are part of the the leading edge of research, and are typically not included in automated structural searches.

A similar argument also applied to the calculation of the critical temperature. Effects that are normally not included may lead the results obtained with standard Éliashberg theory to be under- or overestimated. In particular, it was shown in H_3S that several effects, such as anharmonicity, finite-bandwidth effects, and high-order vertex corrections are all equally important [150], and other effects such as competition with magnetism have not been studied in detail.

2.5 Current Status

As discussed, the computational and experimental exploration of binary hydrides was extremely successful, but has essentially been completed by 2019 [151–153]. The next natural step is the study of ternary, or even more complex hydrides, which brings new exciting possibilities and new challenges. In particular: with two elements other than hydrogen, there is much more freedom in the choice of atoms with different sizes and/or electronegativities. On the other hand, the complexity of first-principles calculations increases drastically, as in ternary hydrides the number of possible compositions grows like the square of the number of atoms in the unit cell – See Chapter 3. In addition, when exploring ternary hydrides there are 6903 possible choices of elements, as opposed to only 118 for binaries.

As of today, there is still limited published research on ternary hydrides. These published papers go either in the direction of trying to find above room-temperature superconductivity at very high pressures, or in that of reducing the stabilization pressure, even if that implies a lower T_c. In one of the very first publications on the topic, Kokail et al. examined the Li-B-H system in an attempt to lower the metallization pressure with respect to H_3S. The authors predicted the formation of a structure with Li_2BH_6 composition, characterized by metallic covalent B-H bonds, with a predicted T_c of 98 K down to 100 GPa. A rather spectacular result was obtained for the Li-Mg-H system, in which a structure with Li_2MgH_{16} composition was predicted to be a *hot* superconductor, with a T_c of 473 K at 250 GPa, although this superconducting phase is not thermodynamically stable, but might be *metastable* – for a discussion of metastability see Chapter 3.

Another promising high-T_c superconductor was identified in the C-S-H system [154], where a structure with CSH_7 composition was predicted to exhibit a T_c of 181 K at 100 GPa. Only a few months later, in the Summer of 2020, Ranga Dias's research group reported the measurement of room-temperature superconductivity in a carbonaceous sulfur hydride, with a measured T_c of 288 K at 267 GPa [6]. This publication was received with great enthusiasm from both the research community and the mainstream media [155]. As of today, neither the composition nor the crystal structure have been identified, despite a few attempts from both the computational [156] and experimental side [157]. The problem of which phase, and which mechanism, leads to room-temperature superconductivity is still under investigation. A doping mechanism of the H_3S structure via $SH_3 \rightarrow CH_3$ or $SH_3 \rightarrow CH_4$ substitution was proposed by Wang et al. [158], and is the most probable.

The great successes in the field of hydrides and the very fast pace of discoveries continue to make research on hydrides extremely promising. The main questions driving research remain whether a high-T_c hydride can be synthesized at room pressure. In a recently published *roadmap*, the leading experts in the field have shared their viewpoints, which are overall quite optimistic [159]. Ternary hydrides are regarded as a promising class of materials, and an interesting question is whether

they will divide into the same two classes as simpler hydrides, i.e. covalent and sodalite-like, or an entirely new behavior will be found. The search for more complex superconducting materials will also require a methodological effort: there is need for more efficient strategies to search for new materials. In particular, interatomic potentials based on machine learning could achieve the same accuracy as DFT as a reduced computational cost, enabling the study of much larger cells [160–162]. Other desirable advancements would be the modeling of unconventional channels for the electron-electron pairing, such as plasmons, excitons, and paramagnons, and their integration in the available programs, to explore more types of superconductors. Meanwhile, studies on ternary hydrides can already be performed. An important question will be whether the formation of promising ternary phases can be inferred from the behavior of the simpler, and well-studied, binary ones, as was demonstrated to work for nitrides [163]. Using the vast amount of data produced on binary hydrides to guide future research, even by data-driven approaches, is certainly a promising strategy.

In this chapter I focused on the most important literature relevant to the field of superconductivity in hydrides, for a complete review see Ref. [52, 56, 151, 164]. In Part II, I will describe my own contributions to research on superhydrides.

Chapter 3

Crystal Structure Prediction

3.1 Thermodynamical stability

In this chapter I will describe the process through which one can predict, fully from first principles, the spatial arrangement that a certain combination of atoms will assume when they condense in crystalline (or molecular) form. In more technical terms this means predicting which *crystal structure* is stable for a given chemical composition. I will start by defining the meaning of *stable*, and of *crystal structure*. Then I will give a mathematical definition of stability for a crystal structure, and mention a few algorithms which can be used to determine which structure is the most stable. In particular, I will focus on genetic algorithms as implemented in the `USPEX` code, because it was the method that has been used throughout this thesis work.

In general terms, the stability of a system is determined by its thermodynamic state, which can be in- or out-of-equilibrium. A system at equilibrium is thermodynamically stable, which means that its macroscopic properties do not change over an extended period of time. In order to describe the thermodynamic state effectively, it is useful to introduce the thermodynamic potentials; i.e. scalar quantities which describe the state of the system in a single number. Several possible potentials exist: internal energy (E), Helmholtz free energy ($F = E-TS$), Enthalpy ($H = E+PV$), and Gibbs free energy ($G = E - TS + PV$), all related by Legendre transforms. In general, an equilibrium state corresponds to the minimum of the relevant thermodynamic potential. In the next paragraph I will shortly discuss the four potentials and their use.

The internal energy E represents the energy of a given configuration of the elementary constituents of the system. In the context of the stability of crystals and molecules, the dominant term is the electronic energy resulting from a specific arrangement of the atoms in the system, plus the repulsion between the ions. A closed system, with constant external parameters (e.g. volume) and entropy, always evolves in such a way that its internal energy is minimized. Therefore, if I find the

configuration for which E is minimum, I find the stable configuration of the system. This principle can be generalized using the other thermodynamic potentials. In particular, when the temperature is held constant, the Helmholtz free energy is minimized; when the pressure is held constant, the enthalpy is minimized, and when pressure and temperature are held constant, the Gibbs free energy is minimized. To simplify the notation, I will generally use the term *energy* when talking about thermodynamical stability, although depending on the presence of pressure and temperature terms one should use the appropriate thermodynamic potential.

In principle, all the thermodynamic potentials can be computed from first principles for a crystalline system. However, the effect of temperature on stability can usually be neglected at the temperatures at which superconductivity takes place (0 to 300 K), as it is typically too small to change the energy ranking of structures. On the other hand, the effect of high pressure on the crystal structure and chemical bonding is prominent. For instance, at 100 GPa the PV term is of the order of 100 meV/atom, which is the same energy scale at which different structures are ranked. When predicting the thermodynamical stability for crystal structures, enthalpy is normally used, and if needed the free energy term is included as a correction [138].

Crystalline solids are materials in which atoms are arranged in a periodic microscopic pattern which extends in all directions up to a macroscopic scale. Common examples are diamonds, table salt, or sugar. The building block of a crystal is called a *unit cell*, i.e. the smallest portion of the crystal which has all the symmetries of the crystal; An example is shown in Fig. 3.1. A crystal can be fully described by repeating the unit cell along three directions, named *unit cell vectors* ($\vec{a}_j$, $j = x, y, z$). The set of points that is generated by all possible integer combinations of the crystal axes is called the *Bravais lattice*, defined by $\vec{R} = n_x\vec{a}_x + n_y\vec{a}_y + n_z\vec{a}_z$, where (n_x, n_y, n_z) is a set of any three integers. The positions of the atoms in the unit cell are defined by the *basis* vectors $\vec{\tau}_i$, with $i = 1, .., N$.

The periodic arrangement of the atoms in its structure is the most important feature of a crystal, which lays the foundation for its mathematical description. In fact, one only needs to specify the position of the atoms in the unit cell (the *basis*) to fully describe the whole crystal, as the rest follows from periodicity. The knowledge of the crystal structure of a material is the essential prerequisite to any further calculation, regardless of the method employed. In practice, predicting the structure of a crystal translates into determining the Bravais lattice and the atomic positions for which the structure is thermodynamically stable. In the next paragraph I will discuss how this applies to the case of a crystal structure.

3.1.1 The potential energy surface: stable and metastable structures

I will now describe how the internal energy is defined for crystalline systems, and how it is related to the internal degrees of freedom of a crystal. Let me start by recalling that within the adiabatic

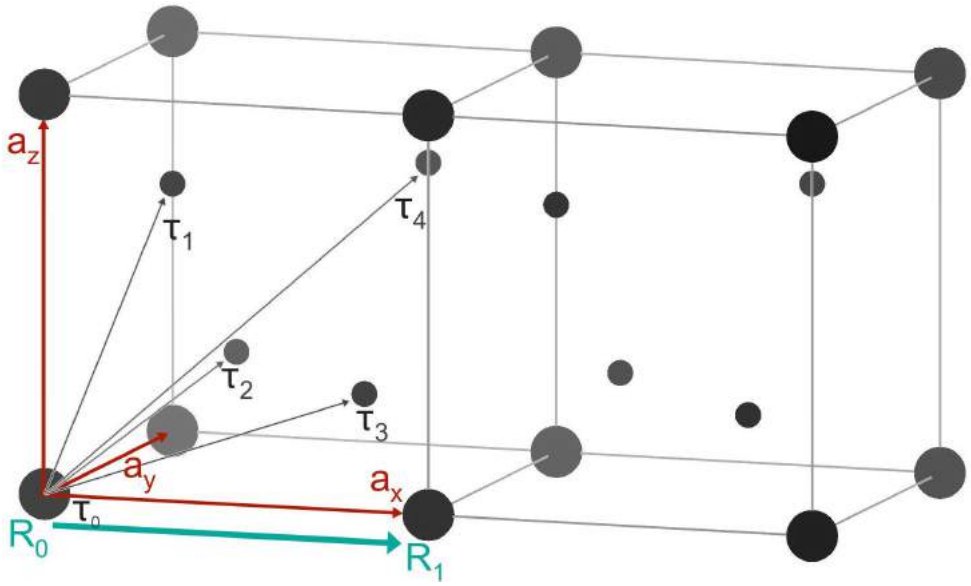

Figure 3.1: Sample crystal structure with five nonequivalent atoms per unit cell. The unit cell is translated along the a_x axis direction by a lattice vector $\vec{R}_1$.

approximation the total energy of the crystal structure is a parametric function of the atomic positions and Bravais lattice vectors, i.e.

$$E = E(\vec{a}_j, \tau_i) \tag{3.1}$$

The specific method used to calculate the energy from the atomic positions can change: force fields [165, 166], machine-learned interatomic potentials [162, 167, 168], Density Functional Theory [169, 170], or tight-binding total-energy [171], are all viable methods. The following discussion holds regardless of the method chosen.

Consider equation 3.1 for a three-dimensional unit cell containing N atoms, and no symmetries. There are a total of 3N+6 degrees of freedom, due to the 3N atomic coordinates and three lattice vectors[1], therefore E (or H) realizes a hypersurface in a (3N+7)-dimensional space. As previously discussed, a stable crystal structure corresponds to one set of $\vec{\tau}_i$, $\vec{a}_j$ for which the energy has a minimum.

See Fig. 3.2 for a simplified illustration of this concept. Each choice of $\vec{\tau}_i$ and $\vec{a}_j$ represents a single crystal structure, and is represented schematically as a point along the xy plane. To each point corresponds an energy value E, and the minima coincide with structures which are stable with respect to small perturbations, i.e. small displacements of the atoms. In general, the structure corresponding to the absolute minimum is the ground-state, and is thermodynamically *stable*, whereas those corresponding to local minima are called *metastable* structures, implying that

[1] The three lattice vectors can be described in terms of their length a, b, and c, and the angles α, β, and γ, between the $b-c$, $a-c$, and $a-b$ axes, respectively. This totals to six degrees of freedom for a triclinic unit cell.

they may form and remain stable for a certain amount of time, although they should, in principle, always tend to return to the absolute minimum.

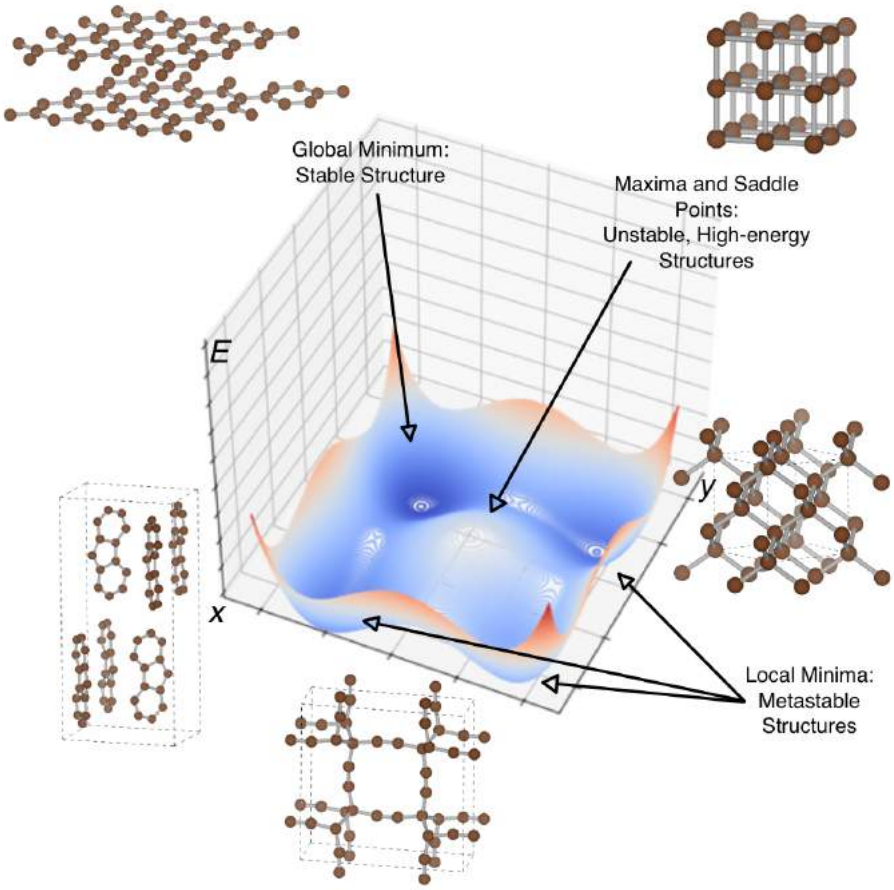

Figure 3.2: Qualitative representation: a potential energy surface with three local minima, one global minimum, and one local maximum. The x and y axes represent two spatial degrees of freedom of the system, while the E axis represents the total energy.

To generalize the concept for enthalpy (H) and free energy (G), one needs a way to calculate *pressure* (P) and entropy (S). Pressure can be calculated easily from the relation $P0 - dE/dV$. Entropy in principle has one contribution from the electronic degrees of freedom, and another from the occupation of the vibrational states. Except for very low temperatures (below 10 K), the phonon contribution is the dominating one [172], and can be calculated as the entropy of a boson ensemble: $F_{ph} = Nk_BT \int_0^\infty ln \left[2sinh\left(\frac{\hbar\omega}{k_BT}\right)\right] F(\omega)d\omega$, where $F(\omega)$ is the phonon density of states [173].

Crystal structures corresponding to *local* minima are called *metastable*. In principle, a system prepared into a metastable state should spontaneously transition to the configuration of the global minimum in a finite time. This implies that the system will have to move from the local minimum to the global minimum (or to another intermediate local minimum), by going through a transition

state, where it crosses a maximum (or a saddle point). The difference in energy from the starting point to the maximum is the so-called *potential barrier* for the transition. The rate at which the transition is realized depends on the ratio between the potential barrier and temperature. If the potential barrier is sufficiently high, the transition might be inhibited altogether. The most famous example of an infinitely long-lived metastable state is diamond. At ambient conditions the ground state of pure carbon is graphite, but the potential barrier between diamond and graphite is so high that diamonds are notoriously *forever*.

The determination of transition states and potential barriers from first-principles is a demanding task, and calculations have been performed only for very simple systems [174]. A promising approach for solid state physics is the Nudged Elastic Band method (NEB) [175], and its extension to variable-cell calculations (VCNEB) [176], which allows one to find the minimum energy path (MEP) between two given minima.

3.2 Phase Diagram

The most interesting parameter in the study of hydrides is pressure, and one is interested in knowing which structure is the most stable as a function of pressure. This information is usually summarized in the form of a *phase diagram*, which in general lists the most stable structure as a function of the relevant thermodynamic variable (typically temperature and/or pressure).

At fixed composition, it is typically sufficient to list the space group to refer to a structure, and show the transitions with differently colored bars, as shown in Fig. 3.3. For each pressure, the enthalpy of possible candidates is calculated, and the lowest-enthalpy structure is determined. The ensemble of pressures for which each structure is stable determines the phase diagram.

The composition is another interesting parameter: as the relative content of the elements in the cell changes, one obtains a different structure. This parameter introduces a complication, as one has to display the structures as a function of composition, as summarized by their chemical formula, e.g. H_2O. Not all compositions are stable. In fact, it might be energetically more favorable for a material to undergo a chemical reaction and decompose into structures with different compositions. To calculate the stability of a composition, one has to consider the energy (enthalpy) variation with respect to all possible decomposition routes. For example, to establish whether H_2O decomposes into its constituent elements, H_2+O_2, one computes the difference: $\Delta H_{H_2O} = H_{H_2O} - (H_{H_2} + 1/2H_{O_2})$. The result is negative, so H_2O does not spontaneously decompose into H_2+O_2. In this procedure, the enthalpy for each composition (e.g. H_{H_2O})) is that of the ground-state structure, so for each composition the minimum of the potential energy surface should be determined.

Mathematically, the set of stable compositions is the smallest *convex* set that contains all other compositions. This can be easily visualized by constructing a diagram where the enthalpy of each

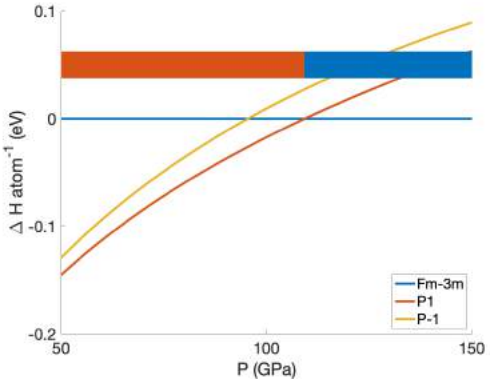

Figure 3.3: Enthalpy as a function of pressure $H(P)$ and calculated phase diagram as a function of pressure for $LaBH_8$. The colored bar marks the pressure range at which each crystal structure is stable. The different structures are identified by their space group.

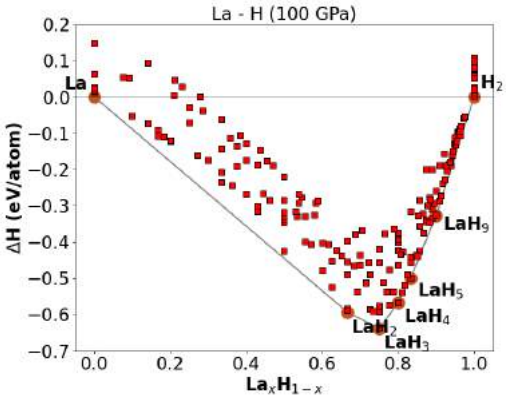

Figure 3.4: binary *convex hull* for the La-H system at 100 GPa. Red squares and orange dots represent thermodynamically unstable and stable composition, respectively. Each point corresponds to a single crystal structure.

structure is shown as a function of composition, and the *convex hull* containing all points is drawn, as in Fig. 3.4. The abscissa represents the possible compositions, as defined by the $La_xH_{(1-x)}$ equation, while the ordinate is the enthalpy difference with respect to the pure elements (formation enthalpy). Every point represents a crystal structure, and the convex hull is the smallest line traced between points so that all the other points are contained. This diagram allows one to see at a glance which compositions are stable.

To reduce confusion, I will name *phase diagram* the fixed-composition phase diagram, and *convex hull* the variable-composition phase diagram.

3.3 Methods For Crystal Structure Prediction

As discussed, crystal structure prediction consists in determining the stable structure at given pressure conditions, knowing only the chemical formula. To tackle this formidable task, several approaches were proposed: *topological* approach which constructs structures with the simplest topology that satisfies the preexisting knowledge on their bonding pattern (e.g. assuming sp^3 hybridization) [177, 178], *data mining* based on correlation with other similar structures [179], and *computational optimization*, which involves the explicit calculation (and minimization) of the appropriate thermodynamic potential, and its exploration [180]. Compared to the other two, computational optimization has the dramatic advantage of being completely unbiased: it makes no assumption on the system, and has completely superseded the others. In practice, it uses an *ab initio* code to calculate the energy of a given configuration of atoms, and uses an *optimization* algorithm to minimize it. The problem of finding the minimum (or maximum) of a function over a

N-dimensional space belongs to the general class of *optimization problems*, which have been widely studied in computer science, mathematics, and economics, as well as physics. Over the early 2000s, several methods have been proposed and used successfully [180]:

- **Simulated annealing** [44] is based on a set of random walkers that explore the potential energy surface. At each step, the walkers have a probability of accepting/refusing a move between two states which depends on their energy difference, and on temperature. In particular, if $E_{i+1} < E_i$ the move is accepted, while if $E_{i+1} > E_i$ the move is accepted if $\exp(-(E_{i+1} - E_i)/T) \geq r$, where r is a uniformly distributed random number, and T is temperature. The commonly used approach consists in starting the calculation at high temperature, and slowly reduce it throughout the calculation. The underlying idea is that at high temperature the system *melts*, i.e. is allowed to visit high-energy states and overcome potential barriers between minima. Then, if the cooling is sufficiently slow, it will crystallize in the most stable form, i.e. reach the minimum of the potential energy surface. The main advantage of simulated annealing is that it finds a minimum of the thermodynamic potential which is *kinetically* stable, meaning that the structure found is likely to remain stable at finite temperature. However, the ideal starting temperature, and the cooling rate are not known and in general not predictable. For instance, this algorithm was applied to alkali metal hydrides (LiBr, LiCl), where metastable structures were predicted and later experimentally synthesized [181–183].

- **Metadynamics** [184, 185] was described as "filling the free energy wells with computational sand" [45]. It is based on the assumption that a small set of numbers, called *collective variables*, can be used to describe univocally the state of the system. The method uses molecular dynamics or Monte Carlo to simulate the evolution of a system under certain thermodynamic conditions. In addition, it introduces a penalty function in the thermodynamic potential by adding a Gaussian function to previously-visited states. By stacking up the penalty factor each time a state is visited, the system is forced to leave an already-visited minimum, and to transition to a different state. Once all of the possible states have been explored, the overall shape of the potential energy surface can be reconstructed as the opposite of the total penalty. The metadynamics approach is able, in principle, to describe not only the minima of the potential energy surface, but also the transition states in-between two minima. In real systems, however, other effects such as impurities, defects, surface states, which are too costly to be included in the simulation, may act as nucleation sites for the transition.

- **Minima hopping** [186, 187] aims at evolving a crystal structure in time so that it reaches the global minimum. It combines two strategies. Starting from a local minimum, the algorithm performs a molecular dynamics evolution with a certain temperature T_i, and the energy is

monitored. The evolution stops after the system has visited N local minima of the potential energy surface. Then, the system undergoes a standard structural optimization ($T = 0$), bringing it to the closest minimum. Three scenarios are now possible: 1) if the system is in the same minimum as in the previous step $E_i = E_{i-1}$ then the temperature is increased and the molecular dynamics restarts; 2) if the system is now in a different minimum which has been visited before, the temperature is increased and the molecular dynamics restarts; 3) if the system is in a different minimum that has never been visited before then it is added to the history, and the temperature is lowered. The main idea is to push the structure away from already-visited minima, by gradually increasing the temperature. In this way the system should *hop* from one minima to the next while going through the *lowest* potential barrier. In fact, according to the Bell-Evans-Polanyi principle, the lowest-energy saddle point of the potential energy surface corresponds to the one going towards a lower-energy minimum. In addition, the molecular dynamics restarts with velocities in the direction in which the curvature of the potential energy surface is small, which grants a higher probability to reach a new minimum in a small number of steps. This method was effective in determining the structure of silicon clusters [46,188], or studying gold nanoclusters [189], phosphorous hydrides [138], and many more.

- ***Ab initio* Random Structure Searching** [190] can be summarized in three steps: 1) randomly generate structures; 2) perform structural optimization to the nearest local minimum; 3) repeat until the minimum does not improve for a certain number of steps (convergence). The structure generation can benefit from information on the system, such as excluding unreasonable bond lengths. This method has the advantage of being computationally very simple and easy to implement; it is available in the AIRSS code [190]. However it is normally less efficient than other methods which use the information gained during the run itself to refine the generation of new candidates. It was used successfully to predict the high-pressure structures of silane (SiH_4) [30], CaC_6 [191], and solid hydrogen [65], to name a few.

- **Particle-Swarm Optimization** [48] is a type of genetic algorithm which mimics the behavior of an intelligent swarm. Each structure represents an individual of a swarm. At each optimization step, the atomic positions within each crystal structure are changed, depending on how much it differs from the one with the lowest energy. The underlying idea is that each individual *shares* the information on its energy with the others, hence each member of the swarm moves in the general direction of the global minimum, with the addition of some degree of randomness to its trajectory. The Particle-Swarm Optimization is implemented in the `CALYPSO` code, where additional features are used to improve the efficiency of the search. In particular, the code generates high-symmetry structures to reduce the number of degrees of freedom of the system, and restrict the search space. In addition, similarity between struc-

tures can be evaluated by checking the first- and second-nearest neighbor distances and bond types. This information is used to discard quasi-identical structures, and increase efficiency. Particle-Swarm Optimization has been used in the prediction of crystal structures for hydrides at high pressure [43, 121, 192].

- **Evolutionary Algorithms** are a type of optimization algorithm based on the concept of *survival of the fittest*. This algorithm is implemented in two different codes: XTalOpt [49] and `USPEX` (Universal Structure Predictor: Evolutionary Xstallography) [47, 124]. Throughout my PhD I have extensively used Evolutionary Algorithms, as implemented in the `USPEX` code to predict the stable compositions and crystal structures. Since it was my method of choice, I will be describe it in more detail in the following section.

3.3.1 Evolutionary Algorithm for crystal structure prediction

Evolutionary algorithms are a class of optimization algorithms inspired by the biological concept of evolution. The object which evolves is the *population*, i.e. a set of *individuals*, and the goal is to find the individual which maximizes a *fitness* function. In the context of crystal structure prediction a single set of positions and cell vectors ($\{\vec{\tau}_i, \vec{a}_j\}$) is an individual, and the fitness function is the total energy (or the relevant thermodynamic quantity, if temperature/pressure are included). The evolutionary algorithm is iterative, and each step is called a *generation*. The steps are summarized below:

- Initialization: randomly generate the initial population
- Iteration: repeat the following until exit conditions are satisfied:

1. Evaluate the fitness of each individual
2. Select the N fittest individuals (parents)
3. Remove the least-fit individuals
4. Breed new individuals from *mutation* or *crossover* of the parents (offspring)

The algorithm is conceptually simple, but its technical implementation for crystal structure prediction is not obvious. In particular, two main questions arise: how is each individual represented and identified? How are mutation and crossover implemented in practice? More than one choice is possible, and led to different implementations in competing software codes [47, 49, 193, 194]. In the following I will describe the USPEX implementation.

In USPEX, each crystal structure is represented by the collection of its fractional atomic coordinates $\vec{\tau}_i$, and lattice vectors $\vec{a}_j$. The fitness is the relevant thermodynamic quantity (energy,

enthalpy), calculated using a first-principles method (DFT or a force field). The selection of parents is operated by choosing among the fittest individuals with a probability that increases with the fitness. The child structures are produced from the parents applying three main operations: *heredity*, *mutation*, and *permutation*, which will now be described.

Heredity: two unit cells are combined together to produce a new unit cell. The challenge is to combine the two parent crystals in a meaningful way. The process, shown in Fig. 3.5 works as follows: one of three lattice vectors $\vec{a}_{ch}$ is chosen randomly. Atoms in the unit cell are shifted along the $\vec{a}_{ch}$ direction by a random fraction between 0 and 1. Fractional coordinates exceeding 1 are folded back to the primitive cell by subtracting one. Then, a value x between 0 and 1 is determined randomly, and the child structure is created by taking every atom with a coordinate projection along $\vec{a}_{ch}$ which is less than x from the first parent (slice 1), and every atom with a coordinate projection which is between x and 1 from the second parent (slice 2). Then, if there are too many atoms, the number is adjusted by removing a few of the atoms in excess at random, while if there are too few, one (or more) atoms are taken from one of the parent structures, and placed in the corresponding slice.

The lattice vectors of the child structure are the weighted average of the lattice vectors of the two parents, with a random weight.

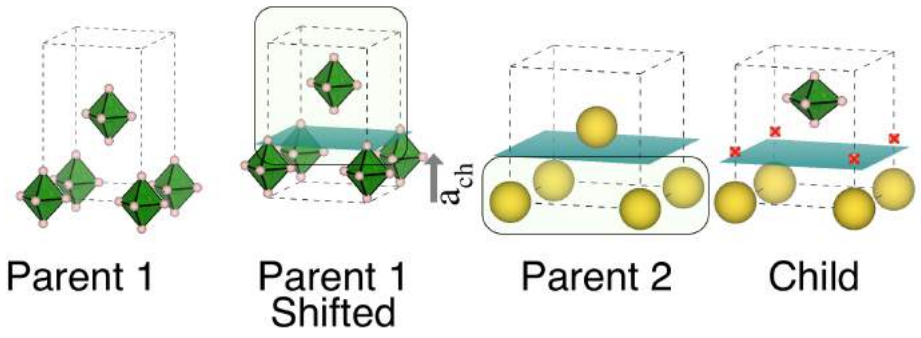

Figure 3.5: Heredity algorithm at work. From left to right: parent 1 structure is chosen, parent 1 structure is shifted by a random amount $\vec{a}_c h$ along the z axis, and a certain value x is chosen (green plane), parent 2 structure is chosen, atoms from one side of parent 1, and from the other side of parent 2 are selected, and atoms in excess are removed.

Mutation: one unit cell is distorted to generate a different unit cell. In particular, the lattice vectors $\vec{a}$ are transformed to new vectors $\vec{a}'$ by applying the deformation:

$$[I + \epsilon_{ij}] = \begin{bmatrix} 1+\epsilon_{11} & \epsilon_{12}/2 & \epsilon_{13}/2 \\ \epsilon_{21}/2 & 1+\epsilon_{22} & \epsilon_{23}/2 \\ \epsilon_{31}/2 & \epsilon_{23}/2 & 1+\epsilon_{33} \end{bmatrix}$$

The ϵ_{ij} values random numbers with a gaussian distribution with zero mean. This operation is equivalent to applying a stress tensor $\overleftrightarrow{\epsilon}$ to the unit cell.

Permutation: A single individual is used to generate a new one by swapping the positions of two atoms of different types. This is done a variable number of times, and can only be done when atoms of different types are present.

The individuals generated by the three variation operators, are then tested against three *hard constraints*. First, the interatomic distance cannot be less than a certain threshold, which depends on the two atomic species and on the pressure. Second, the α, β and γ angles between the lattice vectors cannot be too large or too small (i.e. they cannot deviate too much from 90^o). Third, the lattice vectors cannot be shorter than a certain threshold. These three constraints ensure the stability of the subsequent calculations, as they remove candidate structures that could give rise to numerical errors. In addition, they reduce the size of the search space, by excluding structures which exhibit unphysical bond lengths.

The evolutionary algorithm employing the operations described above is incredibly efficient, and enabled many important computational discoveries [9,39,110]. Its impressive efficiency derives from the fact that it exploits the *locality* of the interatomic interactions. The underlying idea is that the best structures of each generation must have some local fragments in common with the real minima. The variation operators randomly act on crystal structures that are rich in locally optimal fragments, and re-combine them. Generation after generation, the best individuals will be rich in locally optimal fragments, and the probability of randomly combining them in the optimal structure will increase until convergence. Another powerful tool employed by `Uspex` is its *fingerprint* function, i.e. numerical function which uniquely characterizes a crystal structure, based only on information on the structure itself. The difference between two fingerprint functions can be used to define an abstract *distance* between two structure. `Uspex` employs an effective fingerprint function to add a penalty to the fitness of structures that have been already sampled, so that the algorithm does not become trapped in local minima [124,195].

So far I have described the evolutionary algorithm implemented in USPEX, together with the three main variation operators. Implicitly I assumed that the composition of my crystal was kept fixed during the search, which allowed me to define the potential energy surface $E(\vec{\tau}_i, \vec{a}_j)$. The evolutionary algorithm thus defined allows me to determine the optimal crystal structure for a given chemical composition. This is extremely useful for pure elements, or for systems where one already knows the stable chemical composition from experiment. However, this is clearly an important limitation to the goal of materials discovery.

An ambitious goal is to determine, from a given choice of atoms, which are the stable compositions, and for those to determine the crystal structure. This could be done, in principle, by performing one fixed-composition calculation and determine the minimum energy for each compo-

sition. Once this is done, one can construct the convex hull diagram, as described before. The disadvantage of this approach is that out of hundreds of possible compositions only very few are stable, and sampling all of them with the same accuracy is computationally very expensive, and also extremely inefficient. A much more efficient approach is represented by variable-composition search algorithms. In this case, the stable composition and the corresponding stable crystal structure are predicted simultaneously. In USPEX, the variable-composition algorithm is introduced as an extension of the fixed-composition one, with the following changes:

- Start with random structures with random composition, which sample sparsely the phase space of interest.
- Allow variation operators to modify also the chemical composition. This is achieved by removing the correction for the number of atoms in the heredity operator, and by introducing a new operator called *chemical transmutation*, which changes one randomly selected atom into one of the other atomic species present. The permutation operator remains unchanged.
- The fitness function is replaced by the energy per atom minus the energy of the most stable mixture of already sampled structures which gives the same composition.

As mentioned before, variation operators tend to mix and match locally optimal fragments. If a stable structure for a stable composition exists, I can expect its fragments to appear not only for this composition, but also for similar ones, causing close-to-optimal compositions to be sampled more. Conversely, the compositions which are away from stability will tend to be discarded frequently, and as a result will be sampled less frequently. This procedure greatly improves the efficiency of the algorithm, by allowing it to spend less resources to sample unstable compositions, and more on stable ones.

The revolutionary aspect of this approach is that it allows an unbiased and unconstrained search of stable new materials under any thermodynamic condition. The main limitation is represented by the so-called *curse of dimensionality*. This expression, originally coined by Richard Bellman, refers to the fact that in some problems the volume of the search space increases so fast that the amount of data required to achieve statistical significance becomes too large. This principle applies to variable-composition structural searches, and can be seen in action by considering the increase in the number of possible compositions with the increase of number of elements.

Consider a unit cell containing N atoms, and a choice of M possible elements. The number of possible compositions corresponds to the combinatorial problem of calculating how many nonidentical combinations can be made by taking N elements of out M, where each element can be taken more than once. This follows the relation:

$$\binom{N+M-1}{M-1} = \frac{(N+M-1)!}{N!(M-1)!} \tag{3.2}$$

Consider, for example, a unit cell with $N = 16$ atoms. In a binary system, i.e. constituted by the combination of two elements, there are $\binom{17}{1} = 17$ possible compositions. In such systems, the algorithm is normally able to identify the stable compositions and structures by a sampling about one thousand structures. Now consider a ternary system, with the same unit cell. Using again eq. (3.2), I get $\binom{18}{2} = 153$ possible compositions. In this case tens of thousands of structures have to be sampled in order to get to a reliable result. As the number of possible compositions exhibits a factorial increase, the exploration of quaternary (2907 combinations), or even more complex systems is prevented by the sheer size of the search space.

The possible strategies to overcome this problem can be divided into two main categories: 1) reduce the cost of a calculation and 2) develop a more efficient search strategy. The first category requires a method for calculating the total energy (or enthalpy) using less computational resources than Density Functional Theory. One way is using machine-learned interatomic potentials, which promise to achieve an accuracy comparable to DFT at a fraction of the computational cost [160–162]. Another possibility would be to train a deep neural network to directly estimate the energy from the atomic configuration. The second category is more difficult. One possibility could be to construct a set of prototypical structures which encode the most information on the different types of bonding and compositions, to be used as the starting population. If this set contains a few structures which are similar to the optimum, it should be able to give a variable-composition search algorithm a significant head start. This will probably be the major challenge in the field of crystal structure prediction for the far future.

Chapter 4

Ab-initio Theory of Superconductivity

In this chapter, I will give an overview of the theoretical description of superconductivity. In the first section I will shortly discuss the Barden-Cooper-Schrieffer theory (BCS), which offered the first microscopical description of superconductivity; in the second section I will describe in detail the Migdal-Éliashberg theory, which extends BCS theory to the case of non-instantaneous interaction, and discuss how, in combination with Density Functional Perturbation Theory, it can be used to predict the superconducting properties of materials from first principles. I will also shortly discuss Density Functional Theory for Superconductors (SDCFT), an alternative theory for the description of superconductivity based on the introduction of auxiliary densities for ions and Cooper pairs.

4.1 BCS theory

The first microscopic description of superconductivity was published in 1957 by Barden, Cooper and Schrieffer [196]. The so-called BCS theory was soon recognized to describe correctly the essential phenomena observed in superconductors: the opening of a superconducting gap of the order of a few tens of meV in the electronic spectrum below a critical temperature, and the *isotope effect*, i.e. the fact that the critical temperature changes with the mass of the crystal lattice ions M following the relation:

$$T_c \propto M^{-\alpha} \tag{4.1}$$

Where α is material-dependent, but typically $\alpha \sim 0.5$. BCS theory is based on a set of assumptions. Cooper demonstrated that two electrons outside the Fermi surface form a bound state (*Cooper pair*) if an arbitrarily weak attractive interaction is present [197]. Cooper pairs are pairs of electrons of opposite spins and momentum. BCS theory is based on the key idea that electrons near the Fermi

surface experience an *effective* attractive interaction mediated by a *boson*, hence form a coherent state of Cooper pairs.

The starting point is the BCS Hamiltonian $\mathcal{H}_{bcs} = \mathcal{H}_0 + \mathcal{H}_{red}$, where $\mathcal{H}_0$ is the tight-binding Bloch Hamiltonian, and $\mathcal{H}_{red}$ is the BCS reduced hamiltonian, which describes the scattering between electrons of opposite momentum.

$$\begin{aligned} \mathcal{H}_0 &= \sum_{\vec{k}\sigma} \epsilon_{\vec{k}} c^\dagger_{\vec{k}\sigma} c_{\vec{k}\sigma} \\ \mathcal{H}_{red} &= \sum_{\vec{k}\vec{k}'} V_{\vec{k}\vec{k}'} (c^\dagger_{-\vec{k}'\downarrow} c^\dagger_{\vec{k}'\uparrow})(c_{\vec{k}\uparrow} c_{-\vec{k}\downarrow}) \end{aligned} \tag{4.2}$$

Where $c^\dagger_{\vec{k}\sigma}$ and $c_{\vec{k}\sigma}$ are creation and destruction operators that act on electrons with momentum $\vec{k}$ and spin σ. The potential $V_{\vec{k}\vec{k}'}$ represents the effective attractive interaction between electrons with momentum $\vec{k}$ and $\vec{k}'$, and pairs only electrons of opposite spin and momentum. In practice, $V_{\vec{k}\vec{k}'}$ can describe different types of interaction mediated by a boson (phonons, spin fluctuations, plasmons, etc.).

In *conventional* superconductors the attraction is a result of the polarization of the lattice, i.e. the boson which mediates the interaction is a phonon. In the following, I will only discuss conventional, i.e. phonon-mediated, superconductivity.

To find the ground-state of the BCS Hamiltonian, Schrieffer introduced an ansatz for the wave function [198]

$$|\psi_{bcs}\rangle = \prod_{\vec{k}} e^{g_{\vec{k}} c^\dagger_{\vec{k}\uparrow} c^\dagger_{-\vec{k}\downarrow}} |0\rangle \tag{4.3}$$

Where $g_{\vec{k}}$ is a parameter yet to be determined from variational minimization. Using the fact that $c^\dagger_{\vec{k}\uparrow} c^\dagger_{-\vec{k}\downarrow} c^\dagger_{\vec{k}\uparrow} c^\dagger_{-\vec{k}\downarrow} = 0$, eq. (4.3) can be rewritten using the Taylor expansion of the exponential. The resulting normalized wavefunction is:

$$|\psi_{bcs}\rangle = \prod_{\vec{k}} \frac{1 + g_{\vec{k}} c^\dagger_{\vec{k}\uparrow} c^\dagger_{-\vec{k}\downarrow}}{\sqrt{1 + |g_{\vec{k}}|^2}} |0\rangle \tag{4.4}$$

Expanding the product in eq. (4.4) one can see that ψ_{bcs} has nonzero amplitude for all even numbers of electrons. The average number of electrons N_0 however depends on the choice of $g_{\vec{k}}$, with a fractional fluctuation about N_0 proportional to $(N_0)^{-1/2}$. One finds $g_{\vec{k}}$ by variational minimization of the energy with the additional constraint that the number of electrons is fixed at N_0. The quantity to be minimized is:

$$\langle\psi_{bcs}| \mathcal{H}_{bcs} - \mu N_0 |\psi_{bcs}\rangle = \sum_{\vec{k}} 2(\epsilon_{\vec{k}} - \mu) v^2_{\vec{k}} + \sum_{\vec{k}\vec{k}'} V_{\vec{k}\vec{k}'} u_{\vec{k}} v_{\vec{k}} u_{\vec{k}'} v_{\vec{k}'} \tag{4.5}$$

With $u_{\vec{k}} = \frac{1}{\sqrt{1+|g_{\vec{k}}|^2}}$ and $v_{\vec{k}} = \frac{g_{\vec{k}}}{\sqrt{1+|g_{\vec{k}}|^2}}$. Then, from the minimization of eq. (4.5) with respect to $u_{\vec{k}}$ and $v_{\vec{k}}$ one finds:

$$u_{\vec{k}}^2 = \frac{1}{2}\left(1 + \frac{\epsilon_{\vec{k}} - \mu}{E_{\vec{k}}}\right) \tag{4.6}$$

$$v_{\vec{k}}^2 = \frac{1}{2}\left(1 - \frac{\epsilon_{\vec{k}} - \mu}{E_{\vec{k}}}\right) \tag{4.7}$$

$$u_{\vec{k}} v_{\vec{k}} = \frac{\Delta_{\vec{k}}}{2E_{\vec{k}}} \tag{4.8}$$

$$E_{\vec{k}} = \sqrt{(\epsilon_{\vec{k}} - \mu)^2 + \Delta_{\vec{k}}^2} \tag{4.9}$$

Where $E_{\vec{k}}$ is the energy spectrum of the quasiparticles in the superconducting state, which exhibits a *gap* of width $2\Delta_{\vec{k}}$, also called *superconducting gap*. The superconducting gap satisfies the equation:

$$\Delta_{\vec{k}} = \sum_{\vec{k}'} V_{\vec{k}\vec{k}'} \frac{\Delta_{\vec{k}'}}{2E_{\vec{k}'}} \tag{4.10}$$

With the constraint that $2\sum_{\vec{k}} v_{\vec{k}}^2 = N_0$. In order to obtain an explicit expression, one needs to explicitly specify the interaction $V_{\vec{k}\vec{k}'}$. Starting from the idea that the interaction is phonon-mediated, the approximation introduced in the original BCS paper is the BCS potential:

$$V_{\vec{k}\vec{k}'} = \begin{cases} -V < 0 \text{ for } |\epsilon_{\vec{k}}| \text{ and } |\epsilon_{\vec{k}'}| < \hbar\omega_c \\ 0 \text{ otherwise} \end{cases} \tag{4.11}$$

Where $\hbar\omega_c$ is an energy characteristic of the phonon energy scale of the system, such as the Debye frequency ω_D[1]. This means that the attractive potential only affects electrons within a shell of $\pm\hbar\omega_c$ of the Fermi energy. The potential V describes the electron-phonon interaction (*ep*). Using the approximate $V_{\vec{k}\vec{k}'}$ in eq. (4.10) one obtains an expression for the superconducting gap:

$$\Delta_{\vec{k}} = \begin{cases} \Delta_0 = 2\omega_c \exp\left[-\frac{1}{N(\epsilon_F)V}\right] \text{ for } |\epsilon_{\vec{k}}| < \hbar\omega_c \\ 0 \text{ otherwise} \end{cases} \tag{4.12}$$

Where $N(\epsilon_F)$ is the DOS at the Fermi level in the normal state. The product $N(\epsilon_F)V$ is also defined as λ, i.e. the mean *e-ph* interaction parameter. These results can be also extended to finite temperature, as I will now discuss. An insightful method to describe the quasiparticle excitation energies is the one introduced by J. Valatin [199,200], which aims to find a new set of operators $\gamma^\dagger$,

[1] The Debye frequency is a characteristic frequency of the system defined as the frequency at which the integral of the DOS of a linear dispersion with slope c equals the number of atoms in the unit cell, where c is the sound velocity at $\omega = 0$

γ which create and destroy excitations that are still eigenstates of H_{bcs} defined in eq. (4.2). Trying to find the exact operators results in a series up to infinite order, but a closed form can be found by truncating it up to a certain order – in practice it is sufficient to consider linear combinations of $c^\dagger$ and c. One introduces the operators $\gamma^\dagger$ and γ:

$$\gamma^\dagger_{\vec{p}\uparrow} = u_{\vec{p}} c^\dagger_{\vec{p}\uparrow} - v_{\vec{p}} c_{-\vec{p}\downarrow} R^\dagger \tag{4.13}$$

$$\gamma_{-\vec{p}\downarrow} = u_{\vec{p}} c_{-\vec{p}\downarrow} - v_{\vec{p}} R c^\dagger_{\vec{p}\uparrow} \tag{4.14}$$

Where the $R^\dagger$ operator transforms a N-particle state $|N\rangle$ into a N+2-particle one $|N+2\rangle$, and the R operator transforms a N+2-particle state into a N-particle one. The $\gamma^\dagger/\gamma$ operators satisfy Fermi anticommutation relations, and create/destroy non-interacting Fermion excitations when applied to the N-particle ground state $|0, N\rangle$. Following this approach one arrives at the same result of eqs. (4.6)-(4.9), and can write the relation:

$$\langle 0, N+2 | \, c^\dagger_{\vec{k}\uparrow} c^\dagger_{-\vec{k}\downarrow} \, |0, N\rangle = u_{\vec{k}} v_{\vec{k}} = \frac{\Delta_{\vec{k}}}{2E_{\vec{k}}} \tag{4.15}$$

Where $|0, N\rangle$ and $|0, N+2\rangle$ is the ground state of the N- and N+2 particle state. It is straightforward to introduce the effect of temperature by considering instead the matrix element calculated on a thermal ensemble. Considering the diagonalized Hamiltonian: $H_d = \sum_{\vec{k}} E_{\vec{k}} \gamma_{\vec{k}} \gamma^\dagger_{\vec{k}}$, and recalling that $\gamma^\dagger$ creates non-interacting Fermion excitations, one has the partition function:

$$Z = \prod_{\vec{k}} (1 + e^{-\beta E_{\vec{k}}}) \tag{4.16}$$

One can invert eq. 4.13 to write $c^\dagger_{\vec{k}\uparrow} c^\dagger_{-\vec{k}\downarrow}$ in terms of $\gamma^\dagger/\gamma$. Note that the $\gamma^\dagger\gamma^\dagger$ and $\gamma\gamma$ terms do not contribute, as they create orthogonal states. Hence one can write the thermal average:

$$\frac{\sum_n \langle n, N+2 | \, u_{\vec{k}} v_{\vec{k}} \left(\gamma_{-\vec{k}\downarrow} \gamma^\dagger_{-\vec{k}\downarrow} - \gamma^\dagger_{\vec{k}\uparrow} \gamma_{\vec{k}\uparrow} \right) e^{-\beta \sum_{\vec{k}} E_{\vec{k}} \gamma_{\vec{k}} \gamma^\dagger_{\vec{k}}} \, |n, N\rangle}{Z} = u_{\vec{k}}(T) v_{\vec{k}}(T) = \frac{\Delta_{\vec{k}}}{2E_{\vec{k}}} \left(1 - f_{\vec{k}\uparrow} - f_{-\vec{k}\downarrow} \right) \tag{4.17}$$

The sum over n is considered to be over all possible quasiparticle excitations (see Ref. [201] for details), and $f_{\vec{k}\uparrow}$ is the Fermi distribution function:

$$f_{\vec{k}} = \frac{1}{1 + e^{\frac{E_{\vec{k}}}{k_B T}}} \tag{4.18}$$

which here describes the expectation value of the occupation number $\gamma_{\vec{k}\sigma} \gamma^\dagger_{\vec{k}\sigma}$ for the quasiparticles

at temperature T. Using eq. (4.18) into eq. (4.17), one obtains:

$$u_{\vec{k}}(T)v_{\vec{k}}(T) = \frac{\Delta_{\vec{k}}}{2E_{\vec{k}}} \tanh\left(\frac{E_{\vec{k}}}{2k_BT}\right) \tag{4.19}$$

This enters the equation for the gap (eq. (4.10)), which becomes:

$$\Delta_{\vec{k}} = \sum_{\vec{k}'} V_{\vec{k}\vec{k}'} \frac{\Delta_{\vec{k}'}}{2E_{\vec{k}'}} \tanh\left(\frac{E_{\vec{k}}}{2k_BT}\right) \tag{4.20}$$

Again, this equation can be solved by specifying the potential $V_{\vec{k}\vec{k}'}$. Choosing the potential in eq. (4.11), one obtains an equation for the gap as a function of temperature $\Delta(T)$

$$\frac{1}{N(\epsilon_F)V} = \int_0^{\hbar\omega_c} \frac{d\epsilon}{\sqrt{\epsilon^2 + \Delta^2(T)}} \tanh\left(\frac{\sqrt{\epsilon^2 + \Delta^2(T)}}{2k_BT}\right) \tag{4.21}$$

The superconducting gap Δ_0 decreases as T increases, and it becomes zero at the critical temperature T_c. An analytical formula for the T_c can be obtained from eq. (4.21) in the *weak* coupling limit, i.e. $\lambda \ll 1$ by imposing $\Delta(T) = 0$, and integrating by parts:

$$k_BT_c = 1.14\omega_c \exp\left[\frac{1}{N(\epsilon_F)V}\right] \tag{4.22}$$

Using the same approximation on eq. (4.21) in the case of T=0 one also obtains $\Delta(T = 0)$, from which the famous BCS ratio is derived:

$$\frac{2\Delta(T=0)}{k_BT_c} = 3.52 \tag{4.23}$$

Which appeared to be a universal ratio in weak-coupling superconductors. The ratio $\frac{2\Delta(T=0)}{k_BT_c}$, also called BCS ratio, can be used as an estimate of coupling strength, as values significantly larger are an indication that a superconductor is in the strong coupling regime. BCS theory essentially describes all type I superconductors, but fails for compounds with a higher T_c, which often exhibit larger BCS ratios. From eq. (4.22) one can also justify the *isotope effect*, as the T_c is proportional to ω_D, which in elemental superconductors it is proportional to the inverse square root of the atomic mass.

BCS theory was able to explain several experimentally observed effects: the existence of a superconducting gap [202, 203], and the related jump in the specific heat near the critical temperature [204], as well as the effect of the superconducting state on the nuclear spin relaxation time [205], and on acoustic waves propagating in the crystal [206].

4.2 Migdal-Éliashberg Theory

Despite BCS theory being undeniably successful, the T_c equation (eq. (4.22)) fails with many superconductors. The fault is not in the approximation needed to arrive to eq. (4.22), but rather in the starting model, as the Hamiltonian in eq. (4.2) considers an instantaneous pairwise interaction between electrons, which does not describe well the electron-phonon physics [207]. In particular, the *e-ph* interaction causes a mass enhancement of electrons near the Fermi energy, and a finite lifetime of electron quasiparticle states. These effects can be quite strong, and have to be accounted for.

A theory which goes beyond BCS can be constructed using Feynman-Dyson perturbation theory, including the effect of retardation in the interaction. This theory is based on Migdal's theorem [23], who showed that as long as the phonon energy scale is much smaller than the electronic one ($\omega_D \gg \epsilon_F$), high-order corrections to the vertexes can be neglected. The theory was developed by Éliashberg [24] and is called Migdal-Éliashberg theory.

In this section I will first introduce the Migdal-Éliashberg theory of superconductivity within the Nambu-Gor'kov formalism. I will first define the relevant quantities in the metallic state, and then show how they are generalized to the superconducting case. The normal state of the electron quasiparticles is described by their interacting temperature-dependent Green's function G

$$G(\vec{k},\tau) = -\langle T_\tau c_{\vec{k}\sigma}(\tau) c^\dagger_{\vec{k}\sigma}(0)\rangle \tag{4.24}$$

Where T_τ is the time-ordering operator. In absence of spin-dependent interaction the spin variable σ can be omitted to make the notation more compact. As G is anti-periodic in time, its Fourier transform is a discrete sum over Matsubara frequencies.

$$G(\vec{k},\tau) = \frac{1}{\beta}\sum_{n=-\infty}^{+\infty} \exp^{-i\omega_n\tau} G(\vec{k}, i\omega_n) \tag{4.25}$$

Where $\omega_n = (2n+1)\pi/\beta$ are the fermionic Matsubara frequencies and $\beta = \frac{1}{T}$.

In addition to the electron Green's function G, one also needs to define the analogous phonon Green's function D

$$D_{\alpha\beta}(\vec{q},\tau) = -\langle T_\tau u_{\vec{q}\alpha(\tau)} u_{-\vec{q}\beta}(0)\rangle \tag{4.26}$$

Where $u_{\vec{q}\alpha}$ is a *displacement operator* with momentum $\vec{q}$, and Cartesian component α, i.e. a linear combination of phonon destruction and creation operators $a^\dagger_{\vec{q}i}/a_{\vec{q}i}$, with branch index i

$$\vec{u}_{\vec{q}} = \sum_i \Big(\frac{\hbar}{2NM\omega_{\vec{q}i}}\Big)^{1/2} \vec{\epsilon}_{\vec{q}i}(a_{\vec{q}i} + a^\dagger_{-\vec{q}i}) \tag{4.27}$$

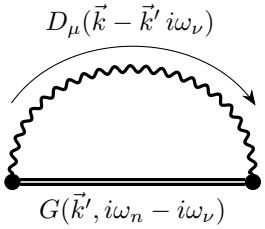

Figure 4.1: The Feynman diagram for the electron-phonon contribution to the electronic self-energy according to Migdal theory. The wavy line is a phonon Green's function D with momentum $\vec{k}-\vec{k}'$ and branch index μ, and the double solid line is a renormalized electron Green's function G. Each vertex introduces an electron-phonon matrix element $|g^{\mu}_{\vec{k}\vec{k}'}|$

Where $\vec{\epsilon}$ is the phonon polarization. D is periodic in τ and thus its Fourier transform is obtained summing over bosonic Matsubara frequencies $\omega_\nu = 2\nu\pi/\beta$:

$$D_{\alpha\beta}(\vec{q},\tau) = \frac{1}{\beta}\sum_{\nu=-\infty}^{+\infty} e^{-i\omega_\nu \tau} D_{\alpha\beta}(\vec{q}, i\omega_\nu) \tag{4.28}$$

The electron self-energy Σ is defined by the Dyson's equation:

$$G(\vec{k}, i\omega_n) = G_0^{-1}(\vec{k}, i\omega_n) - \Sigma(\vec{k}, i\omega_n) \tag{4.29}$$

Migdal's theorem guarantees that the electron-phonon part of Σ (Σ_{ep}) can be expressed using only the lowest-order Feynman diagram, shown in Fig. 4.1. In fact, it shows that higher-order graphs that are not implicitly included in Fig. 4.1 by the use of the self-consistent Green's function are smaller by a factor ω_D/ϵ_F, which is of the order of 10^{-2}-10^{-3}.

The electronic self-energy includes a contribution from the electron-phonon and one from the electron-electron interaction. The second term is assumed to be absorbed in the electronic quasi-particle energies $\epsilon_{\vec{k}\sigma}$. The *residual* repulsive Coulomb interaction, i.e. not causing a simple renormalization of the electronic spectrum, negatively affects the formation of electron-electron pairs in superconductivity. Fortunately this effect is small, and is usually represented with the so-called Morel-Anderson pseudopotential, as I will discuss later in this section.

The electron-phonon self energy diagram is shown in Fig. 4.1. The corresponding expression is:

$$\Sigma_{ep}(\vec{k}, i\omega_n) = -\frac{1}{\beta}\sum_{\vec{k}',\nu,\mu} |g^{\mu}_{\vec{k}\vec{k}'}|^2 D_\mu(\vec{k}-\vec{k}', i\omega_\nu) G(\vec{k}', i\omega_n - i\omega_\nu) \tag{4.30}$$

Where $g^{\nu}_{\vec{k}\vec{k}'}$ is the electron phonon (*e-ph*) matrix element between two Bloch states with momentum

$\vec{k}$ and $\vec{k}'$ and a phonon with branch μ and momentum $\vec{k}-\vec{k}'$, and

$$D_\mu(\vec{q}, i\omega_\nu) = \frac{2\omega_{\vec{q},\mu}}{(i\omega_\nu)^2 - \omega^2_{\vec{q},\mu}} \tag{4.31}$$

The calculation of the matrix element g is discussed in more detail in section 4.3. In practice, by combining eq. (4.29) and (4.30) the normal state properties can be calculated. Before moving on, it is useful to rewrite eq. (4.30) in term of the electron-phonon spectral function α^2F, also called Éliashberg function, which is a crucial quantity in electron-phonon theory:

$$\Sigma_{ep}(\vec{k}, i\omega_n) = T\sum_{\vec{k}',\nu}\int_0^\infty \frac{\alpha^2F(\vec{k},\vec{k}',\Omega)}{N(\epsilon_F)}\left(\frac{2\Omega}{\omega_\nu^2+\Omega^2}\right) G(\vec{k}', i\omega_n - i\omega_\nu) \tag{4.32}$$

with α^2F defined as:

$$\alpha^2F(\vec{k},\vec{k}',\Omega) = \sum_\mu N(\epsilon_F)|g^\mu_{\vec{k}\vec{k}'}|^2\delta(\Omega - \omega_{\vec{k}-\vec{k}',\mu}) \tag{4.33}$$

The Éliashberg function is a dimensionless measure of the amount of *e-ph* coupling between a phonon of energy Ω, and momentum $\vec{k}-\vec{k}'$, and two electrons with momentum $\vec{k}$ and $\vec{k}'$.

In order to describe the superconducting state, each of the quantities so far defined in the normal state has to be generalized to the superconducting phase. In essence, this generalization constitutes Éliashberg theory. The generalization of eq. (4.24) can be written in a compact way using the notation introduced by Nambu [208]. The superconducting state will be characterized by a generalized Green's function $\hat{G}$:

$$\hat{G}(\vec{k},\tau) = -\begin{pmatrix} \langle T_\tau c_{\vec{k}\uparrow}(\tau)c^\dagger_{\vec{k}\uparrow}(0)\rangle & \langle T_\tau c_{\vec{k}\uparrow}(\tau)c_{-\vec{k}\downarrow}(0)\rangle \\ \langle T_\tau c^\dagger_{-\vec{k}\downarrow}(\tau)c^\dagger_{\vec{k}\uparrow}(0)\rangle & \langle T_\tau c^\dagger_{-\vec{k}\downarrow}(\tau)c_{-\vec{k}\downarrow}(0)\rangle \end{pmatrix} \tag{4.34}$$

Intuitively it can already be observed that while G only propagates electrons, the off-diagonal term of eq. (4.34), also called *anomalous* Green's function F, creates or destroys *pairs* of electrons. The off-diagonal term is nonzero only below the superconducting critical temperature —above T_c, $\hat{G}$ becomes identical to G, and the normal state is recovered.

The self-energy for the generalized Green's function $\hat{G}$ is still defined by Dyson's equation

$$\hat{G}^{-1}(\vec{k}, i\omega_n) = \hat{G}_0^{-1}(\vec{k}, i\omega_n) - \hat{\Sigma}(\vec{k}, i\omega_n) \tag{4.35}$$

At this point it is useful to expand the self-energy $\hat{\Sigma}$ in a basis of Pauli matrices, which constitute a complete and orthornomal set:

$$\hat{\tau_0} = \begin{pmatrix} 1 & 0 \\ 0 & 1 \end{pmatrix}, \hat{\tau_1} = \begin{pmatrix} 0 & 1 \\ 1 & 0 \end{pmatrix}, \hat{\tau_2} = \begin{pmatrix} 0 & -i \\ i & 0 \end{pmatrix}, \hat{\tau_3} = \begin{pmatrix} 1 & 0 \\ 0 & -1 \end{pmatrix}, \tag{4.36}$$

The self-energy thus re-written takes the general form:

$$\hat{\Sigma}(\vec{k}, i\omega_n) = i\omega_n \left[1 - Z(\vec{k}, i\omega_n)\right] \hat{\tau}_0 + \chi(\vec{k}, i\omega_n)\hat{\tau}_3 + \phi(\vec{k}, i\omega_n)\hat{\tau}_1 + \bar{\phi}(\vec{k}, i\omega_n)\hat{\tau}_2 \tag{4.37}$$

Where Z, χ, ϕ, and $\bar{\phi}$ are four independent and, in principle, arbitrary functions. The generalized Green's function can be written in the same way.

$$\hat{G}(\vec{k}, i\omega_n) = \left[i\omega_n Z\hat{\tau}_0 - (\epsilon_{\vec{k}} + \chi)\hat{\tau}_3 - \phi\hat{\tau}_1 - \bar{\phi}\hat{\tau}_2\right] / \det(\hat{G}^{-1}) \tag{4.38}$$

The physical meaning of Z, χ, ϕ, and $\bar{\phi}$ can be deduced from eq. (4.38): Z is the electron quasiparticle mass renormalization, χ is a phonon-induced shift in the ground-state electron quasiparticle energies $\epsilon_{\vec{k}}$, while ϕ is the order parameter for the superconducting state (i.e. the density of Cooper pairs). Z and χ are determined by the normal-state self-energy, and are present both above and below T_c, while ϕ is characteristic of the superconducting state, and is non-zero only for $T < T_c$.

The next step is to rewrite the self-energy Feynman diagram for the anomalous Green's function. In Fig. 4.1 I only considered the electron-phonon interaction. For the sake of simplicity, I will neglect the contribution of impurities (non-magnetic and paramagnetic), which leaves only the contribution of electron-phonon and Coulomb interaction. The electron-phonon part can be directly generalized by considering $\hat{\tau}_3\hat{G}\hat{\tau}_3$ instead of G in eq. (4.30).

At this point, it is useful to separate the summations in $\vec{k}$ into a sum over *angular* functions J, and an integral over energies ϵ, following the procedure described by Allen and Mitrovic [207]. Assuming that there is a complete and orthonormal set of functions F such that

$$\sum_{\vec{k}} F_J(\vec{k})F_{J'}(\vec{k})\delta(\epsilon_{\vec{k}} - \epsilon) = \delta_{JJ'}N(\epsilon) = \delta_{JJ'}\sum_{\vec{k}}\delta(\epsilon - \epsilon_{\vec{k}}) \tag{4.39}$$

Where $N(\epsilon)$ is the Density of States. In the case of a spherical energy surface these are spherical harmonics, and for a general case they are named *Fermi surface harmonics* [209], and will depend on the specific Fermi surface. It follows that a generic function $A(\vec{k})$ can be written as

$$A(\vec{k}) = \sum_J A_J(\epsilon)F_J(\vec{k}) \tag{4.40}$$

The benefit of this approach is that it permits a more intuitive reasoning in terms of energy scales.

Using this notation, it is useful to rewrite the generalization of the electron-phonon term of the self-energy $\hat{\Sigma}_{ep}$:

$$\hat{\Sigma}_{ep}(\epsilon, i\omega_n, J) = T\sum_{J',\nu}\int_{-\infty}^{\infty} d\epsilon' \frac{N(\epsilon')}{N(\epsilon_F)} \int_0^{\infty} d\Omega\alpha^2 F_{J,J'}(\epsilon, \epsilon', \Omega)\frac{2\Omega}{\omega_\nu^2 + \Omega^2}\hat{\tau}_3\hat{G}_{J'}(\epsilon', i\omega_n - i\omega_\nu)\hat{\tau}_3 \tag{4.41}$$

When discussing the normal state it was assumed that part of the Coulomb interaction was already included in the renormalization of the electronic eigenenergies $\epsilon_{\vec{k}}$, hence is already included in the *diagonal* part of $\hat{G}$. In the treatment of the superconducting state the quantity to be considered is the *residual* Coulomb interaction, i.e. the off-diagonal part of the electronic self-energy. Although the Coulomb interaction is in general strong, its contribution to the off-diagonal part of the self-energy is quite small, and can be recast into a small parameter using the so-called Morel-Anderson approximation [210]. The main idea is to exploit the fact that the energy scale of superconductivity is much smaller than that of Coulomb interaction. So one introduces a cutoff energy ω_{cut} on the Matsubara frequencies, and shows that

- For $\omega_n > \omega_{cut}$ the Coulomb interaction is the only relevant term in the self-energy $\hat{\Sigma}$. Since this term is the dominant one, this sum can be performed *separately* from the others by introducing a *Coulomb pseudopotential* which incorporates the sum
- For $\omega_n < \omega_{cut}$ the Coulomb interaction does not depend significantly on energy, and can be regarded as constant and isotropic

Using these approximation, the residual Coulomb interaction can be written as:

$$\hat{\Sigma}_C(i\omega_n) = -T \sum_{J',n'}^{|\omega_{n'}<\omega_{cut}|} \mu^*(\omega_{cut}) \int_{-\infty}^{\infty} \hat{\tau}_3 \hat{G}^{od}_{J'}(\epsilon, i\omega_{n'})\hat{\tau}_3 \tag{4.42}$$

Where μ^* is a constant, named the so-called Morel-Anderson pseudopotential [210], as it describes the residual Coulomb interaction between Cooper pairs, accounting for the effect of screening and retardation. In real materials, μ^* is typically found to be between 0.08 and 0.20. A more detailed derivation of eq. (4.42) is given in Appendix B.

At this point, a common approximation is to remove the energy dependence from eq. (4.41). This approximation is justified by the argument that we wish to know the self energy $\Sigma_J(\epsilon, i\omega_n)$ with ϵ and ω_n within ω_D of the Fermi energy. $\alpha^2F(J, H', \epsilon, \epsilon', \Omega)$ is bound in Ω, and thus it its integral in ϵ is important only in a small range around ϵ_F. Except for extremely narrow bands, the DOS $N(\epsilon)$ is also approximately constant in this range, hence this approximation is referred to as *constant DOS* approximation. Thus one approximates eq. (4.41) as:

$$\hat{\Sigma}_{ep}(i\omega_n, J) = T \sum_{J',\nu} \int_0^{\infty} d\Omega \alpha^2 F_{J,J'}(\Omega) \frac{2\Omega}{\omega_\nu^2 + \Omega^2} \int_{-\infty}^{\infty} \hat{\tau}_3 \hat{G}_{J'}(\epsilon', i\omega_n - i\omega_\nu)\hat{\tau}_3 \tag{4.43}$$

The ϵ integral over $\hat{G}$ in eq. (4.42) and (4.43) can be evaluated using eqs. (4.37) and (4.38),

with the consideration that the implicit dependence on ϵ of Z, ϕ and χ is negligible. The result is

$$\int_{-\infty}^{\infty} d\epsilon' \hat{G}_{J'}(\epsilon', \omega_n') = -\pi \sum_{\vec{k}} \left[\frac{i\omega_{n'} Z(\vec{k}, i\omega_{n'})\hat{\tau}_0 + \phi(\vec{k}, i\omega_{n'})\hat{\tau}_1}{\left\{ \left[\omega_{n'} Z(\vec{k}, i\omega_{n'})\right]^2 + \phi(\vec{k}, i\omega_{n'})^2 \right\}} \right]^{1/2} \frac{F_J(\vec{k})\delta(\epsilon_F - \epsilon_{\vec{k}})}{N(\epsilon_F)} \tag{4.44}$$

Then, by combining eqs. (4.38), (4.41), and (4.42), and $\det(\hat{G}^{-1}) = (i\omega_n Z)^2 - (\epsilon_{\vec{k}} + \chi)^2 - \phi^2$ one obtains a set of three equations to be solved self consistently (the gauge with $\bar{\phi} = 0$ is chosen), named Éliashberg equations. Within the *constant DOS* approximation of eq. (4.43), the coefficient for $\hat{\tau}_3$ becomes zero, hence the third equation is $\chi_J(i\omega_n) = 0$ [211].

$$Z_J(i\omega_n) = \delta_{J0} + \frac{\pi T}{|\omega_n|} \sum_{n'} \lambda_{J0}(n - n')\, sign(\omega_n) sign(\omega_{n'}) \tag{4.45}$$

$$\phi_J(i\omega_n) = \pi T \sum_{J'n'} \left[\lambda_{J,J'}(n - n') - \mu^*(\omega_{co})\right] \frac{\Delta_{J'}(i\omega_{n'})}{|\omega_{n'}|} \tag{4.46}$$

Where

$$\Delta_{J'}(i\omega_{n'}) = \frac{\phi_J(i\omega_n)}{Z_J(i\omega_n)} \tag{4.47}$$

is the superconducting gap, and

$$\lambda_{JJ'}(n - n') = \int_0^{\infty} d\Omega \alpha^2 F_{JJ'}(\Omega) \frac{2\Omega}{(\omega_{n-n'})^2 + \Omega^2} \tag{4.48}$$

is the electron-phonon interaction function. Equations (4.45)–(4.46) are the two most important equations which take into account all the details on the electronic and phonon spectrum. The only substantial approximation was done in neglecting the possibility that Coulomb effects could enhance the T_c through plasmonic effects. Through the solution of the two integral equations as a function of temperature, one obtains the superconducting gap Δ, and the mass-enhancement parameter Z along the imaginary axis, whence their analytic continuation onto the real axis can be calculated. The Migdal-Éliashberg equations in J-space are simpler than their equivalent in $\vec{k}$-space, and present a computational advantage, as typically only few J values are needed to accurately describe the superconducting gap [212].

The equivalent Migdal-Éliashberg equations in $\vec{k}$ space can be obtained from eq. (4.40), and are [211]:

$$Z(\vec{k}, i\omega_n) = 1 + \frac{\pi T}{|\omega_n|} \sum_{\vec{k}'n'} \frac{\delta(\epsilon_{\vec{k}'} - \epsilon_F)}{N(\epsilon_F)} \times \lambda(\vec{k}, \vec{k}'; n - n') sign(\omega_n) sign(\omega_{n'}) \tag{4.49}$$

$$Z(\vec{k}, i\omega_n)\Delta(\vec{k}, i\omega_n) = \pi T \sum_{\vec{k}'n'} \frac{\delta(\epsilon_{\vec{k}'} - \epsilon_F)}{N(\epsilon_F)|\omega_{n'}|} \times \left[\lambda(\vec{k}, \vec{k}'; n - n') - \mu^*(\omega_{co})\right] \Delta(\vec{k}', i\omega_{n'}) \tag{4.50}$$

4.2.1 Isotropic gap equations

In most cases, the superconducting gap is fairly isotropic with a few notable exceptions, such as MgB_2 or CaC_6 [213, 214]. Once the approximation of isotropy is made, i.e. it is assumed that the superconducting gap is uniform in $\vec{k}$-space, the Éliashberg equations (eqs. (4.49), (4.50)) become largely simplified, without significant loss in accuracy. Assuming that the gap is isotropic, one can eliminate all sums over $\vec{k}$-space and substitute them with the corresponding average value.

$$\Delta(\vec{k}, i\omega_n) = \langle \Delta(i\omega_n) \rangle_{FS} \tag{4.51}$$

$$Z(\vec{k}, i\omega_n) = Z(i\omega_n) \tag{4.52}$$

and eqs. (4.49), (4.50) become:

$$\begin{aligned} Z(i\omega_n) &= 1 + \frac{1}{|2n+1|} \sum_{n'} \left[\lambda(n-n')\right] sign(\omega_n) sign(\omega_{n'}) \\ \Delta(i\omega_n) Z(i\omega_n) &= \sum_{n'}^{|\omega_{n'}|<\omega_{cut}} \frac{1}{|2n'+1|} \left[\lambda_{FS}(n-n') - \mu^*\right] \Delta(i\omega_n) \end{aligned} \tag{4.53}$$

The elimination of the integrals over the Fermi surface represents an enormous advantage in the numerical solution of these two equations.

4.2.2 Approximate solution: McMillan/Allen-Dynes formula

If one is only interested in the critical temperature, the Migdal-Éliashberg equations can be solved in a linearized form. Excellent approximate equations for T_c have been discussed in the literature. The most famous is the McMillan formula, as it is quoted by Allen and Dynes at the start of Ref. [61]. The formula was originally derived semi-empirically by McMillan in 1968 [62], and modified in 1975 by Allen and Dynes to correctly reproduce the Éliashberg limit for large values of λ [61]. The formula is:

$$T_c = \frac{\omega_{log}}{1.2} exp\left[\frac{-1.04(1+\lambda)}{\lambda(1-0.62\mu^*) - \mu^*}\right] \tag{4.54}$$

where

$$\begin{aligned} \lambda &= 2\int_0^\infty d\Omega \frac{\alpha^2 F(\Omega)}{\Omega} \\ \omega_{log} &= exp\left(\frac{2}{\lambda}\int_0^\infty d\Omega \alpha^2 F(\Omega) \frac{ln(\Omega)}{\Omega}\right) \end{aligned} \tag{4.55}$$

The equation, in its original form, can be derived from the real-axis continuation of eqs. (4.49) and (4.50), by assuming that $\lambda(n-n')$ is constant for small n and n', and zero whenever $2\pi(n+1/2)T_c \geq$

ω_D. The result has a functional form similar to eq. (4.54), and was later adjusted by McMillan to match the numerical solution of the isotropic Éliashberg equations for a model α^2F, hence the *semi-empirically*. The formula is very accurate for values of λ up to around 1.5, while for higher values it starts to underestimate the T_c [61].

As mentioned McMillan/Allen-Dynes equation is very transparent with respect to its parameters: ω_{log}, λ, and μ^*. ω_{log} is a logarithmic average of the phonon frequency, weighted by the Éliashberg function, which in the formula appears as a pre-factor. High-energy phonons are, in fact, crucial ingredient for conventional superconductivity. λ is the integral of the Éliashberg function times the inverse frequency, i.e. a measure of the total electron-phonon coupling strength. As a consequence of the inverse frequency dependence, high-frequency modes tend to contribute less, and low-energy modes tend to contribute more. The effect of μ^* is to decrease the T_c by effectively decreasing λ in the denominator of the exponential. Its effect is more important in weakly-coupled superconductors, as the T_c in eq. (4.54) increases steeply when λ goes from 0 to 1.5, while increasing less for higher values.

In the case of strong coupling the T_c, the critical field, and the gap at $T = 0$ deviate significantly from the BCS values. An approximate generalization the for $2\Delta_0/k_BT_c$ ratio to the strong-coupling regime was introduced by Mitrović et al. [215, 216], who found

$$\frac{2\Delta_0}{k_BT_c} = 3.53\left[1 + 12.5\left(\frac{T_c}{\omega_{log}}\right)^2 \ln\left(\frac{\omega_{log}}{2T_c}\right)\right] \tag{4.56}$$

Hence, the deviation of the $\frac{2\Delta_0}{k_BT_c}$ from 3.53 can be used to evaluate whether a superconductor is in the strong-coupling regime.

An insightful approximate formula for λ in transition metals was presented by Hopfield in 1969 [217]:

$$\lambda = \frac{N(\epsilon_F)}{M}\frac{\langle|g|^2\rangle}{\langle\omega^2\rangle} \tag{4.57}$$

Where $\langle\omega^2\rangle$ is the mean phonon frequency, M is the ion mass, $N(\epsilon_F)$ is the DOS at the Fermi level, and $\langle|g|^2\rangle$ is the average matrix element. Eq. (4.57) also has the merit of being extremely transparent. It suggests that in order to increase the *e-ph* coupling, one has to either increase the DOS at the Fermi level or the matrix elements. On the other hand the ion mass does not significantly affect λ, as a decrease in M is compensated by an increase in $\langle\omega^2\rangle$.

4.3 *Ab-initio* Calculations

The solution of Éliashberg equations, eqs. (4.49) and (4.50) (or their isotropic version), requires the prior knowledge of the Éliashberg function. At the time when Migdal-Éliashberg theory was developed, the quantities needed by the theory could not be computed from first principles. Typically

the Éliashberg function would be extracted from tunneling experiments. A formidable result of the last twenty years, was the implementation of first-principles methods based on Density Functional Theory and its extensions to compute the ground-state properties of electrons, phonons and the electron-phonon coupling. In Fig. 4.2 I show a summary of the quantities required by Migdal-Éliashberg theory, and the computational method with which it can be computed. In the following, I will shortly discuss Density Functional Theory and its extension, and specify how the relevant quantities are computed.

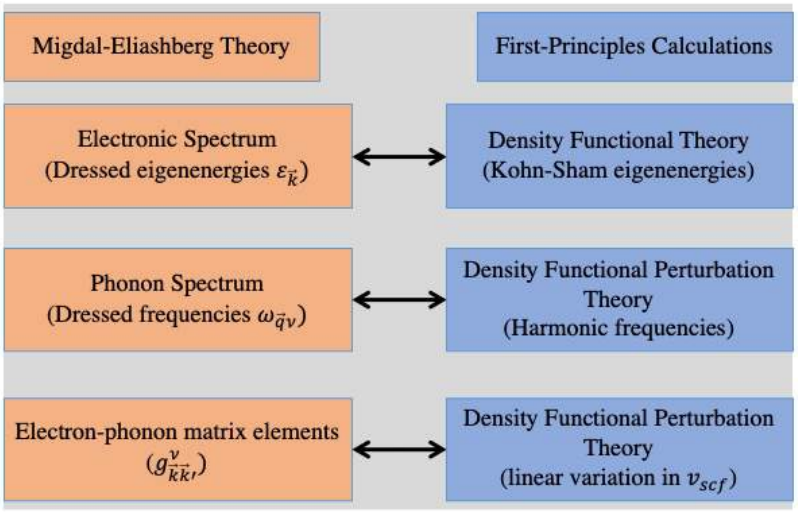

Figure 4.2: Summary of each quantity required by Migdal-Éliashberg theory, and the corresponding method based on DFT to calculate it from first principles.

Electronic Spectrum To describe the electronic spectrum, one can use the eigenenergies ϵ_i of the Kohn-Sham wavefunctions ϕ_i, which are obtained as solution of the Kohn-Sham self-consistent equations, within Density Functional Theory (DFT). In this section I will briefly introduce how the Kohn-Sham eigenenergies are computed.

The starting point is the all-electron Hamiltonian within the Born-Oppenheimer approximation, which states that the dynamics of electrons and ions can be decoupled due to the very large mass disparity [218].

$$\mathcal{H} = T_e + V_{ee} + V_{ei} \tag{4.58}$$

Where

$$T_e = -\frac{1}{2}\sum_{i=1}^{N}\nabla_i^2 \tag{4.59}$$

$$V_{ee} = \frac{1}{2}\sum_{i\neq j}\frac{e^2}{|\vec{r}_i - \vec{r}_j|} \tag{4.60}$$

$$V_{ei} = -\sum_{i,I}\frac{Z_I e^2}{|\vec{r}_i - R_I|} \tag{4.61}$$

In principle, all the information on the N-electron system can be obtained by solving the Schrödinger's equation for the N-electron Hamiltonian of eq. (4.58), i.e. determining the eigenfunctions and the eigenvalues. Finding an exact solution for a large number of electrons, however, is practically impossible. DFT consists in transforming this problem into the one of identifying the functional form of the electron density $n(\vec{r})$, i.e. the probability of finding one of the N electrons in the point $\vec{r}$. DFT is based on the Hohenberg and Kohn theorems [169]. The first theorem states that in a system of N interacting electrons subject to an external potential $V_{ext}(\vec{r},\vec{R})$, with a given ground-state electron density $n_{GS}(\vec{r})$, the external potential V_{ext} is unique up to an additive constant. In the context of condensed matter, typically V_{ext} is the electron-ion potential (V_{ei}), and $\vec{r}$ and $\vec{R}$ represent all the electronic and ionic coordinates, respectively (omitting the indexes for each electron/ion). A given n_{GS} uniquely defines V_{ext}, which uniquely defines the N-electron Hamiltonian. The second theorem states that the Hamiltonian and the ground-state wavefunction can be written as unique *functionals* of the electron density, and the total energy of the electronic ground state, which is also a functional of the electron density n_{GS}, is *variational* in n, hence $E[n] \geq E_{GS}$, and $E[n] = E_{GS}$ only if $n = n_{GS}$.

The next step is to introduce an auxiliary system of N noninteracting electrons. This construction was introduced by Kohn and Sham [170]. Since the electrons in the auxiliary system are noninteracting, one can write the N-electron wavefunction in terms of single-particle states, also named Kohn-Sham orbitals. Kohn and Sham orbitals will obey the Schrödinger equation:

$$\left(-\frac{1}{2}\nabla^2 + v_{scf}(\vec{r})\right)\phi_i(\vec{r}) = \epsilon_i\phi_i(\vec{r}) \tag{4.62}$$

Where ϕ_i are the Kohn-Sham single-particle wavefunctions, and v_{scf} is an external potential such that the ground-state electron density of the Kohn-Sham system is the same as the one of the real system. v_{scf} is defined as

$$v_{scf}[n(\vec{r})] = \frac{e^2}{2}\int\frac{n(\vec{r})n(\vec{r}')}{|\vec{r}-\vec{r}'|}d^3r d^3r' + \frac{\delta E_{xc}[n(\vec{r})]}{\delta n(\vec{r})} + \sum_I\int\frac{Z_I e^2}{|\vec{r}-\vec{R}_I|}d^3r \tag{4.63}$$

E_{xc} is the so-called exchange-correlation energy, which is defined as:

$$E[n] = T_e^0[n] + E_H[n] + E_{ei}[n] + E_{xc}[n] \tag{4.64}$$

Where E is the exact energy of the N-electron system, T_e^0 is the kinetic energy of N noninteracting electrons, E_H is the Hartree energy, and E_{ei} is the electron-ion energy. In other words, E_{xc} includes all terms that are not included in the others, for which one does not have an explicit expression. In principle, if one knew an exact expression for E_{xc}, the solution of the Kohn-Sham equations would be exact. In practice, one needs to introduce an approximation to E_{xc}, such as the so-called Local Density or Generalized Gradient approximations [170, 219]. Equations (4.62) and (4.63) can be solved self-consistently together with the relation between Kohn-Sham orbitals and the electron density:

$$n(\vec{r}) = 2\sum_{i=1}^{N/2} |\phi(\vec{r})|^2 \tag{4.65}$$

From a solution of the Kohn-Sham equations, one obtains the ground-state electron density, and the eigenvalues of the Kohn-Sham system ϵ_i. It is important to underline that these are *not* the eigenvalues of the interacting electron system. In practice, however, the Kohn-Sham eigenvalues were found to reproduce exceptionally well the electronic structure of real materials. Hence, the Kohn-Sham eigenenergies can be used to described the dressed electron eigenenergies $\epsilon_{\vec{k}}$.

Phonon Spectrum Within the Born-Oppenheimer approximation, the total energy of the electrons is a parametric function of the ionic position through the potential $v_{ext}(\vec{r}, \vec{R})$. Hence the total energy of the N-electron system $E(\vec{R})$ is referred to as the Born Oppenheimer energy surface.

Within this approximation, the equilibrium geometry of the system is given by the condition that all the forces acting on the nuclei vanish, i.e.

$$\vec{F}_I = -\frac{\partial E(\vec{R})}{\partial \vec{R}_I} = 0 \tag{4.66}$$

If the system is in its equilibrium geometry, one can calculate the frequency of the ionic oscillations about their equilibrium positions by computing the higher-order derivatives of the total energy with respect to the ionic displacements $\partial \vec{R}_I$. The *harmonic approximation* consists in truncating this to the second-order derivatives. The Hellman-Feynman theorem states that the first derivatives of the energy can be computed by evaluating the perturbed Hamiltonian on the unperturbed wavefunctions – or equivalently of the electron density – while the second derivatives require the second derivatives of the Hamiltonian, and the first derivatives of the wavefunctions, i.e. their *linear response* to a distortion of the nuclear geometry. The procedure of obtaining the linear response of the electron density in the framework of Density Functional Theory is referred

to as *Density Functional Perturbation Theory*, or DFPT. A detailed review of this method was published by S. Baroni [220].

The main advantage of DFPT is the fact that the responses to perturbations with different wavelengths are decoupled, i.e. one writes a momentum-dependent perturbation $\partial^{\vec{q}}_{I,\alpha}$

$$\partial^{\vec{q}}_{I,\alpha} = \sum_{l} e^{i\vec{q}\vec{R}^0_{l,I}} \frac{\partial}{\partial u_{I,\alpha}} \tag{4.67}$$

Where I indicates the atom in the basis, l the unit cell, α the cartesian component. In the case of phonons, $u_{I,\alpha}$ is the displacement of the I-th atom in the basis in the α direction.

This presents a substantial advantage in the calculation of phonons, as the computational workload is independent on the phonon wavevector $\vec{q}$, which enters the equations as a phase factor. Given a phonon with an arbitrary wavevector $\vec{q}$, its frequency can be calculated by solving the secular equation

$$\det \left| \frac{1}{\sqrt{M_I M_J}} \tilde{C}^{\alpha\beta}_{IJ}(\vec{q}) - \omega_{\vec{q}} \right| = 0 \tag{4.68}$$

Where α and β indicate the Cartesian components, and I and J indicate the atoms in the unit celll. $\tilde{C}^{\alpha\beta}_{IJ}(\vec{q})$ is the *dynamical matrix* defined as

$$\tilde{C}^{\alpha\beta}_{IJ}(\vec{q}) = \frac{1}{N_c} \partial^{-\vec{q}}_{I,\alpha} \partial^{\vec{q}}_{J,\beta} E \tag{4.69}$$

Where N_c is the number of unit cells in the crystal.

Electron-phonon matrix elements The *screened* electron-phonon matrix element $g^{\mu}_{\vec{k},\vec{k}+\vec{q}}$ that appears in eq. (4.33) can be calculated within DFPT as the variation up to linear order of the Kohn-Sham self-consistent potential v_{scf} with respect to a collective lattice displacement:

$$g^{\mu}_{\vec{k},\vec{k}+\vec{q}} = \sum_{I,\alpha} \sqrt{\frac{\hbar}{2M_I \omega_{\vec{q},\mu}}} \eta^{\vec{q}\nu}_{I,\alpha} \left\langle \phi_{\vec{k}} \right| \partial^{\vec{q}\mu}_{I,\alpha} v_{scf} \left| \phi_{\vec{k}+\vec{q}} \right\rangle \tag{4.70}$$

Where η is the eigenvector of the phonon with momentum $\vec{q}$ and branch ν with components I and α relative to the atom in the basis and cartesian component. Both the Kohn-Sham wavefunctions $\phi_{\vec{k}}$ and $\phi_{\vec{k}+\vec{q}}$ have the Fermi energy ϵ_F.

Using eq. (4.70) the Éliashberg function can be computed as:

$$\alpha^2 F(\vec{k}, \vec{k}+\vec{q}, \Omega) = N(\epsilon_F) \sum_{\mu=1}^{3N} |g^{\mu}_{\vec{k}\vec{k}+\vec{q}}|^2 \delta(\Omega - \omega_{\vec{q},\mu}) \tag{4.71}$$

Within the isotropic approximation the average of α^2F over the Fermi surface is used:

$$\alpha^2F(\Omega) = N(\epsilon_F)\sum_{\mu=1}^{3N}\int \frac{d^3k}{(2\pi)^3}|g^{\mu}_{\vec{k}\vec{k}+\vec{q}}|^2\delta(\Omega-\omega_{\vec{q},\mu})\delta(\epsilon-\epsilon_{\vec{k}})\delta(\epsilon-\epsilon_{\vec{k}+\vec{q}}) \tag{4.72}$$

Knowing the electron eigenenergies $\epsilon_{\vec{k}}$, the phonon eigenenergies $\omega_{\vec{q},\mu}$, and the electron-phonon spectral function α^2F, the Éliashberg equations can be solved.

Comparison with experiments The ab initio calculation of the *e-ph* matrix elements proved to be extremely successful. This method was first tested on elemental solids by comparing the calculated α^2F, λ and T_c (using the McMillan formula) with the experiments, and was found to be in excellent agreement [221]. In 2001, after superconductivity at 39 K in MgB_2 was discovered [22], the ab initio calculation of the *e-ph* coupling was paramount to understand the origin of its superconducting properties [27, 222, 223].

Wannier Interpolation The evaluation of the Éliashberg function from eq. (4.71) is not difficult. It is, however, impaired by technical challenges. Regardless of the method chosen, the electron-phonon matrix elements must be integrated over reciprocal space in the vicinity of the Fermi surface, with a double δ-function. This integral is extremely sensitive to the details of the Fermi surface, and its accurate estimation requires an extremely fine sampling of reciprocal space. Calculations of superconductive properties remain computationally quite expensive: numerical convergence may require sampling several millions of $\vec{k}$ points [224, 225]. In recent years, this problem was partly overcome by exploiting Wannier functions to interpolate the electron-phonon matrix elements from coarse to fine grids, rather than calculating them [211, 226, 227].

The transformation from the Bloch to the Wannier basis is a Fourier transform:

$$\langle m\vec{R}| = \sum_{n\vec{k}} e^{-i\vec{k}\vec{R}}U_{nm,\vec{k}}\,\langle n\vec{k}| \tag{4.73}$$

Where n and m are band indexes, $\vec{R}$ is a lattice vector, $\langle n\vec{k}|$ indicates a Bloch state, and $\langle m\vec{R}|$ indicates a Wannier function. WFs are orthonormal if $U_{nm,\vec{k}}$ is unitary, but the choice of U is otherwise arbitrary. This freedom arises from the arbitrariness in the definition of the Bloch state $\langle\tilde{\vec{k}}| = e^{i\phi(\vec{k})}\,\langle\vec{k}|$, and implies that the choice of Wannier functions is not unique. A convenient choice of U_{nm} is the one leading to the *Maximally Localized* Wannier functions (MLWFs), i.e. those that minimize the spread Ω in the home unit cell:

$$\Omega = \sum_n \left[\langle \mathbf{0}n|\, r^2\, |\mathbf{0}n\rangle - |\,\langle \mathbf{0}n|\, r\, |\mathbf{0}n\rangle\,|^2\right] \tag{4.74}$$

Similarly, *maximally localized* phonon eigenmodes can be defined as displacements of individual

ions, exploiting the fact that the cell-periodic part of the phonon eigenmodes has the same freedom as the U_{nm} matrix.

The interpolation is based on the fact that the variation of the self-consistent potential δv_{scf} of eq. (4.67) can be rewritten in terms of its gradient in real space, which in metals typically decreases exponentially with distance from each atom, due to screening.

Hence, one writes the transformation from the *ep* matrix element $g^{\mu}_{\vec{k},\vec{k}+\vec{q}}$ of eq. (4.70) to the Wannier representation (omitting band and phonon branch indices):

$$g_{\vec{R}_e\vec{R}_p} = \frac{1}{N_e}\sum_{\vec{k},\vec{q}} e^{-i(\vec{k}\vec{R}_e+\vec{q}\vec{R}_p)} U^{\dagger}_{\vec{k}+\vec{q}} g_{\vec{k},\vec{k}+\vec{q}} U_{\vec{k}} (M_0/M_e)^{1/2} \hat{\epsilon}^{-1}_{\vec{q},p} \tag{4.75}$$

Where $g^{mn,\nu}_{\vec{R}_e\vec{R}_p}$ is the *e-ph* matrix element in real space between an electron with band index m in localized at the origin, an electron with band index n localized in the unit cell $\vec{R}_e$, and a phonon with branch index ν, localized in the unit cell $\vec{R}_p$

$$g^{mn,\nu}_{\vec{R}_e\vec{R}_p} = \langle m\mathbf{0}_e | \nabla_{\tau_{\nu,p}} v_{scf}(\vec{r}) | nR_e \rangle \tag{4.76}$$

Equation (4.76) justifies the effectiveness of Wannier interpolation. By construction, electronic and phonon functions are spatially localized. Therefore, whenever $\vec{R}_e$ or $\vec{R}_p$ are sufficiently distant from the origin $\vec{0}_e$, the whole matrix element will vanish. In particular, when both the electronic Wannier function and the spatial phonon perturbation vanish, the *ep* matrix element also will. This implies that using the Wannier representation, a relatively small supercell is sufficient to accurately describe g at any point in space.

Using the Wannierized form of the *ep* matrix element, one can interpolate it back to any point in reciprocal space. This allows to efficiently evaluate g over millions of $\vec{k}$ points. Conceptually, the procedure is identical to a Fourier interpolation:

1. Start from a function $\tilde{f}(\vec{k})$, calculated on a coarse grid
2. Compute its Fourier antitransform $f(\vec{r}) = \sum_{\vec{k}} e^{i\vec{k}\vec{r}} \tilde{f}(\vec{k})$ using points on the coarse grid
3. Compute the transform of the antitransform, to re-obtain the original function, now on an arbitrarily dense $\vec{k}$-grid: $\tilde{f}(\vec{k}) = \int e^{-i\vec{k}\vec{r}} f(\vec{r}) d^3r$

The details on the implementation of the interpolation scheme for g do not add much to the discussion. For a complete review I refer to Ref. [228] for MLWFs, and to [226, 227] for Wannier interpolation of electron-phonon interactions.

4.4 Superconducting Density Functional Theory

Density Functional Theory for superconductors, sometimes also referred to as SCDFT, is an alternative approach to calculate the superconductive properties of materials from first principles. It was first presented by Oliveira and Gross in 1988 [229], and first implemented in 2005 by M. Lüders et al. [230, 231]. It has been already used successfully to calculate the superconducting properties of simple metals [231], and was shown to exhibit accuracy comparable to Migdal-Éliashberg theory [232, 233].

In its essence, SCDFT is an extension of DFT which can describe the formation of an *anomalous* density. This requires the following changes to the standard DFT formalism:

- The electronic and ionic degrees of freedom are considered simultaneously: the starting Hamiltonian includes the electronic kinetic energy, the electron-electron interaction, the electron-ion interaction, the ion-ion interaction, and the ionic kinetic energy. In principle this is even beyond the Born-Oppenheimer approximation, although in practice the Born-Oppenheimer surface is used to approximate the effective potential for nuclei [234].

- Three independent densities are introduced: the electron density $n(\vec{r})$, the anomalous density $\chi(\vec{r},\vec{r}')$, and the nuclear density $\Gamma(\underline{R})$, where $\underline{R}$ refers to all ionic degrees of freedom. In the spirit of the Hohenberg and Kohn theorems, the three densities are associated to three corresponding potentials: $v^e_{ext}(\vec{r})$ for the electron density, $\Delta_{ext}(\vec{r},\vec{r}')$ for the anomalous density, and $v^n_{ext}(\underline{R})$ for ions. All observables are functionals of the three densities. Following the standard notation, I write the functional dependence as squared brackets, i.e. $f[x(\vec{r})]$ means that f is a functional of $x(\vec{r})$.

With these premises, it is possible to demonstrate that a grand canonical potential $\Omega[n,\chi,\Gamma]$, which is a functional of the three densities, is minimized by the ground-state densities. Ω is:

$$\begin{aligned}\Omega[n,\chi,\Gamma] &= F[n,\chi,\Gamma] + \int d^3r n(\vec{r})\,(v^e_{ext}(\vec{r}) - \mu) \\ &- \int d^3r \int d^3r'\,(\chi(\vec{r},\vec{r}')\Delta^*_{ext}(\vec{r},\vec{r}') + \chi(\vec{r},\vec{r}')^*\Delta_{ext}(\vec{r},\vec{r}')) + \int d^3\underline{R}\Gamma(\underline{R})v^n_{ext}(\underline{R})\end{aligned} \tag{4.77}$$

Where μ is the chemical potential and $F[n,\chi,\Gamma]$ is an universal functional defined as:

$$F[n,\chi,\Gamma] = T^e[n,\chi,\Gamma] + T^n[n,\chi,\Gamma] + U^{en}[n,\chi,\Gamma] + U^{ee}[n,\chi,\Gamma] - \frac{1}{\beta}S[n,\chi,\Gamma] \tag{4.78}$$

Analogously to DFT, one can define an auxiliary Kohn-Sham system, and an effective Kohn-Sham potential, which is equivalent to formally replacing v^e_{ext}, Δ_{ext} and v^n_{ext} of eq. (4.77) with their

Kohn-Sham counterpart v_s^e, Δ_s and v_s^n. The auxiliary system has universal functional $F_s[n,\chi,\Gamma]$:

$$F_s[n,\chi,\Gamma] = T_s^e[n,\chi,\Gamma] + T_s^n[n,\chi,\Gamma] - \frac{1}{\beta}S_s[n,\chi,\Gamma] \tag{4.79}$$

The relationship between F_s and F is obtained by introducing the exchange-correlation functional

$$F[n,\chi,\Gamma] = F_s[n,\chi,\Gamma] + F_{xc}[n,\chi,\Gamma] + E_H^{ee}[n,\chi] + E_H^{en}[n,\Gamma] \tag{4.80}$$

The electron-electron Hartree energy E_H^{ee} now includes the regular Hartree term, plus a contribution from the anomalous density, while the electron-ion Hartree energy E_H^{en} contains the classical part of the interaction and E_H^{en}.

Analogously to standard DFT, the solution of SCDFT is found by minimizing the Kohn-Sham grand-canonical potential to find the ground-state Kohn-Sham wavefunctions. This is achieved by solving self consistently a set of three differential equations, one for nuclei and two for superconducting electrons:

$$\begin{aligned}
&\left[-\sum_\alpha \frac{\nabla_\alpha^2}{2M} + v_s^n(\underline{R})\right]\phi_l(\underline{R}) = \epsilon_l\phi_l(\underline{R}) \\
&\left[-\frac{\nabla^2}{2} + v_s^e(\vec{r}) - \mu\right]u_{n\vec{k}(\vec{r})} + \int d^3r'\Delta_s(\vec{r},\vec{r}')v_{n\vec{k}}(\vec{r}') = \tilde{E}_{n\vec{k}}u_{n\vec{k}}(\vec{r}) \\
&-\left[-\frac{\nabla^2}{2} + v_s^e(\vec{r}) - \mu\right]v_{n\vec{k}(\vec{r})} + \int d^3r'\Delta_s^*(\vec{r},\vec{r}')u_{n\vec{k}}(\vec{r}') = \tilde{E}_{n\vec{k}}v_{n\vec{k}}(\vec{r})
\end{aligned} \tag{4.81}$$

Where $u_{n\vec{k}}$ and $v_{n\vec{k}}$ are the particle and hole amplitudes, respectively. The second and third equations can be solved in the decoupled approximation: $u_{n\vec{k}}(\vec{r}) \approx u_{n\vec{k}}\phi_{n\vec{k}}(\vec{r})$, where ϕ are the solutions of the normal-state Kohn-Sham equations. Within this approximation, the energy $\tilde{E}$ follows the equation $\tilde{E}_{n\vec{k}} = \pm\sqrt{\epsilon_{n\vec{k}}^2 + |\Delta_{n\vec{k}}|^2}$, which allows one to interpret the pair potential Δ as the superconducting gap.

The main difficulty in implementing SCDFT reliably is finding suitable approximations for the exchange-correlation functional, which must also correctly include the dependence on the anomalous density, the electron-phonon interactions, as well as the Coulomb correlation. Few existing approximations are based on many-body perturbation theory, and were used successfully by Lüders et al. [230, 231].

According to the latest benchmarks available, DFPT + Migdal-Éliashberg theory and SCDFT have comparable accuracy in all the conventional superconductors tested [232, 233].

4.5 Other Effects

In this section I will shortly mention other research areas that are relevant to the topic of *ab initio* calculations of superconducting properties, which I did not touch in this thesis and hence I did not discuss in depth. All these effects can affect to some extent the calculation of the superconducting properties discussed in this chapter, and represent current areas of research and developments.

Beyond Migdal-Éliashberg Albeit widely applicable, Migdal's theorem fails for materials in which the phonon energy scale is comparable with the Fermi energy, i.e. $\omega_D \sim \epsilon_F$. In this case, the theory has to include higher-order *nonadiabatic* corrections such as vertex corrections and cross-phonon scattering. The interested reader may refer to the following references [235–237]. Another aspect which goes beyond current implementations of Migdal-Éliashberg theory is the so-called *full-bandwidth* Migdal-Éliashberg, which consists in the removal of the limitation to electrons at the Fermi surface, which had been discussed in Section 4.2.

Anharmonicity An important area of research involves the description of anharmonicity, i.e. higher-order effects which go beyond the harmonic approximation for lattice vibrations. Anharmonic effects were shown to be important in several classes of materials, including superhydrides [133, 143, 238–240]. The importance of anharmonicity to describe effects such as thermal expansion and thermal conductivity was long known [241], but only in the last decade *ab initio* codes to calculate the anharmonic properties of solids were developed. They are based either on the so-called *frozen-phonon* approach, or the self-consistent harmonic approximation. The interested reader can refer to a review of the frozen-phonon methods [242], and the stochastic self-consistent harmonic approximation [243].

Other mediators As mentioned earlier in the chapter, phonons are only one of the many bosons which are present in crystalline materials, any of which may in principle mediate superconductivity. In particular, research efforts have focused on plasmons [244, 245] and spin fluctuations [246].

Current Developments in *ab-initio* Theory of Superconductivity Current developments are going in the following directions

- Improvement in the efficiency of available codes, as calculations are typically limited to systems with less than 20 atoms. The development of the `EPW` code [159, 227], as well as the implementation of Helmholtz-Fermi-surface harmonics [212] go in this direction.
- Improvement of the accuracy of *ab-initio* methods for conventional superconductors. Current implementations of codes which solve the Migdal-Éliashberg equations rely on the constant

DOS approximation and on Migdal's theorem. Approaches that go beyond these two approximations have been already presented in the literature, but are not implemented in the commonly-used codes for *ab initio* calculations [235, 236]. The numerical solution of the Migdal-Éliashberg equations beyond the constant DOS approximation (i.e. *full-bandwidth Migdal-Éliashberg*), is currently under development [159, 237]. The inclusion of nonadiabatic electron-phonon coupling as a future development in SCDFT has being discussed [159].

Part II

Part II: Results and Discussion

Chapter 5

Sodalite-like Yttrium Hydride Clathrates

In this chapter I will discuss the superconducting properties of two sodalite-like hydrides with YH_6 and YH_{10} composition [7], and the onset of the dynamical instability at low pressure. YH_6 and YH_{10} are both high-T_c superconductors, characterized by a peculiar host-guest structure which resembles sodalites, hence the name. The guest atom (yttrium) provides the charge and volume occupation which stabilizes the hydrogen sublattice, which forms a quasi-spherical polyhedron around it. This study was performed in 2019, shortly after the experimental discovery of LaH_{10}, isostructural to YH_{10}, and employed the most advanced methods available to calculate the superconducting T_c. An important question at the time was whether sodalite-like hydrides were in fact a realization of atomic hydrogen, or if the guest atom (yttrium) played an active role in the superconducting properties. The most important results of this study are: (1) the calculation from first principles of the anisotropic superconducting gap, including a first-principles calculation of the Morel-Anderson pseudopotential, which had not been addressed before in the literature, and (2) the analysis of the mechanism leading to the dynamical instability of sodalite-like clathrate hydrides at low pressure. Most of the results presented in the chapter were published in Ref. [7]. The data and the figures, including captions, are reprinted with permission from the involved parts.

The results are presented as follows: in section 5.1 I will discuss the crystal structures of YH_6 and YH_{10}, alongside with the low-T_c structure of YH_3; in sect. 5.2 I will discuss their electronic and superconducting properties; in sect. 5.3 I will examine how pressure affects the dynamical stability and the superconducting properties; sect. 5.4 is dedicated to the conclusions.

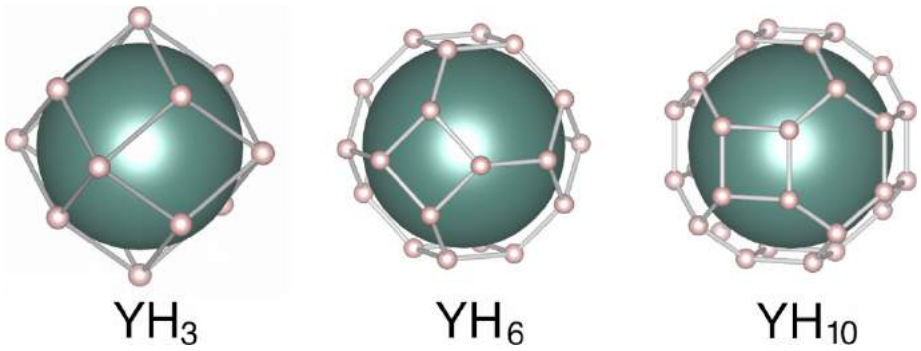

Figure 5.1: The fcc YH_3 (left), bcc YH_6 (center), and fcc YH_{10} (right) crystals are lattices of polyhedral hydrogen cages (H= small pink balls) with an yttrium atom in their middle (Y= green balls, drawn with a radius of 1.62 Å, midway between its core and covalent radius). While the YH_3 and YH_6 cages share all faces, giving rise to a perfect tessellation of space, the YH_{10} cages only share the hexagonal faces. In this picture the H-H distances correspond to an external pressure of 300 GPa: $d_{HH} = 1.74$ Å for YH_3, $d_{HH} = 1.19$ Å for YH_6, and two slightly different lengths $d_{HH} = 1.03$, 1.11 Å for YH_{10} (see text).

The first prediction on the formation of yttrium superhydrides was published by Li et al. in 2015 [140, 146]. The authors predicted the formation of YH_3, YH_4, YH_6, and YH_{10} at 300 GPa, with only YH_6 and YH_{10} being high-T_c. In the same paper, they also predicted the formation of lanthanum hydrides, with a high-T_c LaH_{10} phase isostructural to yttrium. In the Summer of 2018, the formation and superconductivity of LaH_{10} had been experimentally confirmed by two independent groups [3, 36], and sodalite-like hydrides were under the spotlight.

The fact that LaH_{10}, and sodalite-like structures in general, were qualitatively different from H_3S, where sulfur and hydrogen form covalent bonds, was quite clear. To explain their extremely high T_c's, most authors focused on the short H-H distance, between 1.1 and 1.6 Å. Since these values are close to those predicted for atomic hydrogen [134, 247], the mechanism invoked to explain the high-T_c was that sodalite-like hydrides were a realization of atomic hydrogen at low pressure [50, 121, 147]. A similar argument had been already invoked in iron polyhydrides, but it had been demonstrated that the H-H distance alone was not a good descriptor, and that iron hydrides were not superconductors [248, 249], so the hypothesis of *atomic hydrogen* needed to be challenged.

Another point that had to be addressed was the strength of Coulomb interactions. In fact, to reconcile the predictions and the experimental results an anomalously large value had been proposed [50], but this hypothesis was yet untested.

Finally, aside from the similarity with sodalites, crystal structures like that of LaH_{10} had never been observed with hydrogen. The question of which mechanism was leading to their (in)stability was en extremely interesting one. The fact that similar structures were observed for different *guest* elements (Mg, Ca, Y, La) suggested that there should be a general criterion which, if understood, would allow a rational optimization in the choice of the guest element.

To address these questions, I performed a study of the superconducting properties of YH_6 and

YH_{10} using anisotropic Migdal-Éliashberg theory, as implemented in the `EPW` code. I also determined the strength of the screened Coulomb interaction within the GW approximation, as implemented in `SternheimerGW` [250]. Last, I studied the vibrational and superconducting properties as a function of pressure, to identify the source of the instability. The choice of yttrium, over the experimentally discovered lanthanum, was motivated by the fact that, while they are chemically similar (they form the same superhydrides), lanthanum has f orbitals right above the Fermi energy, and these can be problematic for DFT calculations.

The results presented in this chapter disprove the hypothesis that sodalite-like hydrides are atomic hydrogen. In fact, the calculated superconducting gap is isotropic despite an anisotropic orbital character of the Fermi surface, which implies that there is a strong interorbital (Y-H) interaction. From the first-principles calculation of the screened Coulomb interaction I could estimate the value of the Morel-Anderson pseudopotential, which is $\mu^* = 0.11$ for both YH_6 and YH_{10}, in line with that of most metals. Finally, I identified a common denominator in the instability of YH_6, YH_{10}, and YH_3 – a third, low-T_c hydride which I considered to test my observation. In all three cases, the onset of the instability occurs when the average radius of the hydrogen cage becomes larger than the covalent radius of yttrium. The stability does not depend on the details of the enclosed atom other than its size.

5.1 Crystal and Electronic Structure

rhombic dodecahedron	V	$=$	$\frac{16\sqrt{3}}{9}\,\mathrm{d}_{\mathrm{HH}}^3$	$=$	$V_{\mathrm{CELL}} =$	$\frac{a^3}{4}$	(fcc)
truncated octahedron	V	$=$	$8\sqrt{2}\,\mathrm{d}_{\mathrm{HH}}^3$	$=$	$V_{\mathrm{CELL}} =$	$\frac{a^3}{2}$	(bcc)
chamfered cube	V	$=$	$\frac{81+52\sqrt{3}}{9}\,\mathrm{d}_{\mathrm{HH}}^3$	$=\frac{81+52\sqrt{3}}{90+52\sqrt{3}}$	$V_{\mathrm{CELL}} = 0.95$	$\frac{a^3}{4}$	(fcc)

Table 5.1: Geometric relations connecting the the H-H distance d_{HH}, which equals the edge of the polyhedral cage (in the chamfered cube it defines an average length of the two inequivalent edges), the volume of the polyhedral hydrogen cage V, our definition of the average cage radius $\langle \mathrm{R} \rangle$ is the radius of a sphere with volume $V = \frac{4}{3}\pi\langle \mathrm{R}^3 \rangle$ the volume of the primitive unit cell V_{CELL} (which in two out of three of these compounds equals the cage volume), and the lattice parameter a.

The crystal structures of YH_3, YH_6, and YH_{10} are shown in Fig. 5.1. The YH_3 structure was experimentally observed, and its predicted T_c is around 40 K at 18 GPa [251, 252]. In the YH_3 (YH_6) structure shown, each hydrogen atom occupies one of the 14 (24) vertices of the fcc (bcc) Wigner-Seitz primitive cell; in the YH_{10} structure one hydrogen atom occupies each of the 32 vertices of a chamfered cube. For each of these polyhedra, the edge length (H-H distance d_{HH}), the volume V, and the average radius (defined as the radius of the sphere with equal volume),

are connected by simple analytical relations. For instance $d_{\mathrm{HH}} = 0.69\,V^{1/3}$ in YH_3, $0.45\,V^{1/3}$ in YH_6, and $0.38\,V^{1/3}$ in YH_{10}. In practice, the H-H and the Y-H distance, the volume enclosed in the polyhedron, and the volume of the unit cell, all change together, as they are connected by precise geometrical constraints. On the other hand, the guest atom is approximately fixed in size. As I will discuss later, the onset of dynamical instability at low pressure depends precisely on the tightness/looseness of the host hydrogen clathrate network around the guest atom.

Unless otherwise stated, all the results presented are obtained for a pressure of 300 GPa, where both YH_6 and YH_{10} are dynamically stable, and they exhibit the highest T_c.

I will first discuss the electronic structure of YH_6 and YH_{10}. In Fig. 5.2, I show the electronic bands (left) and Densities of States (DOS, right). The color gradient, from blue to orange, indicates the projection onto H and Y states, respectively. In both cases the hydrogen-derived bands are highly dispersive, with a total bandwidth of about 40 eV. Over this energy range the dispersions match rather well the quasi-free-electron bands. An analogous similarity was observed also in H_3S and in atomic hydrogen [134, 253], and is attributed to the high kinetic energy due to the high pressure, which dominates over the other energy terms. The largest deviations from the quasi-free-electron model are found in two energy windows: (*i*) 25 eV below the Fermi level, (*ii*) in a region of ±5 eV around the Fermi level, and are caused by a significant hybridization of H- derived states with Y-4*p*, and Y-4*d*,5*s*, respectively.

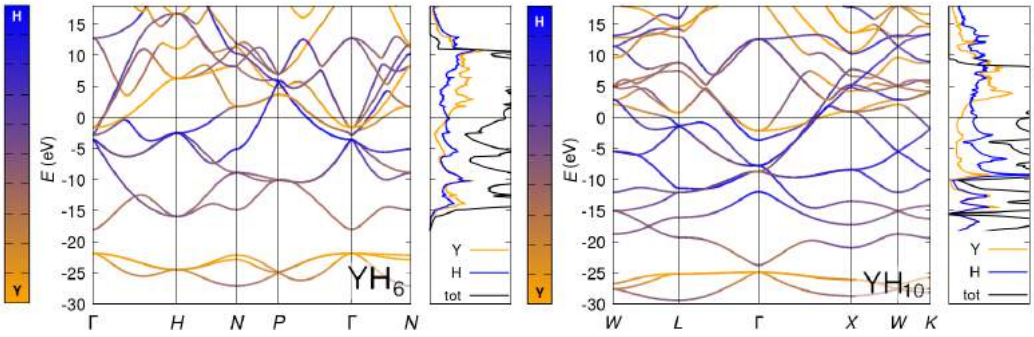

Figure 5.2: Electronic bands (left panel) and DOS (right panel) for YH_6 (left figure) and YH_{10} (right figure) at 300 GPa. In the electronic bands the color gradient indicates the projection onto H (blue) and Y (orange) states, and total DOS (black), partial Y DOS (orange), and partial H DOS (blue). Energies are referred to E_F. The scale limit for the DOS plots is 0.35 st/(eV spin).

At the Fermi level, both H and Y contribute considerably to the electronic structure. In particular, the Y character is stronger around the Brillouin zone center (Γ point), while the H character is stronger at the boundaries. The corresponding Fermi surfaces are shown in Fig. 5.3.

In YH_6 the Fermi surface is characterized by five electron-like sheets one inside another, all around the Γ point, and one hole-like sheet around P, while in YH_{10} there are four electron-like sheets around Γ, and two hole-like sheets around X.

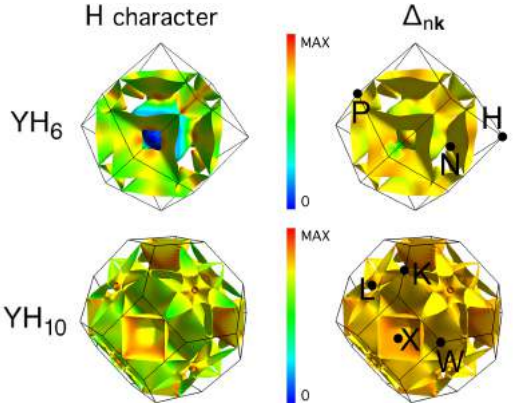

Figure 5.3: Fermi surfaces of YH_6 (top row) and YH_{10} (bottom row) at 300 GPa. In the left panels the color scale spans the projection onto H states, where blue corresponds to 0 and red to 1; in the right panels it spans the values of the anisotropic gap function at 40 K, blue being 0 meV and red the maximum of 59 (74) meV for YH_6 and YH_{10}, respectively.

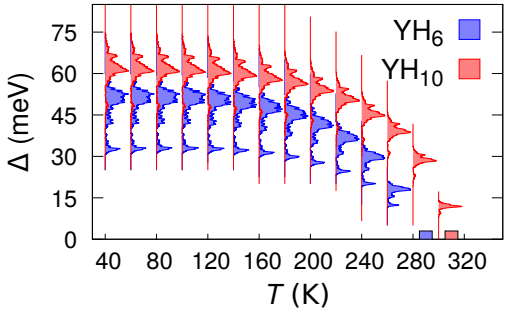

Figure 5.4: Energy distribution of the superconducting gap for YH_6 (blue) and YH_{10} (red) as a function of temperature at 300 GPa. The rectangles show the extrapolated T_c values.

5.2 Electron-Phonon Coupling and Superconductivity

The presence of two or more bands with different orbital character crossing the Fermi level cause a substantial *anisotropy* in the superconducting gap $\Delta_{\mathbf{nk}}$. In particular, this happens when the intraband electron-phonon interaction is significantly different, i.e. the coupling from Y and H is different, and at the same time the interband (or interorbital) interaction is weak, i.e. there is no significant interaction between Y and H [254]. As discussed in Chapter 4, the anisotropic gap can be calculated by solving self-consistently the anisotropic Migdal-Éliashberg equations (eq. (4.49) and (4.50)), as implemented in the `EPW` code. In addition, the screened Coulomb interaction μ, and the Morel-Anderson pseudopotential μ^* can also be calculated entirely from first principles within the *GW* approximation [250, 255]. In Fig. 5.3 I show the Fermi surface for YH_6 and YH_{10}, colored with the hydrogen orbital character (left) and with the superconducting gap (right) at 300 GPa. The Y and H character is unevenly distributed on the Fermi surface for both YH_6 and YH_{10}, but this corresponds to small ($\pm 10\%$) variations of the superconducting gap around its average value. In other words, the superconducting gap is fairly isotropic, despite the different orbital character of the states at the Fermi surface. This result contradicts the idea that sodalite-like clathrate hydrides can be described simply as atomic hydrogen. In fact, if superconductivity was coming from states of H character alone, then one should observe a strong modulation of the superconducting gap on the Fermi surface, with much larger values on portions where the H character is dominant. My calculations indicate the opposite, showing that the Y-H interorbital interactions are important [254]. In fact, due to the quasi-spherical geometry of the system, all

lattice vibrations modulate to some extent the Y-H distance, and consequently also the orbital overlap between Y- and H-derived states.

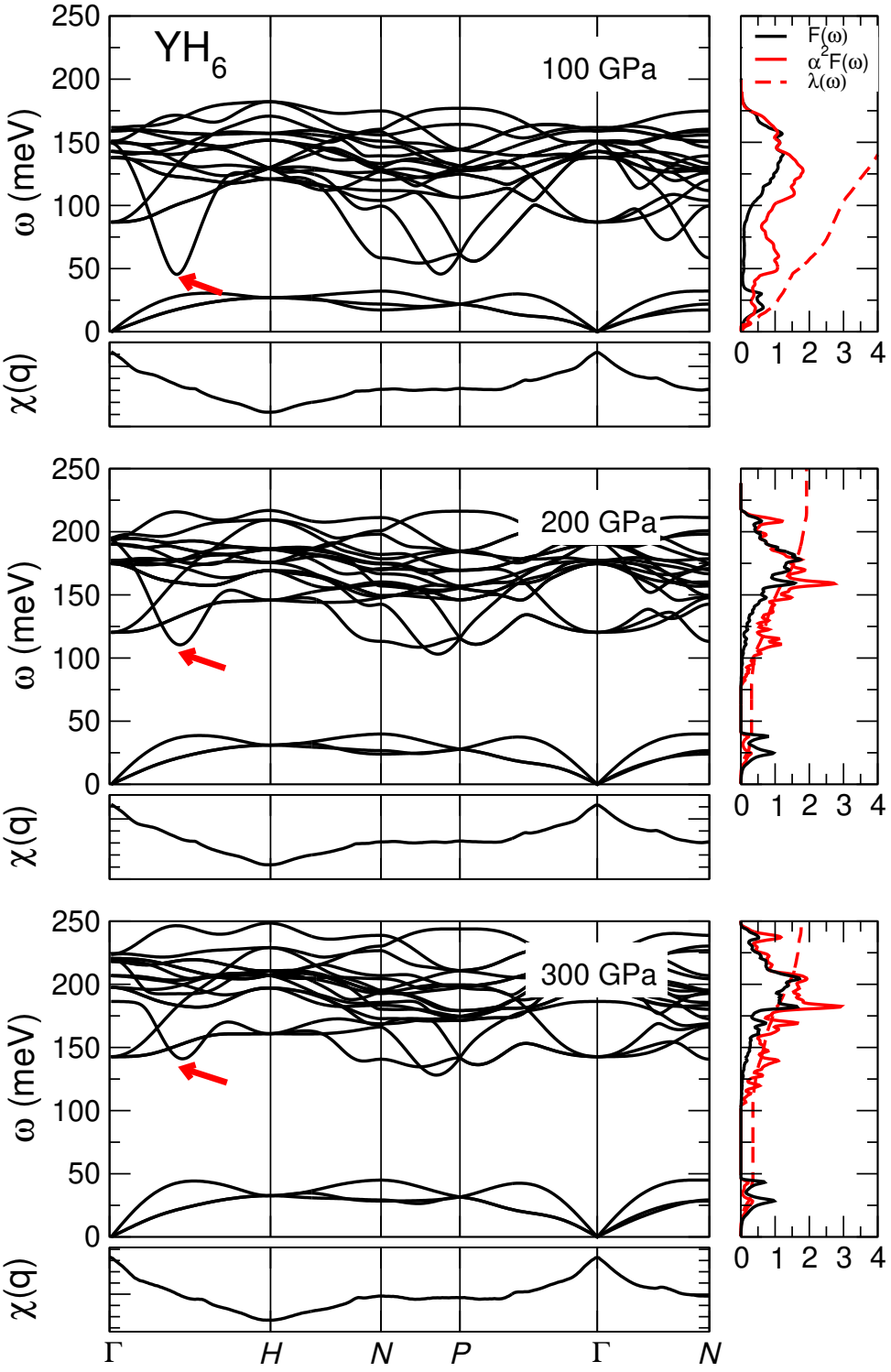

Figure 5.5: Phonon dispersions for YH_6 at 100, 200 and 300 GPa. The phonon DOS (black), Eliashberg function α^2F (red), and integrated *e-ph* coupling λ (dashed red) are shown on the right side. Arrows mark the position of the soft mode and no nesting features at these wave vectors can be observed in the bare static susceptibilities χ (see main text).

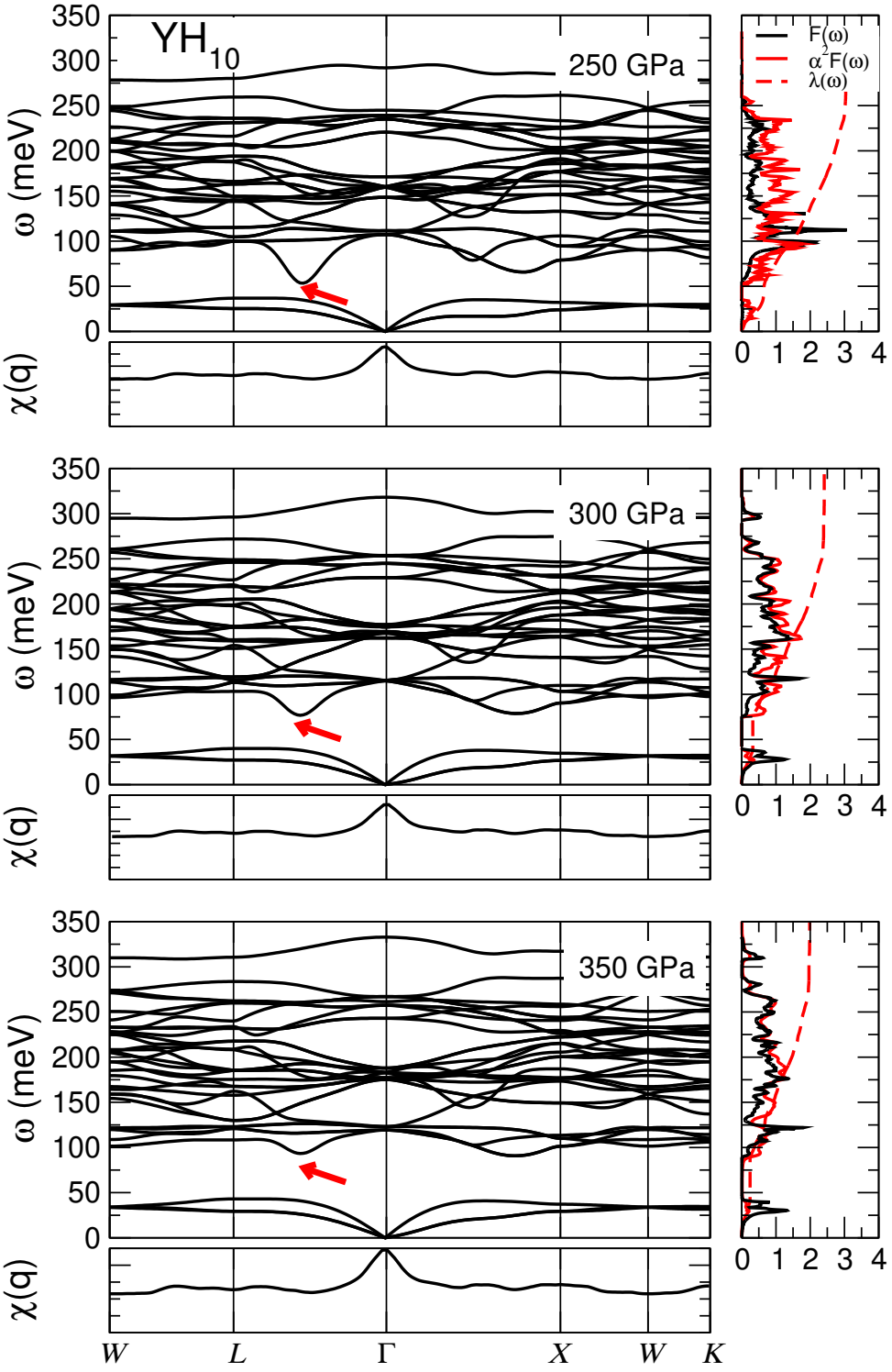

Figure 5.6: Phonon dispersions for YH_{10} at 250, 300 and 350 GPa. The phonon DOS (black), Eliashberg function α^2F (red), and integrated *e-ph* coupling λ (dashed red) are shown on the right side. Arrows mark the position of the soft mode and no nesting features at these wave vectors can be observed in the bare static susceptibilities χ (see main text).

In Fig. 5.4 I show the dependence of the superconducting gap on temperature, the figure is obtained by solving the anisotropic Migdal-Eliashberg equations at various temperatures T, and evaluating the $\omega = 0$ distribution of the resulting gap. Up to approximately 100 K the gap does not change with temperature, and is characterized by a broad peak around 55 meV (65 meV) for YH_6 (YH_{10}), deriving from the regions of the Fermi surface around the P (X) point and a few contributions from the larger sheets around Γ, and a smaller peak around 36 meV (52 meV), originating from the smaller sheets around Γ. The temperature-induced closure of the gap indicates a critical temperature of 290 K for YH_6 and 310 K for YH_{10}. These values are much larger than the results obtained using the Allen-Dynes/McMillan formula: 185 K for YH_6, and 225 K for YH_{10}. The discrepancy is unsurprising, as the formula is known to underestimate the T_c for $\lambda \gg 1$.

The calculation of the Morel-Anderson pseudopotential (μ^*) represented the first *ab initio* estimate of Coulomb screening in hydrogen clathrates. It was obtained by numerically solving the Sternheimer equations [250] to get the screened Coulomb coefficient, which gives $\mu_c = 0.11$ for both YH_6 and YH_{10}. Then μ^* was calculated with $\mu^* = \frac{\mu_c}{1+\mu_c ln(\epsilon_F/\omega_{cut})}$, where ω_{cut} is the cutoff on Migdal-Éliashberg equations (of the order of the largest phonon frequency), and ϵ_F is the bandwidth of the electronic states. The Morel-Anderson renormalization is negligible, giving $\mu^* = 0.11$

5.3 Trends with respect to pressure and cage size

Having discussed the general properties of the superconducting solution at fixed pressure and their relation to the electronic structure, in this section I will analyze in detail the vibrational properties and their dependence on pressure. In Fig. 5.5 I show the phonon dispersion, the phonon DOS, the Éliashberg function [23, 24], and the bare susceptibility for YH_6 at 100, 200, and 300 GPa and in Fig. 5.6 the same quantities for YH_{10} at 250, 300, and 350 GPa. The choice of different pressures is due to the dynamical instability, which in YH_{10} occurs at 226 GPa, while in YH_6 is at 76 GPa. In both systems the Éliashberg spectral function is characterized by a rather uniform distribution of the *e-ph* coupling over all phonons, including the low-energy modes, which are essentially of Y character. This observation implies that there is not a single mode which carries all the *e-ph* coupling, but rather all types of vibrations are significantly coupled. Compared at equal pressure, YH_6 possesses longer and weaker H-H bonds than YH_{10} and this results in a 20% reduction in the frequencies of the highest-energy modes (H-H bond stretching). YH_6 also possesses an overall smaller *e-ph* coupling; at 300 GPa I find $\lambda = 1.73$, whereas I find $\lambda = 2.41$ for YH_{10}. It is also possible to notice a pressure-dependent phonon softening localized in a small region of the Brillouin zone (indicated by a red arrow), eventually leading to a dynamical instability. In principle, the renormalization of the phonon frequencies at a specific wavevector may come either from the *e-ph* matrix element, or from a significant enhancement of the bare susceptibility $\chi^{(0)}(\vec{q})$ due to Fermi

surface nesting, or from a combination of the two. The $\vec{q}$-dependent bare susceptibility, shown in the bottom panels of Fig. 5.5 and 5.6 indicates that it comes from a combination of the two [256].

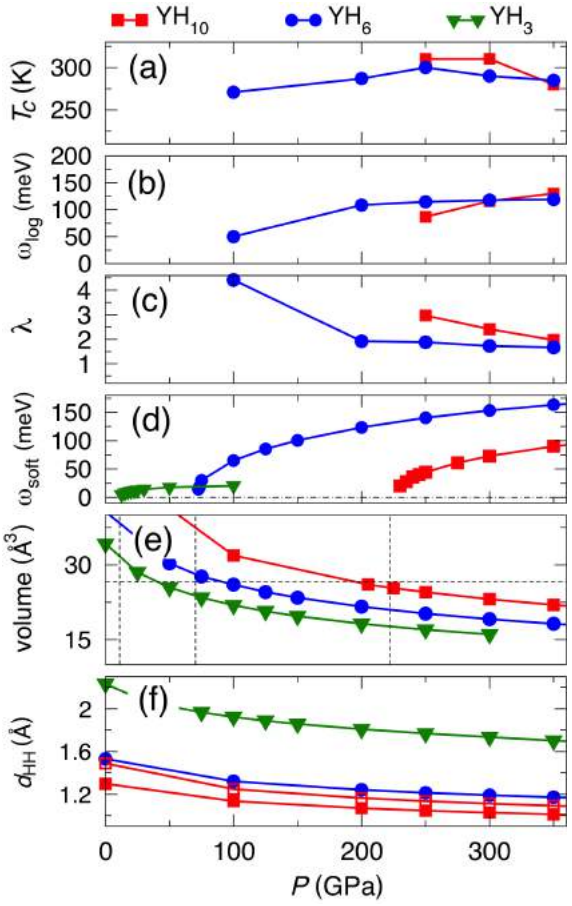

Figure 5.7: Behavior of several properties of YH_3 (green triangles), YH_6 (blue circles) and YH_{10} (red squares) as a function of pressure. (*a*) T_c from anisotropic ME equations ($\mu^* = 0.11$); (*b*)-(*c*) Momenta of the *e-ph*spectral function $\alpha^2F(\omega)$, $\omega_{\log}$ and λ. (*d*) Frequency of the soft mode. (*e*) Volume of the polyhedral cage. (*f*) Nearest-neighbor H-H distance (d_{HH}), see Fig. 5.1. The dashed lines in (*d*) and (*e*) indicate the points where the SLC structures become dynamically unstable.

In Fig. 5.7 I report the trend of several quantities for YH_6 and YH_{10} as a function of pressure. As shown in panel (a), the T_c depends very weakly on pressure in the whole range of dynamical stability. This effect is caused by compensation between the pressure-induced increase of the average phonon frequencies $\omega_{\log}$ – panel (b) – and the decrease of the average *e-ph* coupling λ – panel (c). In panel (d) I show the soft-mode frequency ω_{soft} as a function of pressure. The dynamical instability occurs when $\omega_{soft} = 0$, i.e. at 72 GPa for YH_6, and 226 GPa for YH_{10}, respectively. Close to a dynamical instability the harmonic lattice approximation gradually breaks down, as the structure approaches a pressure where it becomes a *saddle point*, rather than a *minimum* of the potential energy surface. In order to estimate the importance of anharmonic renormalization on the phonon frequencies near the instability, I performed a frozen-phonon calculation of the anharmonic for the frequency of the soft mode [257, 258]. According to my calculation, the soft-mode anharmonic frequency differs significantly from the harmonic one only within 20 GPa of the lattice instability. This indicates that the effect of anharmonicity should become negligible above 100 GPa for YH_6 and above 250 GPa for YH_{10}, and thus will not significantly affect the results on the superconducting gap and T_c.

The occurrence of a similar lattice instability in the two sodalite-like clathrate structures suggests a common origin. In the following, I propose a simple mechanism, which also holds in the structurally related YH_3, which remains dynamically stable down to 11.5 GPa (green triangles in Fig. 5.1). In Panel (e) of Fig. 5.7 I show the volume vs pressure equation of state for YH_3 (green

triangles), YH_6 (blue circles), and YH_{10} (red squares). The vertical lines highlight the pressures at which the dynamical instability occurs in the three compounds. These three lines intersect the $V(P)$ curves approximately at the same volume (27 Å^3), highlighted by the horizontal dashed line. This volume equals that of a sphere of radius ~ 1.9 Å, i.e. the covalent radius of yttrium.

The stabilization mechanism suggested by this observation, which should apply to sodalite-like clathrate hydrides with XH_n formula, is the following: "*the minimum stabilization pressure is dictated by the size of the guest atom X: when the hydrogen cage becomes too loose to constrain this atom in its middle, the H lattice breaks down*" [7]. This hand-waving rule implies that for higher hydrogen content (large n), where the hydrogen clathrate cage is larger and exhibits shorter H-H distances, the stabilization pressure will be also larger. Conversely, structures with a lower hydrogen content will be characterized by larger H-H distances, but cages with a lower radius, and therefore a lower stabilization pressure. On the other hand, structures with high hydrogen content ensure a larger contribution of hydrogen to the electronic and vibrational states, which leads to a higher T_c.

Our argument implies that in sodalite-like hydrides the low-pressure dynamical stability and high-T_c superconductivity compete. In this sense, the YH_6 structure (intermediate cage volume, small d_{HH}) represents an optimal compromise, whereas YH_3 (smallest cage volume, but too large d_{HH}) is stable at low pressure, but has a low T_c, and YH_{10} (smallest d_{HH}, large cage volume) has the highest T_c, but is only stable at very high pressures.

5.4 Discussion and Conclusions

In summary, I have investigated the superconducting properties of two yttrium hydrides, YH_6 and YH_{10}, at high pressure, using *ab initio* anisotropic Migdal-Eliashberg theory, including a first-principles calculation of the Morel-Anderson pseudopotential. The goals were 1) the testing of a hypothesis, according to which sodalite-like hydrides were a realization of atomic hydrogen at low pressure, 2) the *ab initio* calculation of the effect of Coulomb screening, for which anomalously large values had been proposed [50], and 3) the study of the onset of dynamical instability at low pressures.

The anisotropic gap is rather isotropic for both YH_6 and YH_{10}, despite a significantly anisotropic distribution of yttrium and hydrogen states over the Fermi surface. This is a strong evidence of the presence of significant Y-H interorbital interactions which wash out the anisotropy, and indicate that sodalite-like clathrates are not, in fact, a realization of atomic hydrogen.

The T_c calculations are in good agreement with previous predictions of room-temperature superconductivity in this system [140, 146, 147], where isotropic Migdal-Eliashberg theory or the McMillan/Allen-Dynes formula was used, and the empirical value $\mu^* = 0.10$ was assumed. The T_c

of YH_6 was measured experimentally after these results were published. P. Kong et al. reported a T_c of 227 K at 237 GPa [37], while Troyan et al. reported a value of 224 K at 166 GPa [38].

In addition, I computed the Morel-Anderson pseudopotential (μ^*) from first principles, within the *GW* approximation. Its value is close to the standard value recorded for most conventional superconductors (μ^*= 0.11), in contradiction with other studies on the related lanthanum sodalite-like clathrate hydrides, where a much larger value was hypothesized [38,50]. Our results (i) provided an accurate reference for subsequent work on SLC hydrides, justifying the use of *isotropic* Migdal-Éliashberg theory, and (ii) inspired strategies to optimize the properties of other SLC hydrides. As I will show in 7 combining host atoms with different sizes in ternary systems, which I proposed when I published these results, proved to be an effective route to realize my optimization strategy.

Chapter 6

Calcium Boron Hydrides

In this chapter I will present the high-pressure phase diagram of the ternary calcium-boron-hydrogen (Ca-B-H) system, with a focus on how pressures affects the bonding of the elements involved. I used variable-composition evolutionary algorithms for crystal structure prediction to determine the phase diagram, and Density Functional Perturbation Theory to compute the vibrational and superconducting properties. The Ca-B-H system has been extensively studied at ambient pressure, and it is known to form insulating, hydrogen-rich structures. The presence of hydrogen-rich structures, and of covalent bonds involving hydrogen, suggest that, if metallized by pressure, Ca-B-H structures might exhibit high-T_c superconductivity. By calculating the stable phases at various pressures, I was able to identify a pressure range around which all stable structures turn from insulators to metals, and I related the (high) metallization pressure to the strength of the B-H covalent bond. Among the predicted phases, I also identified a high-temperature superconductor with $CaBH_6$ composition, and a predicted T_c of about 110 K. The results presented in this chapter were published in Ref. [8]. The data and the figures, including captions, are reprinted with permission from the involved parts.

The chapter is organized as follows: in section 6.2 I will present the phase diagram at various pressures, and underline the differences among the structural properties of the stable phases with pressure. In section 6.3 I will describe the electronic properties of selected stable and metastable phases, with a specific focus on metallic structures that form at high pressure. In section 6.4, I report the electron-phonon properties, and discuss the specific electronic and structural features responsible for low or high-T_c in the different phases. In section 6.5 I will summarize my results, and draw the main conclusions.

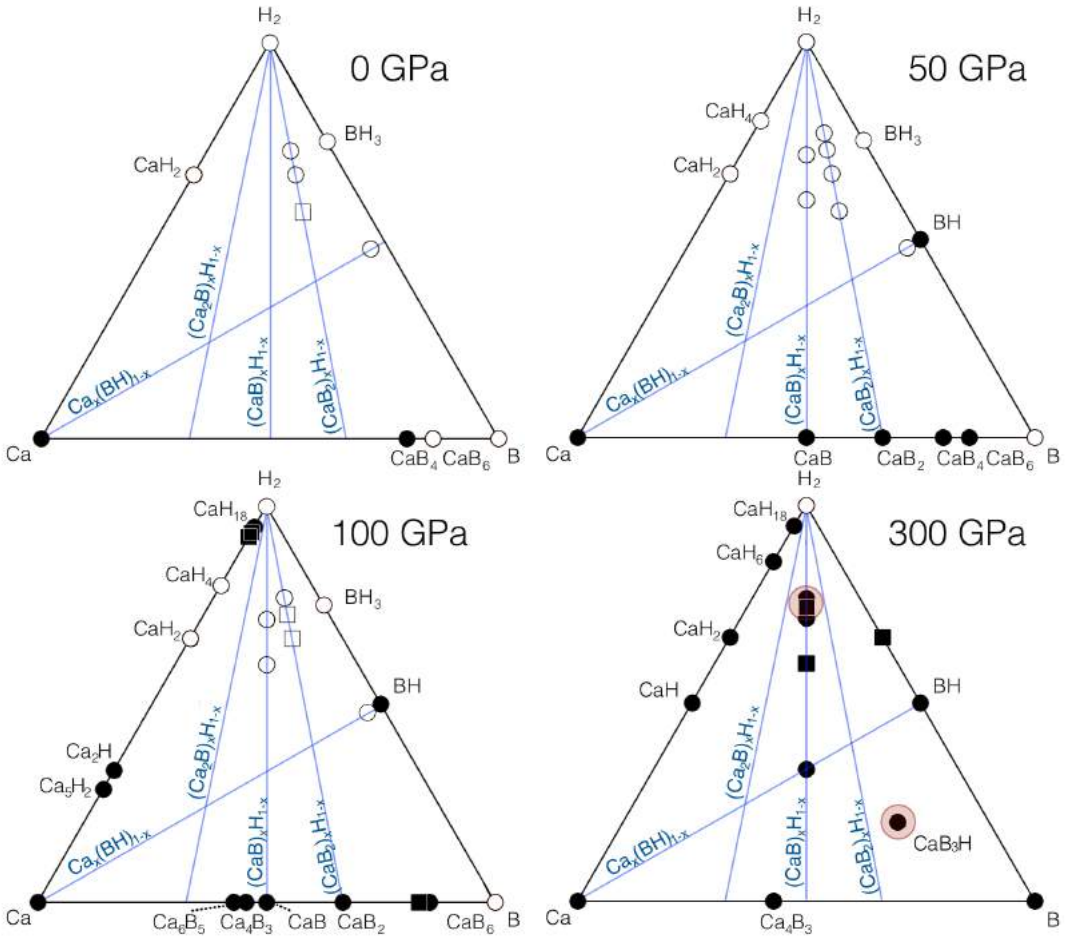

Figure 6.1: Convex hull diagrams for calcium, boron and hydrogen at 0 , 50, 100 and 300 GPa predicted from evolutionary crystal structure prediction calculations. Thermodynamically stable and metastable structures are shown as circles and squares, while empty and filled symbols represent insulating and metallic structures, respectively. Compositions within 50 meV/atom from the hull are considered metastable. Blue lines indicate lines where additional structural searches were carried out. The compositions circled in red - $CaBH_6$, $Ca_2B_2H_{13}$, and CaB_3H exhibit a finite T_c.

6.1 Background

This study was performed in the Summer of 2020, when the computational exploration of binary hydrides under perssure had been nearly completed, while ternary hydrides were essentially unexplored; this study was one of the very first on this topic to perform a full structural search over multiple pressures [42, 43]. In general, the motivation to exploring ternary hydride originated from the idea of exploiting the additional flexibility from the third atom to surpass the properties of binary ones, i.e. finding either a higher T_c or a lower stabilization pressure. The specific choice of the calcium boron hydrogen (Ca-B-H) system was made among the ternary hydrides which were known to form at room pressure. Calcium borohydrides belongs to the larger family of *metal borohydrides* (M-B-H). In general, M-B-H consist of a *weak* (M) and a *strong* (B) hydrogen former,

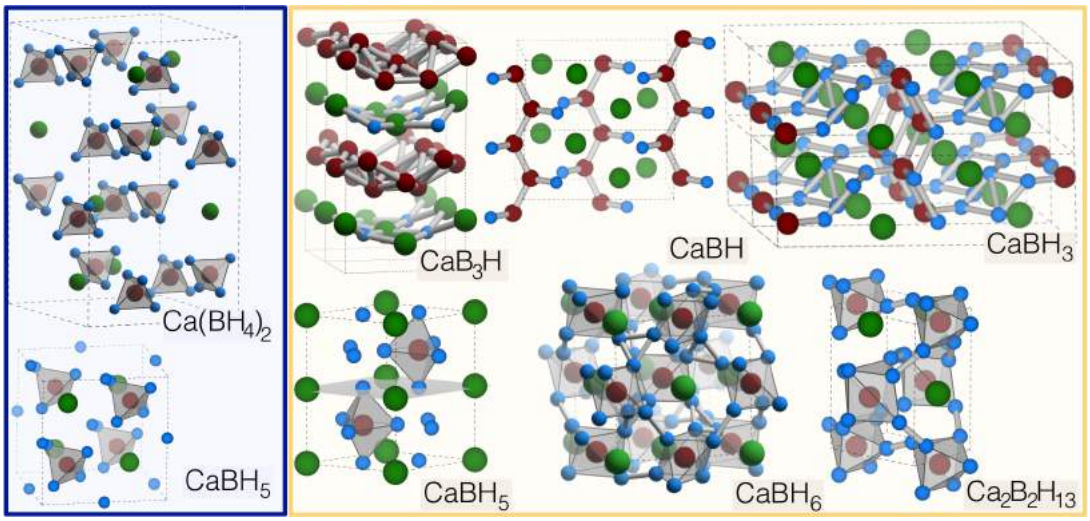

Figure 6.2: Left: crystal structures of the $Fddd$ phase of $Ca(BH_4)_2$ at 0 GPa, and $F\bar{4}3m$ of $CaBH_5$ at 50 GPa. Right: crystal structures of high-pressure $Amm2$ phase of CaB_3H, $Ima2$ phase of CaBH, $C2/m$ phase of $CaBH_3$, $P63mmc$ phase of $CaBH_5$, metastable $Pa\bar{3}$ phase of $CaBH_6$, and Pm phase of $Ca_2B_2H_{13}$. Calcium, boron, and hydrogen are shown as green, red, and turquoise spheres, respectively.

i.e. elements that bind more or less strongly to hydrogen. At room pressure, they form molecular crystals consisting of interstitial M^{+n} cations (n = 1, 2, 3), and n BH_x^- anions (x = 2, 3, 4). The BH_x anions are isostructural to hydrocarbons: polyethylene, ethane, and methane, respectively. The similarity with hydrocarbons and the presence of interstitial metallic ions make these materials rather promising. Hydrocarbons such as polyethylene [259] and methane [260] proved to be extremely difficult to metallize, but exhibit large electron-phonon matrix elements (and thus high T_c) if they can be turned metallic [259]. The presence of an interstitial metal atom could aid the metallization via charge transfer or self-doping.

The phase diagram of the Ca-B-H system at ambient pressure was extensively studied for hydrogen storage applications. The $Ca(BH_4)_2$ phase decomposes upon heating above 300^{o}C through three possible channels: (*i*) towards CaH_2, H_2, and $CaB_{12}H_{12}$; (*ii*) towards CaH_2, CaB_6 and H_2, or (*iii*) through an intermediate $Ca(BH_3)_2$ phase, with a release of H_2 [261–266]. A thorough computational study from Y. Zhang et al. [267] was able to explain this behavior by showing that the three decomposition pathways are all very close in energy. Hence, minimal changes in the experimental conditions can strongly affect the outcome of the decomposition.

The three binary systems which constitute the edges of the ternary convex hull (Ca-B, Ca-H, B-H), were also studied with *ab initio* calculations, and superconductors were predicted to form in all three, with a T_c of 6 K in CaB at about 30 GPa, 235 K in CaH_6, and 21 K in BH, both above 150 GPa [121, 122, 268]. No studies were performed on the high-pressure behavior of the ternary system.

In this study, I studied calcium borohydrides using *ab initio* crystal structure prediction, with

the goal of identifying potential high-T_c superconductors at pressures lower than known binary hydrides (H_3S and LaH_{10}), or with higher T_c.

6.2 Phase diagram

I sampled the full compositional space of the Ca-B-H system at four pressure values: 0, 50, 100, and 300 GPa, employing variable-composition evolutionary algorithms; details on the structural search can be found in Appendix C. The main goal was the identification of the stable compositions at room, intermediate, and extreme pressures. In the unconstrained variable-composition search, more than 3000 unique structures were sampled for each pressure. In addition, I performed additional searches along the $(CaB)_xH_{1-x}$, $(CaB_2)_xH_{1-x}$, $(Ca_2B)_xH_{1-x}$, and $Ca_x(BH)_{1-x}$ pseudo-binary lines, and along the binary Ca_xH_{1-x}, B_xH_{1-x}, and Ca_xB_{1-x} lines, each line adding about 500 structures sampled. After the stable compositions were determined, the lowest-enthalpy structures were then relaxed at intermediate pressures to obtain the pressure-dependent phase diagram, and establish the most stable structure at each pressure.

In Fig. 6.1 I show the ternary convex hulls obtained at 0, 50, 100, and 300 GPa. Circles represent thermodynamically stable compositions, while squares represent metastable ones (i.e. within 50 meV/atom from the convex hull), respectively. Full/empty symbols indicate whether the structure is a metal/nonmetal. It is possible to observe a gradual transition when going from low to high-pressure: (*i*) stoichiometries tend to deviate from those that follow the *textbook* rules of valence, and move towards *chemically forbidden* compositions, and (*ii*) structures tend to go from insulating to metallic behavior. At 300 GPa the transition is complete and all structures on the hull are metallic.

At 0 GPa, my results are in agreement with previous calculations and experiments [264,266–269]. There are two stable compositions along the $Ca(BH_x)_2$ line, i.e. $Ca(BH_3)_2$ and $Ca(BH_4)_2$, along with a third metastable one – $Ca(BH_2)_2$. The crystal structures for all these three compositions contain BH_x^{-1} anions (x = 2, 3, 4), isostructural to their CH_x equivalents (polyethylene, ethane, methane), while Ca^{2+} cations sit in the interstitials. I also reproduce the presence of a stable phase with $CaB_{12}H_{12}$ composition, characterized by $B_{12}H_{12}{}^{2-}$ icosahedra [266,270]. In the top left panel of Fig. 6.2 I show as an example the crystal structure of $Ca(BH_4)_2$.

At 50 GPa, the convex hull remains similar to the ambient pressure one, and the stable structures contain the same motifs present at 0 GPa. In addition, structures with the $Ca(BH_2)_2$, $Ca(BH_5)_2$, $CaBH_3$, and $CaBH_5$ compositions become thermodynamically stable along the $Ca(BH_x)_2$ and $Ca(BH_x)$ lines, as molecular and atomic hydrogen is trapped in the interstitial sites. The same effect – trapping of atomic or molecular hydrogen at high pressures – has been reported in other covalent hydrides. [126]. The crystal structure of $Ca(BH_5)_2$ contains the same BH_4 tetrahedra as

$Ca(BH_4)_2$, with additional H_2 molecules trapped in the interstitial sites. In $CaBH_3$, an isolated H atom sits in the interstitial sites of a Ca tetrahedron, which alternates with BH_2 linear chains, while in $CaBH_5$ a H atom is trapped in the interstitial sites between the BH_4^- tetrahedra – See Fig. 6.2 bottom left panel.

At 100 GPa, the compositions on the $Ca(BH_x)_2$ line become unstable, while those on the $(CaB)H_x$ line ($CaBH_3$ and $CaBH_5$) are stable. In addition, the structure with $CaB_{12}H_{12}$ compositions undergoes a structural transition towards a more densely-packed phase with $R\bar{3}m$ space group. At this pressure, all stable structures are still insulating, but close to metallization. In fact, immediately after this pressure, at 110 GPa, the $CaBH_5$ structure becomes metallic due to the pressure-induced band overlap, and is followed by the others.

At 300 GPa, all stable structures have different compositions, and exhibit completely different structures from those at ambient pressure. The crystal structures of the stable high-pressure phases are shown in the right panel of Fig. 6.2. A complete rearrangement of the bonds has occurred: boron and hydrogen form dense interconnected networks, and the only recognizable hydrocarbon-like motif is polyacetylene, observed in CaBH. The other stable compositions are CaB_3H, $CaBH_5$, and $Ca_2B_2H_{13}$. In addition, all the stable structures are metallic.

The CaB_3H structure is characterized by buckled layers of boron, similar to those predicted for pure boron in Ref. [122]. The boron layers alternate with CaH planes in such a way that the Ca atoms corresponds to the valleys of the B layers. The CaBH structures consists of infinite B-H polyacetylene-like chains in a direction parallel to Ca linear chains. The structure with $CaBH_5$ composition is quite different from the one observed at 50 GPa (left panel of Fig. 6.2), as it is characterized by BH_5 polyhedra (triangular bipyramids), and no interstitial hydrogen.

In addition to the thermodynamically stable phases described above, I also identified a hydrogen-rich, high-symmetry structure with space group $Pa\bar{3}$ with $CaBH_6$ composition, with an enthalpy about 100 meV/atom higher than the convex hull. This structure is characterized by BH_6 6-vertex antiprisms, in which hydrogen sits at the vertexes of the polyhedron, and boron in the center. In this structure, the H-H distance is of approximately 1.2Å, which is rather close to that of atomic hydrogen [247]. A H-H distance between 1 and 1.6 Åis often associated with the formation of a metallic hydrogen sublattice [7, 141], and positively correlates with high-T_c superconductivity. Thus, I decided to add this structure to my pool of candidates for superconductivity.

In Fig. 6.3 I show the pressure-dependent phase diagram for each of the stable Ca-B-H compositions. Most of the compositions that are found on the convex hull at 300 GPa become stable at lower pressure – between 100 and 200 GPa. In particular, around 100 GPa there is a rather clear separation in the phase diagram, which can be divided into a low- and a high-pressure region. The low-pressure region contains $Ca(BH_x)_2$ (x = 2, 3, 4) and $CaB_{12}H_{12}$ compositions; as discussed, these are molecular crystals, with insulating behavior. Between 0 and 50 GPa, the BH_x units rear-

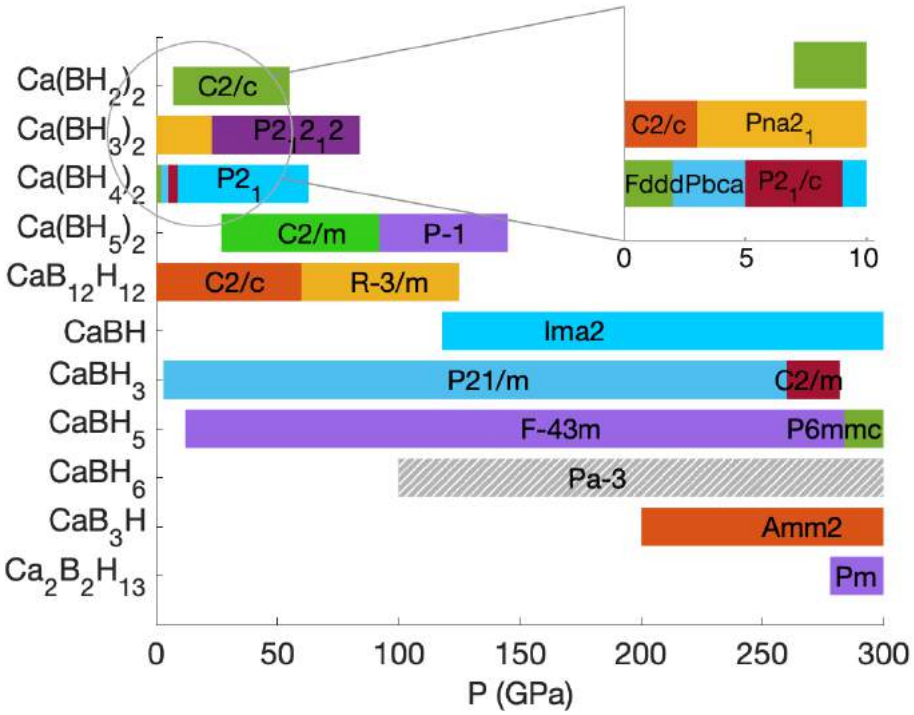

Figure 6.3: Phase diagram for intermediate compositions as a function of pressure. The space group for each phase is indicated on top of the bars. The slashed pattern indicates the dynamical stability of a high-symmetry $CaBH_6$ structure, which is thermodynamically unstable. The inset shows phase transitions between low-pressure structures for $Ca(BH_x)_2$ compositions.

range leading to a series of structural transition, but the B-H bonding remains unaltered. Between 10 and 20 GPa, H-rich stoichiometries such as $Ca(BH_5)_2$, $Ca(BH_3)$ and $Ca(BH_5)$ become stable, as hydrogen is trapped in molecular or atomic form in the space left open by the BH_x molecules. Right above 100 GPa, additional structures become stable along the $Ca(BH)_x$ line; in these structures, the B-H bonding observed at low pressure changes, as the B-H coordination number increases to five or more hydrogen atoms. This qualitative change in the behavior of the B-H sublattice goes in parallel with the onset of metallicity. In fact, the onset of metallic behavior is observed already slightly above 100 GPa in those structures that remain stable up to 300 GPa.

6.3 Electronic Structure

I will now discuss the electronic properties of the structures in the Ca-B-H phase diagram at 300 GPa. Structures that form below 100 GPa are insulating, and therefore not relevant for superconductivity, so I will only shortly discuss the main features of their electronic structure, without showing their Density of States (DOS) [8].

At room pressure, the molecular nature of the hydrocarbon-like, BH_x^- anions, reflects into a molecular-like DOS's, characterized by narrow peaks of both B and H character, and an insulating

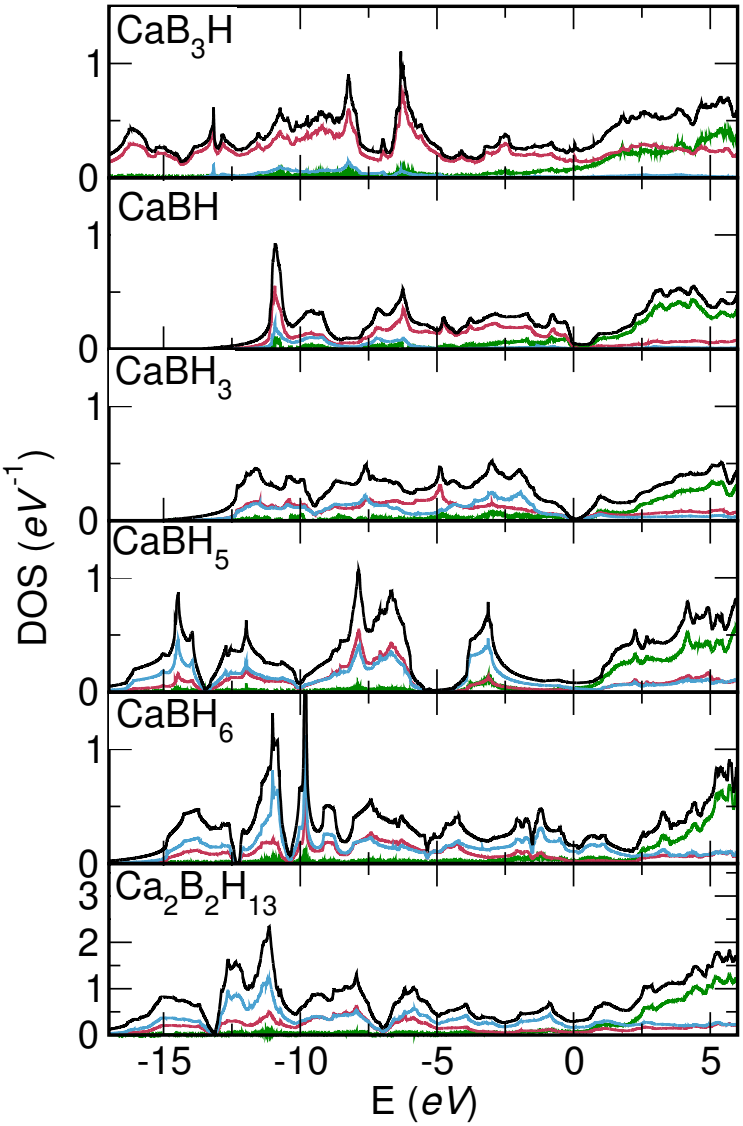

Figure 6.4: Calculated total and projected DOS for stable and metastable calcium boron hydrides at 300 GPa. Black, red, turquoise, and green lines represent the total DOS, and its projection onto B, H, and Ca, respectively. The energy range is shifted with respect to the Fermi level. The DOS is in units of states per eV per formula unit. The Fermi energy corresponds to the zero of the scale. From top to bottom: $Amm2$ - CaB_3H, $Ima2$ - CaBH, $C2/m$ - $CaBH_3$, $P6_3mmc$ - $CaBH_5$, $Pa\bar{3}$ - $CaBH_6$, and the Pm - $Ca_2B_2H_{13}$.

behavior, with band gaps gong from 2.6 eV in $Ca(BH_2)_2$ to 5 eV for $Ca(BH_4)_2$. Ca 4*s* and 3*d* states are found at conduction band bottom. Indeed, the calcium atom is almost fully ionized, the calculated Bader charge is +1.5 *e*. As pressure grows up to 50 GPa, the DOS peaks become broader and tend to merge into a single, continuous band; the band gaps decrease to 1.8 eV for $Ca(BH_2)_2$, 2.1 eV for $Ca(BH_3)_2$, and 3.4 eV for $Ca(BH_4)_2$. The stable compounds at this pressure, with compositions $Ca(BH_5)_2$, $CaBH_3$ and $CaBH_5$, are also insulating, and their band gaps are 4.1, 1.6, and 2.3 eV, respectively. At 100 GPa, all the stable structures but $CaBH_5$ are still insulating. The calculated gaps $Ca(BH_3)_2$, $Ca(BH_4)_2$, $Ca(BH_5)_2$, $CaBH_3$, and $CaB_{12}H_{12}$ are 1.6, 0.5, 1.8, 0.4 and 2.6 eV, respectively. $CaBH_5$, as mentioned, is semimetallic, due to pressure-induced band overlap.

At 300 GPa, in turn, all the stable phases are metallic. Although the metallization pressure is lower, around 150 GPa, I chose to discuss them at 300 GPa, as it is a common pressure to all of them. In Fig.6.4 I show the atom-projected electronic DOS for CaB_3H, CaBH, $CaBH_3$, $CaBH_5$, $CaBH_6$, and $Ca_2B_2H_{13}$.

The DOS behavior in the valence region (-20 to 0 eV) strongly depends on the relative hydrogen content. In CaB_3H and CaBH, the DOS is dominated by states with B character, while hydrogen does play a significant role. On the contrary, in hydrogen-rich structures, a prominent B-H hybridization is visible over all the occupied states; unlike low-pressure, Ca-4*s* states here are present both in the valence and conduction band. Indeed, at this pressure Ca is only in part ionized; on average I calculate a Bader charge of +0.9. The $CaBH_3$ structure is metallic, but exhibits an extremely small DOS at the Fermi level, suggesting a semi-metallic behavior.

In $CaBH_5$ the valence band is also essentially of B and H character, but starting from the Fermi energy, the onset of Ca-3*d* states appears, which contribute to about 50% of the states at the Fermi level. Finally, in $CaBH_6$ and $Ca_2B_2H_{13}$, states in valence are predominantly of B and H character; the fact that B- and H- projected DOS exhibit a rather similar pattern, suggests a certain amount of B-H covalent bonding; the Ca-3*d* states are empty, and lie around 2 eV above the Fermi energy.

It is well known that the Perdew-Burke-Ernzerhof (PBE) exchange-correlation functional employed in my calculations tends to underestimate the band gap, and hence the metallization pressure. To check the validity of this approximation, I recomputed the band gap as a function of pressure for the $P63mmc$ phase of $CaBH_5$ using a HeydScuseriaErnzerhof (HSE) hybrid functional [271], which is better suited for this estimation, although much more expensive computationally. From a comparison of the results obtained with the two functionals, I observed that the PBE functional underestimates the gap by about 1 eV at all pressures. Correcting for this effect, I estimate that the actual metallization pressure of the structures reported will be about 60 GPa higher than the PBE result.

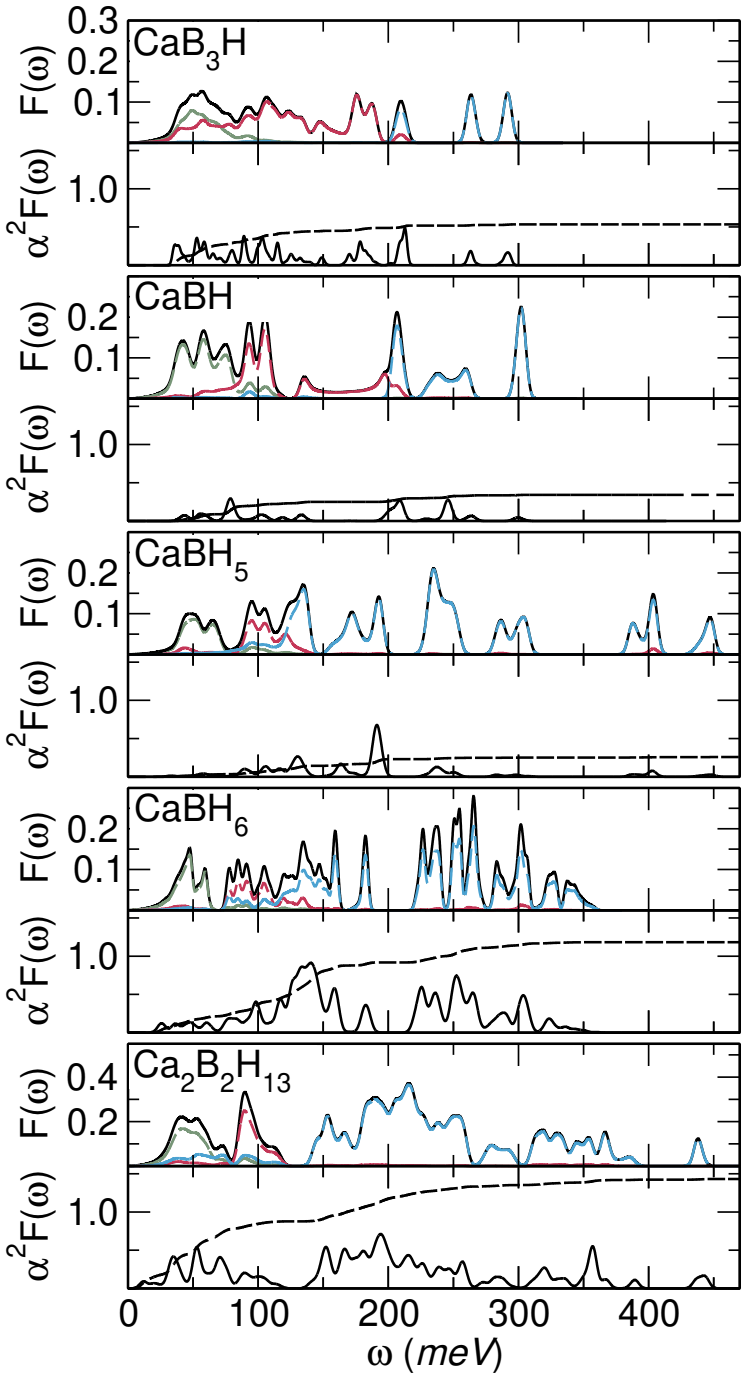

Figure 6.5: Atom-projected phonon DOS ($F(\omega)$), Eliashberg function ($\alpha^2F(\omega)$, solid lines), and frequency-dependent *e-ph* coupling constant ($\lambda(\omega)$, dashed lines) calculated at 300 GPa for the same six high-pressure phases as in Fig. 6.4. The total phonon DOS is shown in black, and its projections on Ca, B, and H, are shown in green, red, and blue, respectively.

6.4 Vibrational Properties and Superconductivity

All high-pressure structures except $CaBH_3$ are good metals, and hence possible high-T_c superconductors. To evaluate their superconducting properties, I computed their electron-phonon properties by means of Density Functional Perturbation theory, as implemented in `Quantum Espresso`, and calculated their T_c using the McMillan formula of eq. (4.54). [25, 220, 272, 273].

In Fig.6.5 I show the calculated total and atom-projected phonon Densities of States (top panels) alongside with the Éliashberg function (bottom panels) for CaB_3H, CaBH, $CaBH_5$, $CaBH_6$, and $Ca_2B_2H_{13}$. The projections have the same color coding as the electronic DOS's in Fig. 6.4.

All the five structures examined exhibit a similar separation of the phonon spectra into three regions: (*i*) a low-energy region, from 0 to 75 meV, mostly characterized by vibrations of the Ca atom, (*ii*) an intermediate region, which goes from 75 to 175 meV, and consists of modes of both B and H character, and (*iii*) a high-energy region, from 175 to 300 meV, which exhibits mostly B-H stretching modes. In addition, $CaBH_5$, $CaBH_6$ and $Ca_2B_2H_{13}$ exhibit a fourth region, which is not present in CaB_3H and CaBH, which only involves vibrations of the H atoms.

It is interesting to compare the phonon DOS with the Éliashberg spectral function, which can be thought of as a phonon Density of States weighted with the electron-phonon coupling [274]. From a direct comparison of the two, one can deduce how the coupling is distributed over phonon modes.

In all the structures examined, I observe that the Éliashberg function does not differ significantly from the phonon DOS, suggesting that all vibrational modes contribute relatively evenly to the total *e-ph* coupling, similarly to the cases of H_3S, LaH_{10}, and other high-pressure hydrides [7, 126, 143, 147].

I also calculated ω_{log} and λ, as defined in eq. (4.55). These two quantities are useful measures of two important physical characteristics of the system: $\omega_{\log}$ is the weighted average frequency of the phonons, while λ is the total intensity with which phonons couple to electrons at the Fermi level. In table 6.1 I report a summary of these quantities, together with the T_cs, estimated using the McMillan equation (eq. (4.54)), using two choices of the Morel-Anderson pseudopotential: $\mu^* = 0.10 - 0.15$. In addition the table also contains the unit cell volume, the DOS (per unit volume) and the fraction of hydrogen states at the Fermi level. The DOS at the Fermi level describes the number of electrons available for superconductivity, and the hydrogen fraction indicates how much hydrogen contributes to these states.

Two structures stand out as high-T_c superconductors: $CaBH_6$ and $Ca_2B_2H_{13}$, which exhibit a $T_c$of 119 and 89 K, respectively. The two structures are both hydrogen-rich and high-symmetry, and remain dynamically stable down to 100 and 200 GPa, respectively, still with a high T_c.

Among the other structures I report a finite T_c (7 K) in CaB_3H. A much lower value is to be expected for this structure, as in the whole valence region the H fraction of the electronic DOS

	P	SG	f.u.	Volume	$N(E_F)$	$\frac{N_H}{N(E_F)}$	λ	$\frac{\lambda}{N(E_F)}$	ω_{log}	T_c
CaB_3H	300	$Amm2$	2	43.6	1.08	0.02	0.48	0.44	78	4-7
CaBH	300	$Ima2$	2	27.9	0.60	0.06	0.14	0.23	97	≤ 0.1
$CaBH_5$	300	$P6mmc$	2	39.9	0.41	0.40	0.26	0.63	131	≤ 0.1
$CaBH_6$	100	$Pa\bar{3}$	4	119.7	0.57	0.73	1.93	3.33	70	100-114
$CaBH_6$	200	$Pa\bar{3}$	4	97.6	0.64	0.67	1.27	1.99	106	97-117
$CaBH_6$	300	$Pa\bar{3}$	4	85.6	0.79	0.67	1.19	1.59	117	97-119
$Ca_2B_2H_{13}$	200	Pm	1	50.2	0.59	0.51	1.23	2.10	59	51-62
$Ca_2B_2H_{13}$	300	Pm	1	43.9	0.67	0.55	1.37	2.07	74	75-89

Table 6.1: Normal and superconducting state properties of the six high-pressure Ca-B-H phases in Fig. 6.4-6.5. Space group (SG), number of formula units, unit cell volume; DOS at the Fermi level - $N(E_F)$, Hydrogen fraction of the total DOS at the Fermi level ($N_H/N(E_F)$), electron-phonon coupling constant (λ), effective *e-ph* matrix element ($\lambda/N(E_F)$), logarithmic-average phonon frequency (ω_{log}), McMillan-Allen-Dynes superconducting T_c – Eq. (4.54), with $\mu^* = 0.10$ and $\mu^* = 0.15$. The DOS at the Fermi level is expressed in states/spin, and is rescaled by volume to allow for an easier comparison between different pressures. The measurement units of the quantities shown in the columns are: P (GPa), Volume (^{3}), $\frac{N_H}{N(E_F)}$ (10^2 states/$eV/^3$), $\frac{\lambda}{N(E_F)}$ (eV^{-1}), ω_{log} (meV), and T_c (K), respectively.

is negligible (around 2%) – See Fig: 6.4. In this structure the boron sublattice dominates both the electronic and vibrational properties, and this leads to an intermediate *e-ph* coupling constant ($\lambda = 0.48$), and a value of ω_{log} sensibly smaller than the typical values for hydrides [56] According to my calculations, the other two compositions stable at 300 GPa, CaBH and $CaBH_5$, should not be superconducting, i.e. I predict a T_c of less than 1 K.

Finding the reason for a low T_c in a compound for which one would expect a high one improves the understanding of features that *suppress* superconductivity. In both these structures, the DOS at the Fermi level is comparable to that of the other Ca-B-H hydrides (rescaled per unit volume in Tab. 6.1), but the value of the parameter $\lambda/N(E_F)$, is much smaller than in the two high-T_c Ca-B-H phases. This parameter essentially filters out the dependence of the coupling from the DOS at the Fermi level, leaving only an estimate of the intrinsic coupling between electrons at the Fermi level and lattice vibrations. In CaBH, the low value of $\lambda/N(E_F)$ is due to the small contribution of hydrogen to the states at the Fermi level ($N_H/N_{tot} = 6\%$), but the same argument does apply to $CaBH_5$. In fact, in this compound about 40% of the states at the Fermi level are H-derived. The origin of the weak *e-ph* coupling in $CaBH_5$ can instead be understood by calculating the so-called Local Density of States (LDOS):

$$N(E, \mathbf{r}) = \sum_n \int \frac{d^3k}{(2\pi)^3} \delta(E - \varepsilon_{n\mathbf{k}}) \left|\psi_{n\mathbf{k}}(\mathbf{r})\right|^2, \tag{6.1}$$

where $\psi_n(\mathbf{k})(\mathbf{r})$ and $\varepsilon_{n\mathbf{k}}$ are the Kohn-Sham eigenfunctions and eigenvalues of the system. The

LDOS represents the real-space distribution of the electronic states at a given energy. In particular, the LDOS at the Fermi energy shows the localization in real space of the electrons which can participate in the superconductivity [249].

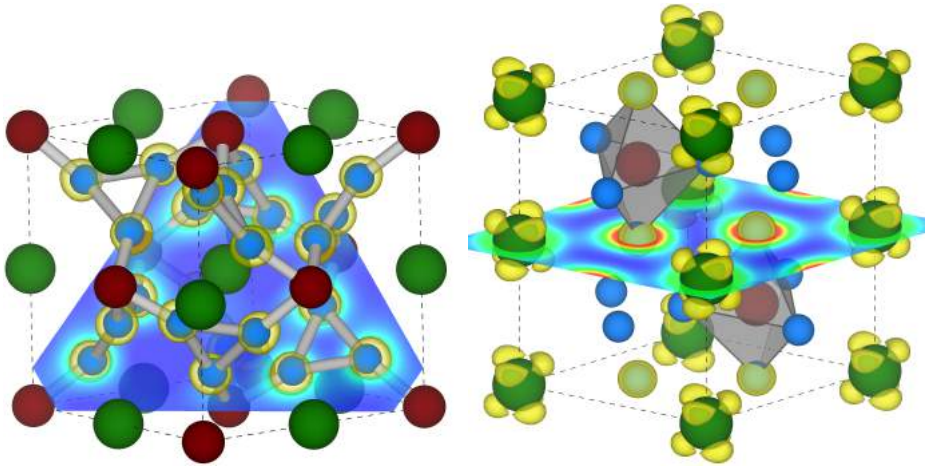

Figure 6.6: LDOS for $CaBH_6$ (left) and $CaBH_5$ (right)The yellow isosurfaces represent the LDOS at 50% of its maximum value. The lattice plane shows the LDOS along the 001 plane of $CaBH_5$ and $1\bar{1}1$ plane of $CaBH_6$. The color scale on the lattice plane goes from the minimum (blue) to the maximum (red) value of the LDOS. The BH_6 antiprisms of $CaBH_6$ are not shown for visual clarity.

In Fig. 6.6 I show a comparison of the LDOS at the Fermi level (yellow isosurface) for both the high-T_c $CaBH_6$ (left) and the non-superconducting $CaBH_5$ (right). In $CaBH_6$, the electronic charge at the Fermi level is concentrated around hydrogen atoms, which are rather close to each other in real space. Vibrations which modulate the H-H distance, have a large effect on the real-space distribution of the electrons at the Fermi level, and thus give rise to large *e-ph* matrix elements. On the contrary, in $CaBH_5$ about half of the charge at the Fermi level is distributed around the Ca atoms along the vertical axis, and the other half is only on those hydrogen atoms that are coplanar to calcium, and at a distance of about 1.8 Å from both Ca and from the nearest coplanar H atom. Hence, none of the lattice vibrations can lead a substantial modulation of the overlap of these charge regions, as they are too isolated in space, and therefore their coupling with phonons is small.

Further support to this interpretation can be drawn from the so-called "fat-band" plot, shown in Fig. 6.7, in which the color of each band (from purple to orange) indicates the amount of projection onto Ca-*d* orbitals. In $CaBH_5$, the whole electron pocket around the Γ point is characterized essentially by Ca-*d* character, while in $CaBH_6$ these states are higher in energy, and do not contribute significantly to the density of states at the Fermi level. In practice, the *d* orbitals of Ca seem play an important role, as they can negatively affect superconductivity in Ca-B-H.

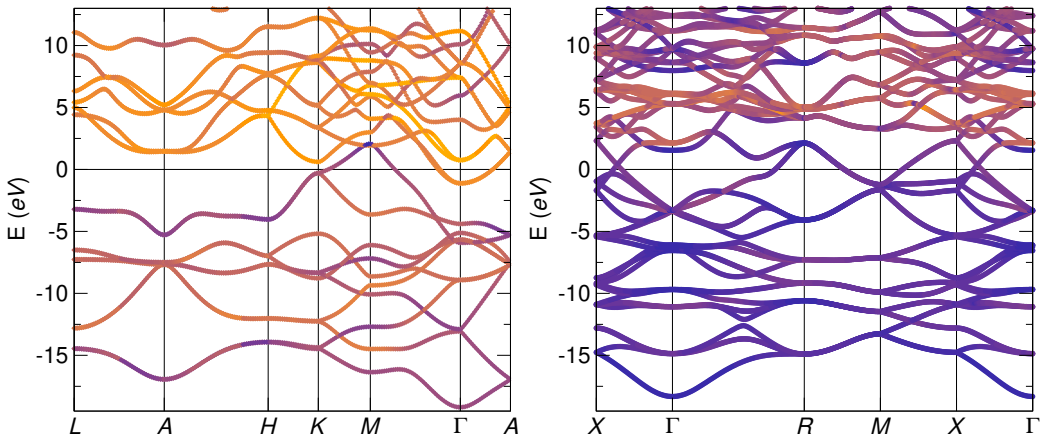

Figure 6.7: Band structure projected onto Ca-d states of $CaBH_5$ (left) and $CaBH_6$ (right) at 300 GPa. Blue to orange color gradient indicates the fraction of Ca-d character.

6.5 Conclusions

In conclusion, in this chapter I have examined the phase diagram of the ternary calcium-boron hydrogen system as a function of pressure from 0 to 300 GPa, using *ab initio* evolutionary crystal structure prediction. In addition, I used Density Functional Perturbation theory to calculate the superconducting properties of promising hydrides, with the aim of identifying new high-T_c superconductors. I worked in the hypothesis that a combination of a weak (Ca) and a strong (B) hydrogen former could stabilize hydrogen-rich structures at moderate pressures, thanks to the additional freedom provided by the different size and electronegativity of the two atoms. The goal was to surpass the superconducting properties of H_3S and LaH_{10}. Since I aimed at an exploratory work, and focus on the *breadth* of the search rather than the accuracy, I neglected anharmonic effects. These were demonstrated to affect both the stabilization pressure and the superconducting properties of hydrides [132, 143], but normally act as higher-order corrections to the static DFT result, and their inclusion was way beyond the scope of my exploratory work.

The results from my structural searches have demonstrated that the Ca-B-H phase diagram is characterized by two different pressure regions: one extending from 0 to about 100 GPa, and another from 100 to 300 GPa. In the low-pressure region, I found structures containing molecular crystals with hydrocarbon-like motifs, which are insulating. As pressure increases the stable structures tend to trap atomic and molecular hydrogen in interstitial sites, although the B-H bonding remains unaltered.

In the high-pressure region, the structures become qualitatively different, as the B-H bonding changes. The stable phases contain dense B-B or B-H sublattices, and are all metallic at 150 GPa. Among the high-pressure phases I identify two structures with a high hydrogen ratio and unusual stoichiometries: $CaBH_6$ and $Ca_2B_2H_{13}$, characterized by the formation of 5- and 6- coordinated BH_5 and BH_6 molecules. For these two phases, at 300 GPa, I estimate a superconducting T_c of 119 and

89 K, respectively. These values are higher than those of the binary B-H high-pressure structures [122], and similar to those predicted for the Li-B-H system [42]. In addition, I find a hydrogen-rich structure with $CaBH_5$ composition which, surprisingly, is not superconducting, despite being metallic and having a relatively high H content. By comparing it to the superconducting structures, I ascribed the absence of superconductivity to the presence of d states of calcium at the Fermi surface, and to the peculiar geometry of the structure, which causes phonons to poorly couple with electrons at the Fermi energy.

The results presented in this study confirmed the potential of ternary hydrides for high-temperature superconductivity, at a time in which very little work had been carried out. In addition, they showed how sensitive the T_c is to the finer details of the crystal structure: even in a system which should in principle host high-T_c superconductivity, such as Ca-B-H, the sT_c depends even drastically from small changes in the specific geometrical configuration.

Among the structures examined for the Ca-B-H system, none could surpass the properties of the best binary hydrides (H_3S and LaH_{10}). In fact, the metallization pressure of the stable Ca-B-H structures is larger than 100 GPa, due to the large electronegativity of boron, which forms closed-shell, insulating structures which are too hard to metallize. In addition, since Ca-d orbitals are close to the valence band, they can easily become occupied, and influence the electronic properties quite strongly. This study encouraged me to continue my search for high-T_c superconductors in ternary hydrides.

Chapter 7

Ternary Lanthanum Hydrides

During the summer of 2020, Grockowiak et al. [51] published a preprint which showed some evidence that *hot* superconductivity may have occurred in a system with lanthanum, hydrogen, and rich with boron and nitrogen. Excited by the possibility that these measurements would be confirmed, I decided to investigate the possibility that a new hot superconducting phase may have formed. I had to narrow down the set of possible candidates, as there were too many possible combinations of elements. Based on the description of the measurements, I formulated the working hypothesis that LaH_{10} formed upon the first heating cycle, and its structure incorporated other elements upon successive heating. Hence, I decided to search superconductivity in all the combinations of lanthanum, hydrogen, and a third element which was present in the experiment. In particular, I performed a systematic study by calculating the ternary convex hull for La-X-H, with X = B, N, Ga, Pt, Au, C. While I did not find any candidate which might explain the hot superconductivity measured in Ref. [51], I did find a very interesting structure with $LaBH_8$ composition, which remains dynamically stable (and superconducting) down to 40 GPa, with an estimated T_c of about 120 K.

In will divide this chapter into two main subsections. The first is dedicated to the search of the *hot* La-X-H superconductor, while the second is a detailed study of the La-B-H system. This study was performed in 2021, and the results were published in Refs. [10] and [9], roughly corresponding to the first and second section, respectively. The data and the figures, including captions, are reprinted with permission from the involved parts.

This chapter is structured as follows: in sect. 7.2.1 I will discuss the thermodynamical stability for six La-X-H ternary hydrides (X = B, N, Ga, C, Pt, Au) at 300 GPa, and shortly mention their superconductivity, or lack thereof. In sect. 7.3.1 I will present the thermodynamical stability for

the La-B-H system at 100 GPa, and discuss the structural properties of the $LaBH_8$ phase.

7.1 Background

In June 2020, Audrey Grockowiak et al. published a preprint on arXiv [51] titled *Hot hydride superconductivity above 550 K*. While performing resistivity measurements on a lanthanum hydride in a magnetic field, the authors observed a drop in resistivity versus temperature compatible with that of a superconducting transition. The experiments were performed in a diamond anvil cell (DAC), and the sample was laser-heated to induce the transition, supposedly to LaH_6 and LaH_{10}. After the first heating cycle, a T_c of 294 K at 180 GPa was measured, and upon subsequent heating cycles, it increased up to 556 K. Neither composition nor the structure of this *hot hydride* superconductor could be determined. However, the authors carefully described in detail the possible elements which were present in the DAC and may have diffused into the sample. In particular, the most prevalent elements in the DAC were pure lanthanum, and ammonia borane (NH_3BH_3), followed by traces of carbon from the epoxy binder, platinum, gallium and gold from the electrodes. Based on the elements present in the cell, and on the description of the experiment, I formulated the working hypothesis that LaH_{10} has formed first, hence the first T_c measured, and upon successive heating cycles it reacted with one of the other elements, forming a ternary La-X-H hydride (X = B, N, Ga, C, Pt, Au).

The discovery of such a *hot* superconductor is extremely exciting. Since in the experiment the superconducting phase could not be determined, I hoped that I could use *ab initio* calculations to identify it. Based on the experience on other high-T_c hydrides, *hot* superconductivity must occur in a high-symmetry metallic phase, with a large hydrogen fraction. In fact, high-symmetry tends to promote states with large Density of States, metallicity is an obvious prerequisite for superconductivity, and large hydrogen fraction is required to have a *hydride* superconductor, and is associated with a higher T_c.

For the six most plausible ternaries, I used variable-composition crystal structure prediction to determine the phase diagram at 300 GPa. The choice of this pressure, higher than the experimental one (180 GPa) was motivated by the fact that static DFT calculations tend to overestimate the stabilization pressure of superhydrides [132, 143], and the fact that higher pressures tend to favor the formation of superhydrides with larger hydrogen content and higher T_c's. Of all phases investigated, only in La-B-H and La-Ga-H I found hydrogen-rich metallic structures that may host *hot* superconductivity. I calculated the T_c's of the most promising phases using Density Functional Perturbation theory and numerically solving the isotropic Migdal-Éliashberg equations. I found the highest T_c in a structure with $LaBH_{17}$ composition –180 K at 300 GPa. This T_c is way too low to explain the measured hot superconductivity, as even in the optimistic scenarios that a form of

doping would enhance the T_c, its value does not go above 300 K.

Among the La-B-H phases at 300 GPa, we also found one with $LaBH_8$ composition. This phase is characterized by a high-symmetry, metallic structure, that made it an ideal candidate for hot superconductivity. At 300 GPa its calculated T_c is only 14 K, which rules out the possibility that it may be the hot superconductor, but it remains dynamically stable down to 50 GPa, where it exhibits a T_c of 126 K. Its crystal structure is similar to that of LaH_{10}, in that they share the same La sublattice, but in $LaBH_8$ the B atom occupy the interstices between La atoms, largely increasing the packing fraction, which stabilizes the H sublattice down to lower pressures.

7.2 Part I: Search of *hot* superconductivity in La-X-H hydrides

7.2.1 Stable La-X-H compositions at 300 GPa

In Fig. 7.1 I show the convex hulls for the six La-X-H hydrides that were more likely to form in the experiment: La-B-H, La-N-H, La-Ga-H, La-C-H, La-Pt-H, and La-Au-H. The convex hulls were first calculated by sampling the different possible compositions (about 3000 structures). The goal in this case was to estimate the shape of the convex hull, and establish which were worth investigating further. As shown in the figure, for La-Ga-H, La-C-H, La-Pt-H, and La-Au-H we predicted no stable compositions, although with Ga several metastable phases were found lying very close to the hull. In La-B-H and La-N-H, on the other hand, I found a plethora of stable phases. Thus, I dedicated my resources to a better sampling of the La-B-H and La-N-H systems where I sampled all compositions, as well as additional pseudo-binaries, and La-Ga-H, where I re-sampled the $(LaGa)_xH_{1-x}$ pseudo-binary. The convex hulls shown in Fig. 7.1 are those after the additional sampling.

In the La-B-H phase diagram I predicted the formation of three stable ternary compositions: $LaBH_8$, $La_2B_6H_5$, and LaB_8H, plus several H-rich metastable phases (within 50 meV/atom from the hull, shown as red squares). Among these, I identified one with $LaBH_{17}$ composition as a promising superconductor due to its hydrogen-rich structure with relatively high symmetry.

In the La-N-H phase diagram, I predicted four stable compositions: LaN_2H_3, LaN_3H_{10}, La_2N_2H, and La_4N_4H, as well as several metastable ones. All stable and metastable structures contain NH_x molecules,arranged in a disordered fashion, and are insulating. Hence, none of these structures is a candidate for high-temperature superconductivity (HTSC).

In La-Ga-H phase diagram I found no stable ternary hydride, although there are several hydrogen-rich structure very close to the convex hull, suggesting that they may in principle form. Among these, I chose three structures with $LaGaH_6$, $LaGaH_{14}$, and $LaGaH_{15}$ composition as representative

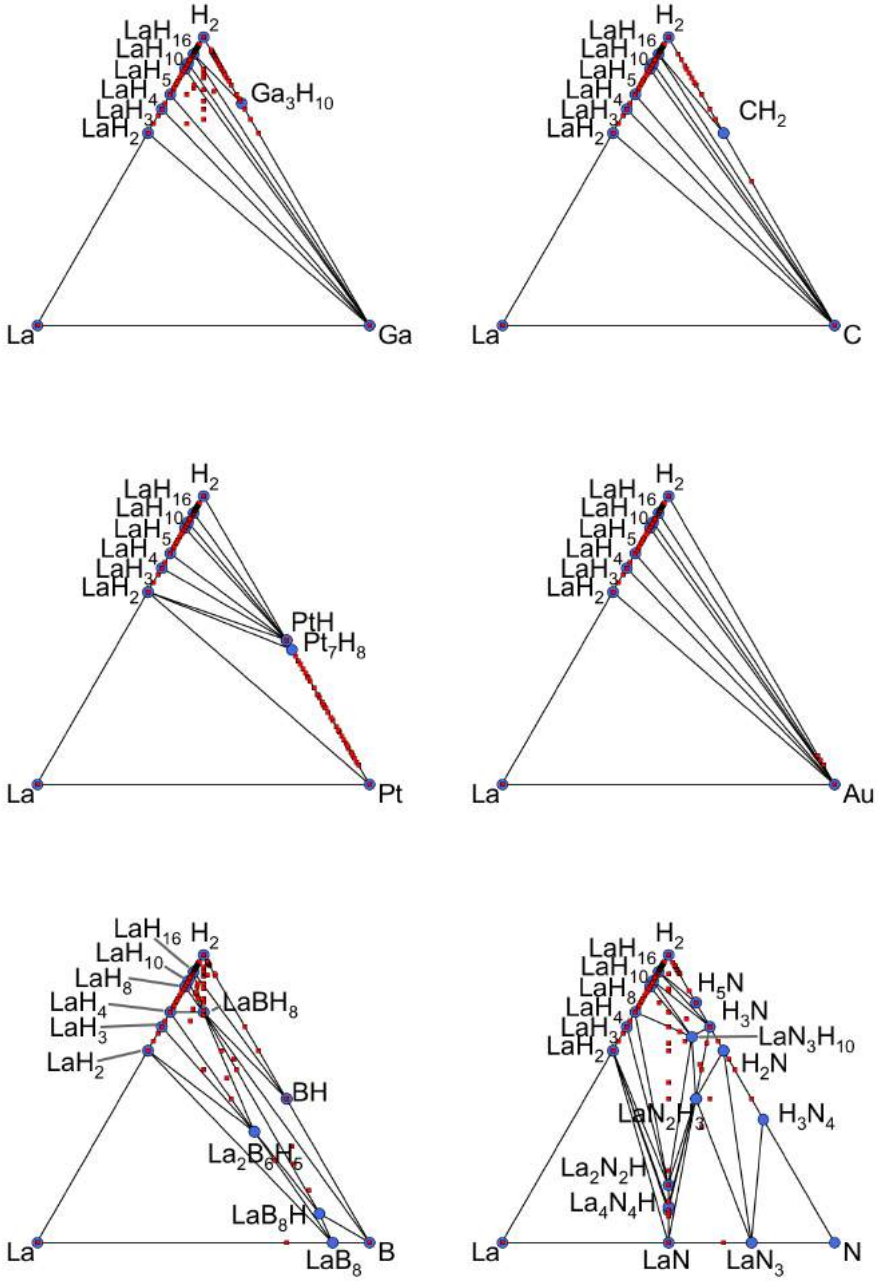

Figure 7.1: Convex hulls for La-Ga-H (top left), La-C-H (top right), La-Pt-H (mid left), La-Au-H (mid right), La-B-H (bottom left) and La-N-H (bottom right), at 300 GPa. Blue circles and red squares represent stable and metastable phases, respectively.

candidates for HTSC in the La-Ga-H system. These structures were all characterized by a relatively symmetric structure, high hydrogen fraction, and intermediate H-H distance.

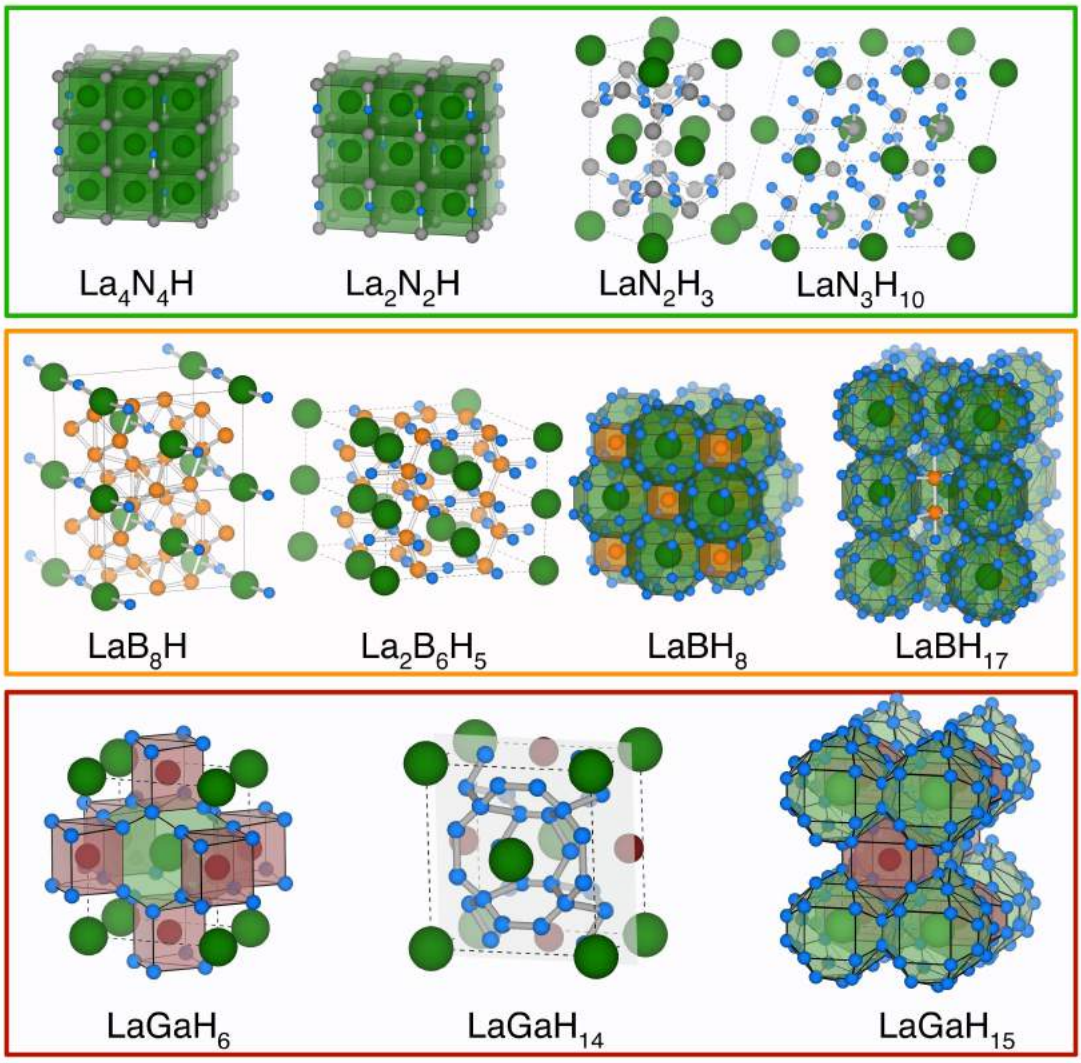

Figure 7.2: Crystal structures of the thermodynamically stable La-B-H and La-N-H phases, and metastable $LaBH_{17}$, $LaGaH_6$, $LaGaH_{14}$, and $LaGaH_{15}$ phases. La, B, N, Ga and H atoms are shown as green, orange, gray, red, and blue spheres, respectively. Polyhedral surfaces match the color of the bonding atom. In $LaGaH_{14}$ the 001 lattice plane is shown to highlight the planar nature of the hydrogen network.

7.2.2 Crystal Structures

Fig. 7.2 shows the crystal structures for the La-B-H, the La-N-H system, as well as the metastable $LaGaH_6$, $LaGaH_{14}$, and $LaGaH_{15}$ structure. The La_4N_4H and La_2N_2H structures exhibit both a cubic La-N sublattice with CsCl arrangement, where hydrogen occupies the interstitial sites and are distant from each other (3.6 and 2.4 Å, respectively). In LaN_2H_3 on the other hand, the

structure presents La layers, alternated with a N-H network with a shorter H-H distance (1.4 Å), while LaN_3H_{10} is characterized by H_2, NH, NH_2, and NH_3 molecules scattered unorderedly around the La atom. Other metastable phases with high hydrogen content also contain disordered H_2 and NH_x molecules ($x = 1, 2, 3, 4$).

The LaB_8H phase presents a dense covalent B-B network, which forms a cylindrical cage around a La atom. This structure is identical to one predicted for LaB_8, with the addition of a hydrogen atom in the interstitial site between two second-nearest La atoms. Here, hydrogen atoms are far apart from each other, with a distance of 3.7 Å. The $La_2B_6H_5$ structure contains two polymeric chains of BH_2 and B_2H_2, linked by a hydrogen atom in common, with a H-H distance of 1.4 Å. The $LaBH_8$ phase is characterized by a close-packed structure formed by a rock-salt La-B sublattice, with eight hydrogen atoms sitting in the interstitial sites. The hydrogen sublattice forms a rhombicuboctahedron around the La atom, and a cube around the B atom. La, B, and H atoms occupy the $4b$, $4a$, and $32f$ Wyckoff positions, respectively. This phase is particularly interesting, as the La sublattice (*fcc*) is identical to that of LaH_{10}, and also exhibits the same lattice parameter. This phase turned out to remain stable down to much lower pressure, and was object of a more focused study. I discussed it in more detail in Section 7.3. Among the metastable phases, I show one with $LaBH_{17}$ composition. The crystal structure exhibits an orthorhombic lattice (α-$LaBH_{17}$), with a polyhedral cage of 32 H atoms around a central La atom. Cages are stacked along the vertical axis, and share a distorted hydrogen hexagon (H-H distance of 0.95 Å). The cages alternate with B_2H_{10} molecules. A higher pressure removes the distortions: at 500 GPa this structure transitions to one with a tetragonal Bravais lattice which is almost degenerate in enthalpy, but presents a higher symmetry (β-$LaBH_{17}$). This effect is probably similar to the one reported for both H_3S and LaH_{10}, where a high-symmetry phase is preceded by slightly distorted ones at lower pressures. In H_3S and LaH_{10} the inclusion of anharmonicity and quantum fluctuations was shown to lower this stabilization pressure [133, 143].

The metastable $LaGaH_6$ structure presents a tetragonal Bravais lattice. The Ga atoms are encased in a rectangular cuboid with hydrogen on the vertexes. The cuboids share a square face with another polyhedron centered in La, with six squared, two hexagonal, and eight rhomboid faces. The shortest H-H distance is in the rhomboid faces, where it is 1.1 Å. $LaGaH_{14}$ presents an orthorhombic lattice in which a dense hydrogen network is sandwiched between La and Ga planes. The H-H distance ranges between 0.9 and 1.2 Å. The $LaGaH_{15}$ structure presents two interpenetrating La and Ga body-centered tetragonal lattices, with a dense hydrogen network around them, and a H-H distance ranging from 0.9 to 1.2 Åas well. Since the three structures exhibit rather similar properties, in the following I will only show the results for $LaGaH_{14}$. A summary of the properties of $LaGaH_6$ and $LaGaH_{15}$ is shown in Tab. 7.2.

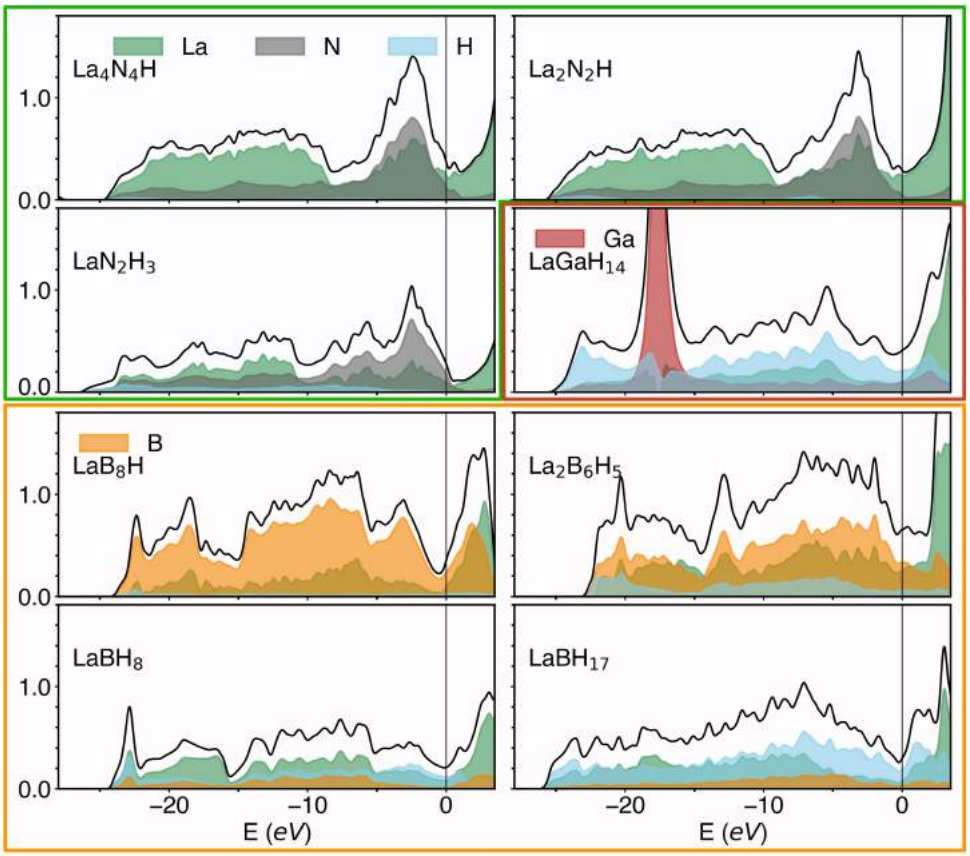

Figure 7.3: Total and atom-projected DOS in units of $spin^{-1}eV^{-1}$ for stable La-N-H, La-B-H phases, and metastable $LaBH_{17}$ and $LaGaH_{14}$ at 300 GPa. The total DOS and its projection onto La, N, B, Ga, and H are shown as black lines, and green, gray, orange, red, and blue filled lines, respectively. The Fermi energy is set as the zero.

7.2.3 Electronic Structure

In Fig. 7.3 I show the total and atom-projected Density of States (DOS) for the metallic La-B-H and La-N-H structures[1], and $LaGaH_{14}$. In La_4N_4H and La_2N_2H, the DOS presents a prevalent La and N character, with no significant contribution from hydrogen. Also LaN_2H_3 the hydrogen contribution is negligible, especially around the Fermi level, where the states are mostly N-derived. LaN_3H_{10} (not shown) is insulating, with a PBE band gap of 2.4 eV. The absence of high-symmetry, hydrogen-rich structures, with a large fraction of H-derived states at the Fermi level indicate that La-N-H compounds do not tend to form superconducting hydrides, as they do not exhibit any of their typical characteristics.

Among the La-B-H structures, the electronic behavior changes significantly with the hydrogen content. In LaB_8H and $La_2B_6H_5$, the partial DOS exhibits a strong B character, with a larger La contribution in the second. In both cases, hydrogen does not play a significant role in the electronic structure, and does not contribute to the states at the Fermi level. In $LaBH_8$ and $LaBH_{17}$, on the other hand, where the hydrogen concentration is higher, the partial DOS presents a stronger hydrogen character. In particular, in $LaBH_8$ the H-derived states contribute significantly in a window of 5 eV around the Fermi level, and the rest of the states derive from lanthanum. Between -25 and -5 eV, the contribution of La and B states is also important, and the similar trend in the projected DOS suggests some degree of covalent bonding. In $LaBH_{17}$ the hydrogen contribution is stronger, while the role of boron appears to be marginal. $LaBH_8$ and $LaBH_{17}$ are reminiscent of binary superhydrides: a high-symmetry structure, intermediate H-H distances (between 1.0 and 1.6 Å), and a large fraction of H-derived states at the Fermi level.

The $LaGaH_{14}$ structure presents a large hydrogen contribution to all occupied states. At -18 eV a narrow peak originating from Ga-*d* states is visible, but it does not exhibit signs of significant hybridization with other states. The three projected DOS's are similar in the -15 to 0 eV range, suggesting hybridization between all three elements. Around the Fermi level the hydrogen contribution is large, consisting of about 60% of the total.

7.2.4 Vibrational Properties and Superconductivity

In order to establish whether any of the newfound phases could be a *hot* superconductor, for each structure I calculated the Éliashberg function using Density Functional Perturbation theory, and used it to numerically solve the isotropic Migdal-Éliashberg equations, which is a more accurate approach in the case of strong coupling ($\lambda \gg 1$), the McMillan formula tends to underestimate the T_c [61]. In Table 7.1 I show a summary of the electronic and superconducting properties for each phase. As anticipated, La-N-H structures are all characterized by an extremely low hydrogen fraction at the Fermi level, and even the metallic ones bad superconductors. Among the La-B-H

[1] LaN_3H_{10} is insulating.

and La-Ga-H compositions, on the other hand, I do find high-T_c in $LaBH_{17}$ and $LaGaH_{14}$. The T_c is higher than 100 K in both cases. This is, however, far too low to explain the observed *hot* superconductivity, calling for further experimental studies which can give some more details on the composition of the supposed *hot* superconductor.

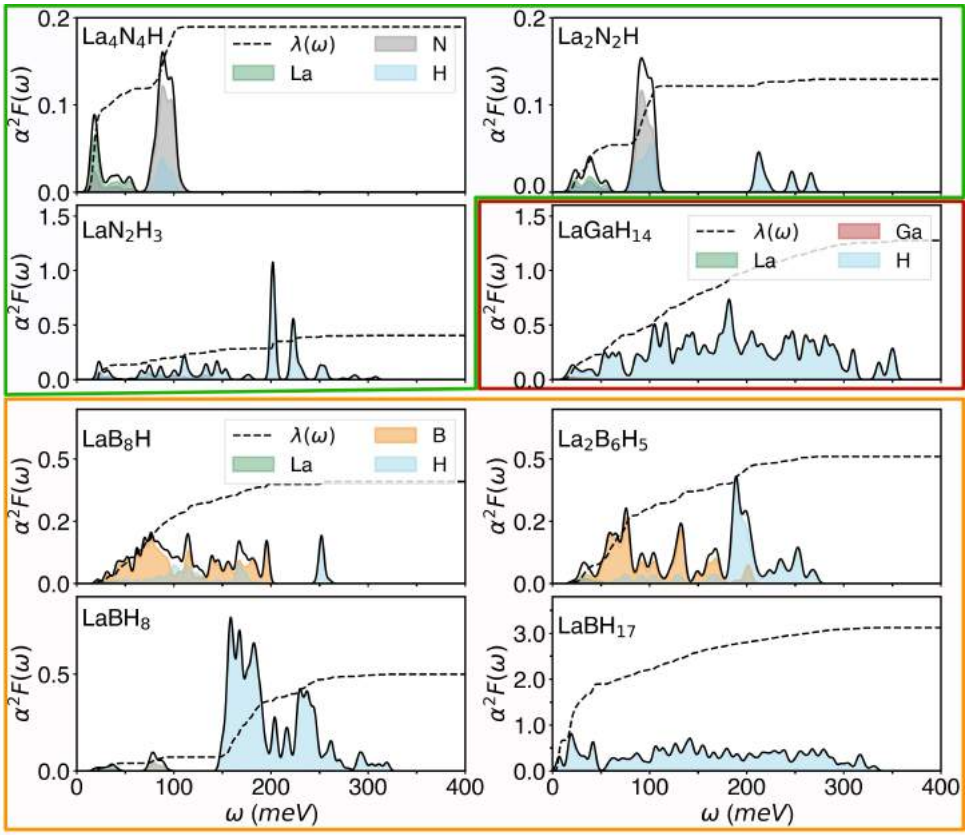

Figure 7.4: Total and atom-projected Eliashberg function [$\alpha^2F(\omega)$, solid lines], and ω-dependent *e-ph*coupling [$\lambda(\omega)$, dashed lines] for stable La-B-H and La-N-H hydrides, and metastable $LaGaH_{14}$ and $LaBH_{17}$. The atom projections on La, B, N, Ga, and H are shown in green, gray, orange, red, and blue, respectively. The Eliashberg function and ω-dependent *e-ph*coupling $\lambda(\omega)$ are defined in the Supplemental Material. **Note:** due to the large differences in values, the y-axis scale is different for each subfigure.

In Fig. 7.4 I report the atom-projected and the total Éliashberg function, along with the frequency-dependent coupling coefficient $\lambda(\omega)$, for the metallic La-B-H, La-N-H phases, and for $LaGaH_{14}$. As shown, in La_4N_4H and La_2N_2H the coupled states derive mostly from nitrogen, and the total coupling is extremely small. In La_4N_4N there are also no states above 200 meV, indicating that in this structure purely hydrogen modes are entirely absent. In LaN_2H_3, the coupled states exhibit an almost pure hydrogen character, but the total coupling is extremely small. The whole spectrum is characterized by narrow peaks between 100 and 250 meV, indicating the presence of dispersionless molecular vibrations.

In LaB_8H boron contributes to most of the *e-ph* spectrum, while in $La_2B_6H_5$ about 30% of the

contributions derive from hydrogen. In these two structures the hydrogen content is low, and the B-B bonds characterize both the electronic and vibrational spectrum. Overall, the integrated coupling is around 0.5. In $LaBH_8$ and $LaBH_{17}$ the *e-ph* spectrum is quite different. In these structures all of the coupling derives from hydrogen modes; in $LaBH_8$ all the coupled modes are concentrated in a region around 200 meV, leading to a very high $\omega_{\log}$, and a small λ. In $LaBH_{17}$ the spectrum is strongly coupled at all energies, and is entirely H-derived. At 300 GPa, α-$LaBH_{17}$ is close to a dynamical instability, as suggested by the large λ, and the small $\omega_{\log}$ (values shown in Table 7.2). At higher pressures the instability disappears, but the increase in $\omega_{\log}$ is compensated by a decrease in λ which leaves the T_c unchanged. $LaGaH_{14}$, similarly to $LaBH_{17}$ exhibits a significant *e-ph* coupling at all energies, as witnessed by the rather linear increase of $\lambda(\omega)$ between 0 and 200 meV. $LaGaH_6$ and $LaGaH_{15}$ behave similarly to $LaGaH_{14}$, although in $LaGaH_6$ the lower hydrogen content reflects in a smaller total coupling. The even contribution of coupling across a large energy range indicates that in $LaBH_8$ $LaBH_{17}$, $LaGaH_6$, $LaGaH_{14}$, and $LaGaH_{15}$, superconductivity originates from the whole hydrogen sublattice, rather than from a single, strongly-coupled mode.

Comp.	S.G.	ΔH $\frac{meV}{atom}$	d_{H-H} (Å)	N(E_F) ($\frac{1}{2}10^3 eV^{-1}Å^{-3}$)	$N_H/N(E_F)$	λ	ω_{log} (K)	T_c^{ME} (K)
La_4N_4H	38	0	3.6	16.9	1%	0.24	434	0
La_2N_2H	63	0	2.6	4.2	3%	0.15	719	0
LaN_2H_3	66	0	1.4	10.3	1%	0.33	966	1
LaN_3H_{10}	1	0	0.74	-	-	-		-
LaB_8H	5	0	3.7	8.3	4%	0.44	973	8
$La_2B_6H_5$	8	0	1.5	12.0	21%	0.47	998	6
$LaBH_8$	225	0	1.33	7.4	62%	0.53	1731	14
α-$LaBH_{17}$	23	33	0.95	7.8	63%	3.3	414	180
LaH_{10}	225	0	1.06-1.14	16.4	62%	1.9	1575	249
$LaGaH_6$	71	12	1.13	6.0	20%	0.63	845	21
$LaGaH_{14}$	35	13	0.89-1.17	10.5	52%	1.25	1134	137
$LaGaH_{15}$	44	11	0.90-1.10	11.7	57%	0.90	1338	95

Table 7.1: Electronic and superconducting properties of selected ternary phases of La-N-H and La-B-H, plus high-symmetry metastable La-Ga-H structures, at 300 GPa. The first column shows the composition, the second column indicates the space group. The fourth column ΔH indicates the enthalpy difference from the convex hull (0 if the structure is *on* the hull). d_{H-H} indicates the average H-H distance in Ångstrom. In the sixth and seventh column the electronic DOS at the Fermi level N(E_F) and its relative hydrogen character are reported. The DOS is shown per unit volume to allow for comparison between different pressures. The electron-phonon coupling coefficient λ and the average phonon frequency ω_{log} are defined in the Supplemental Material. The superconducting critical temperature T_c^{ME} was calculated by solving the isotropic Migdal-Eliashberg equations – for details see the Supplemental Material. $*$ the structure is dynamically unstable near the M point. $**$ cutting imaginary frequencies.

The distance from the convex hull, H-H distance, DOS at the Fermi level, hydrogen fraction of the DOS, λ, $\omega_{\log}$, and T_c for the phases discussed are summarized in Table 7.1. None of the phases exhibits a T_c higher than 200 K, hence none are likely candidates for *hot* superconductivity. As an

additional check, I tried to qualitatively estimate whether some kind of doping effect could increase the T_c of the predicted La-B-H phases. Indeed, in $LaBH_{17}$ the Fermi energy lies in a pseudogap, and an electron doping could increase significantly the DOS at the Fermi level. In an optimistic scenario, I considered a 50% substitution of boron with carbon, corresponding to a doping of $0.50e^-$ per formula unit. This would increase the DOS at the Fermi level by a factor of two. Assuming that as a result the Éliashberg function also doubled, the T_c would increase to about 290 K. This would be a above room temperature, and a remarkable result, but is still far from the 556 K reported. Similar arguments also apply to $LaGaH_{14}$.

7.3 Part II: $LaBH_8$, a low-pressure high-T_c ternary hydride

In Section 7.2, I discussed the *ab initio* study of six La-X-H hydrides at 300 GPa. During this study, I predicted the formation of a structure with $LaBH_8$ composition at 300 GPa, characterized by a peculiar high-symmetry, hydrogen-rich structure. In the previous Section I studied $LaBH_8$ at 300 GPa, where it was characterized by a low T_c. Upon relaxation to lower pressures, however, I notice that this structure remained dynamically stable, and it T_c increased up to about 126 K at 50 GPa. The low stabilization pressure motivated me to study the La-B-H compound with more detail. Interestingly, a structure with an identical M-B sublattice was observed with neutron diffraction on MBH_4 (M = K, Rb, Cs), which only differs by the 1/2 occupancy of the 32f site by hydrogen [275].

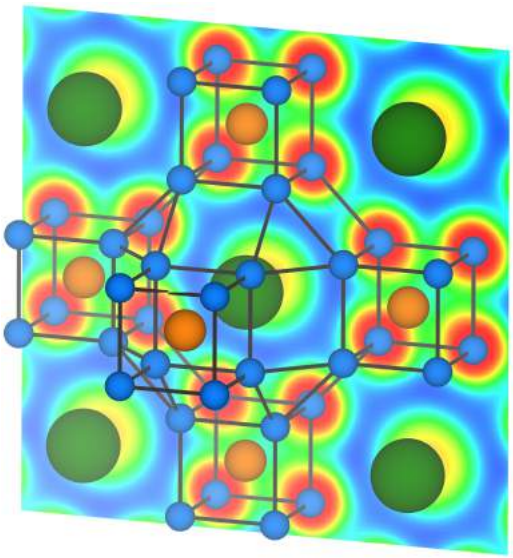

Figure 7.5: Crystal structure of the $Fm\bar{3}m$ phase of $LaBH_8$ (conventional unit cell). La, B, and H atoms are shown as green, orange, and blue spheres, respectively. The Electron Localization Function (ELF) is projected onto the $\bar{1}00$ plane.

7.3.1 Convex hull at 100 GPa

I performed a structural search for the La-B-H system at 100 GPa, where I expected the $LaBH_8$ to be still stable, but also insulating, low-pressure phases to be competitive, based on the experience gained in studying the Ca-B-H system (See Chapter 6), where metallic phases only appeared above 110 GPa. To sample the convex hull as accurately as possible with a reasonable amount of resources, I followed the procedure described by Kvashin et al. [276], which is summarized below:

1. Perform a variable-composition evolutionary search with no restrictions (except the maximum cell size, which was set to 40 atoms). For this search I considered 50 generations with 360 individuals in the first and 250 in the others, for a total of about 12000 structures sampled

2. Re-sample promising binary and pseudo-binary phases: $(LaB)_xH_{1-x}$, La_xH_{1-x}, B_xH_{1-x}, La_xB_{1-x}, for 20 generations with 160 individuals in the first and 60 in the others, for a total of about 1200 structures sampled for each search. Construct a preliminary convex hull.

3. Re-sample specific compositions which are either stable in the preliminary convex hull, or are suggested by the standard rules of chemistry. In particular, I considered $LaBH_8$, $La(BH_2)_3$, $La(BH_3)_3$, and $La(BH_4)_3$. I used a number of atoms corresponding to four formula units, and sampled a total of 20 generations, with 80 individuals in the first, and 60 in the others, for a total of 1200 structures more sampled for each search

4. Perform a second variable-composition evolutionary search, using all the stable structures found in the previous steps as seeds, with a maximum cell size of 40 atoms, sampling for 20 generations, with 250 individuals in each generation, for a total of 5000 structures sampled

5. Collect all the results from the previous search, and construct a second preliminary convex hull. Then, retaining all the structures that were on, or close to, the convex hull, I re-relaxed them with better convergence, and compute the zero-point energy (ZPE). The ZPE was computed by calculating the dynamical matrix at the Γ point only, and using Fourier interpolation to calculate the phonon density of states

6. Add the ZPE to the calculated enthalpies, and construct the final version of the convex hull. The convex hull was constructed using `pymatgen` [277]

In Fig. 7.6 I report the convex hull resulting from the procedure described above. There are four stable compositions: $La(BH_2)_3$, $La(BH_4)_3$, $LaBH_5$, and $LaBH_8$, crystal structures corresponding to these four compositions are shown in Fig. 7.7.

The ground-state structures for the $La(BH_2)_3$ and $La(BH_4)_3$ compositions are characterized by the same molecular, hydrocarbon-like structures already reported for other metal borohydrides [8, 267, 278–280], and analogous to those described in Chapter 6. The structure with $LaBH_5$

composition is characterized by a La-B rocksalt sublattice, and BH_4^- anions, with an additional H atom trapped in the interstitial site of a La tetrahedron. For the $LaBH_8$ composition, the predicted ground-state structure ($P1$ space group) is characterized by a disordered mixture of BH_4^- anions, H_2 molecules, and isolated H atoms. The $LaBH_8$ $Fm\bar{3}m$ phase, described in detail in Section 7.2, was lying only 23 meV/atom above the hull. In Fig. 7.5 I report again the $Fm\bar{3}m$-$LaBH_8$ structure along with the projection of the Electron Localization Function (ELF) onto the $\bar{1}00$ plane, which cuts through one of the faces of the hydrogen cubes around boron. The ELF remains high all along the H-H bonds, while it is smaller along La-H and B-H bonds, indicating that the bonding between these two pairs is less significant. The fact that boron and hydrogen, despite their proximity, do not seem to form a covalent bond is quite unusual. The presence, on the other hand, of a metallic H-H bond suggests that this hydride is similar to sodalite-like hydrides, such as LaH_{10}. According to this interpretation, the La-B sublattice acts as a scaffolding which mechanically confines hydrogen atoms in a small volume [121, 147], with a mechanism that has been intuitively named *chemical pressure* [28]. Indeed, $LaBH_8$ has exactly the same La sublattice as LaH_{10} (face-centered cubic), with the addition of boron atoms filling the interstices between second-nearest La atoms, and increasing the packing fraction by almost 10%. This extremely efficient packing of the $LaBH_8$ is the key to the low-pressure stabilization of the metallic hydrogen sublattice.

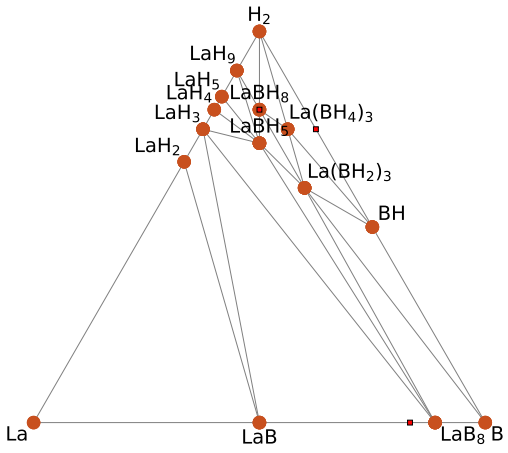

Figure 7.6: Convex hull for the La-B-H system at 100 GPa. Stable compositions are shown as orange dots.

The structures for $La(BH_2)_3$ and $La(BH_4)_3$ are insulating, analogously to other metal borohydrides, while $LaBH_5$ and $Fm\bar{3}m$-$LaBH_8$ are metallic and superconductive.

7.3.2 Stability of $LaBH_8$ $Fm\bar{3}m$ structure

As mentioned before, the $Fm\bar{3}m$-$LaBH_8$ phase is not the ground state structure at 100 GPa, but it lies only 23 meV/atom above the hull, and becomes thermodynamically stable above 110 GPa. In the last two columns of Tab. 7.2, I report the enthalpy difference between the $Fm\bar{3}m$ phase and the convex hull (ΔH_{H}), and between the $Fm\bar{3}m$ and the pure elements (ΔHe). Both values are negative above 110 GPa, as the $Fm\bar{3}m$ phase forms spontaneously above that pressure. At lower pressures the decomposition into pure elements remains unfavorable, but

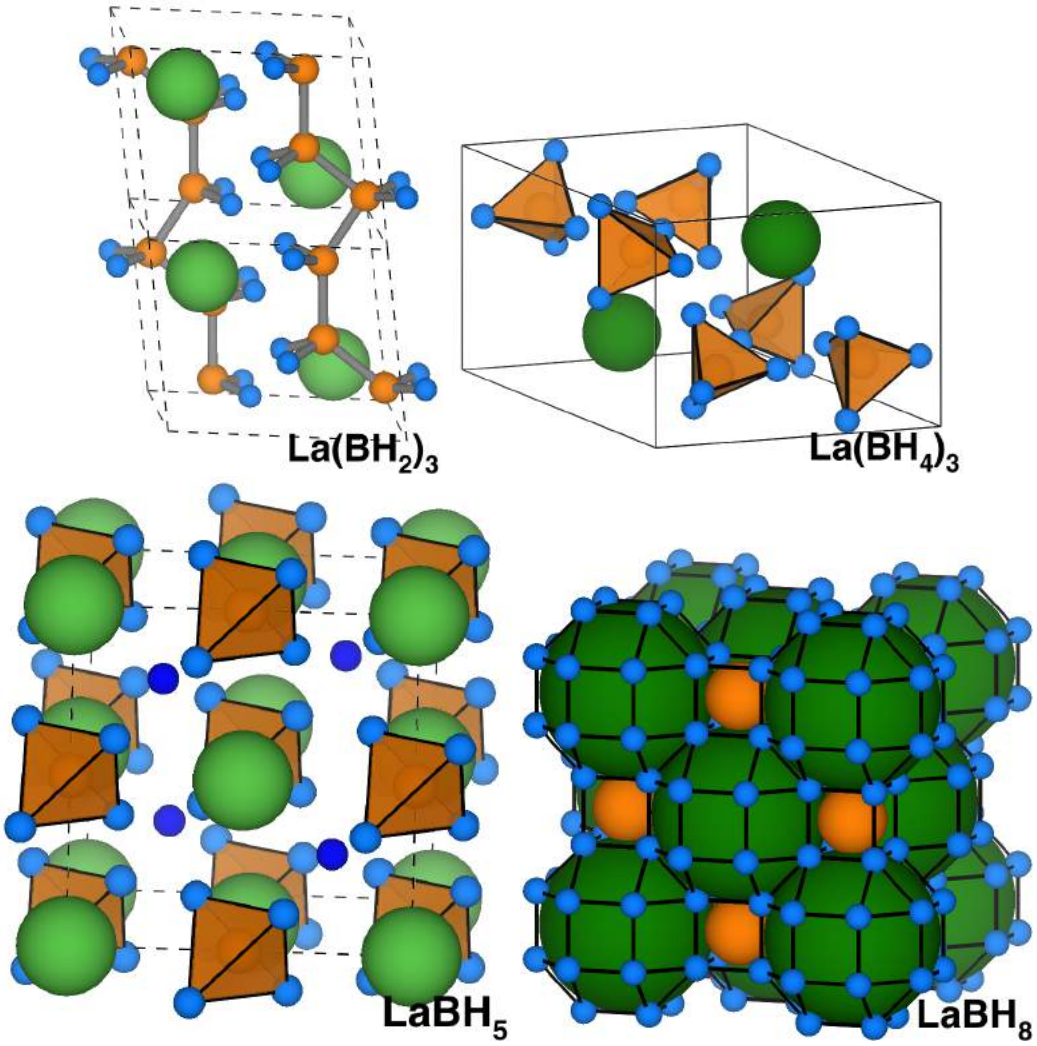

Figure 7.7: Crystal structures of $P2_1/m$-$La(BH_2)_3$, $P6_3m$-$La(BH_4)_3$, $Fm\bar{3}m$-$LaBH_5$, and $Fm\bar{3}m$-$LaBH_8$.

the distance from the convex hull increases up to 125 meV/atom at 50 GPa. While thermodynamical stability implies that the structure will form, it does not say whether it can remain metastable at lower pressures; the stability with respect to decomposition into pure elements, however, is a necessary condition. I calculated the dynamical stability, and found that it is stable down to 40 GPa. Albeit not conclusive, the dynamical stability is an indication that metastability is possible, as it represents a necessary (but not sufficient) condition.

I suggest that the phase could be synthesized at high pressure and quenched down to 40 GPa, thanks to a pressure hysteresis mechanism [281]. A recent computational study by Sun et al. [282] proposed a condition for pressure hysteresis to take place; the authors introduced the idea that a phase which is stable under some thermodynamical conditions can remain (meta)stable, even when its enthalpy is considerably higher than the ground state. This condition does indeed apply to $Fm\bar{3}m$-$LaBH_8$, and it is not unusual in nature to observe metastable structures even with high enthalpy values: black phosphorous [281], or even diamond are examples, in which the metastable phase has an enthalpy hundreds of meV/atom higher than the minimum. Given all the above, even though a quantitative technique for determining the lowest pressure has not been developed, I realistically can consider the structure metastable to a pressure much lower than 110 GPa, and higher than 40 GPa.

Although I cannot determine the minimum pressure at which this phase can be retained, these indications, and the analogy with other superhydrides that were synthesized at pressures lower than predicted, suggest that it should in fact be possible to retain this structure down to pressures in the 50-70 GPa range.

7.3.3 Electronic Structure

In this section I will discuss the electronic properties of $Fm\bar{3}m$-$LaBH_8$ at 50 GPa. I chose this pressure for the discussion because it is where the structure exhibits its high T_c at low pressure, but it is still not too close to the dynamical instability to suffer from strong anharmonic effects. In Fig. 7.8 I report the electronic bands, colored with their hydrogen character, and the atom-projected DOS. In the -20 to -15 eV range, the electronic states exhibit a strong La-5p character, while in the -15 to -5 eV range, the character is B-2s and 2p, and H-1s. The hydrogen character becomes predominant in the -5 to 1 eV range, crossing the Fermi level, where over 60% of the electronic states have H character; the rest comes from the nearby of La-4f states, which are mostly located above the Fermi level.

A band structure formation analysis can bring further insight in the details of the electronic structure. In this analysis, I remove one or more elements from the crystal structure, and recompute the bands. The results provide a sort of *deconstruction* of the band structure, whence I can deduce which elements contribute to their overall shape. In Fig. 7.9 I show a comparison of the $LaBH_8$

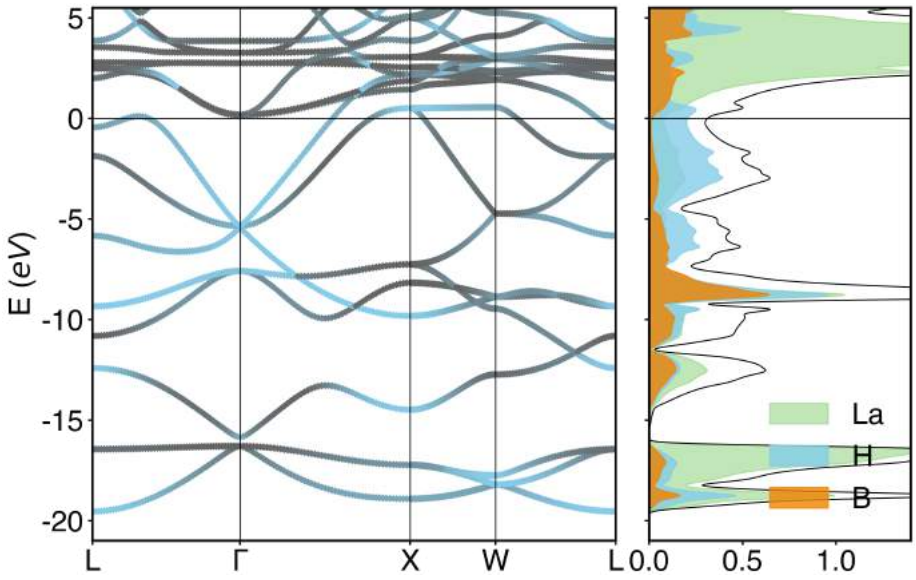

Figure 7.8: Left: electronic band structure of $Fm\bar{3}m$ $LaBH_8$ at 50 GPa, decorated with hydrogen character (blue) vs non-hydrogen character (gray). Right: atom-projected density of states in units of $eV^{-1}spin^{-1}$. Projection onto La, B, and H is shown in green, orange, and blue, respectively. The zero of the energy scale is the Fermi level.

lattice with the LaH_8, BH_8, H_8, and "empty" sublattices. The *empty* lattice approximation shows the free electron behavior, only with the addition of the lattice periodicity. The first thing to observe is that the $LaBH_8$ and LaH_8 bands only differ by a small rearrangement in the -10 to -5 eV range, but both the low-lying states and the states near the Fermi level are very similar. This observation suggests that boron has a small influence on the electronic structure, and only in a narrow energy range, which is away from the Fermi level. Moving on to the BH_8 and H_8 bands, one can see that they differ from $LaBH_8$ in the -20 to -10 and 1 to 5 eV energy ranges, but five bands in the -5 to 0 eV range are present in the H_8 sublattice, hence directly derive from it, and can be easily also identified in the $LaBH_8$, where they remain unperturbed. I conclude this analysis pointing out that while La and B do influence the low-lying occupied and the unoccupied states, all the states around the Fermi level derive from the H sublattice, and are mostly unperturbed. This picture is coherent with a Bader charge analysis [283], which assigns a total charge of +1.5 to La, +0.9 to B, and -0.3 to each H. Charge transfer from B to H is unusual, as in normal conditions the two elements have very close electronegativity, and is a peculiar feature of this structural configuration.

To conclude the description of the electronic structure, in Fig. 7.11 (left panel) I report the Fermi surface, decorated with H character. In the left panel of Fig. 7.11 I show the Fermi surface decorated with H character. It consists of four sheets, all of which have hydrogen character of at least 50%: 1) an electron-like, spherical sheet centered in Γ, which is the largest of the four, 2) a cross-like sheet going from X to W, 3) a small hole pocket centered in the X point, and 4) another hole pocket centered in the L point.

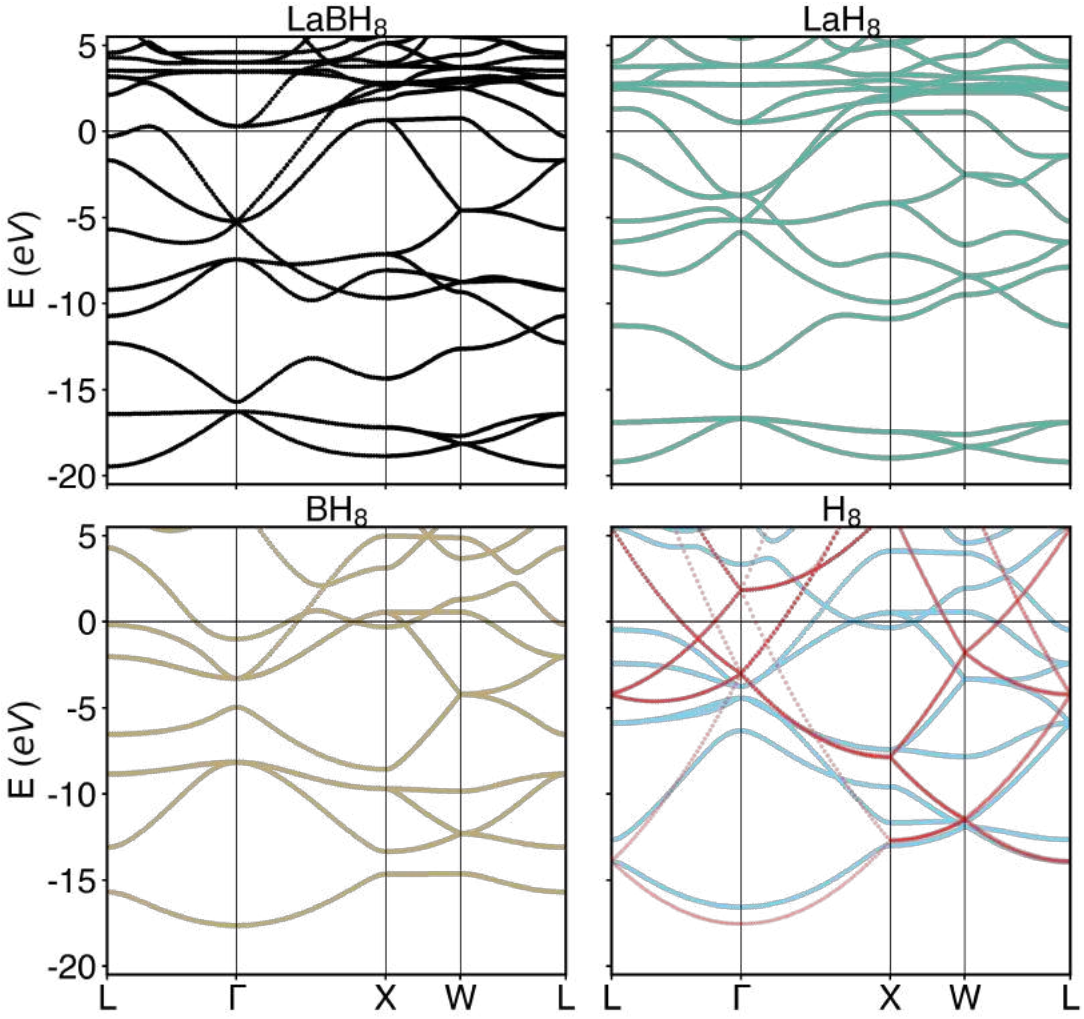

Figure 7.9: Band structure formation for $Fm\bar{3}m$-$LaBH_8$ at 50 GPa. Each panel shows the band structure for the $Fm\bar{3}m$ structure, where one or more element were removed,. Top left: $LaBH_8$, top right: LaH_8, bottom left: BH_8, bottom right: H_8 (blue) and empty lattice approximation (red).

7.3.4 Superconductivity

In this section, I will describe the vibrational and superconducting properties of the $Fm\bar{3}m$-$LaBH_8$ phase, computed using Density Functional Perturbation theory, within the harmonic approximation, and interpolating the *e-ph* matrix elements on a very fine $\vec{k}$ and $\vec{q}$ grid using Wannier interpolation, as implemented in `EPW` [25, 220, 227]. In order to make the calculation truly *ab initio*, I also computed the Morel-Anderson pseudopotential μ^* [210], as defined in eq. (B.19); the value of the average screened Coulomb interaction μ was calculated with the random phase approximation, as implemented in the `SternheimerGW` code [240, 250, 255, 284]. At both 50 and 100 GPa, I find μ^*=0.09, close to the commonly used value of 0.10, and in agreement with the value calculated for YH_6 and YH_{10} [7].

In Fig. 7.10 I report the phonon dispersions decorated with the mode-resolved *e-ph* coupling $\lambda_{\nu\vec{q}}$, the atom-projected Éliashberg function with the frequency-dependent *e-ph* coupling coefficient $\lambda(\omega)$, and the phonon DOS. The contribution of the three elements (La, B, H) to the phonon spectrum is well separated into four parts: 1) the low-energy modes (0 to 30 meV), which exhibit a predominant La character, and give almost no contribution to the total *e-ph* coupling; 2) the mid-low energy modes (30 to 60 meV) of predominantly B character; 3) the mid-high energy modes (60 to 150 eV) of predominant H character, which contribute the most to $\lambda(\omega)$; and 4) the high-energy modes (above 150 meV), of pure hydrogen character, which contribute less to the total coupling due to their high frequency. The B contribution to the phonon DOS is all concentrated in the mid-low energy range, and comes from a single, triply-degenerate, dispersionless branch, which carries very little coupling, as indicated by the negligible contribution of boron to the α^2F. A dispersionless phonon branch is suggestive of noninteracting atoms, and supports the idea that boron is not actively participating in superconductivity.

The *e-ph* coupling is spread over several modes in the mid-high energy region, across the whole Brillouin zone. The exception is a mode at the Γ point with T_{2g} symmetry, which I will refer to as T^*_{2g}. This mode corresponds to a distortion of the tetrahedron formed by nearest-neighbor H atoms, and gives rise to a single, narrow peak in the Éliashberg function around 50 meV. The strongly coupled T^*_{2g} mode is however very localized in reciprocal space, so it only contributes to around 15% of the total coupling (λ). The picture that emerges from this analysis confirms the idea that in $LaBH_8$ superconductivity arises from the H sublattice only, while La and B passively act to stabilize it.

In Tab. 7.2, I summarize the superconducting properties of $LaBH_8$ at 50, 75, and 100 GPa. The two values for T_c, T_c^{AME} and T_c^{IME} represent the T_c obtained from the numerical solution of the anisotropic and isotropic Migdal-Éliashberg equations, respectively [227]. At all pressures the two values are extremely close, suggesting that the gap anisotropy is limited. Indeed the superconducting gap, shown in the right panel of Fig. 7.11, is rather uniform over the Fermi

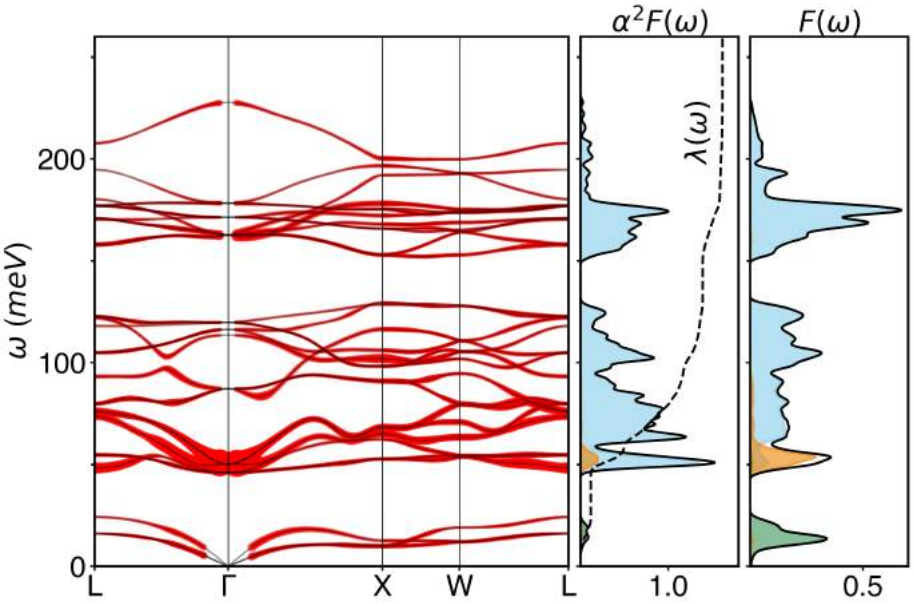

Figure 7.10: Left panel: phonon dispersions of $LaBH_8$ at 50 GPa (black thin lines), decorated with the *e-ph* coupling (red thick lines). Center panel: atom-projected (colored filled lines) and total (black line) Eliashberg function, and its first inverse moment $\lambda(\omega)$ (dashed black line). Right panel: atom-projected (colored filled lines) and total (black line) phonon density of states. Projection onto La, B, and H is shown in green, orange, and blue, respectively.

surface except for a *hotspot* on the pocket centered around L, which carries very little weight in reciprocal space. Considering the average value of the superconducting gap, I obtain a BCS parameter $2\Delta_{\rm iso}(0)/T_c$ of 4.3 at 50 GPa, which confirms that $LaBH_8$ is in the strong-coupling regime.

At pressures higher than 50 GPa, the main difference in the phonon spectrum is a uniform increase of phonon frequencies. This effect causes a decrease of the coupling λ. The average frequency ω_{log} slighlty decreases at 100 GPa, due to a strong pressure-induced hardening of the T^*_{2g} mode, which decreases its *e-ph* coupling. At low pressure, the T^*_{2g} mode is strongly anharmonic, as

P GPa	$N(E_F)$ eV^{-1}	λ	$\omega_{\rm log}$ meV	$T_c^{\rm AME}$ K	$T_c^{\rm IME}$ K	$\Delta_{\rm iso}$ meV	$\Delta H_{\rm H}$ meV/at	$\Delta H_{\rm e}$ meV/at	$2\Delta/T_c$ [a]
50	0.62	1.54	71	126	122	23.5	125	-247	4.3
75	0.60	1.06	91	101	96	16.8	71	-308	3.9
100	0.56	0.64	88	42	32	5.6	23	-337	3.1

Table 7.2: Summary of the main superconducting properties of $LaBH_8$ at 50 and 100 GPa. The DOS at the Fermi level $N(E_F$ in the second column is in units of $eV^{-1}spin^{-1}$. *AME* and *IME* correspond to solutions of the anisotropic and isotropic Migdal-Eliashberg equations, respectively, with $\mu^* = 0.09$. $\Delta_{\rm iso}$ represents the isotropic average of the superconducting gap. $\Delta H_{\rm H}$ and $\Delta H_{\rm e}$ indicate enthalpy differences, including zero-point, of the $Fm\bar{3}m$ phase with respect to the ternary hull, and pure elements.

[a] BSC theory predicts the *universal* value $2\Delta/T_{\rm c} = 3.5$

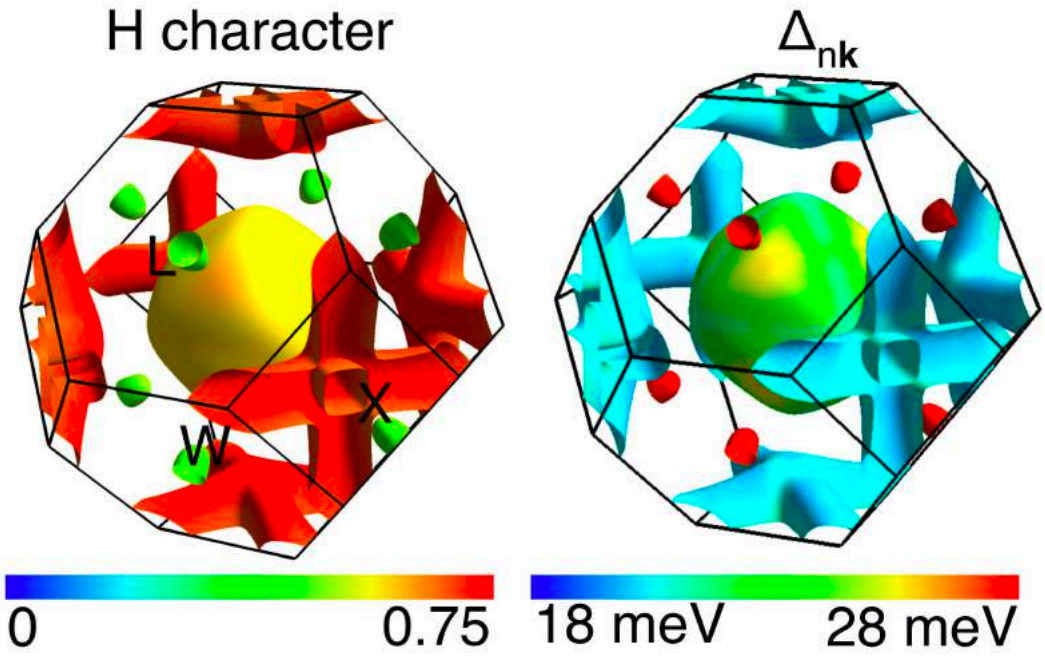

Figure 7.11: Fermi surface of $LaBH_8$ at 50 GPa. Left: decorated with hydrogen character, right: decorated with the value of the superconducting gap. The color scale goes from zero to the maximum value of the H character (0 to 0.75), and the gap (0 to 28 meV), respectively.

it is also the mode which drives the dynamical instability, which occurs around 35 GPa.

In general, anharmonic and quantum effects are demonstrated to strongly affect the stability and the superconductivity of hydrides [133, 143], as the very small mass of hydrogen the proton implies that the Born-Oppenheimer approximation is much worse than in other elements. To estimate the role of anharmonicity in the stability of $LaBH_8$, I recomputed the T^*_{2g} phonon frequency at various pressure using the frozen-phonon approach described by C. Heil et al. in Ref. [240]; the results are shown in Fig. 7.12. As shown, anharmonicity causes a reduction of about 10 meV in the frequencies, which reflects in to an increase of about 5 GPa in the stabilization pressure, which occurs at 40 GPa. The effect on the critical temperature is minor: if the coupling from the T^*_{2g} mode is entirely removed, the T_c changes by about 10 K, indicating that anharmonicity does not strongly affect the superconducting properties.

7.4 Conclusions

In conclusion, inspired by the experimental report of *hot* superconductivity [51], I calculated the stable compositions in the six La-X-H ternary hydrides (X = B, N, Ga, C, Au, Pt) where the hot superconductor was more likely to be found, using evolutionary algorithms for crystal structure prediction. The choice of La-based ternary hydrides was motivated by the experimental report, where a T_c compatible with LaH_{10} was measured at first, and the other elements are chosen as they

were all present in the Diamond Anvil Cell during the experiment. I found no stable phases for C, Au, Pt, and a few metastable ones for Ga (but none stable). In La-B-H and La-N-H I did find several stable ternary compositions: $LaBH_8$, La_2B_6H5, and LaB_8H; and La_4N_4H, La_2N_2H, LaN_2H_3, and LaN_3H_{10}. In addition, I found a metastable $LaBH_{17}$ which exhibits structural features typical of superconductors (high hydrogen content, intermediate H-H distance). I computed the T_c for all the stable phases, and a few of representative metastable ones, by numerically solving the isotropic Migdal-Éliashberg equations. I found the highest T_c's in two structures with $LaGaH_{14}$ (137 K) and $LaBH_{17}$ (180 K), which are way too low to explain the observed *hot* superconductivity, calling for further experimental studies. The fact that both La-B-H and La-Ga-H form high-T_c hydrides suggests that elements from the 13^{th} group, to which both B and Ga belong, might promote the formation of hydrogen-rich, superconducting structures, and are worthy of further investigation.

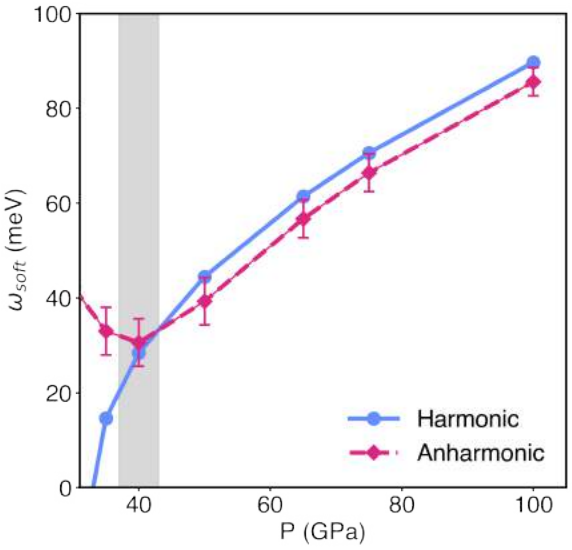

Figure 7.12: Comparison of the harmonic and anharmonic phonon frequency of the T_{2g}^* mode at Γ as a function of pressure. The gray box highlights the region where the dynamical instability occurs.

Among the other phases, I predicted the one with $LaBH_8$ composition to be dynamically stable down to 50 GPa, where it exhibits T_c of 126 K. Following this result, I studied the La-B-H system with more detail down to 100 GPa, performing another, more detailed structural search with variable-composition evolutionary algorithms. I found $LaBH_8$ to be thermodynamically stable above 110 GPa, where it should be possible to synthesize it. Its crystal structure is characterized by an extremely efficient packing, due to a combination of two atoms of different size (La and B) and matching valence, which act as a scaffolding, stabilizing an internal hydrogen sublattice confined therein. I attribute the relatively low stabilization pressure of this structure to this efficient packing, which effectively realizes an example of chemical precompression, similar to the one observed in sodalite-like hydrides.

The prediction of a high-T_c hydride which is dynamically stable at 50 GPa represents an important improvement from the previous record, held by YbH_6 at 70 GPa [285], and the fact that this hydride is characterized by hitherto unexplored structural template is extremely exciting. As it is likely that substitution of other elements in the X and Y sites of the XYH_8 structural template will lead to the discovery of more low-pressure superconductors.

This prediction generated considerable interest in the scientific community [53, 54], as it represents one step towards the low-pressure stabilization of hydride superconductors. Indeed, the structural prototype of $LaBH_8$ leaves room for improvement, as combinations of other elements in the La and B site may optimize its properties, and realize an higher T_c, or a lower stabilization pressure. The perspective of stabilizing a new high-T_c superconductor at ambient pressure, competitive with iron pnictides and cuprates, is indeed extremely exciting.

Half a year after I published these results on arXiv, Liang et al. also published a preprint where they explore the La-B-H phase diagram at 100, 150, 200, and 300 GPa [54] by sampling the La_nB_m (n=1, m=1-6; n=2, m=1) pseudo-binaries, which found the same $LaBH_8$ structure, but did not find any hot superconductor.

Chapter 8

Conclusions and Outlook

In this thesis, I have described my research work on the computational prediction of superhydrides. I had the pleasure to work in a very lively and competitive field, which I saw thrive in front of my eyes.

After more than one century since it was discovered, superconductivity is still the object of intense research. On one side, brilliant theoreticians continue their efforts to understand the microscopic mechanisms that lead to *unconventional* superconductivity for compounds such as cuprates and pnictides, and on the other side, researchers from different backgrounds try to find their holy grail: a high-T_c superconductor at ambient conditions. The fact that this phenomenon continues to draw the attention of so many researchers – and funding agencies! – is not surprising: it is an almost unique example of a macroscopic quantum state, and at the same time a phenomenon which is the key element of many valuable applications. Some are already in use, such as nuclear magnetic resonance or quantum computing, and countless more would become possible with the discovery of a superconductor at room conditions: powerful electromagnets, fusion reactors, lightweight electrical motors, lossless power cables, or even energy storage. Many technological developments depend on the availability of high-T_c superconductors. Finding them has proven to be a difficult task, but recently the scientific community has been doing great progress.

Moreover, in less than one decade, research of conventional superconductivity in hydrogen-rich systems under pressure led to the discovery of several record-breaking high-T_c conventional superconductors, and recently even broke the limit of room temperature, with the measurement of a T_c of 287 K at 267 GPa in a carbonaceous sulfur hydride [6]. In the pursuit of high-T_c superconductivity, first-principles calculations provoked a real *paradigm shift*, and have started to anticipate the experiments. First, the development of crystal structure prediction methods enabled computational physicists to predict whether a certain combination of elements would crystallize at all, and in which form. Second, the use of linear response and Migdal-Éliashberg theory (or SCDFT) also enabled researchers to predict whether a given compound would be a high-T_c superconductor.

Overall, using first-principles calculations it became possible to rapidly explore thousands of hypothetical structures, and to directly indicate the promising materials to the experimentalists. This had lead to a drastic acceleration in the rate of discoveries.

Despite the numerous records broken, hydride-based superconductors are still far from practical applications. The main obstacle is clearly that currently known compounds are only stable at very high pressures, which can only be achieved in laboratory conditions, and samples are extremely small. Nevertheless, there are reasons to be optimistic. The last ten years of research have proven that hydrides are a promising hunting ground, but are very far from having exhausted all possibilities. In particular, the first studies on ternary hydrides have already shown very interesting results, such as the prediction of a *hot* superconductor with Li_2MgH_{16} composition [43], the measurement of room-temperature superconductivity in $C_xS_yH_z$ [6], and the prediction of low-pressure, high-T_c hydride $LaBH_8$, presented in this thesis. With over six thousand possible combinations of elements to choose from, and the possibility to consider even quaternary of more complex hydrides, the future likely holds many surprises. I will now outline some of the most promising directions for future research.

To date, the most pressing goal remains the discovery of a high-T_c superconductor at room pressure, even if not at room temperature. My results on $LaBH_8$ are encouraging and indicate that there is large room for improvement. In fact, while in sodalite-like binary hydrides the superconducting properties were essentially independent from the *guest* atom – Mg, Ca, Y, La – the only tuning parameter being the atomic radius and cage size, ternary structures with dense hydrogen cages like $LaBH_8$ open many more possibilities, as the two guest atoms, La and B, can be changed independently. In analogy with binary sodalite-like clathrates one simple way to identify new potential superconductors would be to consider the XYH_8 structural prototype, and screen via high-throughput methods many possible X and Y candidates, such as X = Mg, Ca, Sr, and Ba and Y = C, Si, Ge, and Sn, just to name a few. Template-based high-throughput screening was applied successfully to ternary *nitrides* [163], and could be equally used on hydrides. The exploration of ternary hydrides is computationally and experimentally challenging, but the recent discoveries demonstrate that it is going to be worthwhile. In order to ease the effort of exploring full ternary phase diagrams, another interesting approach is to improve the efficiency, i.e. identify strategies to reduce the cost of *ab initio* structural searches.

It is likely that research of high-T_c superconductivity in hydrides will continue with the exploration of other ternaries. In particular, combinations of one electropositive atom (alkali metals, alkaline earths, early transition metals) with one from the p block (excluding the most electronegative) seem to be the most promising. However, since the computation of a ternary convex hull is quite costly, an important step will be the identification of some guiding principle to restrict the breadth of the search to the most promising ones. To speed up the calculation of phase diagrams,

for example, one could use a template-based search, directly comparing the enthalpies of a fixed set of *prototypical* structures. This method should enable the rapid identification of pairs of elements which do form stable ternary hydrides, and to efficiently screen out those that do not. I am currently working on a project in this direction. In addition, once a high-T_c ternary hydride is identified, one may attempt to reverse engineer the discovery process, and check whether its structure is stable with other elements, and focus the calculation of the full convex hull for those combinations where that structure is dynamically stable and high-T_c. Moreover, if the amount of data on hydride superconductors keeps growing, and becomes available through data repositories, machine learning approaches based on pattern recognition, or machine-learned interatomic potentials may provide an alternative way to efficiently scan for superhydrides.

Alternatively, high-T_c might also be found in non-hydride conventional superconductors. In particular, covalent metals including boron, carbon and silicon could represent a viable strategy. During these years I participated in a few projects on superconductivity in boron/carbon structures, with some very encouraging results: a calculated T_c of 77 K in a $RbSrB_6C_6$ structure [286], stable at room pressure. While their T_c is unlikely to reach room temperature, for these compounds it is much easier to reduce the stabilization pressure.

While the focus of this thesis is clearly research on superconducting materials, I would like to conclude with a more general consideration. Since the dawn of civilization, the technical capabilities of mankind were constrained by its ability to bend the properties of matter to its will – from the smith unknowingly quenching steel in the martensite phase, to the microchip laboratories implanting phosphorous ions into a silicon wafer. The discovery of a material with a certain property, often serendipitous, opened the possibility to realize a new technology. The recent advancements in computational materials science could change this paradigm, i.e. instead of depending on the known materials, one could indicate a desired property, and find a new material which is exactly as desired – such is the predictive power of first principles methods. Some examples have already been demonstrated, and more may come: ultra-hard materials, metals with a specific plasma frequency, ultra-strong (or high-temperature) magnets, and transparent or flexible metals. As both the crystal structure search methods and the understanding of condensed matter physics improve, the capability of finding the perfect material for any application will increase. Also, as large amounts of data are generated by computational materials scientists, new frontiers open for artificial intelligence; online databases with material properties are also becoming common. The search of high-temperature superconductors, despite its obvious fundamental interest, will have the additional benefit of paving the way to this revolution.

Chapter 9

Bibliography

[1] A. P. Drodzov, M. I. Eremets, I. A. Troyan, V. Ksenofontov, and S. I. Shylin. Conventional superconductivity at 203 Kelvin at high pressures in the sulfur hydride system. *Nature*, 525:73–76, 2015.

[2] Mari Einaga, Masafumi Sakata, Takahiro Ishikawa, Katsuya Shimizu, Mikhail Eremets, Alexander P. Drodzov, Ivan A. Troyan, Naohisa Hirao, and Yasuo Ohishi. Crystal structure of the superconducting phase of sulfur hydride. *Nature Physics*, 12:835–838, 2016.

[3] H. Liu, I. I. Haumov, Z. M. Geballe, M. Somayazulu, J. S. Tse, and R. J. Hemley. Dynamics and superconductivity in compressed lanthanum superhydride. *Phys. Rev. B*, 98:100102, 2018.

[4] Maddury Somayazulu, Muhtar Ahart, Ajay K. Mishra, Zachary M. Geballe, Maria Baldini, Yue Meng, Viktor V. Struzhkin, and Russell J. Hemley. Evidence for superconductivity above 260 K in lanthanum superhydride at Megabar pressures. *Phys. Rev. Lett.*, 122:027001, 2019.

[5] A. P. Drodzov, P. P. Kong, S. P. Besedin, M. A. Kuzonikov, S. Mozaffari, L. Balicas, F. F. Balakirev, D. E. Graf, V. B. Prakapenka, E. Greenberg, D. A. Knyazev, M. Tkacz, and M. I. Eremets. Superconductivity at 250 K in lanthanum hydride under high pressure. *Nature*, 569:528–531, 2019.

[6] Elliot Snider, Nathan Dasenbrock-Gammon, Raymond McBride, Mathew Debessai, Hiranya Vindana, Kevin Vencatasamy, Keith V. Lawler, Ashkan Salamat, and Ranga P. Dias. Room-temperature superconductivity in a carbonaceous sulfur hydride. *Nature*, 586:373–377, 2020.

[7] Christoph Heil, Simone Di Cataldo, Giovanni Battista Bachelet, and Lilia Boeri. Superconductivity in sodalite-like yttrium hydrides. *Phys. Rev. B*, (99):220502, 2019.

[8] Simone Di Cataldo, Wolfgang von der Linden, and Lilia Boeri. Phase diagram and superconductivity of calcium borohydrides at extreme pressures. *Phys. Rev. B*, 102:014516, 2020.

[9] S. Di Cataldo, Christoph Heil, Wolfgang von der Linden, and Lilia Boeri. $LaBH_8$: towards high-T_c low-pressure superconductivity in ternary superhydrides. *Phys. Rev. B*, 104:L020511, 2021.

[10] Simone Di Cataldo, Wolfgang von der Linden, and Lilia Boeri. La-x-h hydrides: is hot superconductivity possible? *arXiv preprint, arXiv:2106.07266*.

[11] N. W. Ashcroft. Metallic hydrogen: A high-temperature superconductor? *Phys. Rev. Lett.*, 21:1748, 1968.

[12] V. L. Ginzburg. Superfluidity and superconductivity in the universe. *J. Stat. Phys.*, 1:3–24, 1969.

[13] E. Wigner and H. B. Huntington. On the possibility of a metallic modification of hydrogen. *Journal of Chemical Physics*, 3:764–770, 1935.

[14] M. I. Eremets and I. A. Troyan. Conductive dense hydrogen. *Nature Materials*, 10:927–931, 2011.

[15] Ranga P. Dias and I. F. Silvera. Observation of the wigner-huntington transition to metallic hydrogen. *Science*, 355:715–718, 2017.

[16] P. Loubeyre, F. Occelli, and P. Dumas. Synchrothron infrared spectroscopic evidence of the probable transition to metal hydrogen. *Nature*, 577:631–635, 2020.

[17] J. J. Gilman. Lithium dihydrogen fluoride - an approach to metallic hydrogen. *Phys. Rev. Lett.*, 26:546–548, 1971.

[18] A. W. Overhauser. Crystal structure of lithium berillium hydride. *Phys. Rev. B*, 35:411–414, 1987.

[19] M. L. Cohen and P. W. Anderson. Comments on the maximum superconducting transition temperature. In American Institute of Physics, editor, *AIP Conference Proceedings*, volume 4, 1972.

[20] Igor I. Mazin. Vitaly ginzburg and high temperature superconductivity: Personal reminiscences. *Physica C*, 468:105–110, 2007.

[21] J. G. Bednorz and K. A. Müller. Possible high-T_c superconductivity in the Ba-La-Cu-O system. *Zeitschrift für Physik B Condensed Matter*, 64:189–193, 1986.

[22] Jun Nagamatsu, Norimasa Nakagawa, Takahiro Muranaka, Yuji Zenitani, and Jun Akimitsu. Superconductivity at 39 K in magnesium diboride. *Nature*, 410(6824):63–64, 2001.

[23] A. B. Migdal. Interaction between electrons and lattice vibrations in a normal metal. *Soviet Phys Jetp*, 34:996–1001, 1958.

[24] G. M. Eliashberg. Interactions between electrons and lattice vibrations in a superconductor. *Soviet Phys Jetp*, 11:696–702, 1960.

[25] S. Y. Savrasov and D. Y. Savrasov. Electron-phonon interactions and related physical properties of metals from linear-response theory. *Phys. Rev. B*, 54:16487, 1996.

[26] I. I. Mazin and V. P. Antropov. Electronic structure, electron-phonon coupling, and multiband effects in MgB_2. *Physica C: Superconductivity*, 385:49–65, 2003.

[27] J. M. An and W. E. Pickett. Superconductivity of MgB_2: Covalent bonds driven metallic. *Phys. Rev. Lett.*, 86:4366–4369, May 2001.

[28] N. W. Ashcroft. Hydrogen dominant metallic alloys: High temperature superconductors? *Phys. Rev. Lett.*, 92:187002, 2004.

[29] Ji Feng, Wojciech Grochala, Tomasz Jaroń, Roald Hoffmann, Aitor Bergara, and N. W. Ashcroft. Structures and potential superconductivity in SiH_4 at high pressure: En route to "metallic hydrogen". *Phys. Rev. Lett.*, 97:017006, 2006.

[30] Chris J. Pickard and R. J. Needs. High-pressure phases of silane. *Phys. Rev. Lett.*, 97:045504, 2006.

[31] Y. Yao, J. S. Tse, Y. Ma, and K. Tanaka. Superconductivity in high-pressure SiH_4. *Europhysics Letters*, 78:37003, 2007.

[32] M. Martinez-Canales, A. Bergara, J. Feng, and W. Grochala. Pressure induced metallization of germane. *J. Phys. Chem. Solids*, 67:2095–2099, 2006.

[33] Eva Zurek, Roald Hoffmann, N. W. Ashcroft, Artem R. Oganov, and Andriy O. Lyakhov. A little bit of lithium does a lot for hydrogen. *PNAS*, 106:17640–17643, 2009.

[34] M. I. Eremets, I. A. Troyan, S. A. Medvedev, J. S. Tse, and Y. Yao. Superconductivity in hydrogen dominant materials: Silane. *Science*, 319:1506–1509, 2008.

[35] Eva Zurek and Wojciech Grochala. Predicting crystal structures and properties of matter under extreme conditions *via* quantum mechanics: the pressure is on. *Phys. Chem. Chem. Phys.*, 17:2917, 2015.

[36] A. P. Drodzov, V. Minkov, S. Besedin, P. Kong, M. Kuzovnikov, D. Knyazev, and M. Eremets. Superconductivity at 215 k in lanthanum hydride at high pressures. *arXiv preprint, arXiv:1808.07039*, 2018.

[37] Panpan Kong, Vasily S. Minkov, Mikhail A. Kuzovnikov, Alexander P. Drodzov, Stanislav P. Besedin, Shirin Mozaffari, Luis Balicas, Fedor Fedorovich Balekirev, Vitali B. Prakapenka, Stella Chariton, Dmitry V. Semenok, Eran Greenberg, and Mikhail Eremets. Superconductivity up to 243 k in yttrium hydrides under high pressure. *Nature Communications*, 12(5075), 2021.

[38] Ivan A. Troyan, Dmitry V. Semenok, Alexander G. Kvashin, Andrey V. Sadakov, Oleg A. Sobolevskiy, Vladimir M. Pudalov, Anna G. Ivanova, V. B. Prakapenka, E. Greenberg, A. G. Gavriliuk, Viktor V. Struzhkin, Aitor Bergara, Ion Errea, Raffaello Bianco, Matteo Calandra, Francesco Mauri, Lorenzo Monacelli, Ryosuke Akashi, and Artem R. Oganov. Anomalous high-temperature superconductivity in YH_6. *Advanced Materials*, 33:2006832, 2021.

[39] Dmitry V. Semenok, Alexander G. Kvashin, Anna G. Ivanova, Volodymyr Svitlyk, Vyacheslav Yu. Fominski, Andrey V. Sadakov, Oleg A. Sobolevskiy, Vladimir M. Pudalov, Ivan A. Troyan, and Artem R. Oganov. Superconductivity at 161 K in thorium hydride ThH_{10}: Synthesis and properties. *Materials Today*, 33:36–44, 2020.

[40] Wuhao Chen, Dmitry V. Semenok, Xiaoli Huang, Haiyun Shu, Xin Li, Defang Duan, Tian Cui, and Artem R. Oganov. High-temperature superconducting phases in cerium superhydride with a T_c up to 115 k below a pressure of 1 megabar. *Phys. Rev. Lett.*, 127:117001, 2021.

[41] Ivan A. Kruglov, Alexander G. Kvashin, Alexander F. Goncharov, Artem R. Oganov, Sergey S. Lobanov, Nicholas Holtgrewe, Shuqing Jiang, Vitali B. Prakapenka, Eran Greenberg, and Alexey V. Yanilkin. Uranium polyhydrides at moderate pressures: Prediction, synthesis and expected superconductivity. *Science Advances*, 4(10), 2018.

[42] Christian Kokail, Wolfgang von der Linden, and Lilia Boeri. Prediction of high-T_c conventional superconductivity in the ternary lithium borohydride system. *Phys. Rev. M*, 1:074803, 2017.

[43] Ying Sun, Jian Lv, Yu Xie, Hanyu Liu, and Yanming Ma. Route to a superconducting phase above room temperature in electron-doped hydride compounds under high pressure. *Phys. Rev. Lett.*, 123:097001, 2019.

[44] M.Deem and J.M.Newsam. Determination of 4-connected framework crystal structures by simulated annealing. *Nature*, 342:260–262, 1989.

[45] Alessandro Laio and Michele Parrinello. Escaping free-energy minima. *PNAS*, 99:12562–12566, 2002.

[46] S. Gödecker, W. Hellmann, and T. Lenosky. Global minimum determination of the Born-Oppenheimer surface within density functional theory. *Phys. Rev. Lett.*, 95:055501, 2005.

[47] Colin W. Glass, Artem R. Oganov, and Nikolaus Hansen. USPEX–evolutionary crystal structure prediction. *Computer Physics Communication*, 175:713–720, 2006.

[48] Yanchao Wang, Jian Lv, Li Zhu, and Yanming Ma. Crystal structure prediction via particle-swarm optimization. *Phys. Rev. B*, 82:094116, 2010.

[49] David C. Lonie and Eva Zurek. XtalOpt: An open-source evolutionary algorithm for crystal structure prediction. *Computer Physics Communications*, 182:372–387, 2011.

[50] Ivan A. Kruglov, Dmitry V. Semenok, Radoslaw Szczęśniak, M. Mahdi Davari Esfahani, Alexander G. Kvashin, and Artem R. Oganov. Superconductivity of LaH_{10}: a new twist of the story. *arXiv preprint, arXiv:1810.01113v1*, 2018.

[51] A. D. Grockowiak, M. Ahart, T. Helm, W. A. Coniglio, R. Kumar, M. Somayazulu, Y. Meng, V. Williams, N. W. Ashcroft, R. J. Hemley, and S. W. Tozer. Hot hydride superconductivity above 550 k. *arXiv preprint, arXiv:2006.03004*, 2020.

[52] Chris J. Pickard, Ion Errea, and Mikhail Eremets. Superconducting hydrides under pressure. *Annual Review of Condensed Matter Physics*, 11:57–76, 2020.

[53] Zihan Zhang, Tian Cui, Michael J. Hutcheon, Alice M. Shipley, Hao Song, Mingyang Du, Vladimir Z. Kresin, Defang Duan, Chris J. Pickard, and Yansun Yao. Design principles for high temperature superconductors with hydrogen-based alloy backbone at moderate pressure. *arXiv preprint, arXiv:2106.09879*.

[54] Xiaowei Liang, Aitor Bergara, Xudong Wei, Xiaoxu Song, Linyan Wang, Rongxin Sun, Hanyu Liu, Russell J. Hemley, Lin Wang, Guoying Gao, and Yongjun Tian. Prediction of high-T_c superconductivity in ternary lanthanum borohydrides. *Phys. Rev. B*, 104:134501, 2021.

[55] M. Rini. Easing the squeeze on superconductors. *Physics*, 14:46, 2021.

[56] José A. Flores-Livas, Lilia Boeri, Antonio Sanna, Gianni Profeta, Ryotaro Arita, and Mikhail Eremets. A perspective on conventional high-temperature superconductors at high pressure: Methods and materials. *Physics Reports*, 856:1–78, 2020.

[57] Kamerlingh Onnes. The superconductivity of mercury. *Comm. Phys. Lab. Univ. Leiden*, 122(122-124), 1911.

[58] Kamerlingh Onnes. Investigations into the properties of substances at low temperatures, which have led, amongst other things, to the preparation of liquid helium. *Nobel Lecture*, 4:306–336, 1913.

[59] W. Meissner and R. Ochsenfeld. Ein neuer effekt bei eintritt der supraleitfähigkeit. *Naturwissenschaften*, 21.44:787–788, 1933.

[60] R. D. Blaugher, A. I. Braginski, B. S. Chandrasekhar, J. Gavaler, C. K. Jones, J. Parker, J. Przybysz, and M. S. Walker. Superconductivity at westinghouse. volume 20. IEEE/SCS & ESAS, 2012.

[61] P. B. Allen and R. C. Dynes. Transition temperature of strong-coupled superconductors reanalyzed. *Phys. Rev. B*, 12:905, 1975.

[62] W. L. McMillan. Transition temperature of strong-coupled superconductors. *Phys. Rev.*, 167:331, 1968.

[63] Lilia Boeri and Giovanni B. Bachelet. Viewpoint: the road to room-temperature conventional superconductivity. *J. Phys.: Condens. Matter*, 31:234002, 2019.

[64] P. Loubeyre, R. LeToullec, D. Hausermann, M. Hanfland, R. J. Hemley, H. K. Mao, and L. W. Finger. X-ray diffraction and equation of state of hydrogen at megabar pressures. *Nature*, 383:702–704, 1996.

[65] Chris J. Pickard and Richard J. Needs. Structure of phase III of solid hydrogen. *Nature Physics*, 3:473–476, 2007.

[66] L. Monacelli, I. Errea, M. Calandra, and F. Mauri. Black metal hydrogen above 360 GPa driven by proton quantum fluctuations. *Nature Physics*, 17:63–67, 2020.

[67] M. K. Wu, J. R. Ashburn, C. J. Torng, P. H. Hor, R. L. Meng, L. Gao, Z. J. Huang, Y. Q. Wang, and C. W. Chu. Superconductivity at 93 K in a new mixed-phase Y-Ba-Cu-O compound system at ambient pressure. *Phys. Rev. Lett.*, 58:908, 1987.

[68] https://www.nobelprize.org/prizes/physics/1987/summary/.

[69] A. Schilling, M. Cantoni, J. D. Guo, and H. R. Ott. Superconductivity above 130 K in the Hg-Ba-Ca-Cu-O system. *Nature*, 363:56–58, 1993.

[70] Yoichi Kamihara, Hidenori Hiramatsu, Masahiro Hirano, Ryuto Kawamura, Hiroshi Yanagi, Toshio Kamiya, and Hideo Hosono. Iron-based layered superconductor: LaOFeP. *J. Am. Chem. Soc.*, 128:10012–10013, 2006.

[71] Yoichi Kamihara, Takumi Watanabe, Masahiro Hirano, and Hideo Hosono. Iron-based layered superconductor: $La[O_{1-x}F_x]FeAs$ (x = 0.05-0.12) with T_c = 26 k. *J. Am. Chem. Soc.*, 130(11):3296–3297, 2008.

[72] J. Orenstein and A. J. Millis. Advances in the physics of high-temperature superconductivity. *Science*, 288:468–474, 2000.

[73] M. R. Norman and C. Pépin. The electronic nature of high temperature cuprate superconductors. *Reports on Progress in Physics*, 66:1547, 2003.

[74] Andrea Damascelli, Zahid Hussain, and Zhi-Xun Shen. Angle-resolved photoemission studies of the cuprate superconductors. *Rev. Mod. Phys*, 75(473), 2003.

[75] Patrick A. Lee, Naoto Nagaosa, and Xiao-Gang Wen. Doping a mott insulator: Physics of high-temperature superconductivity. *Rev. Mod. Phys*, 78(17), 2006.

[76] Peter D. Johnson, Guangyong Xu, and Wei-Guo Yin. *Iron-Based Superconductivity*. Springer Series in Materials Science, 2015.

[77] Andrey Chubukov and Peter J. Hirschfeld. Iron-based superconductors, seven years later. *Physics Today*, 68(6), 2015.

[78] Rafael M. Fernandes and Andrey Chubukov. Low-energy microscopic models for iron-based superconductors: a reivew. *Reports on Progress in Physics*, 80(1), 2016.

[79] H. W. Kroto, J. R. Heath, S. C. O'Brien, R. F. Curl, and R. E. Smalley. C_{60}: Buckminsterfullerene. *Nature*, 318:162–163, 1985.

[80] A. F. Hebard, M. J. Rosseinsky, R. C. Haddon, D. W. Murphy, S. H Glarum, T. T. M. Palstra, A. P. Ramirez, and A. R. Kortan. Superconductivity at 18 k in potassium-doped C_{60}. *Nature*, 350:600–601, 1991.

[81] K. Tanigaki, T. W. Ebbesen, S. Saito, J. Mizuki, J. S. Tsai, Y. Kubo, and S. Kuroshima. Superconductivity at 33 k in $Cs_xRb_yC_{60}$. *Nature*, 352:222–223, 1991.

[82] T. T. M. Palstra, O. Zhou, Y. Iwasa, P. E. Sulewski, R. M. Fleming, and B. R. Zegarski. Superconductivity at 40 k in cesium doped C_{60}. *Solid State Comm.*, 93:327–330, 1995.

[83] O. Gunnarsson. Superconductivity in fullerides. *Rev. Mod. Phys*, 69(2), 1997.

[84] Serena Margadonna and Kosmas Prassides. Recent advances in fullerene superconductivity. *J. Solid State Chem.*, 168:639–652, 2002.

[85] Thomas E. Weller, Mark Ellerby, Siddarth S. Saxena, Robert P. Smith, and Neal T. Skipper. Superconductivity in the intercalated graphite compounds C_6Yb and C_6Ca. *Nature Physics*, 1:39–41, 2005.

[86] E. A. Ekimov, V. A. Sidorov, E. D. Bauer, N. N. Mel'nik, N. J. Curro, J. D. Thompson, and S. M. Stishov. Superconductivity in diamond. *Nature*, 428:542–545, 2004.

[87] J. Kortus, I. I. Mazin, K. D. Belashchenko, V. P. Antropov, and L. L. Boyer. Superconductivity of metallic boron in MgB_2. *Phys. Rev. Lett.*, 86:4656–4659, 2001.

[88] L. Boeri, J. Kortus, and O. K. Andersen. Three-dimensional MgB_2-type superconductivity in hole-doped diamond. *Phys. Rev. Lett.*, 93:237002, 2004.

[89] T. Yokoya, T. Nakamura, T. Matsushita, T. Muro, Y. Takano, M. Nagao, T. Takenouchi, H. Kawarada, and T. Oguchi. Origin of the metallic properties of heavily boron-doped superconducting diamond. *Nature Letters*, 438:647–650, 2005.

[90] Lilia Boeri, Jens Kortus, and O. K. Andersen. Electron-phonon superconductivity in hole-doped diamond: A first principles study. *J. Phys. Chem. Solids*, 67:552–556, 2006.

[91] V. A. Sidorov and E. A. Ekimov. Superconductivity in diamond. *Diamond and Related Materials*, 19:351–357, 2010.

[92] E. Bustarret. Superconductivity in doped semiconductors. *Physica C: Superconductivity and its Applications*, 514:36–45, 2015.

[93] https://www.nobelprize.org/prizes/physics/1946/bridgman/facts/.

[94] C. E. Weir, E. R. Lippincott, A. Van Valkenburg, and E. N. Bunting. Infrared studies in the 1- to 15-micron region to 30,000 atmospheres. *Journal of Research of The National Bureau of Standards*, 63A(1):55–62, 1959.

[95] Natalia Dubrovinskaia, Leonid Dubrovinski, Natalia A. Solopova, Artem Abakumov, Stuart Turner, Michael Hanfland, Elena Bykova, Maxim Bykov, Clemens Prescher, Vitali B. Prakapenka, Sylvain Petitgirard, Irina Chuvashova, Biliana Gasharova, Yves-Laurent Mathis, Petr Ershov, Irina Snigireva, and Anatoly Snigirev. Terapascal static pressure generation with ultrahigh yield strength nanodiamond. *Science Advances*, 2, 2016.

[96] M. Eremets. Megabar high-pressure cells for raman measurements. *J. Raman Spectros.*, 34:515–518, 2003.

[97] https://commons.wikimedia.org/wiki/File:Diamond_Anvil_Cell_-_Cross_Section.svg#/media/File:Diamond_Anvil_Cell_-_Cross_Section.svg.

[98] Jörg Wittig. Superconductivity of cerium under pressure. *Phys. Rev. Lett.*, 21:1250–1252, 1968.

[99] J. Wittig and B. T. Matthias. Superconductivity of barium under pressure. *Phys. Rev. Lett.*, 22:634–636, 1969.

[100] K. J. Dunn and F. P. Bundy. Pressure-induced superconductivity in strontium and barium. *Phys. Rev. B*, 25:194–197, 1982.

[101] Viktor V. Struzhkin, M. I. Eremets, Wei Gan, Ho-Kwang Mao, and Russell J. Hemley. Superconductivity in dense lithium. *Science*, 298:1213–1215, 2002.

[102] Katsuya Shimizu, Hiroto Ishikawa, Daigoroh Takao, Takehiko Yagi, and Kiichi Amaya. Superconductivity in compressed lithium at 20 K. *Nature*, 419:597–599, 2002.

[103] Katsuya Shimizu, Tomohiro Kimura, Shigeyuki Furomoto, Kaiki Takeda, Kazuyoshi Kontani, Yoshichika Onuki, and Kiichi Amaya. Superconductivity in the non-magnetic state of iron under pressure. *Nature*, 412:316–318, 2001.

[104] J. J. Hamlin, V. G. Tissen, and J. S. Schilling. Superconductivity at 17 K in yttrium metal under nearly hydrostatic pressure up to 89 GPa. *Phys. Rev. B*, 73:094522, 2006.

[105] Shingo Okada, Katsuya Shimizu, Tatsuo C. Kobayashi, Kiichi Amaya, and Shoichi Endo. Superconductivity of calcium under high pressures. *J. Phys. Soc. Jpn.*, 65:1924–1926, 1996.

[106] Takahiro Yabuuchi, Takahiro Matsuoka, Yuki Nakamoto, and Katsuya Shimizu. Superconductivity of Ca exceeding 25 K at megabar pressures. *J. Phys. Soc. Jpn.*, 75:083703, 2006.

[107] J. J. Hamlin. Superconductivity in the metallic elements at high pressures. *Physica C*, 514:59–76, 2015.

[108] Artem R. Oganov, Colin W. Glass, and Shigeaki Ono. High-pressure phases of $CaCO_3$: Crystal structure prediction and experiment. *Earth and Planetary Science Letters*, 241:95–103, 2006.

[109] Yanming Ma, Mikhail Eremets, Artem R. Oganov, Yu Xie, Ivan Trojan, Sergey Medvedev, Andriy O. Lyakhov, Mario Valle, and Vitali B. Prakapenka. Transparent dense sodium. *Nature*, 458:182–185, 2009.

[110] Artem R. Oganov, Jiuhua Chen, Carlo Gatti, Yanzhang Ma, Yanming Ma, Colin W. Glass, Zhenxian Liu, Tony Yu, Oleksandr O. Kurakevych, and Vladimir L. Solozhenko. Ionic high-pressure form of elemental boron. *Nature*, 457:863–867, 2009.

[111] Artem R. Oganov, Chris J. Pickard, Qiang Zhu, and Richard J. Needs. Structure prediction drives materials discovery. *Nature Reviews Materials*, 4:331–348, 2019.

[112] N. W. Ashcroft. Hydrogen dominant metallic alloys: High temperature superconductors? *Phys. Rev. Lett.*, 92(18):187002, 2004.

[113] Andreas Züttel. Materials for hydrogen storage. *Materials Today*, 6:24–33, 2003.

[114] J. S. Tse, Y. Yao, and K. Tanaka. Novel superconductivity in metallic SnH_4 under high pressure. *Phys. Rev. Lett.*, 98:117004, 2007.

[115] Xiao-Jia Chen, Jiang-Long Wang, Viktor V. Struzhkin, Ho-Kwang Mao, Russell J. Hemley, and Hai-Qing Lin. Superconducting behavior in compressed solid SiH_4 with a layered structure. *Phys. Rev. Lett.*, 101:077002, 2008.

[116] D. Y. Kim, R. H. Scheicher, S. Lebégue, B. Arnaud, M. Alouani, and R. Ahuja. Crystal structure of the pressure-induced metallic phase of SiH_4 from ab initio theory. *PNAS*, (16454-16459), 105.

[117] Olga Degtyareva, John E. Proctor, Christophe L. Guillaume, Eugene Gregoryanz, and Michael Hanfland. Formation of transition metal hydrides at high pressures. *Solid State Comm.*, 149:1583–1586, 2009.

[118] Xiang-Feng Zhou, Artem R. Oganov, Xiao Dong, Lixin Zhang, Yongjun Tian, and Hui-Tian Wang. Superconducting high-pressure phase of platinum hydride from first principles. *Phys. Rev. B*, 84:054543, 2011.

[119] Duck Young Kim, Ralph H. Scheicher, Chris J. Pickard, R. J. Needs, and R. Ahuja. Predicted formation of superconducting platinum-hydride crystals under pressure in the presence of molecular hydrogen. *Phys. Rev. Lett.*, 107:117002, 2011.

[120] Guoying Gao, Hui Wang, and Yanming Ma. Pressure-induced formation of noble metal hydrides. *J. Phys. Chem. C*, 116:1995–2000, 2012.

[121] Hui Wang, John S. Tse, Kaori Tanaka, Toshiaki Iitaka, and Yanming Ma. Superconductive sodalite-like clathrate calcium hydride at high pressure. *PNAS*, 109:6463–6466, 2012.

[122] Chao-Hao Hu, Artem R. Oganov, Qiang Zhu, Guang-Rui Qian, Gilles Frapper, Andriy O. Lyakhov, and Huai-Ying Zhou. Pressure-induced stabilization and insulator-superconductor transition of BH. *Phys. Rev. Lett.*, 110:165504, 2013.

[123] G. Savini, A. C. Ferrari, and Feliciano Giustino. First-principles prediction of doped graphane as a high-temperature electron-phonon superconductor. *Phys. Rev. Lett.*, 105:037002, Jul 2010.

[124] Andriy O. Lyakhov, Artem R. Oganov, Harold T. Stokes, and Qiang Zhu. New developments in evolutionary structure prediction algorithm USPEX. *Computer Physics Communication*, 184:1172–1182, 2013.

[125] Charles Pépin, Paul Loubeyre, Florent Occelli, and Paul Dumas. Synthesis of lithium polyhydrides above 130 gpa at 300 k. *PNAS*, 112:7673–7676, 2015.

[126] Defang Duan, Yunxian Liu, Fubo Tian, Da Li, Xiaoli Huang, Zhonglong Zhao, Hongyu Yu, Bingbing Liu, Wenjing Tian, and Tian Cui. Pressure-induced metallization of dense $(H_2S)_2H_2$ with high-T_c superconductivity. *Scientific Reports*, 4:6968, 2014.

[127] A. P. Drodzov, M. I. Eremets, and I. A. Troyan. Conventional superconductivity at 190 K at high pressures. *arXiv preprint, arXiv:1412.0460*, 2014.

[128] N. Bernstein, C. S. Hellberg, M. D. Johannes, and I. I. Mazin. What superconducts in sulfur hydrides under pressure and why. *Phys. Rev. B*, 91(060511), 2015.

[129] Christoph Heil and Lilia Boeri. Influence of bonding on superconductivity in high-pressure hydrides. *Phys. Rev. B*, 92:060508(R), 2015.

[130] Ryosuke Akashi. Archetypical "push the band critical point" mechanism for peaking of the density of states in three-dimensional crystals: Theory and case study of cubic H_3S. *Phys. Rev. B*, 101:075126, 2020.

[131] E. J. Nicol and J. P. Carbotte. Comparison of pressurized sulfur hydride with conventional superconductors. *Phys. Rev. B*, 91:220507, 2015.

[132] Ion Errea, Matteo Calandra, Chris J. Pickard, Joseph Nelson, Richard J. Needs, Yinwei Li, Hanyu Liu, Yunwei Zhang, Yanming Ma, and Francesco Mauri. High-pressure hydrogen sulfide from first principles: A strongly anharmonic phonon-mediated superconductor. *Phys. Rev. Lett.*, 114:157004, 2015.

[133] Ion Errea, Matteo Calandra, Chris J. Pickard, Joseph R. Nelson, Richard J. Needs, Yinwei Li, Hanyu Liu, Yunwei Zhang, Yanming Ma, and Francesco Mauri. Quantum hydrogen-bond symmetrization in the superconducting hydrogen sulfide system. *Nature*, 532:81–84, 2016.

[134] Miguel Borinaga, Ion Errea, Matteo Calandra, Francesco Mauri, and Aitor Bergara. Anharmonic effects in atomic hydrogen: Superconductivity and lattice dynamical stability. *Phys. Rev. B*, 93:174308, 2016.

[135] José A. Flores-Livas, Antonio Sanna, and E. K.U. Gross. High temperature superconductivity in sulfur and selenium hydrides at high pressure. *The European Physical Journal B*, 89: 63, 2016.

[136] Shoutao Zhang, Yanchao Wang, Jurong Zhang, Hanyu Liu, Xin Zhong, Hai-Feng Song, Guochun Yang, Lijun Zhang, and Yanming Ma. Phase diagram and high-temperature superconductivity of compressed selenium hydrides. *Scientific Reports*, 5:15433, 2015.

[137] Xin Zhong, Hui Wang, Jurong Zhang, Hanyu Liu, Shoutao Zhang, Hai-Feng Song, Guochun Yang, Lijun Zhang, and Yanming Ma. Tellurium hydrides at high pressures: High-temperature superconductors. *Phys. Rev. Lett.*, 116:057002, 2016.

[138] José A. Flores-Livas, Maximilian Amsler, Christoph Heil, Antonio Sanna, Lilia Boeri, Gianni Profeta, Chris Wolverton, Stefan Goedecker, and E. K. U. Gross. Superconductivity in metastable phases of phosphorus-hydride compounds under high pressure. *Phys. Rev. B*, 93:020508(R), Jan 2016.

[139] A. P. Drodzov, M. I. Eremets, and I. A. Troyan. Superconductivity above 100 K in PH_3 at high pressures. *arXiv:1508.06224*, 2015.

[140] Hanyu Liu, Ivan I. Naumov, Roald Hoffmann, N. W. Ashcroft, and Russell J. Hemley. Potential high-T_c superconducting lanthanum and yttrium hydrides at high pressure. *PNAS*, 114:6990–6995, 2017.

[141] Francesco Belli, Trinidad Novoa, J. Contreras-Garcia, and Ion Errea. Strong correlation between bonding network and critical temperature in hydrogen-based superconductors. *Nature Communications*, 12:5381, 2021.

[142] Alice M. Shipley, Michael J. Hutcheon, Mark S. Johnson, and Richard J. Needs. Stability and superconductivity of lanthanum and yttrium decahydrides. *Phys. Rev. B*, 101:224511, 2020.

[143] Ion Errea, Francesco Belli, Lorenzo Monacelli, Antonio Sanna, Takashi Koretsune, Terumasa Tadano, Raffaello Bianco, Matteo Calandra, Ryotaro Arita, Francesco Mauri, and José A. Flores-Livas. Quantum crystal structure in the 250-Kelvin superconducting lanthanum hydride. *Nature*, 578:66–69, 2020.

[144] Andrew Shamp, Tyson Terpstra, Tiange Bi, Zackary Falls, Patrick Avery, and Eva Zurek. Decomposition products of phosphine under pressure: PH_2 stable and superconducting? *J. Am. Chem. Soc.*, 138:1884–1892, 2016.

[145] Yuhao Fu, Xiangpo Du, Lijun Zhang, Feng Peng, Miao Zhang, Chris J. Pickard, Richard J. Needs, David J. Singh, Weitao Zheng, and Yanming Ma. High-pressure phase stability and superconductivity of pnictogen hydrides and chemical trends for compressed hydrides. *Chem. Mater.*, 28:1746–1755, 2016.

[146] Yinwei Li, Jian Hao, Hanyu Liu, John S. Tse, Yanchao Wang, and Yanming Ma. Pressure-stabilized superconductive yttrium hydrides. *Scientific Reports*, 5:09948, 2015.

[147] Feng Peng, Ying Sun, Chris J. Pickard, Richard J. Needs, Qiang Wu, and Yanming Ma. Hydrogen clathrate structures in rare earth hydrides at high pressures: Possible route to room-temperature superconductivity. *Phys. Rev. Lett.*, 119:107001, 2017.

[148] Liangliang Liu, Chongze Wang, Seho Yi, Kun Woo Kim, Jaeyong Kim, and Jun-Hyung Cho. Microscopic mechanism of room-temperature superconductivity in compressed LaH_{10}. *Phys. Rev. B*, 99:140501(R), 2019.

[149] Ivan A. Kruglov, Dmitry V. Semenok, Hao Song, Radoslaw Szczęśniak, Izabela A. Wrona, Ryosuke Akashi, M. Mahdi Davari Esfahani, Defang Duan, Tian Cui, Alexander G. Kvashin, and Artem R. Oganov. Superconductivity of LaH_{10} and LaH_{16} polyhydrides. *Phys. Rev. B*, 101:024508, 2020.

[150] Ryotaro Arita, Takashi Koretsune, Shiro Sakai, Yusuke Nomura, and Wataru Sano. Nonempirical calculations of superconducting transition temperatures in light-element superconductors. *Advanced Materials*, 29, 2017.

[151] Dmitry V. Semenok, Ivan A. Kruglov, Igor A. Savkin, Alexander G. Kvashin, and Artem R. Oganov. On distribution of superconductivity in metal hydrides. *Current Opinion in Solid State and Materials Science*, 24:100808, 2020.

[152] Tiange Bi, Niloofar Zarifi, Tyson Terpstra, and Eva Zurek. The search for superconductivity in high pressure hydrides. *arXiv preprint, arXiv:1806.00163*, 2018.

[153] Eva Zurek and Tiange Bi. High-temperature superconductivity in alkaline and rare-earth polyhydrides at high pressure: A theoretical perspective. *J. Chem. Phys.*, 150:050901, 2019.

[154] Ying Sun, Yifan Tian, Bowen Jiang, Xue Li, Hefei Li, Toshiaki Iitaka, Xin Zhong, and Yu Xie. Computational discovery of a dynamically stable cubic SH_3-like high-temperature superconductor at 100 GPa via CH_4 intercalation. *Phys. Rev. B*, 101:174102, 2020.

[155] Kenneth Chang. Finally, the first room-temperature superconductor. *The New York Times*, 2020.

[156] Tianchun Wang, Motoaki Hirayama, Takuya Nomoto, Takashi Koretsune, Ryotaro Arita, and José A. Flores-Livas. Absence of conventional room temperature superconductivity at high pressure in carbon doped H_3S. *arXiv preprint, arXiv:2104.03710*, 2021.

[157] Anmol Lamicchane, Ravhi Kumar, Muhtar Ahart, Nilesh P. Salke, Nathan Dasenbrock-Gammon, Elliot Snider, Yue Meng, Barbara Lavina, Stella Chariton, Vitali B. Prakapenka, Maddury Somayazulu, Ranga P. Dias, and Russell J. Hemley. X-ray diffraction and equation of state of the C-S-H room-temperature superconductor. *arXiv preprint, arXiv:2105.06352*, 2021.

[158] Xiaoyu Wang, Tiange Bi, Katherina P. Hilleke, Anmol Lamicchane, Russell J. Hemley, and Eva Zurek. A little bit of carbon can do a lot for superconductivity in H_3S. *arXiv preprint, arXiv:2109.09898*, 2021.

[159] Lilia Boeri et al. The 2021 room-temperature superconductivity roadmap. *J. Phys. Condens. Matter*, In press, 2021.

[160] Tim Mueller, Alberto Hernandez, and Chuhong Wang. Machine learning for interatomic potential models. *J. Chem. Phys.*, 152:050902, 2020.

[161] Yunxing Zuo, Chi Chen, Xiangguo Li, Zhi Deng, Yiming Chen, Jörg Behler, Gábor Csányi, Alexander V. Shapeev, Aidan P. Thompson, Mitchell A. Wood, and Shyue Ping Ong. Performance and cost assessment of machine learning interatomic potentials. *J. Phys. Chem. A*, 124:731–745, 2020.

[162] Ivan S. Novikov, Konstantin Gubaev, Evgeny V. Podryabinkin, and Alexander V. Shapeev. The MLIP package: moment tensor potentials with mpi and active learning. *Mach. Learn.: Sci. Technol.*, 2:025002, 2021.

[163] Wenhao Sun, Christopher J. Bartel, Elisabetta Arca, Sage R. Bauers, Bethany Matthews, Bernardo Orvananos, Bor-Rong Chen, Michael F. Toney, Laura T. Schelhas, William Tumas, Janet Tate, Andriy Zakutayev, Stephan Lany, Aaron M. Holder, and Gerbrand Ceder. A map of the inorganic ternary metal nitrides. *Nature Materials*, 18(732-739), 2019.

[164] Maosheng Miao, Yuanhui Sun, Eva Zurek, and Haiqing Lin. Chemistry under high pressure. *Nature Reviews Chemistry*, 4:508–527, 2020.

[165] J. D. Gale. Empirical potential derivation for ionic materials. *Philosophical Magazine B*, 73:3–19, 1994.

[166] J. D. Gale and Andrew L. Rohl. The general utility lattice program (GULP). *Molecular Simulation*, 29:291–341, 2003.

[167] Daniele Dragoni, Thomas D. Daff, Gábor Csányi, and Nicola Marzari. Achieving DFT accuracy with a machine-learning interatomic potential: Thermomechanics and defects in bcc ferromagnetic iron. *Phys. Rev. M*, (2), 2018.

[168] Volker L. Deringer and Gábor Csányi. Machine learning based interatomic potential for amorphous carbon. *Phys. Rev. B*, 95:094203, 2017.

[169] P. Hohenberg and W. Kohn. Inhomogeneous electron gas. *Phys. Rev.*, 136:B864, 1964.

[170] W. Kohn and L. J. Sham. Self-consistent equations including exchange and correlation effects. *Phys. Rev.*, 140:A1133, 1965.

[171] Ronald E. Cohen, M. M. Mehl, and Dimitrios A. Papaconstantopoulos. Tight-binding total-energy method for transition and noble metals. *Phys. Rev. B*, 50:14694(R), 1994.

[172] N. Ashcroft and N. Mermin. *Solid State Physics*, chapter 23. Harcourt College Publishers, 1976.

[173] A. Maraudin, P. A. Flinn, and R: A. Coldwell-Horsfall. Anharmonic contributions to vibrational thermodynamic properties of solids: Part i. general formulation and application to the linear chain. *Annals of Physics*, 15:337–359, 1961.

[174] Xiao Dong, Xiang-Feng Zhou, Guang-Rui Qian, Zhisheng Zhao, Yongjun Tian, and Hui-Tian Wang. An *ab initio* study on the transition paths from graphite to diamond under pressure. *J. Phys. Condens. Matter*, 25:145402, 2013.

[175] Graeme Henkelman. A climbing image nudged elastic band method for finding saddle points and minimum energy paths. *The Journal of Chemical Physics*, 113:9901, 2000.

[176] Guang-Rui Qian, Xiao Dong, Xiang-Feng Zhou, Yongjun Tian, Artem R. Oganov, and Hui-Tian Wang. Variable cell nudged elastic band method for studying solid-solid structural phase transitions. *Comp. Phys. Communications*, 184:2111–2118, 2013.

[177] Vladislav A. Blatov. Multipurpose crystallochemical analysis with the program package topos. *IUCr CompComm Newsletter*, 7:4–38, 2006.

[178] Vladislav A. Blatov, Alexander P. Shevchenko, and Davide M. Proserpio. Applied topological analysis of crystal structures with the program package topos. *Crystal Growth & Design*, 14:3576–3586, 2014.

[179] Detlef W. M. Hofmann and Joannis Apostolakis. Crystal structure prediction by data mining. *J. of Mol. Struct.*, 647:17–39, 2003.

[180] Artem R. Oganov, editor. *Modern Methods of Crystal Structure Prediction*. Wiley-VCH Verlag GmbH & Co. KGaA, 2011.

[181] P. Željko P Ĉanĉarević, J. Christian Schön, and M. Jansen. Stability of alkali metal halide polymorphs as a function of pressure. *Chem. Asian J.*, 3:561–572, 2008.

[182] Y. Liebold-Ribeiro, D. Fischer, and M. Jansen. Experimental substantiation of the "energy landscape concept" for solids: Synthesis of a new modification of LiBr. *Angew. Chem. Int. Ed.*, 47:4428–4431, 2008.

[183] A. Bach, D. Fischer, and M. Jansen. Synthesis of a new modification of lithium chloride confirming theoretical predictions. *Z. Anorg. Chem.*, 635:2406–2409, 2009.

[184] R. Martonak, A. Laio, and M. Parrinello. Predicting crystal structures: The Parrinello-Rahman method revisited. *Phys. Rev. Lett.*, 90:075503, 2003.

[185] R. Martonak, A. Laio, M. Bernasconi, C. Ceriani, P. Raiteri, F. Zipoli, and M. Parrinello. Simulation of structural phase transitions by metadynamics. *Z. Krist.*, 220:489–498, 2005.

[186] S. Gödecker. Minima hopping: An efficient search method for the global minimum of the potential energy surface of comples molecular systems. *J. Chem. Phys.*, 120:9911–9917, 2004.

[187] Maximilian Amsler and Stefan Goedecker. Crystal structure prediction using the minima hopping method. *J. Chem. Phys.*, 133:224104, 2010.

[188] W. Hellmann, R. G. Hennig, S. Gödecker, S. Umrigar, and C. J. Delley. Questioning the existence of a well defined ground state for silicon clusters. *Phys. Rev. B*, 75:085411, 2007.

[189] K. Bao, S. Gödecker, S. Koga, F. Lancon, and A. Neelov. Structure of large gold clusters obtained by global optimization using the minima hopping method. *Phys. Rev. B*, 79:041405, 2009.

[190] Chris J. Pickard and R. J. Needs. *Ab initio* random structure searching. *J. Phys. Condens. Matter*, 23:053201, 2011.

[191] Gábor Csányi, Chris J. Pickard, B. D. Simons, and R. J. Needs. Graphite intercalation compounds under pressure: A first-principles density functional theory study. *Phys. Rev. B*, 75:085432, 2007.

[192] Yinwei Li, Jian Hao, Hanyu Liu, Yangling Li, and Yanming Ma. The metallization and superconductivity of dense hydrogen sulfide. *J. Chem. Phys.*, 140:174712, 2014.

[193] T. S. Bush, C. R. A. Catlow, and P. D. Battle. Evolutionary programming for predicting inorganic crystal structures. *J. Mater. Chem.*, 5:1269–1272, 1995.

[194] D. M. Deaven and K. M. Ho. Molecular geometry optimization with a genetic algorithm. *Phys. Rev. Lett.*, 75:288–291, 1995.

[195] Artem R. Oganov and Mario Valle. How to quantify energy landscapes of solids. *The Journal of Chemical Physics*, 130:104504, 2009.

[196] J. Bardeen, L. N. Cooper, and J. R. Schrieffer. Theory of superconductivity. *Phys. Rev.*, 108:1175, 1957.

[197] Leon N. Cooper. Bound electron pairs in a degenerate fermi gas. *Phys. Rev.*, 104:1189–1190, 1956.

[198] J. R. Schrieffer. *Theory of Superconductivity (1st ed.)*. CRC Press, 1999.

[199] J. G. Valatin. Comments on the theory of superconductivity. *Il Nuovo Cimento*, VII:843–857, 1958.

[200] N. N. J. Bogolubov and D. N. Zubarev. On the theory of superfluidity. *Journal of Physics*, 1:23–32, 1947.

[201] J. G. Valatin. *Lectures in Theoretical Physics*, volume VI, chapter Theory of Superfluids, pages 292–325. University of Colorado Press, 1963.

[202] James Nicol, Sidney Shapiro, and Paul H. Smith. Direct measurement of the superconducting energy gap. *Phys. Rev. Lett.*, 5(10):461–464, 1960.

[203] Ivar Giaever. Energy gap in superconductors measured by electron tunneling. *Phys. Rev. Lett.*, 5(4):147–148, 1960.

[204] G. Seidel and P. H. Keesom. Specific heat of gallium and zinc in the normal and superconducting states. *Phys. Rev.*, 112:1083–1088, 1958.

[205] F. Reif. Study of superconducting hg by nuclear magnetic resonance techniques. *Phys. Rev.*, 106:208–220, 1957.

[206] Moises Levy. Ultrasonic attenuation in superconductors for $ql < 1$. *Phys. Rev.*, 131:1497–1500, 1639.

[207] Philip B. Allen and Božidar Mitrović. *Theory of Superconducting T_c*, volume 37. Solid State Physics, 1983.

[208] Yoichiro Nambu. Quasi-particles and gauge invariance in the theory of superconductivity. *Phys. Rev.*, 117:648–663, 1960.

[209] Philip B. Allen. Fermi-surface harmonics: A general method for nonspherical problems. applications to boltzmann and eliashberg equations. *Phys. Rev. B*, 13:1416, 1976.

[210] P. Morel and P. W. Anderson. Calculation of the superconducting state parameters with retarded electron-phonon interaction. *Physical Review*, 125:1263, 1962.

[211] E. R. Margine and F. Giustino. Anisotropic migdal-eliashberg theory using wannier functions. *Phys. Rev. B*, 87:024505, 2013.

[212] Jon Lafuente-Bartolome, Idoia G. Gurtubay, and Asier Eiguren. Symmetric helmholtz fermi-surface harmonics for an optimal representation of anisotropic quantities on the fermi surface: Application to the electron-phonon problem. *Phys. Rev. B*, 102:165113, 2020.

[213] A. Floris, A. Sanna, M. Lüders, G. Profeta, N. N. Lathiotakis, M. A. L. Marques, C. Franchini, E. K.U. Gross, A. Continenza, and S. Massidda. Superconducting properties of MgB_2 from first principles. *Physica C*, 456:45–53, 2007.

[214] A. Sanna, G. Profeta, A. Floris, A. Marini, E. K.U. Gross, and S. Massidda. Anisotropic gap of superconducting CaC_6: A first-principles density functional calculation. *Phys. Rev. B*, 75:020511(R), 2007.

[215] Božidar Mitrović, H. G. Zarate, and J. P. Carbotte. The ratio $2\Delta/k_BT_c$ within eliashberg theory. *Phys. Rev. B*, 29:184–190, 1984.

[216] F. Marsiglio and J. P. Carbotte. Strong-coupling corrections to bardeen-cooper schrieffer ratios. *Phys. Rev. B*, 33:6141–6146, 1986.

[217] J. J. Hopfield. Angular momentum and transition-metal superconductivity. *Physical Review*, 186(2):443–451, 1969.

[218] M. Born and J. R. Oppenheimer. On the quantum theory of molecules. *Ann. Physik*, 84:457, 1927.

[219] John P. Perdew, Kieron Burke, and Matthias Ernzerhof. Generalized gradient approximation made simple. *Phys. Rev. Lett.*, 77:3865, 1996.

[220] Stefano Baroni, Stefano de Gironcoli, Andrea Dal Corso, and Paolo Giannozzi. Phonons and related crystal properties from density-functional perturbation theory. *Rev. Mod. Phys*, 73:515, 2001.

[221] S. Y. Savrasov. Linear-response theory and lattice dynamics: a muffin-tin-orbital approach. *Phys. Rev. B*, 54:16470–16486, 1996.

[222] Amy Y. Liu, I. I. Mazin, and Jens Kortus. Beyond eliashberg superconductivity in MgB_2: Anharmonicity, two-phonon scattering, and multiple gaps. *Phys. Rev. Lett.*, 87:087005, 2001.

[223] Y. Kong, O. V. Dolgov, O. Jepsen, and O. K. Andersen. Electron-phonon interaction in the normal and superconducting states of MgB_2. *Phys. Rev. B*, 64:020501(R), 2001.

[224] Deepa Kasinathan, J. Kuneš, A. Lazicki, H. Rosner, C. S. Yoo, R. T. Scalettar, and W. E. Pickett. Superconductivity and lattice instability in compressed lithium from Fermi surface hot spots. *Phys. Rev. Lett.*, 96:047004, 2006.

[225] Matteo Calandra and Francesco Mauri. Electron-phonon coupling and phonon self-energy in MgB_2: Interpretation of MgB_2 Raman spectra. *Phys. Rev. B*, 71:064501, 2005.

[226] Feliciano Giustino, Marvin L. Cohen, and Steven G. Louie. Electron-phonon interaction using Wannier functions. *Phys. Rev. B*, 76:165108, 2007.

[227] S. Poncé and. E. R. Margine, C. Verdi, and F. Giustino. EPW: Electron-phonon coupling, transport and superconducting properties using maximally localized Wannier functions. *Comp. Phys. Communications*, 209:116–133, 2016.

[228] Nicola Marzari, Arash A. Mostofi, Jonathan R. Yates, Ivo Souza, and David Vanderbilt. Maximally localized Wannier functions: Theory and applications. *Rev. Mod. Phys*, 84:1419, 2012.

[229] L. N. Oliveira, E. K. U. Gross, and W. Kohn. Density-functional theory for superconductors. *Phys. Rev. Lett.*, 60:2430–2433, 1988.

[230] M. Lüders, M. A. L. Marques, N. N. Lathiotakis, A. Floris, G. Profeta, L. Fast, A. Continenza, S. Massidda, and E. K. U. Gross. *Ab initio* theory of superconductivity. i. density functional formalism and approximate functionals. *Phys. Rev. B*, 72:024545, 2005.

[231] M. A. L. Marques, M. Lüders, N. N. Lathiotakis, G. Profeta, A. Floris, L. Fast, A. Continenza, E. K. U. Gross, and S. Massidda. *Ab initio* theory of superconductivity. ii. applications to elemental metals. *Phys. Rev. B*, 72:024546, 2005.

[232] A. Sanna, C. Pellegrini, and E. K. U. Gross. Combining eliashberg theory with density functional theory for the accurate prediction of superconducting transition temperatures and gap functions. *Phys. Rev. Lett.*, 125:057001, 2020.

[233] Mitsuaki Kawamura, Yuma Hizume, and Taisuke Ozaki. Benchmark of density functional theory for superconductors in elemental materials. *Phys. Rev. B*, 101:134511, 2020.

[234] Martin Lüders, M. A. L. Marques, A. Floris, G. Profeta, N. N. Lathiotakis, C. Franchini, A. Sanna, A. Continenza, S. Massidda, and E. K. U. Gross. Density functional theory for superconductors. *Psi-k newsletter*, 76:54, 2006.

[235] C. Grimaldi, L. Pietronero, and S. Strässler. Nonadiabatic superconductivity. ii. generalized eliashberg equations beyond migdal's theorem. *Phys. Rev. B*, 52:10530–10546, 1995.

[236] C. Grimaldi, L. Pietronero, and S. Strässler. Nonadiabatic superconductivity: Electron-phonon interaction beyond migdal's theorem. *Phys. Rev. Lett.*, 75:1158–1161, 1995.

[237] Fabian Schrodi, Peter M. Oppeneer, and Alex Aperis. Full-bandwidth eliashberg theory of superconductivity beyond migdal's approximation. *Phys. Rev. B*, 102:024503, 2020.

[238] L. Boeri, G. B. Bachelet, E. Cappelluti, and L. Pietronero. Small fermi energy and phonon anharmonicity in MgB_2 and related compounds. *Phys. Rev. B*, 65:214501, 2002.

[239] Ion Errea, Matteo Calandra, and Francesco Mauri. First-principles theory of anharmonicity and the inverse isotope effect in superconducting palladium-hydride compounds. *Phys. Rev. Lett.*, 111:177002, 2013.

[240] Christoph Heil, Samuel Poncé, Henry Lambert, Martin Schlipf, Elena R. Margine, and Feliciano Giustino. Origin of superconductivity and latent charge density wave in NbS_2. *Phys. Rev. Lett.*, 119:087003, 2017.

[241] N. Ashcroft and N. Mermin. *Solid State Physics*, chapter 25. Harcourt College Publishers, 1976.

[242] Yi Wang, Shun-Li Shang, Huazhi Fang, Zi-Kui Liu, and Long-Qing Chen. First-principles calculations of lattice dynamics and the thermal properties of polar solids. *npj Computational Materials*, 2:16006, 2016.

[243] Lorenzo Monacelli, Raffaello Bianco, Marco Cherubini, Matteo Calandra, Ion Errea, and Francesco Mauri. The stochastic self-consistent harmonic approximation: calculating vibrational properties of materials with full quantum and anharmonic effects. *J. Phys. Condens. Matter*, 33:363001, 2021.

[244] W. Kohn and J. M. Luttinger. New mechanism for superconductivity. *Phys. Rev. Lett.*, 15:524, 1965.

[245] Ryosuke Akashi and Ryotaro Arita. Density functional theory for plasmon-assisted superconductivity. *J. Phys. Soc. Jpn.*, 83:061016, 2014.

[246] Tôru Moriya and Kazuo Ueda. Spin fluctuations and high temperature superconductivity. *Advances in Physics*, 49:555–606, 2000.

[247] Jeffrey M. McMahon and David M. Ceperley. High-temperature superconductivity in atomic metallic hydrogen. *Phys. Rev. B*, 84:144515, 2011.

[248] C. M. Pépin, G. Geneste, A. Dewaele, M. Mezouar, and P. Loubeyre. Synthesis of FeH_5: A layered structure with atomic hydrogen slabs. *Science*, 357:382–385, 2017.

[249] Christoph Heil, Giovanni B. Bachelet, and Lilia Boeri. Absence of superconductivity in iron polyhydrides at high pressures. *Phys. Rev. B*, 97:214510, 2018.

[250] Feliciano Giustino, Marvin L. Cohen, and Steven G. Louie. GW method with the self-consisten Sternheimer equation. *Phys. Rev. B*, 81:115105, 2010.

[251] A. Machida, A. Ohmura, T. Watanuki, K. Aoki, and K. Takemura. Long-period stacking structures in yttrium trihydride at high pressure. *Phys. Rev. B*, 76:052101, 2007.

[252] Duck Young Kim, Ralph H. Scheicher, and Rajeev Ahuja. Predicted high-temperature superconducting state in the hydrogen-dense transition-metal hydride YH_3 at 40 K and 17.7 gpa. *Phys. Rev. Lett.*, 103:077002, 2009.

[253] Wataru Sano, Takashi Koretsune, Terumasa Tadano, Ryosuke Akashi, and Ryotaro Arita. Effect of van hove singularities on high-T_c superconductivity in H_3S. *Phys. Rev. B*, 93:094525, 2016.

[254] H. Suhl, B. T. Matthias, and L. R. Walker. Bardeen-cooper-schrieffer theory of superconductivity in the case of overlapping bands. *Phys. Rev. Lett.*, 3:552, 1959.

[255] Henry Lambert and Feliciano Giustino. *Ab initio* Sternheimer-GW method for quasiparticle calculations using plane waves. *Phys. Rev. B*, 88:075117, 2013.

[256] Christoph Heil, Heinrich Sormann, Lilia Boeri, Markus Aichhorn, and Wolfgang von der Linden. Accurate bare susceptibilities from full-potential *ab initio* calculations. *Phys. Rev. B*, 90:115143, 2014.

[257] Pui K. Lam and Marvin L. Cohen. *Ab initio* calculation of phonon frequencies of al. *Phys. Rev. B*, 25:6139, 1982.

[258] Feliciano Giustino. *Materials Modelling using Density Functional Theory: Properties and Predictions*. Oxford University Press, 2014.

[259] José A. Flores-Livas, Migle Grauzinyte, Lilia Boeri, Gianni Profeta, and Antonio Sanna. Superconductivity in doped polyethylene at high pressure. *The European Physical Journal B*, 91:176, 2018.

[260] M. Martinez-Canales and A. Bergara. No evidence of metallic methane at high pressure. *High Pressure Research*, 26:369–375, 2006.

[261] M. D. Riktor, M. H. Sorby, K. Chlopek, M. Fichtner, F. Buchter, A. Züttel, and B. C. Hauback. *In situ* synchrotron diffraction studies of phase transitions and thermal decomposition of $Mg(BH_4)_2$ and $Ca(BH_4)_2$. *Journal of Materials Chemistry*, 17:4939–4942, 2007.

[262] M. D. Riktor, M. H. Sørby, K. Chlopek, M. Fichtner, and B. C. Hauback. The identification of a hitherto unknown intermediate phase CaB_2H_x from decomposition of $Ca(BH_4)_2$. *Journal of Materials Chemistry*, 19(2754-2759), 2009.

[263] Yigang Yan, Arndt Remhof, Daniel Rentsch, Andreas Züttel, Santanab Giri, and Puru Jena. A novel strategy for reversible hydrogen storage in $Ca(BH_4)_2$. *Chem. Commun.*, 51:11008, 2015.

[264] Yoonyoung Kim, Son-Jong Hwang, Jae-Hyeok Shim, Yong-Su Lee, Heung Nam Han, and Yong Whan Cho. Investigation of the dehydrogenation reaction pathway of $ca(bh_4)_2$ and reversibility of intermediate phases. *J. Phys. Chem. C*, 116:4330–4334, 2012.

[265] Yoonyoung Kim, Son-Jong Hwang, Young-Su Lee, Jin-Yoo Suh, Heung Nam Han, and Yound Whan Cho. Hydrogen back-pressure effects on the dehydrogenation reaction of $Ca(BH_4)_2$. *J. Phys. Chem. C*, 116:25715–25720, 2012.

[266] V. Ozolins, E. H. Majzoub, and C. Wolverton. First-principles prediction of thermodynamically reversible hydrogen storage reactions in the Li-Mg-Ca-B-H system. *J. Am. Chem. Soc.*, 131:230–237, 2009.

[267] Yongsheng Zhang, Eric Majzoub., Vidvus Ozolins, and Chris Wolverton. Theoretical prediction of different decomposition paths for $Ca(BH_4)_2$ and $Mg(BH_4)_2$. *Phys. Rev. B*, 82:174107, 2010.

[268] Sheena Shah and Aleksey N. Kolmogorov. Stability and superconductivity of Ca-B phases at ambient and high pressure. *Phys. Rev. B*, 88:014107, 2013.

[269] Philippe C. Aeberhard, Keith Refson, Peter P. Ewards, and William I. F. David. High-pressure crystal structure prediction of calcium borohydride using density functional theory. *Phys. Rev. B*, 83:174102, 2011.

[270] Vitalie Stavila, Jae-Hyuk Her, Wei Zhou, Son-Jong Hwang, Chul Kim, Leigh Anna M. Ottley, and Terrence J. Udovic. Probing the structure, stability and hydrogen storage properties of dodecahydro-*closo*-dodecaborate. *Journal of Solid State Chemistry*, 183:1133–1140, 2010.

[271] Jochen Heyd and Gustavo E. Scuseria. Hybrid functionals based on a screened coulomb potential. *J. Chem. Phys.*, 118:8207, 2003.

[272] Paolo Giannozzi, Stefano Baroni, Nicola Bonini, Matteo Calandra, Roberto Car, Carlo Cavazzoni, Davide Ceresoli, Guido L. Chiarotti, Matteo Cococcioni, and Ismaila Dabo. QUANTUM ESPRESSO: a modular and open-source software project for quantum simulation of materials. *J. Phys.: Condens. Matter*, 21:395502, 2009.

[273] Paolo Giannozzi, O. Andreussi, T. Brumme, O. Bunau, M. Buongiorno Nardelli, M. Calandra, R. Car, C. Cavazzoni, D. Ceresoli, M. Cococcioni, N. Colonna, I. Carnimeo, A. Dal Corso, S. de Gironcoli, P. Delugas, R. A. DiStasio, A. Ferretti, A. Floris, G. Fratesi, G. Fugallo, R. Gebauer, U. Gerstmann, F. Giustino, T. Gorni, J. Jia, M. Kawamura, H-Y Ko, A. Kokalj, E. Kücükbenli, M. Lazzeri, M. Marsili, N. Marzari, F. Mauri, N. L. Nguyen, H-V Nguyen, A. Otero de-la Roza, L. Paulatto, S. Poncé, D. Rocca, R. Sabatini, B. Santra, M. Schlipf, A. P. Seitsonen, A. Smogunov, I. Timrov, T. Thonhauser, P. Umari, N. Vast, X. Wu, and S. Baroni. Advanced capabilities for materials modelling with quantum espresso. *J. Phys.: Condens. Matter*, 29:465901, 2017.

[274] J. P. Carbotte. Properties of boson-exchange superconductorsa. *Rev. Mod. Phys*, 62:1027, 1990.

[275] G. Renaudin, S. Gomes, H. Hagemann, L. Keller, and K. Yvon. Structural and spectroscopic studies on the alkali borohydrides MBH_4 (M = Na, K, Rb, Cs). *Journal of Alloys and Compounds*, 375:98–106, 2004.

[276] Alexander G. Kvashin, Christian Tantardini, Hayk A. Zakaryan, Yulia A. Kvashina, and Artem R. Oganov. Computational search for new W-Mo-B compounds. *Chem. Mater.*, 32:7028–7035, 2020.

[277] Shyue Ping Ong, William Davidson Richards, Anubhav Jain, Geffroy Hautier, Michael Kocher, Shreyas Cholia, Dan Gunter, Vincent L. Chevrier, Kristin A. Persson, and Gerbrand Ceder. Python materials genomics (pymatgen): A robust, open-source python library for materials analysis. *Comp. Mat. Sc.*, 68:314–319, 2013.

[278] Mark Paskevicius, Lars H. Jepsen, Pascal Schouwink, Radovan Cerný, Dorthe B. Ravnsbaek, Yaroslav Filinchuk, Martin Dornheim, Flemming Besenbacher, and Torben R. Jensen. Metal borohydrides and derivatives - synthesis, structure and properties. *Chem. Soc. Rev.*, 46:1565–1634, 2017.

[279] Jakob B. Grinderslev, Morten B. Ley, Young-Su Lee, Lars H. Jepsen, Mathias Jørgensen, Young Whan Cho, Jørgen Skibsted, and Torben R. Jensen. Ammine lanthanum and cerium borohydrides, $M(BH_4)_3 \cdot NH_3$; trends in synthesis, structures, and thermal properties. *Inorganic Chemistry*, 59:7768–7778, 2020.

[280] Line H. Rude, Thomas K. Nielsen, Dorthe B. Ravnsbaek, Ulrike Bösenberg, Morten B. Ley, Bo Richter, Lene M. Arnbjerg, Martin Dornheim, Yaroslav Filinchuk, Flemming Besenbacher, and Torben R. Jensen. Tailoring properties of borohydrides for hydrogen storage: A review. *Phys. Status Solidi*, 208:1754–1773, 2011.

[281] José A. Flores-Livas, Antonio Sanna, Alexander P. Drodzov, Lilia Boeri, Gianni Profeta, Mikhail Eremets, and Stefan Goedecker. Interplay between structure and superconductivity: Metastable phases of phosphorous under pressure. *Phys. Rev. Materials*, 1:024802, 2017.

[282] Wenhao Sun, Stephen T. Dacek, Shyue Ping Ong, Geoffroy Hautier, Anubhav Jain, William Davidson Richards, Anthony C. Gamst, Kristin A. Persson, and Gerbrand Ceder. The thermodynamic scale of inorganic crystalline metastability. *Science Advances*, 2(11), 2016.

[283] E. Sanville, S. D. Kenny, R. Smith, and G. Henkelmann. An improved grid-based algorithm for Bader charge allocation. *J. Comp. Chem.*, 28:899–908, 2007.

[284] Keun-Ho Lee, K. J. Chang, and Marvin L. Cohen. First-principles calculations of the Coulomb pseudopotential μ^*: Application to Al. *Phys. Rev. B*, 52:1425, 1995.

[285] Hao Song, Zihan Zhang, Tian Cui2, Chris J. Pickard, Vladimir Z. Kresin, and Defang Duan. High tc superconductivity in heavy rare earth hydrides: correlation between the presence of the f states on the fermi surface, nesting and the value of T_c. *arXiv:2010.12225*, 2020.

[286] Simone Di Cataldo, Shadi Qulaghasi, Giovanni B. Bachelet, and Lilia Boeri. High-T_c superconductivity in doped boron-carbon clathrates. *arXiv preprint, arXiv:2110.05333*, 2021.

[287] Stephen L. Adler. Quantum theory of the dielectric constant in real solids. *Phys. Rev.*, 126:413, 1962.

[288] Lars Hedin. New method for calculating the one-particle green's function with application to the electron-gas problem. *Phys. Rev.*, 139:A796, 1965.

[289] Simone Di Cataldo, Christoph Heil, Wolfgang von der Linden, and Lilia Boeri. $LaBH_8$: the first low-pressure superhydride. *arXiv preprint, arXiv:2102.11227*, 2021.

[290] D. R. Hamann. Optimized norm-conserving vanderbilt pseudopotentials. *Phys. Rev. B*, 88:085117, 2017.

[291] Arash A. Mostofi, Jonathan R. Yates, Giovanni Pizzi, Young-Su Lee, Ivo Souza, David Vanderbilt, and Nicola Marzari. An updated version of wannier90: A tool for obtaining maximally-localised wannier functions. *Comp. Phys. Communications*, 185:2309–2310, 2014.

[292] G. Kresse and J. Furthmüller. Efficient iterative schemes for *ab-initio* total-energy calculations using a plane-wave basis set. *Phys. Rev. B*, 54:11169, 1996.

[293] K. Momma and F. Izumi. VESTA: a three-dimensional visualization system for electronic and structural analysis. *J. Appl. Cryst.*, 41:653–658, 2008.

[294] M. Kawamura. Fermisurfer: Fermi-surface viewer providing multiple representation schemes. *Comp. Phys. Communications*, 239:197, 2019.

Part III

Part III: Appendixes

Appendix A

List of Publications

In this section I have included a list of the works I have published during my PhD.

A.1 Publications Discussed in this Thesis

- C. Heil, S. Di Cataldo, G. B. Bachelet, and L. Boeri, *Superconductivity in sodalite-like yttrium hydride clathrates*, Physical Review B **99**, 220502(R), (2019)
- S. Di Cataldo, W. von der Linden, and L. Boeri, *Phase diagram and superconductivity of calcium borohydrides at extreme pressures*, Physical Review B **102**, 014516 (2020)
- S. Di Cataldo, C. Heil, W. von der Linden, and L. Boeri, *$LaBH_8$: the first high-T_c low-pressure superhydride*, Physical Review B **104**, L020511 (2021)
- S. Di Cataldo, W. von der Linden, L. Boeri, *La-X-H hydrides: is hot superconductivity possible?*, arXiv preprint, arXiv:2106.07266, accepted in npj: Computational Materials

A.2 Other Publications

- S. Saha, S. Di Cataldo, M. Amsler, W. von der Linden, and L. Boeri, *High-temperature conventional superconductivity in the boron-carbon system: Material trends*, Physical Review B **102**, 024519 (2020)
- F. M. Rohrhofer, S. Saha, S. Di Cataldo, B. C. Geiger, W. von der Linden, L. Boeri, *Importance of feature engineering and database selection in a machine learning model: A case study on carbon crystal structures*, arXiv preprint, arXiv:2102.00191 (2021)
- S. Di Cataldo, S. Qulaghasi, G. B. Bachelet, L. Boeri *High-T_c Superconductivity in doped boron-carbon clathrates*, arXiv preprint, arXiv:2110.05333

Appendix B

Derivation of the Morel-Anderson pseudopotential

In this section I will derive the Morel-Anderson pseudopotential in the calculation of the superconducting state Green's function. The main difference between the electron-electron and the electron-phonon interaction is that there is no equivalent of Migdal's theorem for the former. This means that there is no justification for limiting the diagrammatic expansion up to a certain order. This makes an accurate evaluation of Coulomb effects in the normal state a quite formidable task.

The Coulomb interaction in the Hamiltonian is

$$H_C = \sum_{\vec{q}\vec{G}} \frac{4\pi e^2}{|\vec{q}+\vec{G}|^2} \rho^{\dagger}_{\vec{q}+\vec{G}} \rho_{\vec{q}+\vec{G}} \tag{B.1}$$

Where $\rho_{\vec{q}+\vec{G}}$ is the Fourier transform of the electron density operator

$$\rho_{\vec{q}+\vec{G}} = \sum_{\vec{k}\vec{k}'} \langle \vec{k}' |\, e^{-i(\vec{q}+\vec{G})\vec{r}} \,| \vec{k} \rangle \, c^{\dagger}_{\vec{k}'} c_{\vec{k}} \tag{B.2}$$

The first- and second-order diagrams of the self-energy expansion are shown in Fig. B.1 Graphs

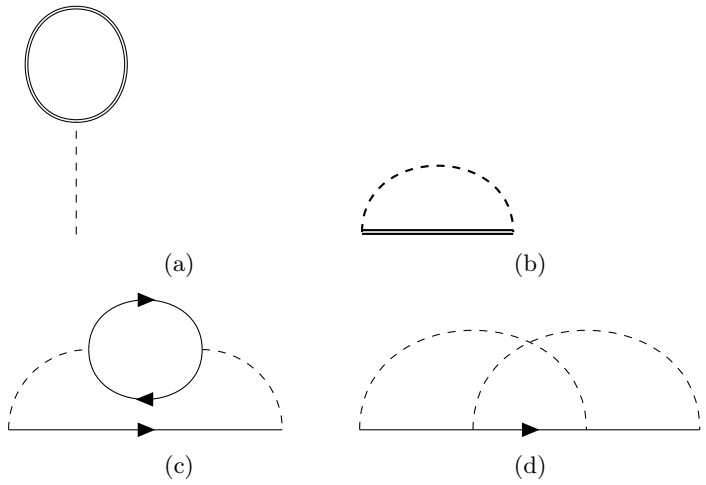

Figure B.1: First- and second- order diagrams of the electronic self-energy. (a) and (b) are the Hartree and Fock diagrams. (b) and (c) are the second-order corrections to the Hartree-Fock theory.

(a) and (b) correspond to the Hartree and Fock terms Σ_H and Σ_F:

$$\Sigma_H(\vec{k}, i\omega_n) = 2\sum_{\vec{q}\vec{G}} \frac{4\pi e^2}{|\vec{G}|^2} \langle \vec{k}| \, e^{-i\vec{G}\vec{r}} \, |\vec{k}\rangle \, \langle \vec{k} - \vec{Q}| \, e^{i\vec{G}\vec{r}} \, |\vec{k} - \vec{q}\rangle \, T\sum_{\nu} G(\vec{k} - \vec{q}, i\omega_n - i\omega_\nu) \tag{B.3}$$

$$\Sigma_F(\vec{k}, i\omega_n) = -\sum_{\vec{q}\vec{G}} \frac{4\pi e^2}{|\vec{q} + \vec{G}|^2} | \, \langle \vec{k} - \vec{q}| \, e^{-i(\vec{q}+\vec{G})\vec{r}} \, |\vec{k}\rangle \, |^2 T\sum_{\nu} G(\vec{k} - \vec{q}, i\omega_n - i\omega_\nu) \tag{B.4}$$

Where the complete (self-consistent) electron Green's function G was used in place of G_0. The only two second-order diagrams that were not implicitly included by using G are (c) and (d) of Fig. B.1. In the model considered, an infinite series of graph is kept for diagram (c) (shown in Fig. B.2), while the diagram (d) of Fig. B.1 is neglected. The diagram of Fig. B.1 contains the screening by electronic polarization of the Coulomb interaction of the Fock graph, and is named Σ_{SC}. It is useful to define the electron-hole propagator χ (analogous to the electron Green's function), which is related by its analytic continuation onto the real axis with the electronic density-density susceptibility.

$$\chi_{\vec{G}\vec{G}'}(\vec{q}\tau) = -\langle \, T_\tau \rho_{\vec{q}+\vec{G}}(\tau) \rho^\dagger_{\vec{q}+\vec{G}'}(0) \rangle \tag{B.5}$$

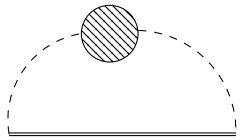

(a)

Figure B.2: Feynman diagram for the self-consistent Fock term, including screening by electronic polarization.

In equations, Σ_{SC} is analogous to Σ_{ep} (eq. (4.30)) (where χ is analogous to the phonon propagator D):

$$\begin{aligned}\Sigma_{SC}(\vec{k}, i\omega_n) = -T\sum_{\vec{q}\vec{G}\vec{G}'}\sum_{\nu} \langle \vec{k}| \, \frac{4\pi e^2}{|\vec{q}+\vec{G}|^2} e^{+i(\vec{q}+\vec{G}')\vec{r}} \, |\vec{k} - \vec{q}\rangle \;\; \chi_{\vec{G}\vec{G}'}(\vec{k} - \vec{k}', i\omega_\nu) \\ \times \langle \vec{k} - \vec{q}| \, \frac{4\pi e^2}{|\vec{q}+\vec{G}'|^2} e^{+i(\vec{q}+\vec{G}')\vec{r}} \, |\vec{k}\rangle \;\; G(\vec{k} - \vec{q}, i\omega_n - i\omega_\nu)\end{aligned} \tag{B.6}$$

and one can define the electron Coulomb spectral function $\mathcal{S}(\vec{k}, \vec{k}', \Omega)$:

$$\begin{aligned}\mathcal{S}(\vec{k}, \vec{k}', \Omega) = \left(-\frac{1}{\pi}\right) N(\epsilon_F) \mathrm{Im} \left(\sum_{\vec{G}\vec{G}'}^{max} \langle \vec{k}| \, \frac{4\pi e^2}{|\vec{q}+\vec{G}|^2} e^{+i(\vec{q}+\vec{G})\vec{r}} \, |\vec{k}'\rangle \;\; \chi_{\vec{G}\vec{G}'}(\vec{q}, \omega + i\delta) \right. \\ \left. \times \langle \vec{k}'| \, \frac{4\pi e^2}{|\vec{q}+\vec{G}'|^2} e^{+i(\vec{q}+\vec{G}')\vec{r}} \, |\vec{k}\rangle \right)\end{aligned} \tag{B.7}$$

The calculation of $\mathcal{S}$ is a difficult task, which does not add to the discussion. It is sufficient to know that it can be computed within certain approximations [250, 287, 288]. Then one can rewrite the self-energy in terms of $\mathcal{S}$:

$$\Sigma_{SC}(\vec{k}, i\omega_n) = T\sum_{\vec{k}', \nu} \int_0^\infty d\Omega \frac{\mathcal{S}(\vec{k}, \vec{k}', \Omega)}{N(\epsilon_F)} \frac{2\Omega}{\omega_\nu^2 + \Omega^2} G(\vec{k}', i\omega_n - i\omega_\nu) \tag{B.8}$$

Which can also be expressed by splitting the splitting the sums over $\vec{k}$ into a discrete sum over the

angular part J and an integral over the energy ϵ:

$$\Sigma_{SC,J}(\epsilon, i\omega_n) = T\sum_{J'}\int_{-\infty}^{\infty} d\epsilon' \frac{N(\epsilon')}{N(0)} \int_0^{\infty} d\Omega \mathcal{S}_{JJ'}(\epsilon, \epsilon', \Omega) \frac{2\Omega}{\omega_\nu^2 + \Omega^2} G(\epsilon', i\omega_n - i\omega_\nu) \tag{B.9}$$

This formula is the analogous of eq. (4.32), except that the Éliashberg function $\alpha^2 F$ is replaced by the Coulomb spectral function $\mathcal{S}$. The main difference is that in the case of $\alpha^2 F$ there was an obvious cutoff to the integral, as the maximum phonon energy is bound. In the case of $\mathcal{S}$ there is not. In fact, $\mathcal{S}$ has to be integrated up to energies of the order of 50-100 eV. The treatment of Coulomb effects in the normal state is, in fact, quite difficult. When discussing the effect of the Coulomb interaction on superconductivity, however, the argument can be greatly simplified.

In fact, one assumes that the Coulomb interaction in the *normal* state has already been treated in the calculation of the band structure $\epsilon_{\vec{k}}$, and in the phonon dispersion $\omega_{\vec{q}\nu}$. Hence, in the superconducting state one only has to consider the remaining part of the self-energy. One can write the remaining part of the Coulomb self energies $\hat{\Sigma}_{SC}$ and $\hat{\Sigma}_F$ as:

$$\begin{aligned}\hat{\Sigma}_{SC}(\vec{k}, i\omega_n) = T\sum_{\vec{k}',\nu}\int_{-\infty}^{\infty} d\epsilon' \frac{N(\epsilon')}{N(\epsilon_F)} \int_0^{\infty} d\Omega \frac{\mathcal{S}(J, J', \epsilon, \epsilon', \Omega)}{N(\epsilon_F)} \\ \times \frac{2\Omega}{\omega_\nu^2 + \Omega^2} \hat{\tau}_3 \left[\hat{G}_{J'}(\epsilon', i\omega_n - i\omega_\nu) - \hat{G}^N_{J'}(\epsilon', i\omega_n - i\omega_\nu)\right] \hat{\tau}_3\end{aligned} \tag{B.10}$$

and

$$\begin{aligned}\hat{\Sigma}_F = -T\sum_{J'\nu}\int_{-\infty}^{\infty} d\epsilon' N(\epsilon') V_{JJ'}(\epsilon, \epsilon') \\ \times \frac{2\Omega}{\omega_\nu^2 + \Omega^2} \hat{\tau}_3 \left[\hat{G}_{J'}(\epsilon', i\omega_n - i\omega_\nu) - \hat{G}^N_{J'}(\epsilon', i\omega_n - i\omega_\nu)\right] \hat{\tau}_3\end{aligned} \tag{B.11}$$

The difference $\hat{G}_{J'} - \hat{G}^N_{J'}$ originates from the fact that the Coulomb contribution to $\hat{\Sigma}$ in the normal state is already included in the band structure $\epsilon_{\vec{k}}$, and the difference avoids double-counting it in Σ. One then notes that as T approaches T_c, $\hat{G}_{J'} - \hat{G}^N_{J'}$ approaches the off-diagonal part of $\hat{G}$, named $\hat{G}^{od}$. This approximation remains good even far from T_c, hence one can assume that $\hat{G}_{J'} - \hat{G}^N_{J'}$ is well approximated by $\hat{G}^{od}$, which is the part that must be treated in the description of superconductivity.

At this point one would like to introduce a cutoff on the summation over ω_ν in eq. (B.10) and (B.11). The summation over ω_ν in eq. (B.11) can be split by introducing a cutoff ω_c for eq. (B.11) and splitting the sum into $\omega_{n'} > \omega_c$ and $\omega_{n'} < \omega_c$, with $\omega_{n'} = \omega_n - \omega_\nu$. For ω_c sufficiently large, Σ_{SC} is going to be small because of the $\frac{2\Omega}{\omega_\nu^2 + \Omega^2}$ denominator, hence the approximation:

$$\hat{\tau}_3 \hat{G}^{od}(\vec{k}', i\omega_n') \hat{\tau}_3 \xrightarrow{|\omega_n'| > \omega_c} \frac{-\hat{\Sigma}_F^{od}}{(i\omega_n')^2 - \epsilon_{\vec{k}'}^2} \tag{B.12}$$

Also assuming that $\omega_c \gg Z, \chi, \phi$. Then, one can put the part of the sum with $|\omega_n| > \omega_c$ onto the right side of eq. (B.11) and write:

$$\begin{aligned}\sum_{J'}\int_{-\infty}^{\infty}\left(\delta_{JJ'}\delta(\epsilon - \epsilon') - T\sum_{n'}^{|\omega_n'| > \omega_c} N(\epsilon') \frac{V_{JJ'}(\epsilon, \epsilon')}{(i\omega_n')^2 - \epsilon'^2}\right) \hat{\Sigma}_{F,J'}(\epsilon') \\ = -T\sum_{n'}^{|\omega_n'| < \omega_c}\sum_{J'}\int_{-\infty}^{\infty} d\epsilon' N(\epsilon') V_{JJ'}(\epsilon, \epsilon') \hat{\tau}_3 \hat{G}^{od}(\epsilon', i\omega_{n'}) \hat{\tau}_3\end{aligned} \tag{B.13}$$

Eq. (B.13) can be inverted, defining R as its inverse. R must satisfy the relation:

$$\sum_{J'}\int_{-\infty}^{\infty}\left(\delta_{JJ'}\delta(\epsilon-\epsilon')-T\sum_{n'}^{|\omega_{n'}|>\omega_c}N(\epsilon')\frac{V_{JJ'}(\epsilon,\epsilon')}{(i\omega_{n'})^2-\epsilon'^2}\right)R_{J'J''}(\epsilon'\epsilon'',\omega_c)=\delta_{JJ'}\delta(\epsilon-\epsilon'') \quad \text{(B.14)}$$

At this point one can define the Coulomb *pseudopotential* U, which satisfies the equation:

$$U_{JJ'}(\epsilon,\epsilon',\omega_c)=N(\epsilon_F)\sum_{J''}\int_{-\infty}^{\infty}d\epsilon'' R_{JJ''}(\epsilon,\epsilon'',\omega_{cut})V_{J''J'}(\epsilon'',\epsilon') \quad \text{(B.15)}$$

Using U one can rewrite $\hat{\Sigma_F}$ as:

$$\hat{\Sigma}_F(\epsilon,i\omega_n)=-T\sum_{n',J'}^{|\omega_{n'}|<\omega_c}\int_{-\infty}^{\infty}d\epsilon'\frac{N(\epsilon')}{N(\epsilon_F)}U_{JJ'}(\epsilon,\epsilon',\omega_c)\hat{\tau}_3\hat{G}^{od}(\epsilon',i\omega_n)\hat{\tau}_3 \quad \text{(B.16)}$$

The difference between eq. (B.16) and eq.(B.11) is that now the summation is up to ω_c, and all terms at higher energy were re-cast into the interaction $V \to U$.

The next step is to consider the sum of both pieces of the Coulomb self-energy $\hat{\Sigma}_C = \hat{\Sigma}_F + \hat{\Sigma}_{SC}$. A procedure formally identical to the one for $\hat{\Sigma}_F$ can be applied again, this time by introducing a second cutoff ω_{cut} which is a few times the largest phonon frequency, e.g. $\omega_{cut} > 5\omega_D$. Again, one splits $\hat{\Sigma}_C$ into a sum for $\omega_c > |\omega_{n'}| > \omega_{cut}$, and $|\omega_{n'}| < \omega_{cut}$. Then one can approximate $\hat{\Sigma}^{od}_{C,J}(\epsilon,i\omega'_n) \xrightarrow{|\omega_{n'}|>\omega_{cut}} \hat{G}^{od}(\epsilon,i\omega'_n)$, invert the equation, and write an effective potential U^*:

$$\begin{aligned}U^*_{JJ'}(\epsilon,\epsilon',\omega_{cut}) &= U_{JJ'}(\epsilon,\epsilon',\omega_c)+\int_0^{+\infty}\frac{2\Omega}{\omega_\nu^2+\Omega^2}\mathcal{S}(J,J',\epsilon,\epsilon',\Omega)+\\ T\sum_{n',J''}^{\omega_c>|\omega_{n'}|>\omega_{cut}}&\int_{-\infty}^{\infty}d\epsilon''\frac{U_{JJ'}(\epsilon,\epsilon',\omega_c)+\int_0^{+\infty}\frac{2\Omega}{\omega_\nu^2+\Omega^2}\mathcal{S}(J,J',\epsilon,\epsilon',\Omega)}{(i\omega_{n'})^2-\epsilon''^2}U^*_{J''J'}(\epsilon,\epsilon';\omega_{cut})\end{aligned} \quad \text{(B.17)}$$

At this point, $\hat{\Sigma}_C$ only contains a summation up to ω_{cut}, which is a few times the typical phonon frequency. Within this range one can assume the Coulomb interaction to be so slowly-varying that it is essentially independent from energy and isotropic. This assumption is justified *a posteriori* by the fact that the estimated effect of the residual Coulomb interaction is small. Within these approximations, the Coulomb pseudopotential can be approximated by a constant $U^{tot}_{JJ'}(\epsilon\epsilon';\omega_{cut}) = \mu(\omega_{cut})$.

The result is a simplified equation for the Coulomb interaction:

$$\hat{\Sigma}_C(i\omega_n,\vec{k})=-T\sum_{J',n'}^{|\omega_{n'}<\omega_c|}\mu^*_{JJ'}(\omega_c)\int_{-\infty}^{\infty}\hat{\tau}_3\hat{G}^{od}(\epsilon,i\omega_{n'})\hat{\tau}_3 \quad \text{(B.18)}$$

An expression of μ^* can be found by making a model for the ϵ and ϵ' dependence of $N(\epsilon)$ and $U^*_{JJ'}(\epsilon,\epsilon')$, i.e. assume that they are both constant for $|\epsilon|$ and $|\epsilon'|$ smaller than ω_{cut} and zero otherwise. Within this energy-independent model one finds:

$$\mu^*(\omega_{cut}) = \mu/\left[1+\mu log(\omega_c/\omega_{cut})\right] \quad \text{(B.19)}$$

Typically the term $log(\omega_c/\omega_{cut})$ is of the order of 5, as ω_{cut} is of the order of the plasma frequency ($\sim$50 eV), while ω_{cut} is of the order of the Debye frequency($\sim$0.50 eV). While the calculation of μ^* involves several approximations, the result is a small treatable number, which only lightly affects superconductivity. In most materials, μ^* is found to be between 0.08 and 0.20. The smallness of μ^* justifies the crude approximations made, as in general its effects on superconductivity are not particularly strong.

Appendix C

Computational Details

In this Chapter I report the details of the calculations presented in Chapters 5, 6, and 7, corresponding to Refs. [7–9, 289]. This chapter is divided into three sections, each corresponding to the Chapter with the same name, for an easier consultation.

C.1 Sodalite-like Yttrium Hydride Clathrates

The calculations were performed using Density Functional Theory (DFT) and employing "optimized norm-conserving Vanderbilt" (ONCV) pseudopotentials. The exchange-correlation part was treated within the Generalized Gradient Approximation, within the Perdew-Burke-Ernzerhof framework. In the yttrium pseudpotential the semi-core states ($4s$, $4p$, $5s$) are included [219, 290]. I used Quantum Espresso to calculate the electronic structure and the lattice dynamics [272, 273], the Epw code [211, 227] to calculate and interpolate the electron-phonon interaction, and to solve numerically the Migdal-Éliashberg equations. To generate maximally-localized Wannier functions (MLWF) I employed the Wannier90 code [291].

A cutoff of 90 Ry (1200 eV) was used on the plane waves expansion of the wavefunctions. To calculate the ground-state charge density, the integration over the Brillouin zone was carried out using a Monkhorst-Pack (MP) **k**-grid and a Methfessel-Paxton smearing, converging energies within 1 mRyd/atom. Denser MP grids (up to $24 \times 24 \times 24$) were used to calculate the DOS, which was integrated using the tetrahedron method.

To obtain the crystal structures as a function of pressure, structural relaxations were performed until forces between atoms were less than 5×10^{-5} Ry/au. Vibrational properties were calculated on $4(6) \times 4(6) \times 4(6)$ **q**-grids for YH_3 and YH_6 (YH_{10}), and interpolated on denser **q**-grids through Fourier interpolation.

To accurately describe the superconducting properties, the *e-ph* matrix elements were interpolated onto $32 \times 32 \times 32$ $\vec{k}$ and $\vec{q}$ grids, within EPW. For the electronic part, the Y (s, p, d) and H-s atomic orbitals were used as a starting guess for the Wannier functions. In the calculations of the superconducting properties in Epw, 100 Matsubara frequencies were been used for the summation along the imaginary axis. The integration over $\vec{k}$-space were performed replacing the Dirac deltas with Lorentzians of width 150 meV for electrons and 0.15 meV for phonons.

Within SternheimerGW [250, 255], $12 \times 12 \times 12$ Brillouin zone grids were used to solve the Sternheimer equations with an energy cutoff of 8 Ry for the dielectric matrix of 8 Ry. The average of the screened Coulomb interaction was performed on the same $12 \times 12 \times 12$ grid.

C.2 Calcium Boron Hydrides

To construct the Ca-B-H phase diagram, variable-composition structural searches were carried out at fixed pressure using evolutionary algorithms as implemented in the Universal Structure Predictor: Evolutionary Xtallography software (USPEX) [47, 124]. An *anti-seeding* technique was used to

avoid oversampling of the same minima and ensure a better exploration of the phase space. Each individual in the structural search underwent a five-step relaxation to efficiently minimize stress and forces, calculated within DFT. The DFT calculations were performed using the Vienna ab-initio software package (VASP) [292], using Projector Augmented Waves (PAW) pseudopotentials with Perdew-Burke-Ernzerhof (PBE) exchange-correlation functional. The plane waves expansion of the wavefunction was truncated at an energy cutoff of 600 eV, while the reciprocal-space integration was carried out on a Monkhorst-Pack grid in $\vec{k}$ space with a 0.04 spacing in units of $\frac{2\pi}{\text{Å}}$, and a Gaussian smearing of 0.05 eV.

The ternary convex hulls in Fig.6.1 were constructed as follows: first, an exploratory run was carried out using a variable-composition evolutionary algorithm on the full compositional space, for a total of about 2000 structures per pressure, with a variable number of atoms/cell, ranging from 8 to 16.

After this preliminary search, some of the stable compositions at room pressure were already correctly identified. To further improve the sampling, I performed additional variable-compositions searches for the following pseudo-binaries: $(Ca_1B_2)_{1-x}H_x$, $(Ca_2B_2)_{1-x}H_x$, $(Ca_2B_1)_{1-x}H_x$, and $Ca_{1-x}(BH)_x$, $Ca_{1-x}B_x$, $Ca_{1-x}H_x$, and $B_{1-x}H_x$, with about 250 structures per pseudo-binary, and a number of atoms per unit cell between 8 and 18. This was sufficient to reproduce results from Refs [121,122,268], suggesting that this approach is in fact a good compromise between a complete exploration of possible compositions, and a sufficient sampling of the configuration space of each composition.

Finally, I performed additional fixed-composition structural searches for the compositions which resulted to be stable. This allowed me to further refine the prediction of the crystal structures, and resolve finer enthalpy differences, which are particularly subtle in molecular crystals. Structures in literature which had a cell size exceeding these parameters were included by hand.

After these exploratory runs, an additional structural relaxation was performed for stable and metastable structures, until each component of the force acting on atoms were lower than 1 meV/Å; finally, the total energy (or enthalpy) was computed using the tetrahedron method for $\vec{k}$-space integration, with a resolution of 0.03 $\frac{2\pi}{\text{Å}}$. The figures of the convex hulls were constructed using the python library Pymatgen [277].

The phase diagram in Fig.6.3 was obtained calculating the equation of state $E(V)$ for each stable and metastable phase identified at 0, 50, 100, and 300 GPa; the obtained relation was then fitted using the Birch-Murnaghan equation $E(V) = E_{BM}(V)$. The pressure could then be interpolated using the analytic formula derived from $P = -\partial E_{BM}(V)/\partial V$ which allowed an accurate interpolation over the intermediate pressures.

The calculations of the electronic structure, lattice dynamics, and superconductivity, were carried out with `QUANTUM` Espresso (QE) using Norm-conserving (NC) pseudopotentials, and Perdew-Burke-Ernzerhof (PBE) exchange-correlation functional. A cutoff of 80 Ry was used for the plane-wave expansion of the wave functions. Due to the different DFT code and pseudopotential, the structures were re-relaxed in QE until each component of the force on each atom was lower than 2 meV/Å. The ground-state charge density was calculated using a 0.06 Ry Methfessel-Paxton smearing and a $6 \times 6 \times 6$ Monkhorst-Pack grid in reciprocal space for integration over the Brillouin zone. Phonon calculations were performed on a $2 \times 2 \times 2$ Monkhorst-Pack grid in reciprocal-space, and the electron-phonon matrix element were integrated over the Fermi surface using a $24 \times 24 \times 24$ grid, and a Gaussian smearing with a width of 270 meV. The phonon density of states was obtained by integrating over a $20 \times 20 \times 20$ grid, obtained through Fourier interpolation of the dynamical matrices.

The figures of the crystal structures were realized using VESTA (**V**isualization for **E**lectronic and **ST**ructural **A**nalysis) [293]

C.3 Ternary Lanthanum Hydrides

C.3.1 Part I: Search of *hot* superconductivity

The convex hulls were computed employing evolutionary algorithms for variable-composition crystal structure prediction as implemented in `USPEX` [47, 124]. To ensure a robust and fast relaxation towards the local minimum, every individual was relaxed using a five-step process to minimize stress and forces, calculated within DFT. DFT calculations were performed using the Vienna *ab initio* Software Package (`VASP`) [292], with projector augmented waves (PAW) pseudopotentials with a Perdew-Burke-Ernzerhof (PBE) exchange-correlation functional. A progressively tighter convergence was used at each relaxation step, up to a cutoff on the expansion of the wavefunction in plane waves of 600 eV; and a MP grid in $\vec{k}$ space with a 0.04 $\frac{2\pi}{\text{Å}}$ spacing, and a Methfessel-Paxton smearing with a width of 0.03 eV for reciprocal-space integration. The validity of the pseudopotentials was cross-checked by comparing the result from VASP with the one from Quantum ESPRESSO. In fact, electronic structure and superconductivity calculations were performed with `Quantum ESPRESSO` (QE), using Norm-Conserving pseudopotentials. Among all the structures examined, both VASP and QE gave identical results.

The ternary hulls were constructed following the multi-step procedure proposed by Kvashin et al. [276]:

1. Perform a preliminary variable-composition evolutionary search with a maximum number of atoms in the unit cell equal to 20, so that the number of possible compositions is not too large. For this search I considered 30 generations with 200 individuals in the first, and 60 individuals in each subsequent generation. This level of accuracy is not sufficient to correctly identify the minima of the enthalpy for many compositions, but it is useful to preliminary assess the possible formation of intermediate ternary phases.

2. Extend the search to binary phases on the edges of the ternary hull, and for selected pseudo-binaries, the latter with a larger unit cell (up to 40 atoms). The pseudo-binary phases which were re-sampled are: $(LaN)_xH_{1-x}$, $(LaN_2)_xH_{1-x}$, $(LaN_3)_xH_{1-x}$, $(LaH_{10})_x(NH_3)_{1-x}$, $(LaH_{10})_x(NH_5)_{1-x}$, $(LaH_{16})_x(NH_3)_{1-x}$, $(LaH_4)_x(NH_2)_{1-x}$, $(LaB)_xH_{1-x}$, $(LaB_3)_xH_{1-x}$, $(LaH_2)_x(BH)_{1-x}$, $(LaH_3)_x(BH)_{1-x}$, $(LaH_4)_x(BH)_{1-x}$, $(LaH_8)_x(BH)_{1-x}$, $(LaH_{10})_x(BH)_{1-x}$, $(LaH_{16})_x(BH)_{1-x}$, $(LaGa)_xH_{1-x}$, and $(LaPt)_xH_{1-x}$

3. **Only for La-N-H and La-B-H**. Motivated by the presence of stable ternary phases, I performed a second variable-composition evolutionary search. All the stable structures found in the previous steps were used as seeds, in order to provide the algorithm with a good starting guess. In this run the maximum cell size was set to 40 atoms, and a population of 250 individuals was employed for 20 generations

4. The convex hulls in Fig. 6.1 were constructed using `pymatgen` [277], including structures from all the previous structural searches.

The figures of the crystal structures were realized using the VESTA software (Visualization for electronic and structural analysis) [293].

Calculations of electronic structure, lattice dynamics and superconductivity were carried out within DFT and DFPT as implemented in `Quantum ESPRESSO` (QE) [25, 220, 272–274] using Optimized Norm-conserving Vanderbilt Pseudopotentials (ONCV) [290]. An energy cutoff of 80 Ry was used for the plane-wave expansion of the wavefunction.

Due to the different pseudopotential used between VASP and QE, the structures were re-relaxed in QE until the component of each force acting on single atoms was lower than 2 meV/Å. The ground-state charge density was calculated using a 0.04 Ry smearing and a 6 x 6 x 6 grid in reciprocal space for integration over the Brillouin zone. Phonon calculations were performed on a 4 x 4 x 4 MP grid for $LaBH_8$, and a 2 x 2 x 2 grid for La_4N_4H, La_2N_2H, LaN_2H_3, LaB_8H, $La_2B_6H_5$, and a 3 x 3 x 3 grid for $LaBH_{17}$, $LaGaH_6$, $LaGaH_{14}$, $LaGaH_{15}$, and $LaPtH_6$. The phonon density of states was obtained by integrating over a 16 x 16 x 16 $\vec{q}$ grid, obtained via Fourier interpolation from the calculated dynamical matrices.

The integration of the electron-phonon matrix elements over the Fermi surface was carried out on a 24 x 24 x 24 $\vec{k}$ grid, using a Gaussian smearing with a width of 200 meV.

C.3.2 Part II: $LaBH_8$

To identify the stable compositions for the La-B-H system at 100 GPa, I again performed a variable-composition structural search using the algorithm implemented in `USPEX` [47, 124]. The parameters employed for the DFT part of the structural relaxation (energy cutoff, integration over reciprocal space, structural relaxation) are identical to those of Part I. Again I followed the multi-step procedure proposed by Kvashin et al. [276], which was described in the previous section, this time with a much more thorough sampling, and the inclusion of the zero-point energy. In particular:

1. I started by performing a first, exploratory variable-composition evolutionary search with a maximum of 40 atoms per unit cell. For this search I considered 50 generations with 360 individuals in the first, and 250 individuals in each subsequent generation (for a total of about 12000 structures).

2. I re-sampled the pseudo-binary phases $(LaB)_xH_{1-x}$ (max 48 atoms) and the binary phases La_xH_{1-x}, B_xH_{1-x}, La_xB_{1-x} (max 20 atoms). I sampled a population of 160 individuals in the first, and 60 in the next, for 20 generations.

3. To improve the sampling over particularly relevant compositions, I re-sampled the following using fixed-composition structural searches: $LaBH_8$, $La(BH_2)_3$, $La(BH_3)_3$, $La(BH_4)_3$. In each search I used a maximum number of atoms in the cell corresponding to 4 formula units. I sampled a population of 80 individuals in the first, and 60 in the next generations, for a total of 20 generations.

4. I performed a second variable-composition search using all the stable structures found in the previous steps as seeds, with a maximum cell size of 40 atoms, a population size of 250 individuals, and 20 generations

5. At this stage, I combined all the searches to construct a preliminary convex hull. The structures whose composition was predicted to be thermodynamically stable were retained, as well as metastable ones with energy within 100 meV/atom. These were relaxed again with tighter constraints.

6. The zero-point energy (ZPE) of all the structures retained at the previous step was estimated by integrating the phonon density of states, calculated using Fourier interpolation from a Γ-only phonon calculation. The calculated values of the ZPE were added to the total energy.

7. With the calculated enthalpies, now including ZPE corrections, I constructed the convex hull in Fig.7.6 using `pymatgen` [277].

Calculations of electronic structure, lattice dynamics and electron-phonon properties were carried out like in Part II.

Due to the different pseudopotential employed in QE, the structure of $LaBH_8$ was re-relaxed until each component of the forces acting on atoms was less than 1 meV/Å. Calculations of the ground-state charge density were carried out using a 0.04 Ry smearing and a 8 x 8 x 8 grid for integration over the reciprocal space. The band structure was obtained by performing a non-self-consistent calculation on a high-symmetry path, starting from the previously-calculated ground-state charge density. The electronic density of states was obtained from another non-self-consistent calculation on a 30 x 30 x 30 Monkhorst-Pack $\vec{k}$-grid, and the tetrahedron integration method. The phonon calculation was performed on a 6 x 6 x 6 reciprocal-space grid ($\vec{q}$). The phonon DOS was obtained by integrating over a Fourier-interpolated 16 x 16 x 16 $\vec{q}$ grid, using a Gaussian smearing with a width of 2 meV. The atom-projected phonon DOS and Éliashberg function were obtained using the components of the phonon eigenvector relative to each atom as weight in the integration.

For the calculation of the anisotropic superconducting gap I used Wannier interpolation of the *e-ph* matrix elements, as implemented in EPW [227] . The anisotropic Migdal-Eliashberg equations

were solved self-consistently by integrating over a 30 x 30 x 30 $\vec{q}$ and 30 x 30 x 30 and 60 x 60 x 60 $\vec{k}$ grid. The figures of the hydrogen character and superconducting gap over the Fermi surface were constructed using FermiSurfer [294].

Appendix D

Example of Input files

In the following sections, I will add as reference a sample input files for the calculations presented in this thesis.

D.1 Structure Search with USPEX

This is a sample input file for a variable-composition structural search using `Uspex` version 9.4.4.

```
PARAMETERS EVOLUTIONARY ALGORITHM
****************************************
*      TYPE OF RUN AND SYSTEM            *
****************************************
USPEX   : calculationMethod (USPEX, VCNEB, META)
301        : calculationType (dim,: 0-3; mol.: 0/1; varcomp: 0/1)
1            : optType (1=enth., 2=vol., 3=hardn., 4=struc_order,...)
1            : AutoFrac
% atomType
X   Y   X
% EndAtomType
** Define variable "blocks" of compositions.
** In this case all combinations are allowed
% numSpecies
1  0  0
0  1  0
0  0  1
% EndNumSpecies
16     : minAt (min cell size)
32     : maxAt (max cell size)
****************************************
*               POPULATION             *
****************************************
200     : populationSize (individuals per generation)
250     : initialPopSize  (individuals in the first generation)
80       : numGenerations (how many generations)
10       : stopCrit (stop after best individual is the same for N generations)
0        : reoptOld (re-optimize individuals)
0.6     : bestFrac (fraction of individuals to be passed to next generation)
********************************
* VARCOMP VARIABLE *
********************************
```

```
30 : firstGeneMax (how many different composition in the first generation)
****************************************
*          VARIATION OPERATORS           *
****************************************
0.50  : fracGene (fraction of generation produced by heredity)
0.20  : fracRand (fraction of generation produced randomly from space groups)
0.20  : fracAtomsMut (fraction of the generation produced by softmutation)
0.10  : fracLatMut (fraction of the generation produced by softmutation)
********************************
* VARCOMP OPERATOR  *
********************************
0.20  : fracTrans
****************************************
*           ANTISEED SETTINGS          *
****************************************
10      : antiSeedsActivation
0.01    : antiSeedsMax
0.006   : antiSeedsSigma
****************************************
*   DETAILS OF AB INITIO CALCULATIONS   *
****************************************
% abinitioCode (select DFT code, 1 for VASP; multi-step relaxation)
1 1 1 1 1
% ENDabinit
% KresolStart (resolution in k-space)
0.14 0.12 0.1 0.08 0.04
% Kresolend
% commandExecutable
mpirun -np 4 vasp_std >& out1
mpirun -np 4 vasp_std >& out2
mpirun -np 4 vasp_std >& out3
mpirun -np 4 vasp_std >& out4
mpirun -np 4 vasp_std >& out5
% EndExecutable
2          : whichCluster (0: no-job, 1: local, 2: remote)
250      : numParallelCalcs
200      : 100 : ExternalPressure
folder_name: remoteFolder
```

D.2 Solution of the anisotropic M-É equations with EPW

This is a sample input file for the Wannier interpolation of the *e-ph* matrix elements, and solution of the anisotropic MigdalÉliashberg equations using `EPW` version 5.2.

```
EPW
\&inputepw
prefix      = 'LaBH8',
amass(1)    = 138.90547,
amass(2)    = 10.811,
amass(3)    = 1.007
outdir      = './output/'

ep_coupling = .true.    ! run e-p coupling calculation
elph        = .true.        ! calculate e-p coefficients
kmaps       = .true.    ! read 'prefix.kmap' and 'prefix.kgmap' from file
epbwrite    = .false.    ! write e-p relevant data to file (Bloch)
epbread     = .false.   ! read e-p relevant data from file (Bloch)
epwwrite    = .true.    ! (false) write e-p relevant data to file (Wannier)
epwread     = .false.   ! (true) read e-p relevant data from file (Wannier)
nbndsub     = 21         ! Number of wannier functions to utilize
nbndskip    = 1         ! The number of bands lying below the disentanglement
! window in the calculation of the Wannier functions
etf_mem      = 1        ! 0: All the fine Bloch-space el-ph matrix elements
!    are stored in memory (faster)
! 1: More IO (slower), but less memory required
! 2: Even slower, but less memory than etf_mem = 1
max_memlt    = 7.40     ! Maximum memory that can be allocated per pool

!-----  Wannier90 input ------------
wannierize   = .true.  ! calculate Wannier functions and write file 'filukk'
! if false, read file 'filukk' from disk
num_iter     = 1000
bands_skipped = 'exclude_bands = 1'
nbndsub     = 29
nbndskip    = 1
dis_win_max  =  36.0
dis_win_min  =  -5.0
dis_froz_max  =   16.3
dis_froz_min  =   13.3
wdata(1)     = 'dis_num_iter  = 1000'
wdata(2)     = 'num_bands = 30'
wdata(3)     = 'guiding_centres = .false.'
wdata(4)     = 'use_ws_distance = .true.'
wdata(5)     = 'fermi_surface_plot = true'
wdata(6)     = 'bands_plot         = true'
wdata(7)     = 'begin kpoint_path'
wdata(8)     = 'L  0.500  0.500  0.500   G  0.000  0.000  0.000'
wdata(9)     = 'G  0.000  0.000  0.000   X  0.500  0.000  0.500'
wdata(10)    = 'X  0.500  0.000  0.500   W  0.500  0.250  0.750'
wdata(11)    = 'W  0.500  0.250  0.750   L  0.500  0.500  0.500'
wdata(12)    = 'end kpoint_path'
!-------------------------------------
iverbosity  = 2         ! 0 = short, 1 = verbose, 2 = verbose for sc
eps_acustic = 15.0       ! Lower boundary for the phonon frequency
```

```
fsthick     = 0.8       ! Width of the FS window to take into account (eV)
degaussw    = 0.150     ! Smearing in the energy-conserving delta (0.025 eV)
nsmear      = 1         ! N. diff. smearings to calculate the ph. self-energy (1)
degaussq    = 0.150     ! Smearing for sum over q in the e-ph coupling (meV)
nqstep      = 500       ! N. of steps used to calculate the a2f (500)
nqsmear     = 20        ! N. of diff. smearings to calculate the a2f (10)
eliashberg  = .true.    ! Solve the Eliashberg equations and calc. a2F
ephwrite    = .true.    !  Write .ephmat files
laniso = .true.      ! solve the anis. equations on the Im-axis.
limag  = .true.      ! solve the Im-axis Eliashberg equations.
lpade  = .true.      ! Pade approximants to continue to real-axis.
conv_thr_iaxis = 1.0d-5 ! Convergence threshold for Eliashberg (1.d-05)
wscut = 1.0               ! Upper limit for Matsub. sum (1.d0 eV)
nstemp   = 21            ! Number of temps for Eliashberg equations
tempsmin =  25.00    ! min. temp
tempsmax = 155.00   ! max. temp
nsiter   = 500          ! Number of iter. for scf cycle of Eliashberg eq.
muc = 0.10              ! Morel-Anderson pseudopotential

dvscf_dir = './output/save'  ! path to phonon files
asr_typ   = 'crystal'             ! Crystal acoustic sum rule
lifc          = .false.               ! Read q2r.x force constant file (ifc.q2r)

nk1  = 6                ! Dimensions of the coarse electronic grid, corresponds
nk2  = 6                ! to the nscf calculation and wfs in the outdir
nk3  = 6
nq1  = 6                ! Dimensions of the coarse phonon grid, corresponds
nq2  = 6                ! to the nqs list
nq3  = 6
mp_mesh_k = .true.      ! fine electronic mesh is in the IBZ
nkf1 = 60
nkf2 = 60
nkf3 = 60
nqf1 = 30
nqf2 = 30
nqf3 = 30
/
```